CLICK CHEMISTRY APPLICATIONS FOR SURFACES

A Dissertation
Presented to
The Academic Faculty

by

Jennifer Marie Beveridge

In Partial Fulfillment
of the Requirements for the Degree
Doctor of Philosophy in the
College of Sciences

Georgia Institute of Technology
December 2018

CLICK CHEMISTRY APPLICATIONS FOR SURFACES

Approved by:

Professor M.G. Finn, Advisor
School of Chemistry and Biochemistry
Georgia Institute of Technology

Professor Ronghu Wu
School of Chemistry and Biochemistry
Georgia Institute of Technology

Professor Adegboyega Oyelere
School of Chemistry and Biochemistry
Georgia Institute of Technology

Professor Carsten Sievers
School of Chemical Engineering
Georgia Institute of Technology

Professor Raquel Lieberman
School of Chemistry and Biochemistry
Georgia Institute of Technology

Date Approved: October 22, 2018

This thesis is dedicated to Sr. Marilyn McCusker, who has throughout her life instilled a love of science to all of her students at Bishop McDevitt High School.

ACKNOWLEDGEMENTS

I am extremely grateful for the support provided by my family and friends over these past few years. In particular I would like to thank my parents, siblings, fellow Georgia Tech chemistry classmates, and the choir at the Shrine of the Immaculate Conception.

I would like to thank some of the people who provided guidance and assistance to the research detailed herein, including my advisor, Professor M.G. Finn, and labmates, as well as Dr. Walter Henderson, Dr. Rebhadevi Monikandran, Dr. Jie Xu, Dr. Todd Walters, and Dr. Raghunath Dasari. I also would like to thank all those who have made research available to students as well as those who contribute to making research available to all, including open-access journals, as well as the countless librarians who have helped digitize old papers and facilitate interlibrary loans.

TABLE OF CONTENTS

ACKNOWLEDGEMENTS **iv**

LIST OF TABLES **viii**

LIST OF FIGURES **xi**

LIST OF SYMBOLS AND ABBREVIATIONS **xix**

SUMMARY **xxi**

CHAPTER 1. INTRODUCTION **1**
1.1 An Introduction to Click Chemistry **1**
1.1.1 Origins 1
1.1.2 Mechanism 2
1.1.3 Applications 3
1.2 Introduction to Click Chemistry on Surfaces **4**
1.3 Introduction to instrumentation and methodologies **5**
1.3.1 X-ray Photoelectron Spectroscopy (XPS) 5
1.3.2 Variable-Pressure Scanning Electron Microscopy (VP-SEM) 6
1.3.3 Contact Angle Measurement 7
1.3.4 Nuclear Magnetic Resonance (NMR) Spectroscopy 8
1.3.5 Infrared (IR) Spectroscopy 8
1.3.6 Working with azide 9

CHAPTER 2. KINETICS of COPPER(I) AZIDE ALKYNE CYCLOADDITION WITHIN and AMONG LIPID BILAYERS **10**
2.1 Abstract **10**
2.2 Introduction to reactions in and between lipid membranes **10**
2.3 An Introduction to Click Chemistry with Lipids **11**
2.4 Experimental **14**
2.4.1 Zeta Potential Measurements 14
2.4.2 Dynamic Light Scattering (DLS) 14
2.4.3 Synthesis of lipid compounds 15
2.4.4 Vesicle Creation and Composition 24
2.4.5 Kinetics 27
2.5 Results **28**
2.5.1 Kinetics of small molecule substrates in free solution 28
2.5.2 Kinetics of one substrate in-membrane and other CuAAC partners in solution 31
2.5.3 Reactions between vesicles 36
2.5.4 Physical properties of vesicles pre- and post-CuAAC 38
2.6 Discussion **41**
2.7 Conclusion **43**

2.8 Acknowledgement 43

CHAPTER 3. COVALENT FUNCTIONALIZATION OF FLEXIBLE POLYVINYL CHLORIDE TUBING VIA COPPER(I) CATALYZED AZIDE ALKYNE CYCLOADDITION 44
3.1 Abstract 44
3.2 An Introduction to Flexible Plastics and Their Application 44
3.3 Experimental 46
3.3.1 XPS measurements 47
3.3.2 TGA/DSC measurements 48
3.3.3 Contact angle measurements 48
3.3.4 Young's modulus and hardness measurements 48
3.3.5 SEM 49
3.3.6 Alkyne synthesis 49
3.4 Results 54
3.4.1 Azidation of tubing 54
3.4.2 Whole tube modification 104
3.4.3 Copper(I)-catalyzed azide-alkyne cycloaddition to azidated substrates 108
3.4.4 Tetrazole formation from cyanated substrates 118
3.4.5 Characterization of material properties after modification 126
3.5 Discussion 132
3.6 Conclusion 133
3.7 Acknowledgement 134

CHAPTER 4. COVALENT FUNCTIONALIZATION of SU-8 NEGATIVE PHOTORESIST VIA COPPER(I) CATALYZED AZIDE ALKYNE CYCLOADDITION 135
4.1 Abstract 135
4.2 Introduction to SU-8 negative photoresist 135
4.3 Experimental 138
4.3.1 Printed photomasking 138
4.3.2 Alkyne synthesis 139
4.3.3 XPS measurements 139
4.3.4 SEM 140
4.3.5 Atomic Force Microscopy (AFM) 140
4.3.6 Contact angle measurements 140
4.3.7 Bacterial Culture and Growth 141
4.3.8 Red blood cell isolation 141
4.3.9 Chinese Hamster Ovary (CHO) cell growth 142
4.3.10 Microscopy 142
4.3.11 Fluorescence quantitation 142
4.3.12 Methyl Methacrylate (MMA) Polymerization from the SU-8 surface 142
4.3.13 4-Vinylpyridine Polymerization from the SU-8 surface 143
4.4 Results 143
4.4.1 Azidation of SU-8 143
4.4.2 CuAAC on azidated SU-8 substrates 154
4.4.3 Characterization of Materials 169

4.4.4 Biological Interactions with CuAAC-modified SU-8 173
4.5 Discussion 179
4.6 Conclusions 180
4.7 Acknowledgement 180

CHAPTER 5. OUTLOOK FOR FURTHER DEVELOPMENT 182
5.1 Further Developments with Lipids 182
5.2 Further Developments with PVC 182
5.2.1 Surfaces to prevent biofouling 182
5.3 Further Development with SU-8 183
5.3.1 Better surface adhesion for SU-8 substrates 183
5.3.2 SU-8 developments to reduce fragility 183
5.3.3 Rad-Hard Electronics 184
5.3.4 Implantable electronics 184
5.3.5 Sensors 184

REFERENCES 186

LIST OF TABLES

Table 1. Lipid composition in vesicles. 25
Table 2. Conditions for the reaction of 7-hydroxy-3-azidocoumarin CuAAC with 2-methyl-3-butyn-1-ol as depicted in Figure 22. 29
Table 3. Concentrations of reagents used to produce plots in Figure 25. 33
Table 4. Radius and zeta potential for nonfluid vesicles pre- and post- CuAAC. 39
Table 5. Radius and zeta potential for semi-fluid vesicles pre- and post- CuAAC. 40
Table 6 – Solvent tolerances for endotracheal tubing. This table reports the approximate largest amount of organic co-solvent (v/v) in water in which tubing can be immersed overnight, at room temperature before becoming inflexible as judged by simple handling. 54
Table 7. IR and XPS analysis for ET azidated (48h) with various phase transfer catalysts. Intensity of azide IR signal was normalized to the intensity of the resultant azide peak from azidation with Aliquat 336. 56
Table 8. XPS survey integration for unmodified ET. 58
Table 9. XPS survey integration for ET azidated with tetrabutylammonium bromide. .. 59
Table 10. XPS survey integration for ET azidated with Aliquat 336. 61
Table 11. XPS survey integration for ET azidated with cetylpyridinium chloride. 63
Table 12. XPS survey integration for ET azidated with tetraphenylphosphonium bromide. 65
Table 13. XPS survey integration for ET azidated with benzyldimethyltetradecylammonium chloride. 67
Table 14. XPS survey integration for ET azidated with tetrabutylammonium iodide..... 69
Table 15. XPS survey integration for ET azidated with hexadecyltrimethylammonium chloride. 70
Table 16. XPS survey integration for ET azidated with tetrabutylammonium nitrate. ... 72
Table 17. XPS survey integration for ET azidated with tetrabutylammonium cyanide. . 73
Table 18. XPS survey integration for ET azidated with tetrabutylammonium bisulfate. 75
Table 19. XPS survey integration for ET azidated with tetrabutylammonium tetrafluoroborate. 76
Table 20. IR azide peak intensity and percent nitrogen from XPS from phase transfer catalysts for azidation. 81
Table 21. XPS integration for cross-sectioned azidated ET as a function of PTC. Tetrabutylammonium bromide--close to edge of cross-section. 83
Table 22. XPS integration for cross-sectioned azidated ET as a function of PTC. Tetrabutylammonium bromide-- approximately 1/4 of the way through the cross-section. 84
Table 23. XPS integration for cross-sectioned azidated ET as a function of PTC. Tetrabutylammonium bromide-- midway way through the cross-section. 85
Table 24. XPS integration for cross-sectioned azidated ET as a function of PTC. Cetylpyridinium chloride --close to edge of cross-section. 86
Table 25. XPS integration for cross-sectioned azidated ET as a function of PTC. Cetylpyridinium chloride -- approximately 1/4 of the way through the cross-section. 87

Table 26. XPS integration for cross-sectioned azidated ET as a function of PTC. Cetylpyridinium chloride -- midway through the cross-section. 88
Table 27. XPS integration for cross-sectioned azidated ET as a function of PTC. Tetraphenylphosphonium bromide --close to edge of cross-section. 89
Table 28. XPS integration for cross-sectioned azidated ET as a function of PTC. Tetraphenylphosphonium bromide -- approximately 1/4 of the way through the cross-section. 90
Table 29. XPS integration for cross-sectioned azidated ET as a function of PTC. Tetraphenylphosphonium bromide -- midway through the cross-section. 91
Table 30. XPS integration for cross-sectioned azidated ET as a function of PTC. Benzyldimethyltetradecylammonium chloride --close to edge of cross-section. 92
Table 31. XPS integration for cross-sectioned azidated ET as a function of PTC. Benzyldimethyltetradecylammonium chloride --approximately 1/4 of the way through the cross-section. 93
Table 32. XPS integration for cross-sectioned azidated ET as a function of PTC. Benzyldimethyltetradecylammonium chloride --midway through the cross-section. 94
Table 33. XPS integration for cross-sectioned azidated ET as a function of PTC. Tetrabutylammonium iodide --close to edge of cross-section. 95
Table 34. XPS integration for cross-sectioned azidated ET as a function of PTC. Tetrabutylammonium iodide --approximately 1/4 of the way through the cross-section. 96
Table 35. XPS integration for cross-sectioned azidated ET as a function of PTC. Tetrabutylammonium iodide --midway through the cross-section. 97
Table 36. XPS integration for cross-sectioned azidated ET as a function of PTC. Hexadecyltrimetylammonium chloride --close to edge of cross-section. 98
Table 37. XPS integration for cross-sectioned azidated ET as a function of PTC. Tetrabutylammonium iodide --approximately 1/4 of the way through the cross-section. 99
Table 38. XPS integration for cross-sectioned azidated ET as a function of PTC. Hexadecyltrimetylammonium chloride--approximately 1/4 of the way through the cross-section. 100
Table 39. XPS integration for cross-sectioned azidated ET as a function of PTC. Aliquat 336 (12 h azidation)--close to edge of cross-section. 101
Table 40. XPS integration for cross-sectioned azidated ET as a function of PTC. Aliquat 336 (12 h azidation)--approximately 1/4 of the way through the cross-section. 102
Table 41. XPS integration for cross-sectioned azidated ET as a function of PTC. Aliquat 336 (12 h azidation)-- midway through the cross-section. 103
Table 42. Optimization of conditions for CuAAC on azidated ET 110
Table 43. XPS integration for azidated ET clicked with QA alkyne (1) 112
Table 44. XPS integration for azidated ET clicked with perfluoro alkyne (2) 114
Table 45. XPS integration for azidated ET clicked with PEG_{2000} alkyne (3) 116
Table 46. XPS integration for azidated ET clicked with pyridinium alkyne (4) 118
Table 47. XPS summary for ET cyanated with various PTCs 119
Table 48. XPS integration for ET cyanated with cetylpyridinium chloride 120
Table 49. XPS integration for ET cyanated with tetrabutylammonium cyanide 122
Table 50. XPS integration for ET cyanated with Aliquat 336 124

Table 51. XPS integration for cyanated ET reacted with sodium azide and zinc bromide to form a 1*H*-tetrazole, then reacted with potassium carbonate and 2,3,4,5,6-pentafluorobenzyl bromide to make the alkylated tetrazole 125
Table 52. XPS survey integration for control sample, subject to the same conditions for substituted tetrazole formation but without base. 126
Table 53. Contact angle measurements for unmodified and modified ET and CT 127
Table 54. Indentation analysis of unmodified and modified ET. 129
Table 55. Azidation conditions screened for azidating SU-8 substrates. 144
Table 56. XPS integration table for SU-8 samples treated to azidation conditions of 480 mM NaN_3 and 240 mM oxone in 8 mL of water / acetonitrile (1:9) for 3 hours. 145
Table 57. XPS integration table for SU-8 samples treated to azidation conditions of 480 mM NaN_3, 240 mM oxone, and 20 mM TBAB in 8 mL of water / acetonitrile (1:9) for 3 hours..... 147
Table 58. XPS integration table for SU-8 samples treated to azidation conditions of 480 mM NaN_3 in pH = 9 sodium phosphate buffer. (Note: Starred peaks were integrated by the XPS software, although at the particular peak, the instrument was unable to discern between noise in the signal and an actual peak.) 148
Table 59. XPS survey integration for SU-8 samples treated to 480 mM NaN_3 and 240 mM NH_4Cl in 8 mL of methanol / water (8:1). 150
Table 60. XPS integration for azidated SU-8 prepared through the optimized deposition and azidation 152
Table 61. XPS integration for azidated SU-8 subject to CuAAC with trimethylprop-2-yn-1-aminium iodide. 155
Table 62. XPS survey integration for azidated SU-8 clicked with propargyl alcohol... 157
Table 63. XPS integration for azidated SU-8 reacted via CuAAC with a clickable initiator, propargyl 2-bromo-2-methylpropionamide..... 161
Table 64. XPS integration for azidated SU-8 clicked with clickable initiator, then subject to ATRP conditions with MMA. 164
Table 65. XPS survey spectrum integration for azidated SU-8 clicked with clickable initiator, then subject to ATRP conditions with 4VP. 167
Table 66. Measured contact angle for SU-8 substrates..... 170

LIST OF FIGURES

Figure 1. Scheme for copper(I)-catalyzed azide alkyne cycloaddition reaction. 1
Figure 2. Current understanding of the CuAAC reaction mechanism, as detailed by Worrell et. al.[4] 2
Figure 3. Example ligands to accelerate the CuAAC reaction. 3
Figure 4. Lipids systems devised for CuAAC from the literature or commercially available. 13
Figure 5. Synthesis of 3-azido-2-oxo-2H-chromen-7-yl-2-(octadecylamino)acetate 15
Figure 6. ^{1}H-NMR spectrum for 3-azido-2-oxo-2H-chromen-7-yl-2-(octadecylamino)acetate 16
Figure 7. Synthesis of N-(prop-2-yn-1-yl)octadecan-1-amine 16
Figure 8. 1H-NMR spectrum for N-(prop-2-yn-1-yl)octadecan-1-amine 17
Figure 9. ^{13}C-NMR spectrum for N-(prop-2-yn-1-yl)octadecan-1-amine 18
Figure 10. Synthesis of 1-azidohexadecane. 18
Figure 11. ^{1}H-NMR spectrum for 1-azidohexadecane. 19
Figure 12. ^{13}C-NMR spectrum for 1-azidohexadecane 20
Figure 13. IR spectrum for 1-azidohexadecane 20
Figure 14. Reaction scheme for synthesis of tris((1-hexadecyl-1H-1,2,3,-triazol-4-yl)methyl)amine 21
Figure 15. NMR spectrum for tris((1-hexadecyl-1H-1,2,3,-triazol-4-yl)methyl)amine. . 22
Figure 16. IR spectrum for tris((1-hexadecyl-1H-1,2,3,-triazol-4-yl)methyl)amine. 22
Figure 17. Reaction scheme for 6-(4-((octadecylamino)methyl)-1H-1,2,3-triazol-1-yl)-7-oxo-7,8-dihydronaphthalen-2-yl octadecylglycinate. 23
Figure 18. NMR spectrum for 6-(4-((octadecylamino)methyl)-1H-1,2,3-triazol-1-yl)-7-oxo-7,8-dihydronaphthalen-2-yl octadecylglycinate, with calibration peaks (for percent of triazole formed) identified. 24
Figure 19. Lipid vesicle preparation scheme. 27
Figure 20. Vesicles created for kinetics experimentation. 27
Figure 21. Kinetics of 7-hydroxy-3-azidocoumarin CuAAC with 2-methyl-3-butyn-1-ol when excited at 404 nm. 28
Figure 22. Representative kinetic traces for the reaction of 7-hydroxy-3-azidocoumarin CuAAC with 2-methyl-3-butyn-1-ol, demonstrating background subtraction. 30
Figure 23. Representative determination of initial kinetics for 7-hydroxy-3-azidocoumarin CuAAC with 2-methyl-3-butyn-1-ol 30
Figure 24. Scheme depicting overall lipid CuAAC research process and findings. 31
Figure 25. CuAAC experimental rate order plots for: A) 7-hydroxy-3-azidocoumarin in solution. B) 2-methyl-3-butyn-2-ol in solution. C) Cu-THPTA complex in solution with catalytic copper conditions. D) Cu in solution. E) Azide-lipid, in membrane. F) Alkyne-lipid, in membrane. G) Cu + lipid-ligand, in membrane. H) Cu + lipid-ligand, in membrane. Concentrations for all plots are depicted in Table 3. 32
Figure 26. CuAAC reactions between vesicle-supported reactants. Azide- or alkyne-lipids were incorporated at 2 mole-% with respect to lipid molecules in synthetic vesicles. The resulting vesicles are represented in cartoon form on the right; note that azide and

alkyne groups are displayed on the interior membrane surface as well, but are not shown in the cartoon. In all cases, overall concentrations were as follows: [1] = 19 μM; [2] = 19 μM; [$CuSO_4$] = 12 μM; [NaAsc] = 4 mM; [THPTA] = 60 μM. "Nonfluid" denotes vesicles made with 98% DPPC; "semi-fluid" denotes vesicles made with an 81:19 DPPC:DOPC molar ratio at 98% in the membrane. 35
Figure 27. CuAAC reactions of azide, alkyne, and ligand lipids incorporated at 2% into 19:81 DPPC vesicles, under the same conditions as Figure 26. 37
Figure 28. Cartoon representation of functionalized lipid exchange either before or after triazole formation, to give non-aggregated triazole-bearing vesicles. 38
Figure 29. Characterization of vesicles before and after CuAAC reactions. Semi-fluid vesicles contain 19% DOPC; non-fluid vesicles are composed entirely of DPPC. Results with non-fluid vesicles (DPPC only) are shown on top; semi-fluid vesicles (19% DOPC, 81% DPPC) are shown on the bottom. (A,C) dymanic light scattering. (B,D) zeta potential..... 41
Figure 30. Modification of flexible PVC by nucleophilic substitution and subsequent reactions with modified PVC. 47
Figure 31. Reaction scheme for the synthesis of trimethylprop-2-yn-1-aminium iodide (1) 49
Figure 32. ^{1}H-NMR spectrum for trimethylprop-2-yn-1-aminium iodide (1) 50
Figure 33. Reaction scheme for the synthesis of perfluoro-N-(prop-2-yn-1-yl)nonanamide (2) 50
Figure 34. ^{1}H-NMR spectrum for perfluoro-N-(prop-2-yn-1-yl)nonanamide (2) 51
Figure 35. ^{19}F-NMR spectrum for perfluoro-N-(prop-2-yn-1-yl)nonanamide (2). 52
Figure 36. Reaction scheme for the synthesis of 1-(undec-10-yn-1-yl)pyridin-1-ium (4) 52
Figure 37. ^{1}H-NMR spectrum for 1-(undec-10-yn-1-yl)pyridin-1-ium (4) 53
Figure 38. ^{13}C-NMR spectrum for 1-(undec-10-yn-1-yl)pyridin-1-ium (4) 53
Figure 39. Relative activity of phase transfer catalysts in the azidation of PVC tubing (450 mM NaN_3, 9 mM PTC, 80 °C, 48 h). 55
Figure 40. IR spectrum for unmodified ET. 57
Figure 41. XPS survey spectrum for unmodified ET. 57
Figure 42. IR spectrum for ET azidated with tetrabutylammonium bromide..... 58
Figure 43. XPS survey spectrum for ET azidated with tetrabutylammonium bromide... 59
Figure 44. XPS nitrogen spectrum for ET azidated with tetrabutylammonium bromide. 60
Figure 45. IR spectrum for ET azidated with Aliquat 336. 60
Figure 46. XPS survey spectrum for ET azidated with Aliquat 336. 61
Figure 47. XPS nitrogen spectrum for ET azidated with Aliquat 336. 61
Figure 48. IR spectrum for ET azidated with cetylpyridinium chloride. 62
Figure 49. XPS survey spectrum for ET azidated with cetylpyridinium chloride. 62
Figure 50. Nitrogen XPS spectrum for ET azidated with cetylpyridinium chloride. 63
Figure 51. IR spectrum for ET azidated with tetraphenylphosphonium bromide. 64
Figure 52. XPS survey spectrum for ET azidated with tetraphenylphosphonium bromide. 64
Figure 53. XPS nitrogen spectrum for ET azidated with tetraphenylphosphonium bromide. 65

Figure 54. IR spectrum for ET azidated with benzyldimethyltetradecylammonium chloride. 66
Figure 55. XPS survey spectrum for ET azidated with benzyldimethyltetradecylammonium chloride..... 66
Figure 56. XPS nitrogen survey for ET azidated with benzyldimethyltetradecylammonium chloride..... 67
Figure 57. IR spectrum for ET azidated with tetrabutylammonium iodide..... 68
Figure 58. XPS survey spectrum for ET azidated with tetrabutylammonium iodide..... 68
Figure 59. IR spectrum of ET azidated with hexadecyltrimethylammonium chloride.... 69
Figure 60. XPS survey spectrum for ET azidated with hexadecyltrimethylammonium chloride. 70
Figure 61. IR spectrum for ET azidated with tetrabutylammonium nitrate..... 71
Figure 62. XPS survey spectrum for ET azidated with tetrabutylammonium nitrate..... 71
Figure 63. IR spectrum for ET azidated with tetrabutylammonium cyanide. 72
Figure 64. XPS survey spectrum for ET azidated with tetrabutylammonium cyanide. .. 73
Figure 65. IR spectrum for ET azidated with tetrabutylammonium bisulfate. 74
Figure 66. XPS survey spectrum for ET azidated with tetrabutylammonium bisulfate. . 74
Figure 67. IR spectrum for ET azidated with tetrabutylammonium tetrafluoroborate. ... 75
Figure 68. XPS survey spectrum for ET azidated with tetrabutylammonium tetrafluoroborate..... 76
Figure 69. IR spectrum for ET azidated with tetraoctylammonium bromide..... 77
Figure 70. XPS survey spectrum for ET azidated with tetraoctylammonium bromide... 78
Figure 71. XPS nitrogen scan for ET azidated with tetraoctylammonium bromide..... 78
Figure 72. Results of azidation reactions of varying duration and temperature on endotracheal tubing using aqueous solutions of 480 mM sodium azide and 11 mM Aliquat® 336. The color of each box approximates the color of the resulting tubing. NR = no observed reaction as indicated by IR; max signal = maximum intensity of the organic azide IR stretching band at 2107 nm..... 79
Figure 73. Correlation of percent nitrogen from XPS with IR azide peak intensity. 81
Figure 74. XPS analyses of a representative sample (12 h, 80 °C, with Aliquat® 336) showing azidation at the surface but not in the interior. 82
Figure 75. Key for cross-section data. 82
Figure 76. XPS spectra of cross-sectioned azidated ET as a function of PTC. Tetrabutylammonium bromide--close to edge of cross-section..... 83
Figure 77. XPS spectra of cross sectioned. Azidated ET as a function of PTC. Tetrabutylammonium bromide--approximately 1/4 of the way through the cross-section. 84
Figure 78. XPS spectra of cross sectioned. Azidated ET as a function of PTC. Tetrabutylammonium bromide--midway way through the cross-section..... 85
Figure 79. XPS spectra of cross-sectioned azidated ET as a function of PTC. Cetylpyridinium chloride --close to edge of cross-section. 86
Figure 80. XPS spectra of cross-sectioned azidated ET as a function of PTC. Cetylpyridinium chloride --approximately 1/4 of the way through the cross-section..... 87
Figure 81. XPS spectra of cross-sectioned azidated ET as a function of PTC. Cetylpyridinium chloride --midway through the cross-section. 88

Figure 82. XPS spectra of cross-sectioned azidated ET as a function of PTC. Tetraphenylphosphonium bromide --close to edge of cross-section. 89
Figure 83. XPS spectra of cross-sectioned azidated ET as a function of PTC. Tetraphenylphosphonium bromide --approximately 1/4 of the way through the cross-section. 90
Figure 84. XPS spectra of cross-sectioned azidated ET as a function of PTC. Tetraphenylphosphonium bromide --midway through the cross-section. 91
Figure 85. XPS spectra of cross-sectioned azidated ET as a function of PTC. Benzyldimethyltetradecylammonium chloride --close to edge of cross-section. 92
Figure 86. XPS spectra of cross-sectioned azidated ET as a function of PTC. Benzyldimethyltetradecylammonium chloride --approximately 1/4 of the way through the cross-section. 93
Figure 87. XPS spectra of cross-sectioned azidated ET as a function of PTC. Benzyldimethyltetradecylammonium chloride --midway through the cross-section. 94
Figure 88. XPS spectra of cross-sectioned azidated ET as a function of PTC. Tetrabutylammonium iodide --close to edge of cross-section. 95
Figure 89. XPS spectra of cross-sectioned azidated ET as a function of PTC. Tetrabutylammonium iodide --approximately 1/4 of the way through the cross-section. 96
Figure 90. XPS spectra of cross-sectioned azidated ET as a function of PTC. Tetrabutylammonium iodide --midway through the cross-section. 97
Figure 91. XPS spectra of cross-sectioned azidated ET as a function of PTC. Hexadecyltrimetylammonium chloride --close to edge of cross-section. 98
Figure 92. XPS spectra of cross-sectioned azidated ET as a function of PTC. Hexadecyltrimetylammonium chloride --approximately 1/4 of the way through the cross-section. 99
Figure 93. XPS spectra of cross-sectioned azidated ET as a function of PTC. Hexadecyltrimetylammonium chloride--midway through the cross-section. 100
Figure 94. XPS spectra of cross-sectioned azidated ET as a function of PTC. Aliquat 336 (12 h azidation)--close to edge of cross-section. 101
Figure 95. XPS spectra of cross-sectioned azidated ET as a function of PTC. Aliquat 336 (12 h azidation)--approximately 1/4 of the way through the cross-section. 102
Figure 96. XPS spectra of cross-sectioned azidated ET as a function of PTC. Aliquat 336 (12 h azidation)--midway through the cross-section. 103
Figure 97. IR of food grade PVC both before (blue) and after azidation (red) 104
Figure 98. Diagram of whole-tube azidation setup. Green: catheter tubing to be azidated. Blue: silicone tubing used to encase the catheter tubing and solution. Purple: 3-way connector, through which the catheter tubing is fed. Orange: connective silicone tubing. Arrows show fluid flow direction. 105
Figure 99. IR spectrum for whole-tube azidation for the lower outside region. 106
Figure 100. IR spectrum for whole-tube azidation for the lower inside region. 106
Figure 101. IR spectrum for the whole-tube azidation for the mid-outside region. 106
Figure 102. IR spectrum for the whole-tube azidation for the mid-inside region. 107
Figure 103. IR spectrum for the whole-tube azidation for the high-outside region. 107
Figure 104. IR spectrum for the whole-tube azidation for the high-inside region. 107
Figure 105. Alkynes used for CuAAC with ET. 108

Figure 106. Results of CuAAC reactions at varying temperatures with different alkyne substrates (5 mM) in an aqueous solution of 44 mM $CuSO_4$ and 190 mM sodium ascorbate. The color of each box approximates the color of the resulting tubing. The reaction outcome ("minimal," "complete," etc.) refers to the percent of PVC-azide IR signal that is diminished after the reaction, noting that exposure to the reaction conditions without alkyne gave no loss in this signal; numerical values are approximate (±10%). All reaction times were 4.5 hours with the exception of the quaternary amine 1, which was reacted overnight. Alkynes 2-4 were reacted in the presence of 21 mM Aliquat® 336. 109
Figure 107. Tubing samples (left to right): unmodified endotracheal tubing, azidated (80 °C, 12 h), CuAAC with 2 (60 °C, overnight), cyanated (80 °C, 3 days), and pentafluorobenzyl tetrazole functionalized via tetrazole. 109
Figure 108. IR spectrum demonstrating the effect of pH on CuAAC reaction through the reduction of the azide peak. 110
Figure 109. IR spectrum for azidated ET clicked with QA (1) 111
Figure 110. XPS spectrum for azidated ET clicked with QA alkyne (1) 111
Figure 111. Nitrogen XPS spectrum for azidated ET clicked with QA alkyne (1) 112
Figure 112. IR spectrum for ET clicked with perfluoro alkyne (2) 113
Figure 113. XPS spectrum for ET clicked with perfluoro alkyne (2) 113
Figure 114. Nitrogen XPS spectrum for azidated ET clicked with perfluoro alkyne (2) 114
Figure 115. IR spectrum for azidated ET clicked with PEG_{2000} alkyne (3) 115
Figure 116. XPS spectrum for azidated ET clicked with PEG_{2000} alkyne (3) 115
Figure 117. Nitrogen XPS spectrum for azidated ET clicked with PEG_{2000} alkyne (3) 116
Figure 118. IR spectrum for azidated ET clicked with pyridinium alkyne (4) 117
Figure 119. XPS Spectrum for azidated ET clicked with pyridinium alkyne (4) 117
Figure 120. Nitrogen XPS spectrum for azidated ET clicked with pyridinium alkyne (4) 118
Figure 121. IR spectrum for ET cyanated with cetylpyridinium chloride 119
Figure 122. XPS spectrum for ET cyanated with cetylpyridinium chloride 120
Figure 123. Nitrogen XPS spectrum for ET cyanated with cetylpyridinium chloride .. 121
Figure 124. IR spectrum for ET cyanated with tetrabutylammonium cyanide 121
Figure 125. XPS spectrum for ET cyanated with tetrabutylammonium cyanide 122
Figure 126. Nitrogen XPS for ET cyanated with tetrabutylammonium cyanide 122
Figure 127. IR spectrum for ET cyanated with Aliquat 336 123
Figure 128. XPS spectrum for ET cyanated with Aliquat 336 123
Figure 129. Nitrogen XPS spectrum for ET cyanated with Aliquat 336 124
Figure 130. XPS survey spectrum for cyanated ET reacted with sodium azide and zinc bromide to form a 1*H*-tetrazole, then reacted with potassium carbonate and 2,3,4,5,6-pentafluorobenzyl bromide to make the alkylated tetrazole 125
Figure 131. XPS survey spectrum for control sample, subject to the same conditions for substituted tetrazole formation but without base. 126
Figure 132. TGA of unmodified and modified ET 127
Figure 133. TGA of ET incubated in water and in water with PTC, but without presence of nucleophile 128
Figure 134. SEM images of endotracheal tubing after the indicated treatment. Magnification of top and bottom images: unmodified = 350x, 1000x; azidated = 350x,

1000x; CuAAC of alkyne 1 = 270x, 4000x; CuAAC of alkyne 2 = 350x, 950x; CuAAC of alkyne 3 = 370x, 1000x; CuAAC of alkyne 4 = 350x, 1000x. 129
Figure 135. SEM images of catheter tubing after the indicated treatment. Magnification of top and bottom images: unmodified = 350x, 1000x; azidated = 370x, 900x; CuAAC of alkyne 1 = 350x, 1000x; CuAAC of alkyne 2 = 370x, 1000x; CuAAC of alkyne 3 = 350x, 1000x; CuAAC of alkyne 4 = 370x, 1000x. 130
Figure 136. SEM images of ET treated with CuAAC solvents and reagents, demonstrating surface deformations are only occurring when CuAAC is transpiring. .. 131
Figure 137. AFM images of the PVC surfaces for ET before and after modifications and average roughness for each surface. 132
Figure 138. SU-8 monomer. 136
Figure 139. Summary of previous SU-8 chemical modifications. 137
Figure 140. Summary of azide nucleophilic attack at epoxides from the literature. 138
Figure 141. Examples of photomasked SU-8 patterns. 139
Figure 142. XPS spectrum for SU-8 sample treated to azidation conditions of 480 mM NaN_3 and 240 mM oxone in 8 mL of water / acetonitrile (1:9) for 3 hours. 145
Figure 143. XPS nitrogen spectrum for SU-8 samples treated to azidation conditions of 480 mM NaN_3 and 240 mM oxone in 8 mL of water / acetonitrile (1:9) for 3 hours. ... 146
Figure 144. XPS spectrum for SU-8 samples treated to azidation conditions of 480 mM NaN_3, 240 mM oxone, and 20 mM TBAB in 8 mL of water / acetonitrile (1:9) for 3 hours. 146
Figure 145. XPS nitrogen spectrum for for SU-8 samples treated to azidation conditions of 480 mM NaN_3, 240 mM oxone, and 20 mM TBAB in 8 mL of water / acetonitrile (1:9) for 3 hours. 147
Figure 146. XPS spectrum for SU-8 samples treated to azidation conditions of 480 mM NaN_3 in pH = 9 sodium phosphate buffer. 148
Figure 147. XPS nitrogen spectrum for SU-8 samples treated to azidation conditions of 480 mM NaN_3 in pH = 9 sodium phosphate buffer. 149
Figure 148. XPS spectrum for SU-8 samples treated to 480 mM NaN_3 and 240 mM NH_4Cl in 8 mL of methanol / water (8:1). 149
Figure 149. XPS nitrogen spectrum for SU-8 samples 480 mM NaN_3 and 240 mM NH_4Cl in 8 mL of methanol / water (8:1). 150
Figure 150. XPS spectrum for azidated SU-8 prepared through the optimized deposition and azidation. 152
Figure 151. XPS nitrogen spectrum for azidated SU-8 prepared through the optimized deposition and azidation. 153
Figure 152. XPS carbon spectrum for azidated SU-8 prepared through the optimized deposition and azidation. 153
Figure 153. XPS spectrum for azidated SU-8 subject to CuAAC with trimethylprop-2-yn-1-aminium iodide. 155
Figure 154. XPS nitrogen spectrum for azidated SU-8 subject to CuAAC with trimethylprop-2-yn-1-aminium iodide. 156
Figure 155. XPS carbon spectrum for azidated SU-8 subject to CuAAC with trimethylprop-2-yn-1-aminium iodide. 156
Figure 156. XPS survey spectrum for azidated SU-8 clicked with propargyl alcohol. . 157
Figure 157. Nitrogen XPS scan for azidated SU-8 clicked with propargyl alcohol. 158

Figure 158. All scale bars are 200 microns. A) Control: Brightfield image of azidated SU-8, subjected to click conditions without the addition of copper, for a TAMRA-alkyne. B) Brightfield image of azidated SU-8, subjected to click conditions for a TAMRA-alkyne. C) Control: Fluorescent image of azidated SU-8, subjected to click conditions without the addition of copper, for a TAMRA-alkyne. D) Fluorescent image of azidated SU-8, subjected to click conditions for a TAMRA-alkyne..... 159
Figure 159. Fluorescent intensity across Figure 158 images C and D..... 160
Figure 160. Structure of the clickable ATRP initiator, propargyl 2-bromo-2-methylpropionamide 160
Figure 161. XPS spectrum for azidated SU-8 reacted via CuAAC with a clickable initiator, propargyl 2-bromo-2-methylpropionamide..... 161
Figure 162. Nitrogen XPS spectrum for azidated SU-8 reacted via CuAAC with a clickable initiator, propargyl 2-bromo-2-methylpropionamide. 162
Figure 163. Bromine XPS spectrum for azidated SU-8 reacted via CuAAC with a clickable initiator, propargyl 2-bromo-2-methylpropionamide. 162
Figure 164. XPS carbon spectrum for azidated SU-8 reacted via CuAAC with a clickable initiator, propargyl 2-bromo-2-methylpropionamide..... 163
Figure 165. XPS spectrum for azidated SU-8 clicked with clickable initiator, then subject to ATRP conditions with MMA. 164
Figure 166. XPS nitrogen spectrum for azidated SU-8 clicked with clickable initiator, then subject to ATRP conditions with MMA. 165
Figure 167. XPS bromine spectrum for azidated SU-8 clicked with clickable initiator, then subject to ATRP conditions with MMA. 165
Figure 168. XPS carbon spectrum for azidated SU-8 clicked with clickable initiator, then subject to ATRP conditions with MMA. 166
Figure 169. Image of azidated SU-8, subjected to CuAAC with a clickable ATRP initiator, then subject to ATRP conditions with 4-vinyl pyridine. The color of the sample changed from clear to brown during the reaction and could not be removed by extensive rinsing with water and methanol. 166
Figure 170. XPS survey spectrum for azidated SU-8 clicked with clickable initiator, then subject to ATRP conditions with 4VP. 167
Figure 171. XPS nitrogen spectrum for azidated SU-8 clicked with clickable initiator, then subject to ATRP conditions with 4VP. 168
Figure 172. XPS bromine spectrum for azidated SU-8 clicked with clickable initiator, then subject to ATRP conditions with 4VP. 168
Figure 173. XPS carbon spectrum for azidated SU-8 clicked with clickable initiator, then subject to ATRP conditions with 4VP. 169
Figure 174. SEM images for unmodified SU-8. 170
Figure 175. SEM images of azidated SU-8. 171
Figure 176. SEM images of azidated SU-8 clicked with quaternary amine. 171
Figure 177. SEM images of azidated SU-8 reacted via CuAAC with a clickable initiator, propargyl 2-bromo-2-methylpropionamide. 172
Figure 178. SEM images from azidated SU-8 clicked with clickable initiator, then subject to ATRP conditions with 4VP. 172
Figure 179. Top left: Brightfield image of CHO cells on SU-8 substrate (bottom half of image). Top right: Fluorescent image of CHO cells on SU-8 substrate with Sytox red.

Bottom left: Brightfield image of CHO cells on SU-8 substrate (top half of image). Bottom right: Fluorescent image of CHO cells on SU-8 substrate with Sytox red. All scale bars are 200 μm. 173
Figure 180. Brightfield images of red blood cells on SU-8 substrates at 100x whole field views. 174
Figure 181. All images at 60 minutes, following a 20 minute settling time. All scale bars are 50 μm. Top left: Brightfield image of E. coli DH5α on ITO glass (left) and azidated SU-8 clicked with propargyl alcohol (right) with Sytox red. Top right: Fluorescent image of E. coli DH5α on ITO glass (left) and azidated SU-8 clicked with propargyl alcohol (right) with Sytox red. Bottom left: Brightfield image of E. coli DH5α on ITO glass (left) and azidated SU-8 clicked with QA (right). Bottom right: Fluorescent image of E. coli DH5α on ITO glass (left) and azidated SU-8 clicked with QA (right) with Sytox red. 175
Figure 182. All images at 270 minutes, following a 20 minute settling time. All scale bars are 50 μm. Top left: Brightfield image of E. coli DH5α on ITO glass (left) and azidated SU-8 clicked with propargyl alcohol (right) with Sytox red. Top right: Fluorescent image of E. coli DH5α on ITO glass (left) and azidated SU-8 clicked with propargyl alcohol (right) with Sytox red. Bottom left: Brightfield image of E. coli DH5α on ITO glass (left) and azidated SU-8 clicked with QA (right). Bottom right: Fluorescent image of E. coli DH5α on ITO glass (left) and azidated SU-8 clicked with QA (right) with Sytox red. 176
Figure 183. All images at 330 minutes, following a 20 minute settling time. All scale bars are 50 μm Top left: Brightfield image of E. coli DH5α on ITO glass (left) and azidated SU-8 clicked with propargyl alcohol (right) with Sytox red. Top right: Fluorescent image of E. coli DH5α on ITO glass (left) and azidated SU-8 clicked with propargyl alcohol (right) with Sytox red. Bottom left: Brightfield image of E. coli DH5α on ITO glass (left) and azidated SU-8 clicked with QA (right). Bottom right: Fluorescent image of E. coli DH5α on ITO glass (left) and azidated SU-8 clicked with QA (right) with Sytox red. 177
Figure 184. Fluorescence quantitation for DH5α killing activity of quaternary amine SU-8..... 178
Figure 185. All images at 330 minutes, following a 20 minute settling time. All scale bars are 50 μm. Top left: Brightfield image of S. aureus on ITO glass (left) and azidated SU-8 clicked with propargyl alcohol (right) with Sytox red. Top right: Fluorescent image of S. aureus on ITO glass (left) and azidated SU-8 clicked with propargyl alcohol (right) with Sytox red. Bottom left: Brightfield image of S. aureus on ITO glass (left) and azidated SU-8 clicked with QA (right). Bottom right: Fluorescent image of S. aureus on ITO glass (left) and azidated SU-8 clicked with QA (right) with Sytox red.. 179

LIST OF SYMBOLS AND ABBREVIATIONS

4VP	4-vinylpyridine
AFM	atomic force microscopy
ATRP	atom transfer radical polymerization
CT	catheter tubing
CuAAC	copper(I)-catalyzed azide-alkyne cycloaddition
DEHP	bis(2-ethylhexyl phthalate)
DMEM	Dulbecco's modified eagle medium
DLS	dynamic light scattering
DMF	N,N-dimethylformamide
DOPC	1,2-dioleoyl-sn-glycero-3-phosphocholine
DPPC	1,2-dipalmitoyl-sn-glycero-3-phosphocholine
DSC	differential scanning calorimetry
EDTA	ethylenediaminetetraacetic acid
ET	endotracheal tubing
EtOAc	ethyl acetate
Hex	hexanes
IR	infrared spectroscopy
MMA	methyl methacrylate
MS	mass spectrometry

NMR	nuclear magnetic resonance
PBS	phosphate buffered saline
PEDOT	poly(3,4-ethylenedioxythiophene)
PEG	polyethylene glycol
PMMA	polymethyl methacrylate
PTC	phase transfer catalyst
PVC	polyvinyl chloride
QA	quaternary ammonium cation
Rf	retention factor
SEM	scanning electron microscopy
TBTA-COOH	4,4',4''-(((nitrilotris(methylene))tris(1H-1,2,3-triazole-4,1-diyl))tris(methylene))tribenzoic acid
TGA	thermogravimetric analysis
THPTA	tris(3-hydroxypropyltriazolylmethyl)amine
VP-SEM	variable pressure scanning electron microscopy
XPS	x-ray photoelectron spectroscopy

SUMMARY

Copper(I) catalyzed azide alkyne cycloaddition (CuAAC) is a powerful tool that allows for diverse functionalization from azide and alkyne precursors. This research probed the kinetics of the CuAAC reaction in- and between- lipid membranes, as well as used it to modify SU-8 and flexible PVC polymers post-polymerization while maintain key polymer properties. These applications make click chemistry relevant to materials in new ways and will allow for the derivatization of these materials that is limited only by the user's creativity.

To study the CuAAC reaction in and between membranes, this research sought to answer two key questions: 1) Are the kinetics of the CuAAC reaction in-membrane comparable to the reaction in solution and 2) Is CuAAC reactivity similar to other reactivity that has been observed between membranes, like that of Menger and co-workers? Through this research it was determined that the reaction was comparable to the reaction in solution in that the rate order was approximately first order with respect to azide and alkyne and approximately second order with respect to the copper-ligand complex. Additionally, reactivity was observed between vesicles with no signs of aggregation, and for fluid lipid systems the intravesicular reaction was significantly faster than the intervesicular reaction, similar to the work of Menger et. al.; this suggests that similar to Menger, lipid transfer between vesicles is likely occurring prior to CuAAC.

In the interests of devising hospital tubing that either kills bacteria on contact or reduces bacterial adhesion, hospital-grade endotracheal tubing and catheter tubing made of flexible polyvinyl chloride (PVC) was subjected to azidation with the aid of a phase

transfer catalyst and subsequent CuAAC, which allowed for diverse functionalization. During azidation and CuAAC, tubing samples became discolored, measurably harder (although still deformable), and in some situations cracked, although these side effects could be mitigated through a decreased reaction time, choice of phase transfer catalyst, and decreased reaction temperature. Another small nucleophile, cyanide, was also substituted onto the PVC, which suggests that this methodology of substituting PVC with the aid of a phase transfer catalyst is applicable to other small nucleophiles. This work allows for the diverse functionalization of flexible PVC tubing, useful for work to reduce biofouling and limit bacterial contamination of surfaces.

SU-8 is a negative photoresist used for electronics and microelectromechanical systems and there has been interest in the past few years of making this surface chemically addressable. This research sought to make the SU-8 surface directly accessible via click chemistry. Following photo-crosslinking of the SU-8 polymer, the remaining surface exposed epoxides were azidated and subsequently clicked with a variety of alkynes including an alkyne quaternary ammonium cation, an alkyne TAMRA dye, and an alkyne clickable initiator (that was then subject to ATRP conditions with methyl methacrylate or 4-vinyl pyridine). Resultant surfaces were demonstrated to be biocompatible and the surface decorated with the quaternary ammonium cation was shown to have bactericidal effects against *E. coli* DH5α. This work allows for the direct functionalization for the SU-8 polymer and is applicable to applications including electronics and sensors.

CHAPTER 1. INTRODUCTION

1.1 An Introduction to Click Chemistry

1.1.1 Origins

The term 'click chemistry' is used to denote reactions that are modular, wide-in-scope, high-yielding, produce inoffensive byproducts, are stereospecific, that can be performed in simple reaction conditions with readily available reagents, in a solvent that is easily removed or benign, with simple product isolation.[1] This class of reactions is broad, including nucleophilic opening of "spring-loaded" rings and cycloaddition reactions, but of particular note is the copper(I)-catalyzed azide alkyne cycloaddition reaction (CuAAC), in which an azide and a terminal alkyne form a regioselective 1,4-disubstituted-1,2,3-triazole, as depicted in Figure 1.[2,3,4]

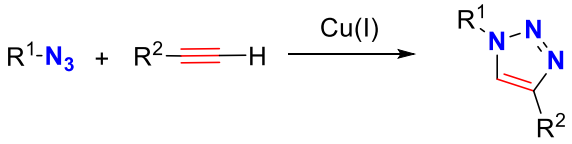

Figure 1. Scheme for copper(I)-catalyzed azide alkyne cycloaddition reaction.

These reactions were first reported in the early 2000's[1,3] and have since become ubiquitous to synthetic chemistry and a key tool of drug discovery and chemical biology, as they provide a simple means to create diverse functionality.

1.1.2 Mechanism

While appearing similar in reagents to Huisgen azide-alkyne 1,3-dipole addition,[5] the presence of copper(I) salts or copper(II) salts and a reducing agent (e.g., sodium ascorbate) enables regioselectivity, a lower reaction temperature, as well as much faster kinetics (approximately 10^6 times faster than without copper).[6,7] Current understanding of the reaction mechanism is that the reaction proceeds via the coordination of two-copper atoms to the alkyne for activation, followed by a cyclic addition, which gives rise to solely the 1,4-disubstituted product as depicted in Figure 2,[4] whereas the Huisgen reaction (without copper, but with heat) also produces the 1,5-disbustituted product.

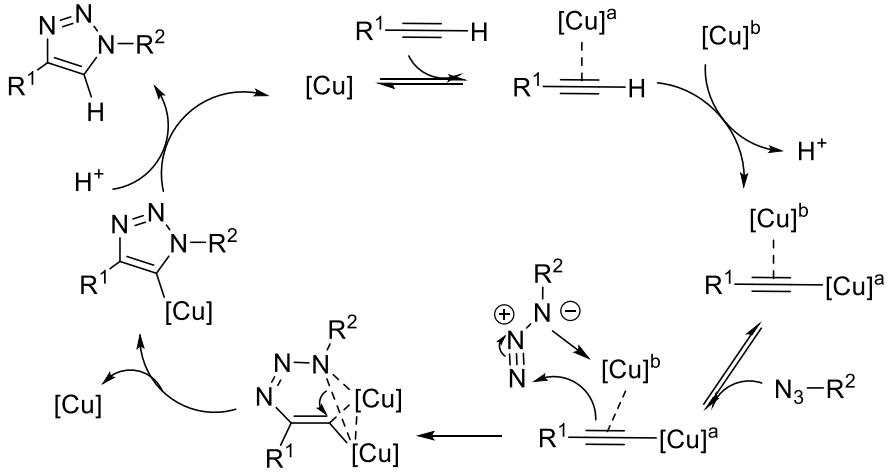

Figure 2. Current understanding of the CuAAC reaction mechanism, as detailed by Worrell et. al.[4]

Copper-chelating ligands, often polytriazoles or benzimidazole-based, can drastically accelerate the CuAAC reaction[8,9] by stabilizing the copper in its +1 oxidation state (limiting oxidation and disproportionation) and enhancing its catalytic efficiency.[10]

Examples of ligands that accelerate the CuAAC reaction (by no means an exhaustive list) can be found in Figure 3.

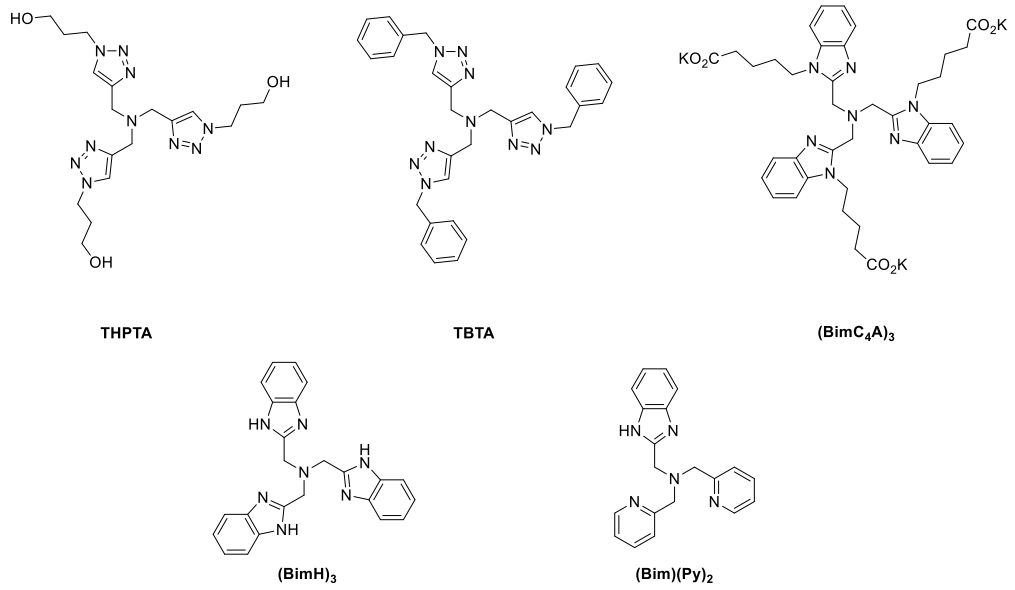

Figure 3. Example ligands to accelerate the CuAAC reaction.

1.1.3 Applications

Click chemistry has applications in a diverse range of fields, including bioconjugation,[10] dendrimer synthesis,[11,12,13] combinatorial science and drug discovery,[14,15,16] polymer ligation,[17,18,19,20] and surface science.[21,22,23,24] For each of these applications, a number of parameters can be altered to optimize the CuAAC reaction, including concentration of reagents, copper(I) source, choice of ligand, concentrations of copper(I) and ligand, and solvent choice.[25,26] The integration of CuAAC allows for diverse functionalization from relatively easily obtained (and often commercially available) precursors.

1.2 Introduction to Click Chemistry on Surfaces

In order to introduce clickable functionalities (azides and alkynes) to assembled materials surfaces, the functional moieties can either be introduced pre- or post- assembly. For lipid assemblies, incorporation of azide and alkyne functional groups is nearly always performed on the individual lipids before vesicle, micelle, or supported bilayer formation, due in part to the challenge of chemically addressing lipids once assembled and the tendency of some synthetic lipid systems to aggregate in undesirable ways over time. In the literature, for polymers, a number of examples of pre-polymerization incorporation can be found, which make azides or alkynes a part of the monomer for a broad range of materials including poly(3,4-ethylenedioxythiophene) (PEDOT), polyurethane, and SU-8.[27,28,29] Post-polymerization functionalization is somewhat more rare in the literature for a number of reasons. First, it requires that there be some sort of moiety available on the polymer surface that can be manipulated to incorporate the azide or alkyne functional group. Secondly, it requires there be a means by which to modify the moiety that does not harm the polymer or substrate and allows it to maintain its desired material properties. Finally, it requires that the moiety be present in a significant enough amount on the surface to effect enough of a change for both function (as desired) and for analysis to confirm subsequent modification. Examples of this in the literature include modifications of polymethyl methacrylate (PMMA) and PVC.[30,31] More methods to incorporate azide or alkyne functional groups post-polymerization could provide more tools for the polymer chemist or materials engineer to specifically tailor materials as desired.

1.3 Introduction to instrumentation and methodologies

Detailed here are the technologies used to complete research for this thesis, including some of the key parameters used, how relevant signals present, and the challenges encountered.

1.3.1 X-ray Photoelectron Spectroscopy (XPS)

X-ray photoelectron spectroscopy is a technique used to analyse materials that provides information about composition and structure. In particular, it was used for this research to provide a means of surface elemental analysis and to confirm and understand surface modifications made to polymers.

1.3.1.1 Key parameters and challenges

Under x-ray energy for XPS, some functional groups of interest degrade, which can challenge analysis. Of particular interest, azides degrade over time under x-ray energy,[32] thus to mitigate this, the number of scans was limited for survey and nitrogen spectra. 1-H tetrazoles have been reported to be unstable to XPS analysis, and indeed, increased pressure was observed in the instrument upon XPS analysis of suspected tetrazoles (Section 3.4.4); thus, some samples are unable to be analyzed via XPS.

1.3.1.2 Relevant signals of note

Beyond standard elemental signals that indicate the presence of a particular atom, azides exhibit a characteristic double-peak XPS spectrum within the nitrogen region, with an integration for the peaks of 2:1. This characteristic peak degrades over time under x-

ray, and once the azide is subject to a CuAAC reaction to form a 1,2,3-triazole, the double peak is no longer present, and instead presents as one peak.[32]

Carbon XPS can also be useful in evaluating modification of surfaces and materials. Carbonyls and esters exhibit shifted peaks (~288 eV, as compared to the typical carbon 285), and when present in combination with aliphatic, aromatic, or other carbon groups, can appear as nonsymmetrical overlapping peaks.[33]

1.3.2 Variable-Pressure Scanning Electron Microscopy (VP-SEM)

Variable pressure scanning electron microscopy was used for this research to qualitatively evaluate modified surfaces, which included looking for surface inhomogeneity, cracking, and deformation at a microscopic level.

1.3.2.1 How the technology works

Scanning Electron Microscopy uses a focused electron beam to produce high resolution images of a surface. As an accelerating voltage is applied, electrons interact with the surface, to create secondary electrons, backscattered electrons, and x-rays, which are collected by detectors to provide information about the surface. Factors that influence the signal output include the applied voltage, the probe current, as well as the particular sample. In typical SEM, a surface needs to be conductive in order to be able to produce a good image; in VP-SEM, however, the instrument is run under less of a vacuum, which allows for non-conductive surfaces to be imaged. This alleviates the need to spin coat a surface with a conductive metal before use.[34]

1.3.2.2 Key parameters and challenges

For a number of surfaces under VP-SEM, analysis can negatively impact the surface. As VP-SEM samples are not spin-coated with metal as are typical SEM samples, the surface itself can degrade which can become evident as either noted differences between areas previous scanned and areas not previously scanned (often appearing as an outline of the previous viewing area), or by the development of additional surface cracking over time. To minimize this, parameters including probe current, accelerating voltage, and working distance can be altered.

Additionally, at times charges can build up on surfaces, which leads to poor image quality, as indicated by aberrant lines appearing on scans and images that are not a part of the actual surface. To reduce this charging, copper tape as a bridge between the surface and the metal sample plate can be used to direct a charge away from the material surface or the vacuum being applied to the analysis chamber can be reduced, although this can lead to a loss of resolution.

1.3.3 Contact Angle Measurement

The measurement of a surface's contact angle provides information as to the relative hydrophobicity (or hydrophilicity) of a surface. This is done by placing a small drop of water (kept consistent between samples) on the material surface, then using a high resolution camera to image the water-surface interface. Software then measures the angle at which the water contacts the surface. In general, these images need to be taken quickly to limit spreading that may change the contact angle over time.

1.3.3.1 Key parameters and challenges

For measuring contact angles on curved or inhomogeneous surfaces, it is important that the samples be flattened as possible within the camera view-frame and that a number of measurements are taken across the surface to insure the measurements are representative. It also must be noted that measurements should be taken at different locations on a surface, as once the surface is pre-wet from another drop, the contact angle of that point again will differ from the original measurement until it has completely dried.

1.3.4 Nuclear Magnetic Resonance (NMR) Spectroscopy

1.3.4.1 Key parameters and challenges

In general, terminal alkynes on high resolution instruments exhibit a triplet chemical shift, with a small coupling constant (J = 1 or 2). 1,5-disubstituted-1,2,3-triazoles exhibit a chemical shift of ~8.2 ppm for the triazole proton. Perfluorocompounds often are not analysed by carbon NMR, as fluorine splits the carbon signals.

1.3.5 Infrared (IR) Spectroscopy

1.3.5.1 Key parameters and challenges

Peaks relevant to works detailed in this document are the azide stretch (strong, ~2100 cm^{-1}), cyano stretch (weak, ~2200 cm^{-1}), and chloride stretch (medium, ~610 cm^{-1}). Challenges to using IR include the need for complete contact of solid samples with the attenuated total reflectance (ATR) single crystal, which makes it difficult to analyse

samples deposited on glass surfaces, or samples that are not easily crushed or deformed with the application of modest force.

1.3.6 Working with azide

As a matter of safety, a number of precautions were taken in working with azides. Namely, sodium azide was kept from metal and from coming into contact with acid. Azide was quenched following use by the procedure detailed by Presolski, Hong, Cho, and Finn, whereby solutions of azide in a large volume of water were **first** treated with sodium nitrite, **then** slowly acidified in dilute solution until a drop of the solution on starch-iodide paper appeared purple.[6]

CHAPTER 2. KINETICS OF COPPER(I) AZIDE ALKYNE CYCLOADDITION WITHIN AND AMONG LIPID BILAYERS

2.1 Abstract

The kinetics of copper(I)-catalyzed azide alkyne cycloaddition (CuAAC) were evaluated for the reactions of membrane-bound reagents. The kinetic order of the CuAAC reaction was the same as for reagents free in solution. For reactions between vesicles, in a limited fluidity environment, reactions took place with no aggregation or change in vesicle size, which suggests the transfer of lipids from one vesicle to another occurs before the ligation, presumably because the intravesicular reaction is significantly faster than the intervesicular reaction. A membrane-bound copper-binding ligand showed mild acceleration over the reaction without a copper-binding ligand; however, the copper-binding ligand in solution provided the best reaction acceleration for membrane-bound lipid substrates. This work provides the basic framework to understand CuAAC with membrane-bound substrates.

2.2 Introduction to reactions in and between lipid membranes

Lipids are necessary for biological systems, as they provide a means of molecular compartmentalization in cells and are involved in cell signaling processes. The physical properties of lipid membranes are of great importance and have strong effects on cellular trafficking and nutrition.[35] The ability to modify membrane components and properties in a controlled manner is therefore desirable, and so the role of lipid bilayers as an environment for chemical reactions is of fundamental and applied interest.

Membrane fluidity is also an important regulated property in cells as, for example, in lipid raft microdomains.[36] Lipids near membrane-bound proteins can have widely varying fluidity, from highly disordered (liquid-like) phases for membrane proteins anchored by alpha helices, to highly ordered (solid-like) phases for membrane proteins in which anchored domains show hydrophobic phase matching.[37] The definitive biological roles of gel-phase and liquid-ordered phase lipids has yet to be elucidated,[38] yet further investigations into reactivity and membrane properties of these systems may shed light on the ability of differing lipid phases to control and facilitate biological processes.

The consequences of constraining lipophilic reactants in a two-dimensional bilayer have been studied in a variety of ways. Menger and coworkers studied membrane-anchored cholesterol-based nucleophiles and electrophiles, and found for fluid POPC membranes that initial rates of intravesicular reactions were more than 300 times faster than the corresponding intervesicular reaction. Thus, lipid movement within such a bilayer induced many more successful nucleophile-electrophile interactions than vesicular collision.[39] This system was also found to undergo facile transfer of lipid molecules between colliding membranes,[40] a process that has been explored by many investigators and is known to be influenced by several factors including local geometric constraints at the collision site,[41,42] electrostatic interactions between vesicles,[43] and protein facilitation.[44]

2.3 An Introduction to Click Chemistry with Lipids

Given its use in a wide variety of reactions with biomolecules, including its use on lipids and lipid-anchored compounds in cells incorporated by metabolic labeling,[45] we chose to study the copper(I)-catalyzed azide-alkyne cycloaddition (CuAAC) reaction in the context of lipid membranes. In solution, the CuAAC reaction exhibits complex,[4] yet well-

defined kinetics,[46] which can be accelerated through use of a Cu(I)-binding ligand.[26] Several studies have employed azide-alkyne cycloaddition reactions of various types for lipid substrates and membrane-bound components. Alkyne-modifed lipids have been used with CuAAC as a tool for evaluating lipid-modifying enzymes.[47] Photocrosslinkable azide-modified lipids have been used to study protein-lipid interactions in mitochondrial inner membrane vesicles,[48] and strain-promoted azide-alkyne cycloaddition has been employed to allow for dynamic cellular imaging.[49] Because of their utility and bioorthogonal nature, azide and alkyne modified lipids are commercially available. The pairing of CuAAC with alkyne and azide lipid substrates can provide a powerful means to probe biological systems by covalently labeling target membranes and membrane leaflets, as other means of labeling lipids directly has proven difficult given the small size of the lipids and the often large size of the fluorescent probes.[50]

We describe here an exploration of the rates of CuAAC reactions with lipid-anchored substrates and catalysts in an effort to develop a clear picture of the kinetic consequences of lipid-phase reactivity. This work follows the creative assembly by Deveraj and coworkers of hyrophobic azide and alkyne components into membrane-sustaining lipids by membrane-embedded CuAAC catalysts.[51] Figure 4 depicts some of the lipid constructs that have been created for CuAAC.

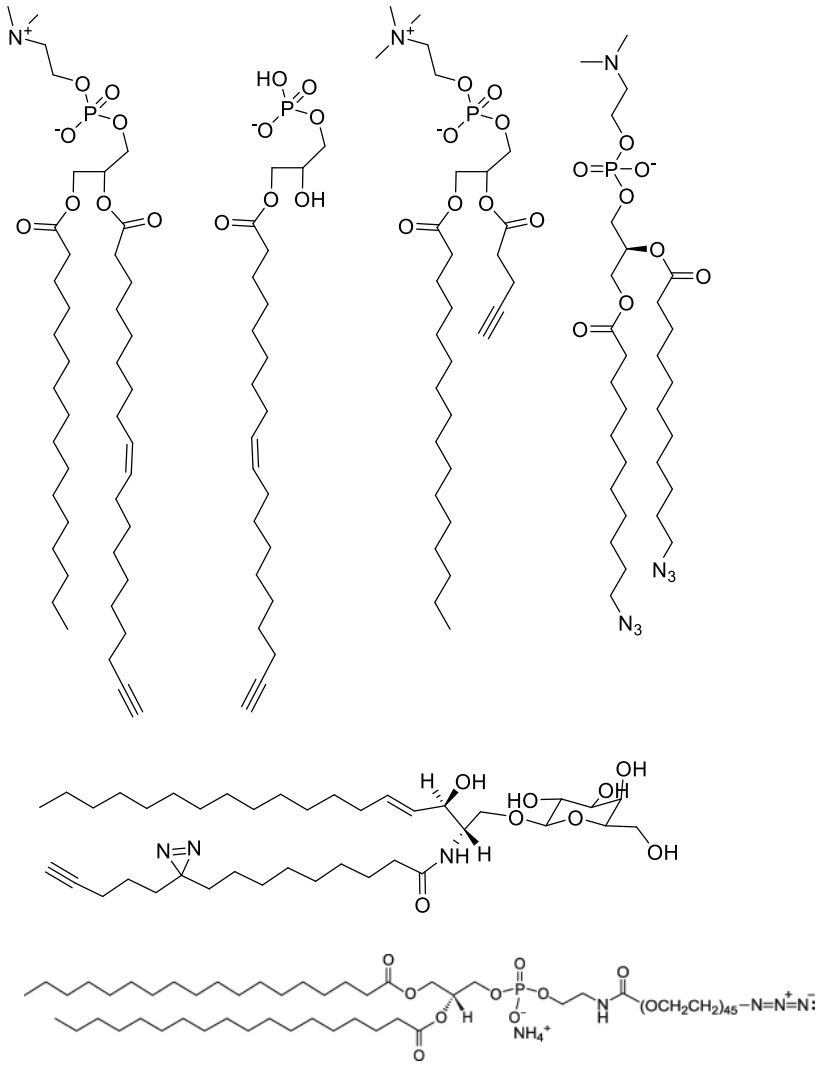

Figure 4. Lipids systems devised for CuAAC from the literature or commercially available.

With the use of these azide and alkyne lipids, however, there has been no thorough investigation of kinetics for CuAAC within a lipid membrane, or between lipid membranes. This research asks, 'What are the kinetics of CuAAC in and between lipid membrane systems, and how does this compare with other reactions between membrane-bound lipids or CuAAC in three-dimensions?' Once clicked, this research also evaluated how CuAAC altered membrane properties, including vesicle size and charge. It was anticipated that

CuAAC kinetics in the lipid phase would be similar to that of the CuAAC reaction in solution, that the lipid ligand would accelerate the CuAAC reaction similar to the work of Deveraj et. al., and that the reactions in and between vesicles would exhibit behavior similar to that observed by Menger and coworkers.

2.4 Experimental

2.4.1 Zeta Potential Measurements

Zeta potential measurements were performed on a Malvern Zetasizer instrument. For each sample, 1 mL of the lipid solution was placed in the cuvette such that the solution touched both electrodes. Measurements were taken both before and after CuAAC for each combination of vesicles.

2.4.2 Dynamic Light Scattering (DLS)

DLS was performed on a Wyatt Dynapro plate reader dynamic light scattering instrument. For all samples, care was taken to minimize micelle creation, which was mitigated through extensive sonication, limited membrane fluidity (micelles were always present when incorporation of the lyso-like lipids was attempted with a fully Egg-PC system, so a limited amount of fluidity was obtained by mixing a small amount of DOPC with a predominantly DPPC system), and thorough centrifugation where the very top-most part of the supernatant was discarded. Micelles display on DLS as particles between 5 and 10 nm radius, whereas small unilamellar vesicles created by this process range from 30 to 60 nm radius.

2.4.3 Synthesis of lipid compounds

Unless otherwise noted, all reagents were purchased from commercial suppliers. DOPC and DPPC were purchased from Avanti Polar Lipids.

2.4.3.1 Synthesis of 3-azido-2-oxo-2H-chromen-7-yl-2-(octadecylamino)acetate

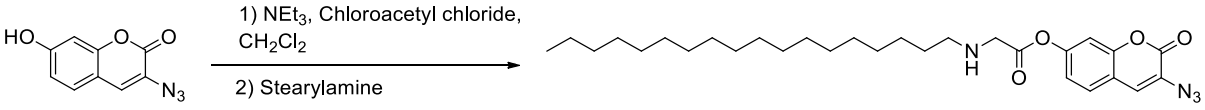

Figure 5. Synthesis of 3-azido-2-oxo-2H-chromen-7-yl-2-(octadecylamino)acetate

7-hydroxy-3-azidocoumarin was synthesized as described by Sivakumar et al.[52] 7-hydroxy-3-azidocoumarin (20 mg, 0.098 mmol, 1 equiv.) and triethylamine (41 μL, 0.3 mmol, 3 equiv.) were stirred in dichloromethane at room temperature in the dark for 5 minutes before chloroacetyl chloride (16 μL, 0.196 mmol, 2 equiv.) was added. This was stirred without light for 10 minutes, at which point stearylamine (53 mg, 0.196 mmol, 2 equiv.) was added. This was stirred for 1 hour at room temperature and purified by medium-pressure chromatography over silica gel (Biotage Isolera) with hexane/ethyl acetate gradient (Rf = 0.28 for 1:5 EtOAc/Hex). The product was obtained as a yellow solid with 13% yield and was extremely photosensitive, especially when dissolved in halogenated solvents.

^{1}H-NMR ($CDCl_3$, 500 MHz): δ (ppm) 0.91 (t, 3H, J= 7 Hz), 1.28 (m, 24H), 1.58 (t, 2H, J= 7 Hz), 3.33 (q, 2H, J= 7 Hz), 4.09 (s, 2H), 4.36 (s, 1H), 6.62 (s,1H), 6.58 (m, 1H), 7.19 (s, 1H), 7.32 (d, 1H, J= 8 Hz).

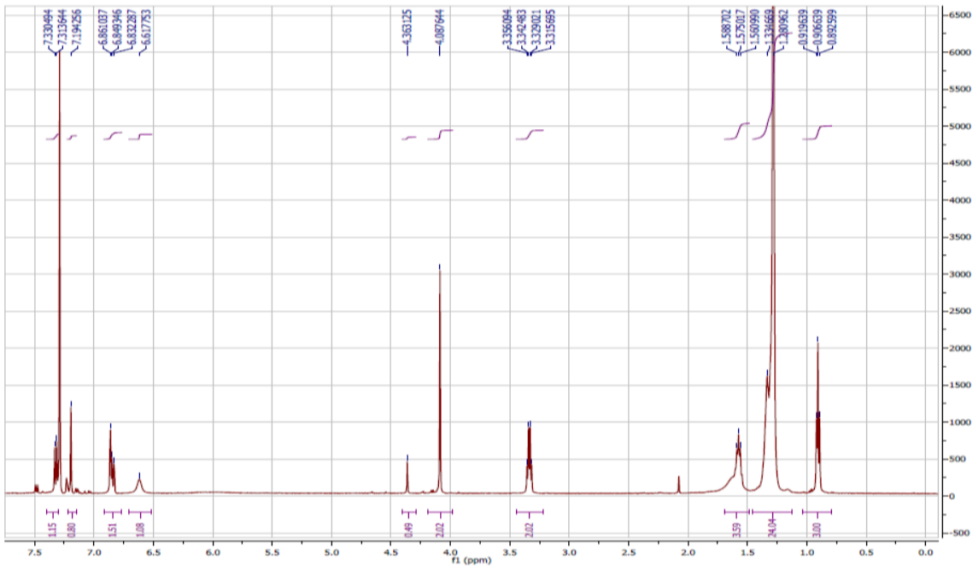

Figure 6. ^{1}H-NMR spectrum for 3-azido-2-oxo-2H-chromen-7-yl-2-(octadecylamino)acetate

IR (cm^{-1}): 3289 (secondary amine), 2138 (azide), 1697 (carbonyl), 1642 (carbonyl).

2.4.3.2 Synthesis of N-(prop-2-yn-1-yl)octadecan-1-amine

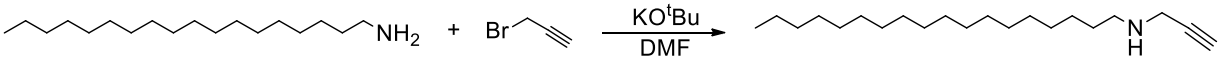

Figure 7. Synthesis of N-(prop-2-yn-1-yl)octadecan-1-amine

Stearylamine (50 mg, 0.186 mmol, 1 equiv.) and potassium tert-butoxide (62 mg, 0.557 mmol, 3 equiv.) were combined in DMF (8 mL). The system was purged with nitrogen and heated to 40 °C. Propargyl bromide (18 μL, 0.204 mmol, 1.1 equiv) was added and the solution was stirred overnight at 40 °C. The reaction was quenched with water and extracted with dichloromethane. The solution was dried over sodium sulfate. Solvent was removed by rotary evaporation with toluene azeotrope to yield a yellow powder and the

compound was purified via flash chromatography over silica gel with a hexane/ethyl acetate gradient (Rf = 0.87 for 1:1 EtOAc/Hex). The product was obtained with 56% yield.

^{1}H-NMR ($CDCl_3$, 500 MHz): δ (ppm) 0.90 (t, 3H, J = 7 Hz), 1.28 (m, 26H), 1.53 (p, 2H, J= 7 Hz), 2.28 (t, 1H, J= 2 Hz), 2.60 (t, 2H, J= 7 Hz), 3.51 (d, 2H, J = 2 Hz).

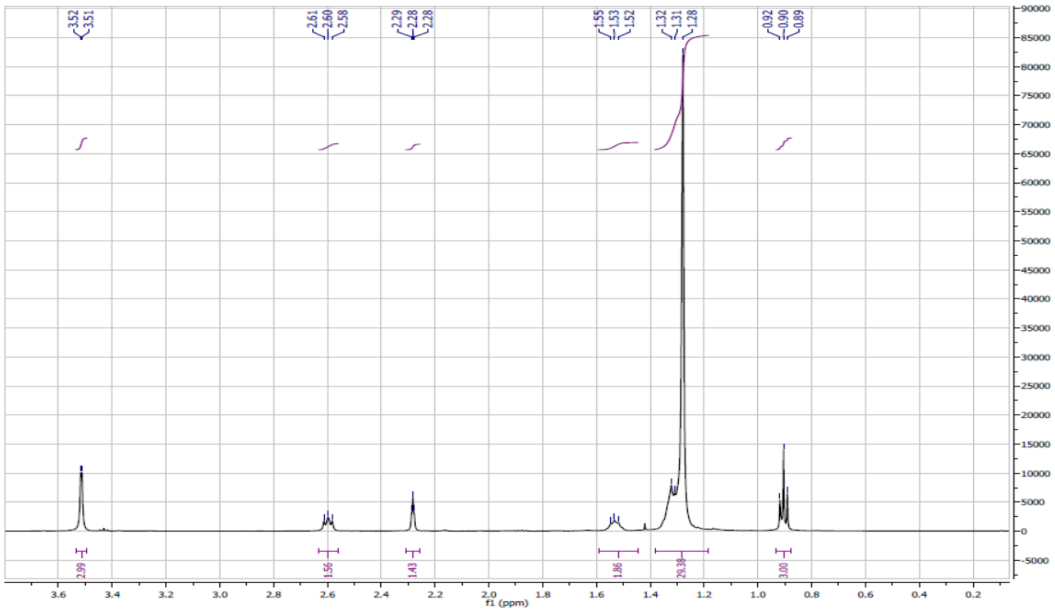

Figure 8. 1H-NMR spectrum for N-(prop-2-yn-1-yl)octadecan-1-amine

^{13}C-NMR ($CDCl_3$, 500 MHz) δ(ppm) 13.9, 22.5, 26.9, 27.1, 29.2, 29.5, 31.8, 41.9, 52.8, 73.5.

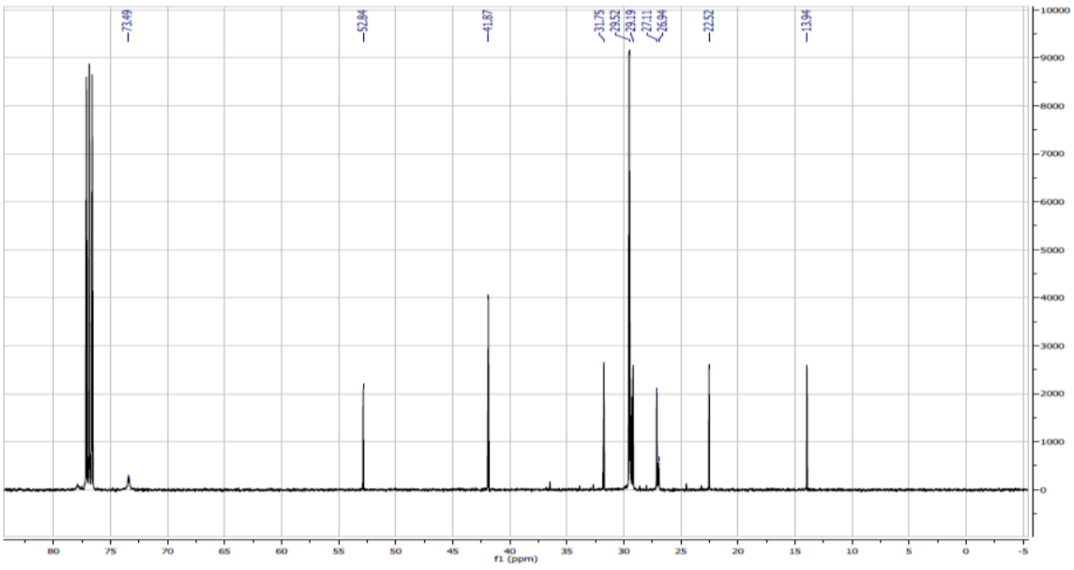

Figure 9. ^{13}C-NMR spectrum for N-(prop-2-yn-1-yl)octadecan-1-amine

Mass Spec: (M + K^+) 346.50.

IR (cm^{-1}): 3290 (alkyne), 3120 (secondary amine), and 2120 (terminal alkyne).

2.4.3.3 Synthesis of 1-azidohexadecane

Figure 10. Synthesis of 1-azidohexadecane.

1-bromohexadecane (4.4 mL, 14.4 mmol, 1 equiv.) and sodium azide (1.88 g, 28.8 mmol, 2 equiv.) were combined in DMF and heated to 50 °C for 24 h. After cooling, solvent was removed via rotary evaporation with toluene azeotrope. The product was dissolved in dicholoromethane and washed three times with water. The product was purified by flash chromatography over silica gel and eluted with 100% hexanes. Column fractions were checked via TLC after dunking in a triphenylphosphine solution in DCM,

followed by a ninhydrin solution and heating to yield purple spots on the silica. The product was obtained as a clear liquid following removal of hexanes by rotary evaporation, in quantitative yield.

^{1}H-NMR ($CDCl_3$, 500 MHz): δ (ppm) 0.91 (t, 3H, J = 7Hz), 1.31 (m, 26H), 1.63 (p, 2H, J = 7 Hz), 3.28 (t, 2H, J = 7 Hz).

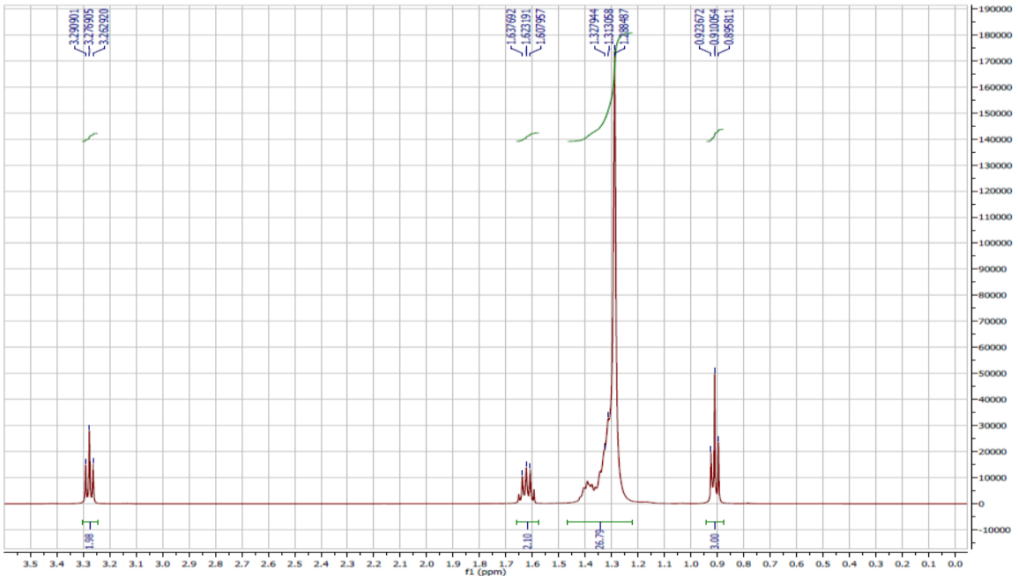

Figure 11. ^{1}H-NMR spectrum for 1-azidohexadecane.

^{13}C-NMR ($CDCl_3$, 500 MHz) δ(ppm) 13.9, 22.5, 26.6, 29.0, 29.5 (m), 31.8, 51.3.

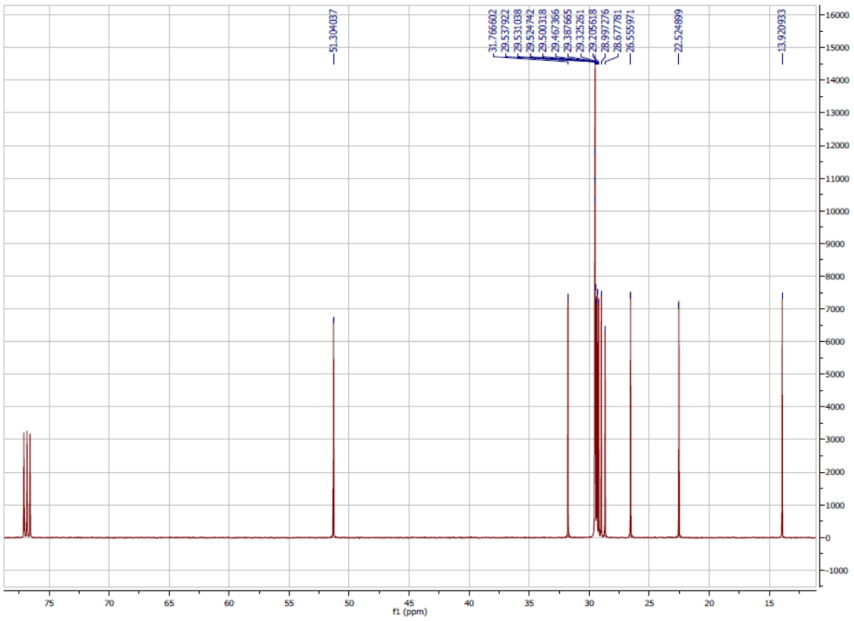

Figure 12. ^{13}C-NMR spectrum for 1-azidohexadecane

IR (cm^{-1}): 2093 (azide).

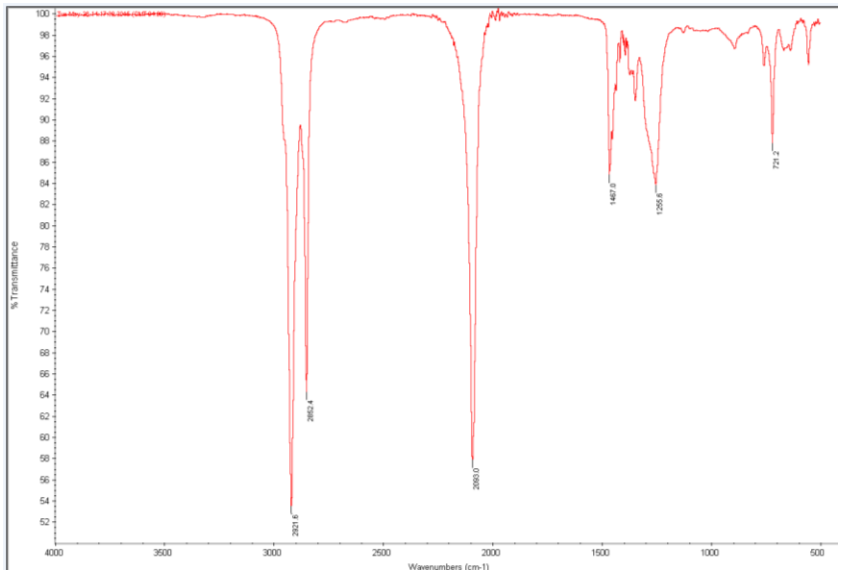

Figure 13. IR spectrum for 1-azidohexadecane

2.4.3.4 Synthesis of tris((1-hexadecyl-1*H*-1,2,3,-triazol-4-yl)methyl)amine

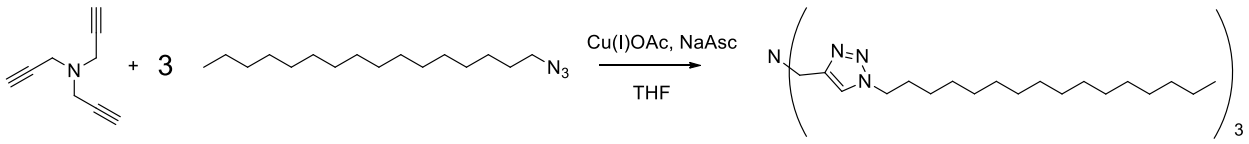

Figure 14. Reaction scheme for synthesis of tris((1-hexadecyl-1H-1,2,3,-triazol-4-yl)methyl)amine

Based on synthesis by Soriano del Amo et. al.,[53] tripropargylamine (324 μL, 2.29 mmol, 1 equiv.), 1-azidohexadecane (2.1 g, 7.89 mmol, 3.45 equiv.), copper(I) acetate (63 mg, .33 mmol, 0.15 equiv.), and sodium ascorbate (273 mg, 1.38 mmol, 0.6 equiv.) were combined in dry THF in a 20 mL scintillation vial. This vial was sealed under argon, parafilmed, and heated to 60 °C overnight while stirring. After removing from heat, this was placed in an ice bath and filtered. The solid was rinsed with excess cold THF and further recrystallized in THF to produce an off-white solid with 77% yield.

^{1}H-NMR ($CDCl_3$, 500 MHz): δ (ppm) 0.91 (t, 9H, J = 7 Hz), 1.34 (m, 78H), 1.95 (br. s, 6H), 3.77 (br. s, 6H), 4.38 (br. s, 6H), 7.81 (br. s, 3H).

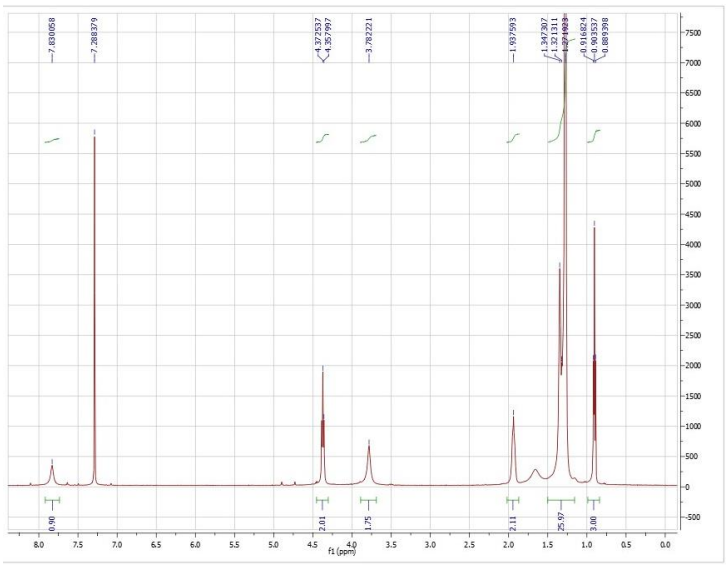

Figure 15. NMR spectrum for tris((1-hexadecyl-1H-1,2,3,-triazol-4-yl)methyl)amine.

Mass Spec: $(M + H^+)$ 934.75.

IR (cm^{-1}): 3131 (C-H in triazole).

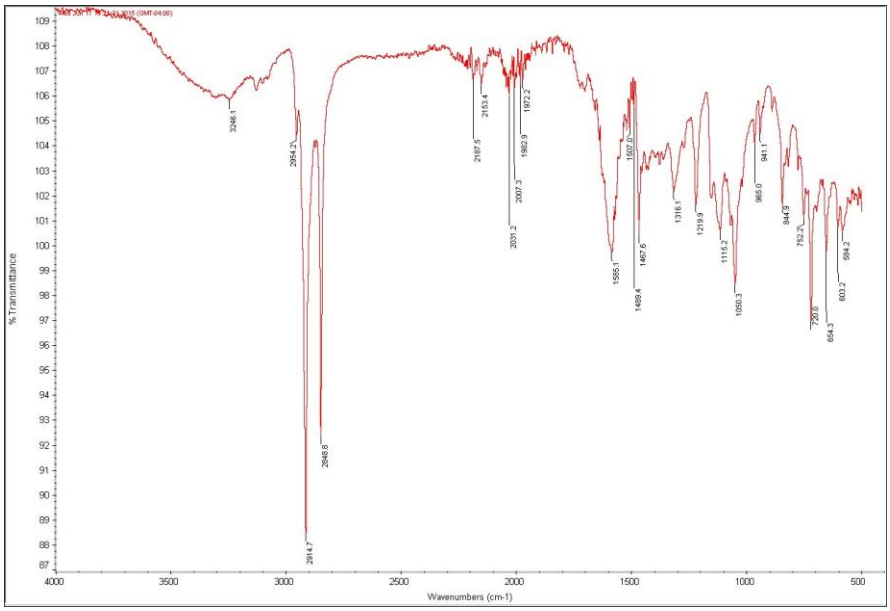

Figure 16. IR spectrum for tris((1-hexadecyl-1H-1,2,3,-triazol-4-yl)methyl)amine.

2.4.3.5 Synthesis of 6-(4-((octadecylamino)methyl)-1H-1,2,3-triazol-1-yl)-7-oxo-7,8-dihydronaphthalen-2-yl octadecylglycinate

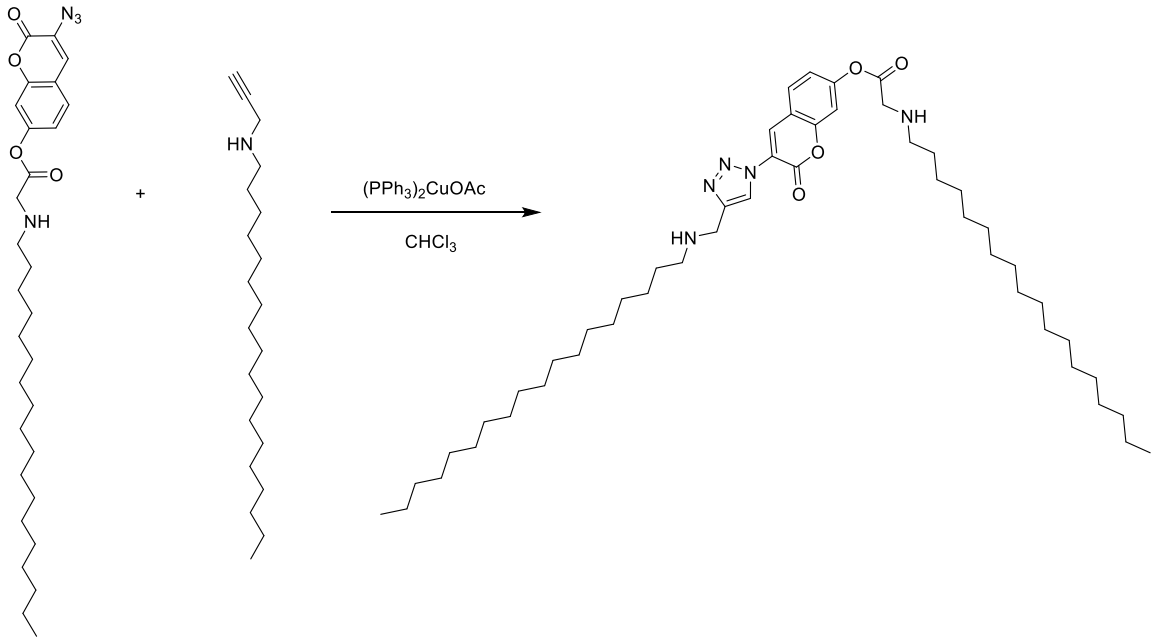

Figure 17. Reaction scheme for 6-(4-((octadecylamino)methyl)-1H-1,2,3-triazol-1-yl)-7-oxo-7,8-dihydronaphthalen-2-yl octadecylglycinate.

3-azido-2-oxo-2H-chromen-7-yl-2-(octadecylamino)acetate (10 mg, 0.019 mmol, 1 equiv.) and N-(prop-2-yn-1-yl)octadecan-1-amine (16 mg, 0.057 mmol, 3 equiv.) were combined in 10 mL chloroform with $(PPh_3)_2CuOAc$ (5 mg, 0.007 mmol, 0.25 equiv.). This reaction was shielded from light and reacted at room temperature for 3 hours. The solvent was removed by rotary evaporation. Following a preparatory TLC with 3:20 ethyl acetate / hexanes, the product was obtained as a co-eluent mixture with unreacted 3-azido-2-oxo-2H-chromen-7-yl-2-(octadecylamino)acetate to yield 5.5 mg of a product that contained 24% of the formed triazole (evaluated by NMR integration). This was incorporated into lipid vesicles and the vesicle solution was used to standardize fluorescence output of kinetics traces.

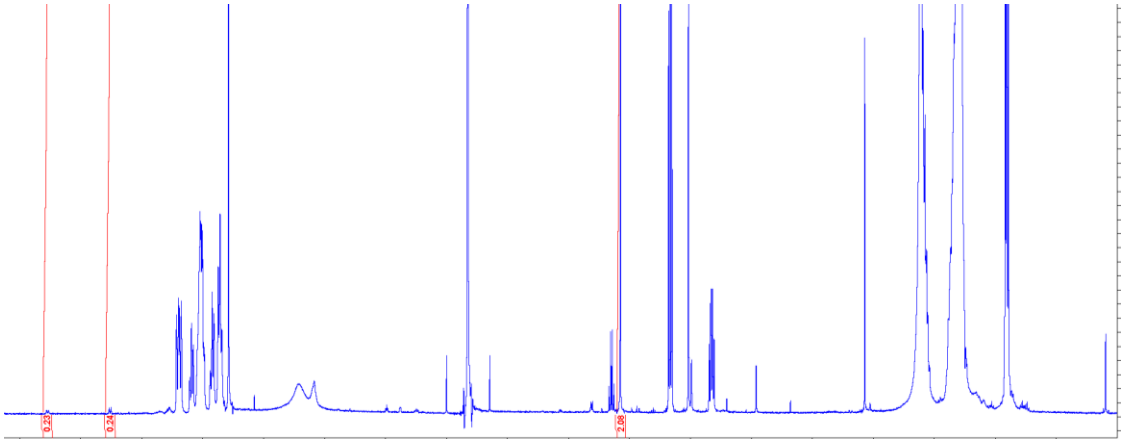

Figure 18. NMR spectrum for 6-(4-((octadecylamino)methyl)-1H-1,2,3-triazol-1-yl)-7-oxo-7,8-dihydronaphthalen-2-yl octadecylglycinate, with calibration peaks (for percent of triazole formed) identified.

2.4.4 Vesicle Creation and Composition

All vesicles were comprised of 2% synthesized lipid and 98% of either DPPC or DPPC / DOPC.

Table 1. Lipid composition in vesicles.

Nonfluid V1	373μL of 10 mg/mL DPPC, 147 μL of 1 mg/mL **1**, 85 μL of 1 mg/mL stearylamine
Semifluid V1	298 μL of 10 mg/mL DPPC, 80 μL of 10 mg/mL DOPC, 147 μL of 1 mg/mL **1**, 85 μL of 1 mg/mL stearylamine
Nonfluid V2	373 μL of 10 mg/mL DPPC, 88 μL of 1 mg/mL **2**, 85 μL of 1 mg/mL stearylamine
Semifluid V2	298 μL of 10 mg/mL DPPC, 80 μL of 10 mg/mL DOPC, 88 μL of 1 mg/mL 2, 85 μL of 1 mg/mL stearylamine
Nonfluid V3	373 μL of 10 mg/mL DPPC, 256 μL of 1 mg/mL 3, 153.6 μL of 1 mg/mL stearylamine
Semifluid V3	298 μL of 10 mg/mL DPPC, 80 μL of 10 mg/mL DOPC, 256 μL of 1 mg/mL **3**, 153.6 μL of 1 mg/mL stearylamine
Nonfluid V4	373 μL of 10 mg/mL DPPC, 147 μL of 1 mg/mL **1**, 88 μL of 1 mg/mL **2**, 8.2 μL of 1 mg/mL stearylamine
Semifluid V4	298 μL of 10 mg/mL DPPC, 80 μL of 10 mg/mL DOPC, 147 μL of 1 mg/mL 1, 88 μL of 1 mg/mL 2, 8.2 μL of 1 mg/mL stearylamine
Nonfluid V5	373 μL of 10 mg/mL DPPC, 147 μL of 1 mg/mL **1**, 256 μL of 1 mg/mL **3**, 76.8 μL of 1 mg/mL stearylamine
Semifluid V5	298 μL of 10 mg/mL DPPC, 80 μL of 10 mg/mL DOPC, 147 μL of 1 mg/mL **1**, 256 μL of 1 mg/mL **3**, 76.8 μL of 1 mg/mL stearylamine
Nonfluid V6	373 μL of 10 mg/mL DPPC, 88 μL of 1 mg/mL **2**, 256 μL of 1 mg/mL **3**, 76.8 μL of 1 mg/mL stearylamine
Semifluid V6	298 μL of 10 mg/mL DPPC, 80 μL of 10 mg/mL DOPC, 88 μL of 1 mg/mL **2**, 256 μL of 1 mg/mL **3**, 76.8 μL 1 mg/mL stearylamine
Nonfluid V7	373 μL of 10 mg/mL DPPC, 147 μL of 1 mg/mL **1**, 88 μL of 1 mg/mL **2**, 256 μL of 1 mg/mL **3**
Semifluid V7	298 μL of 10 mg/mL DPPC, 80 μL of 10 mg/mL DOPC, 147 μL of 1 mg/mL **1**, 88 μL of 1 mg/mL **2**, 256 μL of 1 mg/mL **3**

Small unilamellar vesicles (SUVs) were created by a method similar to that described by Abramson et al.[54] Standard lipids (DPPC or a DPPC/DOPC mixture) were mixed with a small percentage (2% of overall lipid composition) of the azide-, alkyne-, or ligand containing compound of interest in chloroform (or with stearylamine to create equal synthetic lipid concentration, depending on the vesicle), and the solvent was evaporated in a round-bottomed flask to create a thin film coating the glass, as depicted in Figure 19. The film was further dried under a stream of nitrogen gas, and was then rehydrated in a sterile-filtered phosphate buffer (0.2 M pH 7) overnight at 4°C, sealed under argon. The mixture was then gently warmed with a heat gun while swirling until no lipid film remained visible on the sides of the flask and the solution appeared homogenous. Each sample was transferred to a vial and sonicated with cavitation for 1.5 minutes (5 seconds on, 2 seconds rest, for 26 cycles) at room temperature with a probe tip sonicator, followed by centrifugation at 160,000 x g (41,000 rpm) at 25 °C for two hours. The top-most portion of the supernatant was discarded and the remainder of the supernatant was used without further manipulation; all vesicles were used within 24 h of their preparation. Lipid bilayer formation was verified with FM 1-43 dye by comparing the fluorescence of the sample with lipids to a sample without lipid, with the understanding that samples lacking lipid bilayers would display little to no fluorescence whereas for samples with bilayer present the dye exhibits a greatly increased fluorescence. Vesicle size and charge were characterized before and after CuAAC reactions by dynamic light scattering (DLS) and zeta potential measurement.

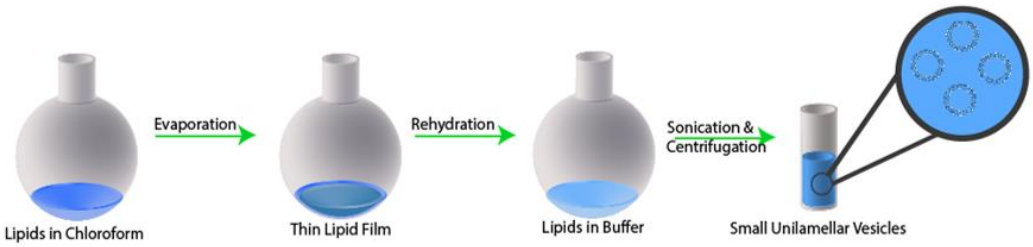

Figure 19. Lipid vesicle preparation scheme.

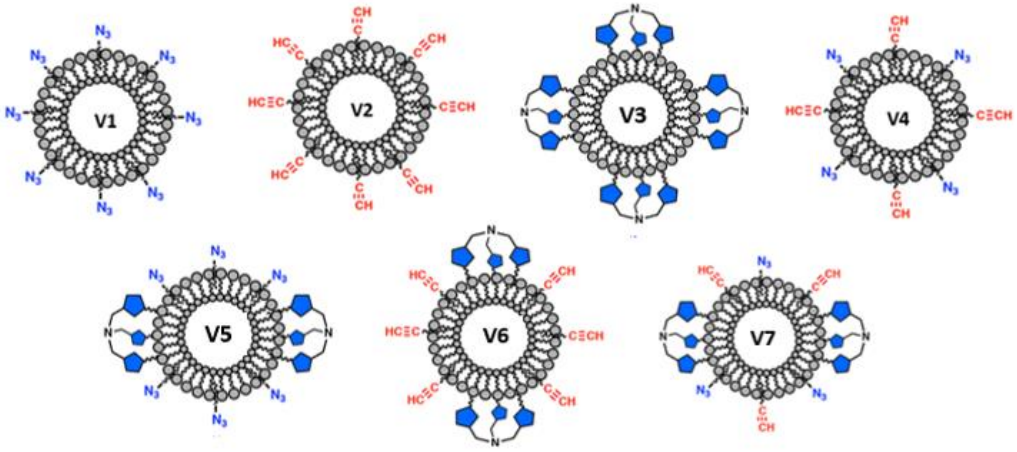

Figure 20. Vesicles created for kinetics experimentation.

In total, seven different types of vesicles were created, which represent the maximum number of ways lipid azide, alkyne, and ligand could be either alone in a membrane, or in combination with other lipid CuAAC reagents.

2.4.5 Kinetics

CuAAC reactions were performed in black, clear-bottomed optically transparent 96-well plates. Stock solutions were prepared 5x more concentrated than the planned reaction solution, each in the same sterile-filtered sodium phosphate buffer (0.2 M, pH 7). To each well was added, in order, equal volumes freshly-prepared $CuSO_4$ solution, ligand solution,

alkyne solution, and azide solution. The reaction was initiated by the addition of sodium ascorbate solution to each well, and the fluorescence was monitored over time with a ThermoFisher Varioskan plate reader. A small amount of background signal (fluorescence over time without copper) was subtracted from the raw fluorescence kinetic trace for each run, as depicted in Figure 22.

2.5 Results

2.5.1 Kinetics of small molecule substrates in free solution

The azide functionality present on 7-hydroxy-3-azidocoumarin quenches the fluorescence that is typical of this coumarin class of compounds. When the molecule is converted to a triazole, however, it exhibits fluorescence when excited (λ_{ex} = 404 nm, λ_{ex} = 476 nm). The fluorescent spectrum of this reaction over time is depicted in Figure 21.

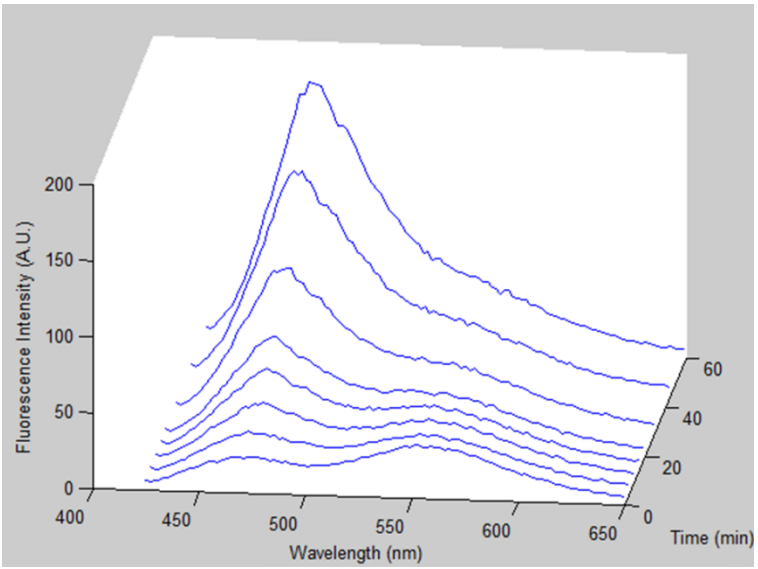

Figure 21. Kinetics of 7-hydroxy-3-azidocoumarin CuAAC with 2-methyl-3-butyn-1-ol when excited at 404 nm.

To verify the performance of the reactants and conditions used in this study in homogenous solution, the rates of reactions of 7-hydroxy-3-azidocoumarin with a representative aliphatic alkyne, 2-methyl-3-butyn-2-ol, were measured in the absence of lipid using varying amounts of azide, alkyne, and catalyst (5:1 molar ratio of ligand THPTA and Cu(I) ions[55]). The expected kinetic parameters[26] were observed: first-order dependence on azide, slightly less than first order on alkyne, and second order dependence on catalyst.

Table 2. Conditions for the reaction of 7-hydroxy-3-azidocoumarin CuAAC with 2-methyl-3-butyn-1-ol as depicted in Figure 22.

	Concentration
Azide	Varying by a factor of 2
Alkyne	370 μM
$CuSO_4$	12 μM
THPTA	60 μM
NaAsc	4 mM
Control (reaction mixture without $CuSO_4$) fluorescence trace subtracted from active kinetics traces.	

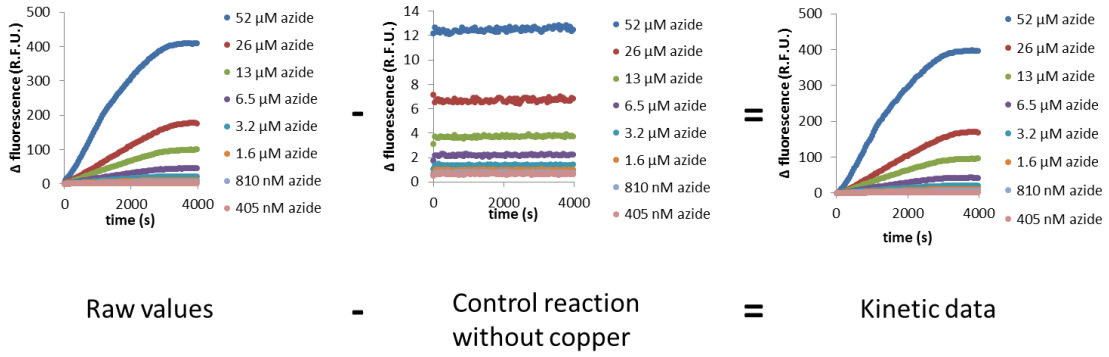

Figure 22. Representative kinetic traces for the reaction of 7-hydroxy-3-azidocoumarin CuAAC with 2-methyl-3-butyn-1-ol, demonstrating background subtraction.

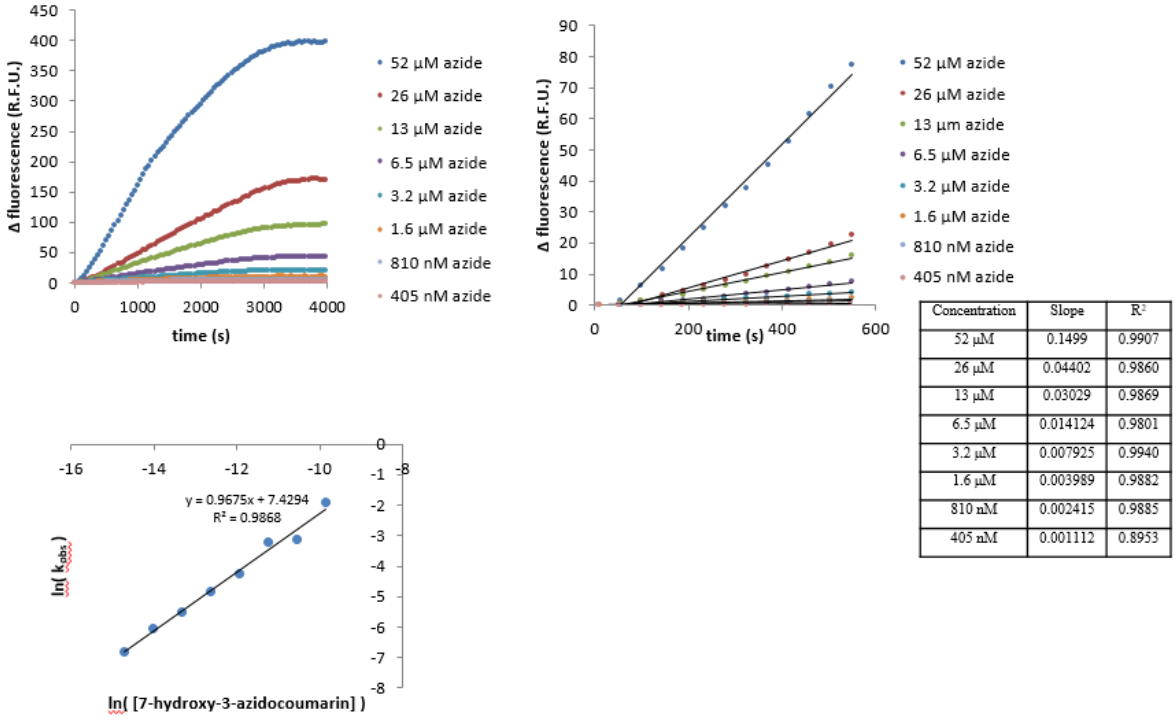

Concentration	Slope	R^2
52 µM	0.1499	0.9907
26 µM	0.04402	0.9860
13 µM	0.03029	0.9869
6.5 µM	0.014124	0.9801
3.2 µM	0.007925	0.9940
1.6 µM	0.003989	0.9882
810 nM	0.002415	0.9885
405 nM	0.001112	0.8953

Figure 23. Representative determination of initial kinetics for 7-hydroxy-3-azidocoumarin CuAAC with 2-methyl-3-butyn-1-ol.

2.5.2 Kinetics of one substrate in-membrane and other CuAAC partners in solution

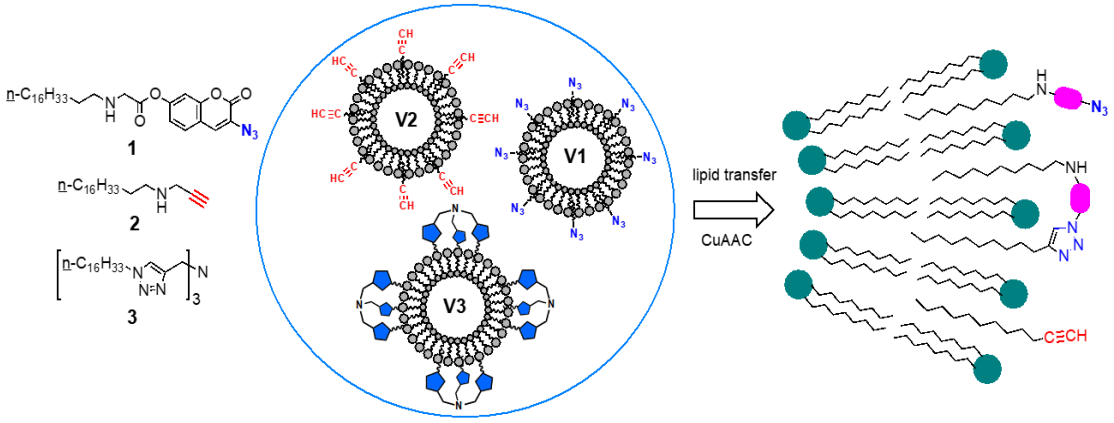

Figure 24. Scheme depicting overall lipid CuAAC research process and findings.

Reaction kinetics were also evaluated for reactions in which one of the components (azide, alkyne, or copper-binding ligand) was displayed in a non-fluid DPPC small unilamellar vesicle (**V1**, **V2**, or **V3**, respectively), and the other components were present in solution. Similar apparent rate orders were observed for these membrane-displayed species compared to free solution reactions.

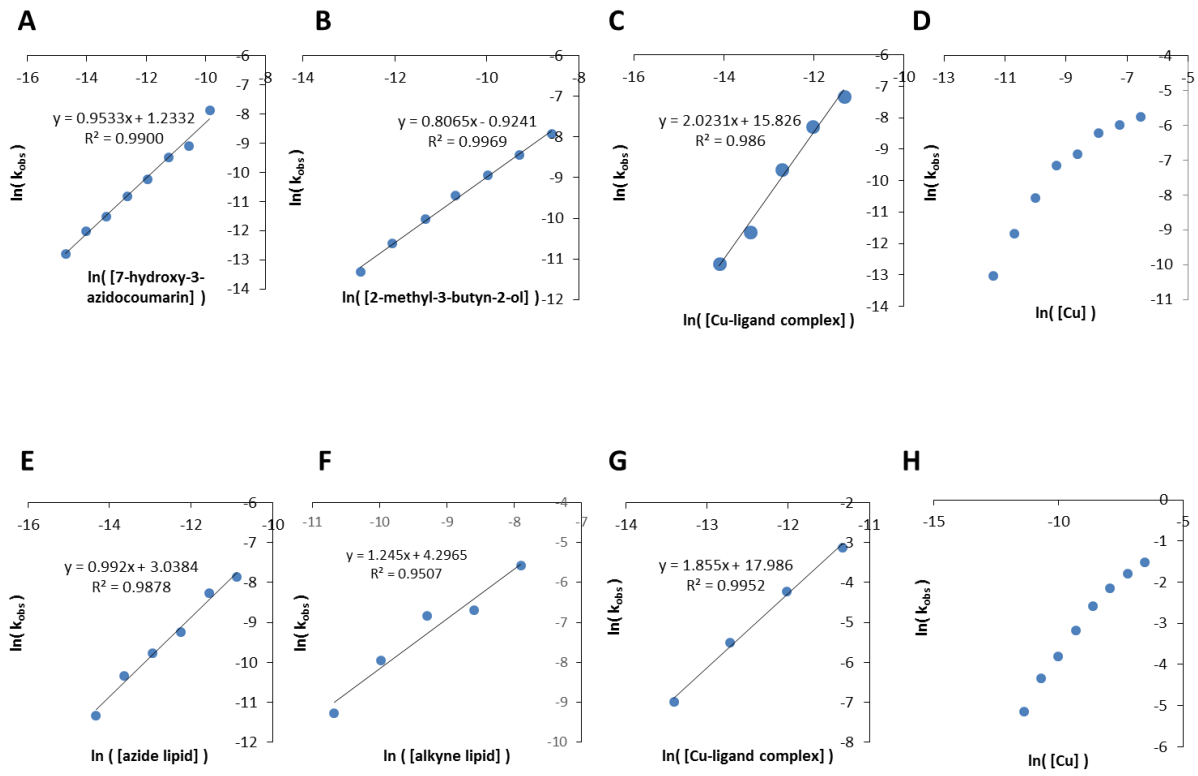

Figure 25. CuAAC experimental rate order plots for: A) 7-hydroxy-3-azidocoumarin in solution. B) 2-methyl-3-butyn-2-ol in solution. C) Cu-THPTA complex in solution with catalytic copper conditions. D) Cu in solution. E) Azide-lipid, in membrane. F) Alkyne-lipid, in membrane. G) Cu + lipid-ligand, in membrane. H) Cu + lipid-ligand, in membrane. Concentrations for all plots are depicted in Table 3.

Table 3. Concentrations of reagents used to produce plots in Figure 25.

	A	B	C	D	E	F	G	H
Azide	405 nM -52 μM	52 μM	52 μM	52 μM	590 nM - 19 μM	52 μM	52 μM	52 μM
Alkyne	370 μM	2.9 μM - 185 μM	370 μM	92 μM	370 μM	590 nM - 19 μM	370 μM	370 uM
$CuSO_4$	12 μM	12 μM	1.5 μM - 12 μM	11 μM - 1.4 mM	12 μM	12 μM	1.5 μM - 12 μM	11 μM - 1.4 mM
Ligand	60 μM	60 μM	5x Cu	60 μM	60 μM	60 μM	1.1 μM – 9 μM	9 μM
NaAsc	4 mM	4 mM	4 mM	4 mM	4 mM	4 mM	4 mM	4 mM

Note that the apparent second-order dependence of the reaction on vesicle-bound Cu-ligand concentration only requires two Cu atoms to associate with a single ligand in the catalytically-active complex, as we have proposed earlier based on the unusual coordination properties of the tris(triazolylmethyl)amine series of ligands.[6] Increasing Cu concentration relative to constant concentrations of ligand also showed similar rate patterns, supporting the assumption that the CuAAC reaction behaves similarly when one of the reagents or the catalyst is displayed on a lipid bilayer.

When incorporated into lipid bilayers consisting primarily of saturated lipid tails, the unsaturated lipid DOPC can perturb lipid packing thereby enhancing overall membrane

fluidity.[56] The effect of fluidity on reactions between vesicle-supported azide and alkyne was assessed by comparing reactions in which reactants were displayed in an ordered membrane (DPPC-only) membrane *vs*. a more fluid one (19% DOPC in DPPC, a mixture chosen to give the same size vesicles with good stability as well as to allow for facile incorporation of synthetic lipids, and designated "semi-fluid" below). As shown in Figure 26, the initial rates of reaction in panels A and C are similar, but differ significantly in extent of completion, indicating that the reaction of alkyne in the nonfluid lipid membrane shuts down faster. Anchoring of azide-lipid in either type of vesicle gave very similar reactions with either form of the alkyne vesicle.

It should be noted for these kinetics, that the greatest anticipated degree of CuAAC completion is 50%, as only the outer leaflet of the vesicle would be available for reaction, although each of the azide, alkyne, or ligand lipids would be incorporated (presumably evenly) throughout both leaflets of the vesicle.

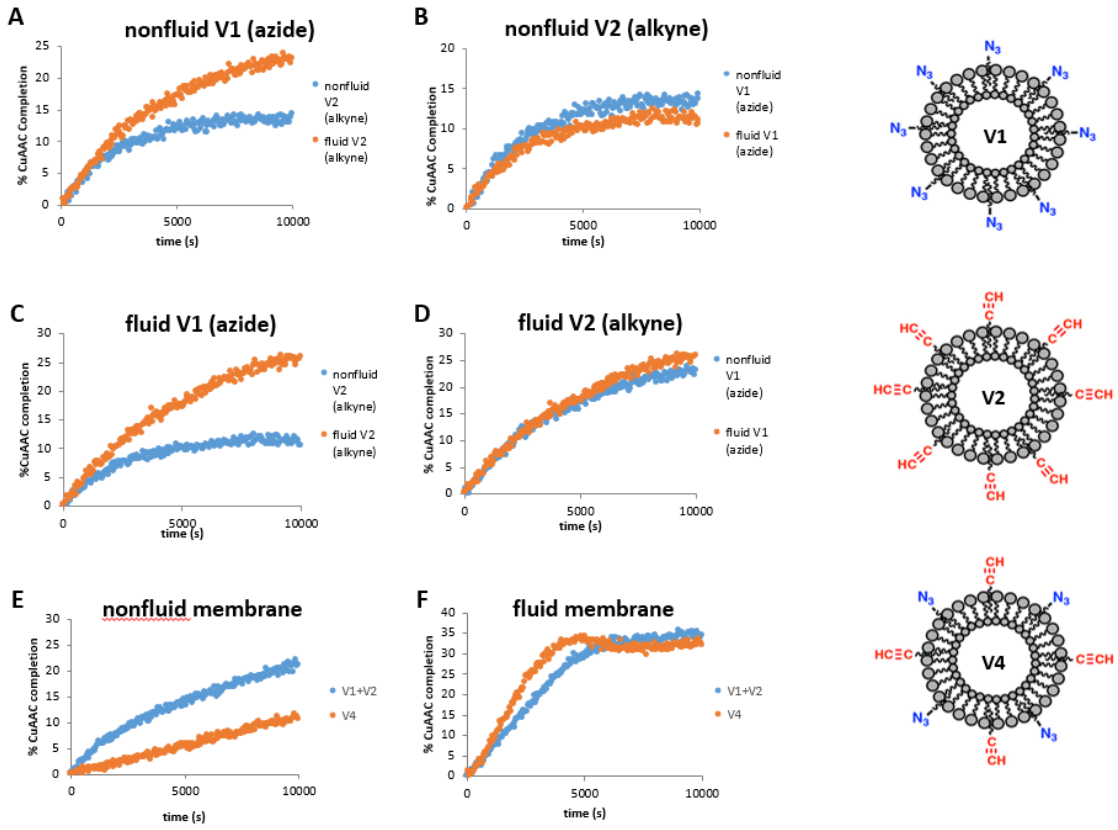

Figure 26. CuAAC reactions between vesicle-supported reactants. Azide- or alkyne- lipids were incorporated at 2 mole-% with respect to lipid molecules in synthetic vesicles. The resulting vesicles are represented in cartoon form on the right; note that azide and alkyne groups are displayed on the interior membrane surface as well, but are not shown in the cartoon. In all cases, overall concentrations were as follows: [1] = 19 μM; [2] = 19 μM; [$CuSO_4$] = 12 μM; [NaAsc] = 4 mM; [THPTA] = 60 μM. "Nonfluid" denotes vesicles made with 98% DPPC; "semi-fluid" denotes vesicles made with an 81:19 DPPC:DOPC molar ratio at 98% in the membrane.

The greater dependence of alkyne reactivity on the membrane environment may be due to several factors. First, alkyne **2**, being a secondary amine, is likely to interact differently with the phosphocholine head groups of the vesicle lipids than coumarin azide **1**, and may therefore be less accessible. In addition, the CuAAC reaction relies on the catalyst's ability to escape the formation of unproductive coordination complexes with both alkyne and ligand.[6,26] This requires Cu ligand exchange to be relatively fast. A certain

level of membrane fluidity may be necessary to achieve alkyne accessibility to azide and catalyst, and Cu(I) accessibility to the proper ligands for triazole formation.

2.5.3 Reactions between vesicles

The importance of bilayer mobility was further highlighted by comparisons of reactions between azide **1** and alkyne **2** associated with different vesicles (**V1** + **V2**) *vs.* the corresponding intra-vesicular reaction (**V4**), at the same overall concentrations of functional groups and lipid. Thus, for non-fluid vesicles, the communication between azide and alkyne is so poor that reactions *between* vesicles was found to be faster (Figure 26 panel E). When membrane fluidity was increased (Figure 26 panel F), both reactions sped up to exhibit similar profiles, with the intra-vesicular process slightly faster.

Vesicles were also prepared incorporating the hydrophobic ligand **3**, similar to the one prepared by Devaraj and coworkers to catalyze CuAAC reactions in the lipid phase.[51] Thus, vesicle **V3** provided only a very slight rate acceleration of the reaction of **V1**+**V2** (both systems in the presence of the same amount of $CuSO_4$ precursor and sodium ascorbate), whereas added THPTA was much more effective (Figure 27 bottom). While it might be expected to be difficult for three different vesicles to come together for this process, the co-incorporation of ligand **3** in the same vesicle with azide (**V5**), alkyne (**V6**), or both (**V7**) gave little or no initial rate acceleration and poorer catalyst turnover (Figure 27 top and bottom). It will be interesting to test the role of the mobility of the membrane-anchored catalyst: in this case, the three lipophilic tails of ligand **3** are likely to restrict the lateral mobility of the ligand in any lipid bilayer.

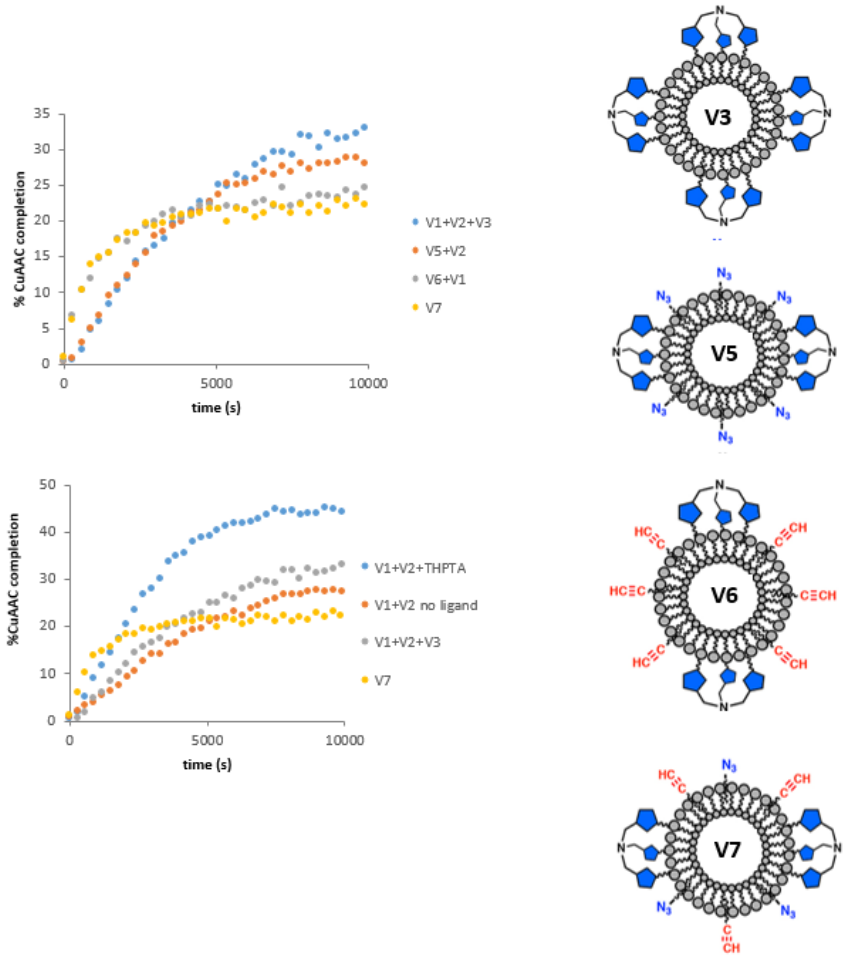

Figure 27. CuAAC reactions of azide, alkyne, and ligand lipids incorporated at 2% into 19:81 DPPC vesicles, under the same conditions as Figure 26.

Reactions between azide- and alkyne-containing vesicles (**V1** and **V2**) mediated by solution-phase Cu-THPTA produced no aggregates or detectable changes in vesicle size (Figure 29), as would be expected if the triazoles linked vesicles together or induced vesicle fusion. This suggests that the functionalized molecules are able to transfer between vesicles, either before or after the CuAAC reaction, as illustrated in Figure 28. One would expect single-tailed lipid molecules such as **1** and **2** to undergo such transfer faster than molecules bearing two (triazole product) or three (ligand **3**) anchoring hydrocarbon chains.

Consistent with relatively fast inter-vesicle transfer is the observation of only minor rate differences between the inter- and intra-vesicular reactions shown above.

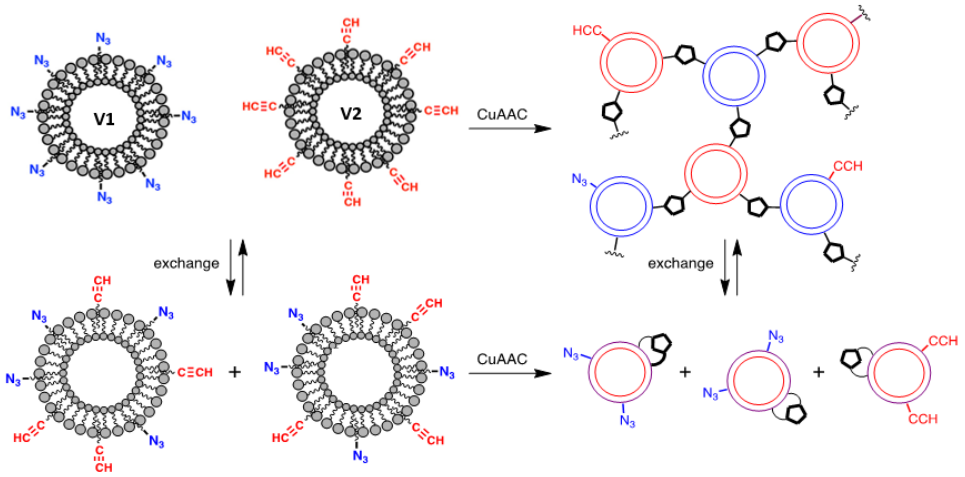

Figure 28. Cartoon representation of functionalized lipid exchange either before or after triazole formation, to give non-aggregated triazole-bearing vesicles.

2.5.4 Physical properties of vesicles pre- and post-CuAAC

As detailed in

Table 4, Table 5, and Figure 29 the physical properties of the synthetic vesicles, including size and charge, remained similar. This suggests that aggregation is not occurring as a result of the CuAAC reaction. DLS information on sizing also confirms that lipids are not present in micelles, which would present as particles in the 5-10 nm range.

Table 4. Radius and zeta potential for nonfluid vesicles pre- and post- CuAAC.

	Pre-CuAAC		Post-CuAAC	
Vesicle Type	Average Radius (nm)	Zeta Potential (mV)	Average Radius (nm)	Zeta Potential (mV)
Azide	40.3 ± 0.2	2.49 ± 0.21	40.2 ± 0.6	4.33 ± 0.28
Alkyne	33.4 ± 0.3	5.27 ± 0.06	35.2 ± 0.4	3.88 ± 0.34
Ligand	39.6 ± 0.7	4.61 ± 0.34	40.8 ± 1.4	4.91 ± 0.19
Azide/Alkyne	32.6 ± 0.4	2.40 ± 0.26	32.5 ± 0.8	2.36 ± 0.01
Azide/Ligand	46.2 ± 0.5	3.24 ± 0.39	43.5 ± 1.4	3.92 ± 0.21
Alkyne/Ligand	45.2 ± 2.0	4.25 ± 0.09	43.9 ± 1.9	4.42 ± 0.18
Azide/Alkyne/Ligand	41.6 ± 0.6	3.38 ± 0.19	36.8 ± 1.1	3.22 ± 0.13
Azide+Alkyne	35.1 ± 0.2	2.09 ± 0.10	36.1 ± 0.6	2.56 ± 0.27
Azide+Ligand	39.6 ± 1.3	5.31 ± 0.26	48.2 ± 0.8	5.63 ± 0.21
Alkyne+Ligand	42.7 ± 1.1	5.86 ± 0.25	42.1 ± 1.5	4.86 ± 0.08
Azide+Alkyne+Ligand	40.2 ± 0.7	4.86 ± 0.08	39.9 ± 1.3	5.84 ± 0.17

Table 5. Radius and zeta potential for semi-fluid vesicles pre- and post- CuAAC.

	Pre-CuAAC		Post-CuAAC	
Vesicle Type	Average Radius (nm)	Zeta Potential (mV)	Average Radius (nm)	Zeta Potential (mV)
Azide	50.9 ± 0.5	4.12 ± 0.19	55.2 ± 0.5	4.59 ± 0.28
Alkyne	48.0 ± 1.0	5.43 ± 0.48	45.6 ± 1.7	5.44 ± 0.20
Ligand	55.5 ± 0.6	6.09 ± 0.17	61.0 ± 1.4	6.65 ± 0.13
Azide/Alkyne	45.1 ± 1.5	4.31 ± 0.19	43.0 ± 1.7	4.12 ± 0.24
Azide/Ligand	48.3 ± 2.4	6.01 ± 0.44	49.1 ± 1.5	5.23 ± 0.31
Alkyne/Ligand	50.1 ± 1.3	6.14 ± 0.50	48.0 ± 1.1	5.88 ± 0.15
Azide/Alkyne/Ligand	48.9 ± 1.3	4.18 ± 0.29	46.6 ± 1.5	5.55 ± 0.19
Azide+Alkyne	48.1 ± 1.2	5.67 ± 0.44	51.2 ± 1.0	5.13 ± 0.47
Azide+Ligand	55.8 ± 0.5	6.54 ± 0.33	53.9 ± 1.2	6.50 ± 0.40
Alkyne+Ligand	53.6 ± 0.8	6.64 ± 0.50	52.3 ± 1.5	5.98 ± 0.33
Azide+Alkyne+Ligand	59.3 ± 1.5	6.12 ± 0.29	54.8 ± 1.7	6.34 ± 0.09

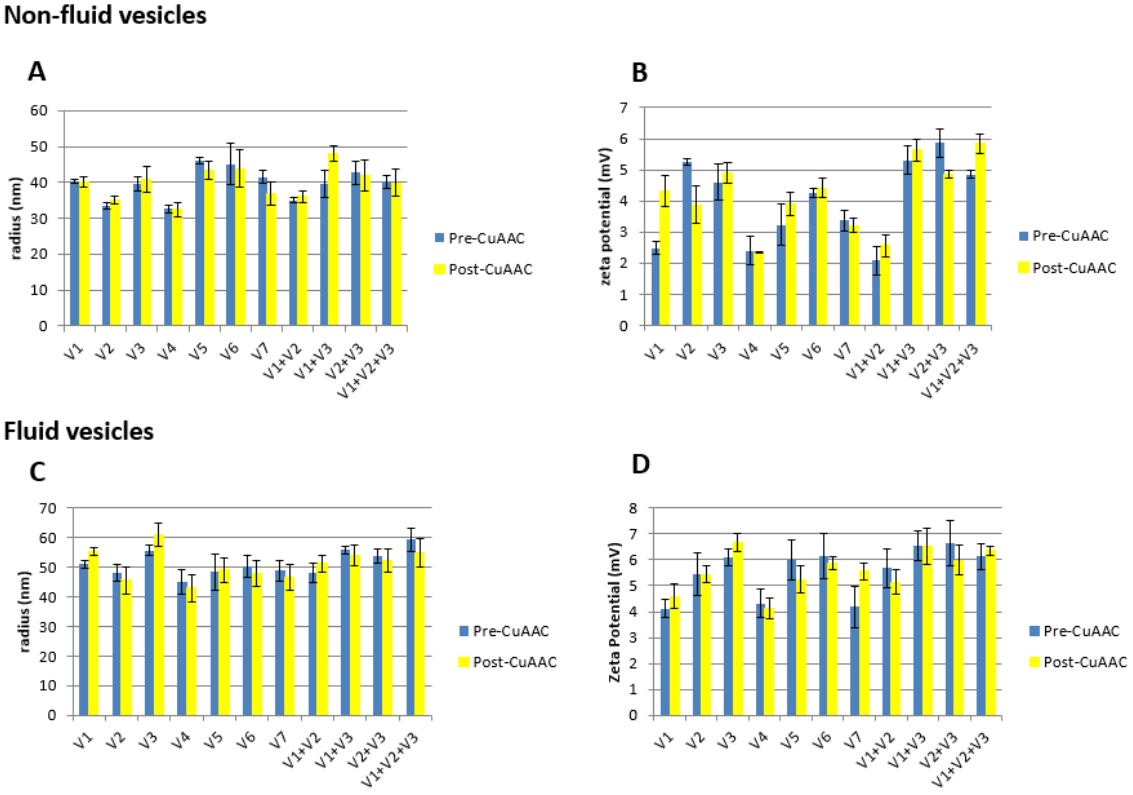

Figure 29. Characterization of vesicles before and after CuAAC reactions. Semi-fluid vesicles contain 19% DOPC; non-fluid vesicles are composed entirely of DPPC. Results with non-fluid vesicles (DPPC only) are shown on top; semi-fluid vesicles (19% DOPC, 81% DPPC) are shown on the bottom. (A,C) dymanic light scattering. (B,D) zeta potential.

2.6 Discussion

The rate order for the reactions between lipids was determined via pseudo-first order kinetics by evaluating the slope of the plots of the natural log of the concentration of the reagent in question (which had been varied over each set of experiments) and the natural log of the initial rate (linear portion). For lipid bound CuAAC reactants, it was determined that the rate orders were approximately first order with respect to azide, approximately first

order with respect to alkyne (although a rate order of less than one suggests some inhibition, which in this case likely derives from the formation of extended copper-acetylide species), and approximately second order with respect to the copper-ligand complex. This is as anticipated and is comparable to the rate order of the reagents in free solution for CuAAC.

The lipid ligand was shown to accelerate CuAAC reactivity within the membrane, although this accelerations was much less than the acceleration provided by THPTA in solution. This acceleration was most drastic when the click ligand and the alkyne were in the same membrane, which suggests that this arrangement allows for the preformation of the copper-acetylide species, prior to reactivity with the azide.

The lipids both before and after CuAAC showed no aggregation within the given time-frame, yet, the reaction between azide and alkyne occurred in situations where the azide was in one vesicle and the alkyne in another. Based upon the results demonstrated by Menger and coworkers, as well as the faster reactivity of the intravesicular reaction for fluid lipid systems and that the lipids studied were lyso-like lipids, it is suspected that this reaction between an azide bearing vesicle and an alkyne bearing vesicle proceeds through lipid transfer between vesicles, prior to the CuAAC reaction. Further reactions with modified substrates that would be less likely to dissociate from the membrane may elucidate this mechanism more clearly. This work provides context to the CuAAC reaction in and within lipid membranes that would be applicable to cell and vesicle work, although the particular use of the lipids chosen for this system are not ideal for obtaining optimum reactivity for CuAAC in-membrane as the lipid systems were only limitedly fluid and the synthetic lipids were quite dissimilar from biological lipids.

2.7 Conclusion

The reactivity of lipid membrane-bound substrates can be affected by a number of factors, including fluidity, concentration, and other components in the membrane. In general, greater CuAAC reactivity was observed with more fluid lipid systems. Modest increases in rate were observed for low concentrations of a lipid ligand catalyst in the membrane, however a solution-phase ligand proved more effective at presenting copper to reactive substrates in the membrane. Additionally, evidence suggesting lipid transfer between vesicles was observed for reactions between vesicles, although the detailed mechanism of lipid transfer between vesicles was not elucidated. Further development of CuAAC with lipid substrates could allow for bioorthogonal symmetric membrane leaflet labeling as well as providing a better understanding of this tool to probe membrane systems.

2.8 Acknowledgement

This work was performed in coordination with Dr. Michael Baksh who taught how to make and characterize small unilamellar vesicles and use equippment, Josiah Davidson who optimized sonication conditions to reduce micelle occurrence, and Haley Chenot who assisted with sample preparation. We thank Breanne Hamlett for synthesizing additional supplies of $(PPh_3)_2CuOAc$ and Dr. Roman Valiulin, Dr. Zhishuai Geng, and Dr. Craig McKay for helpful conversations, as well as Jenny Cheng for assistance with equipment.

CHAPTER 3. COVALENT FUNCTIONALIZATION OF FLEXIBLE POLYVINYL CHLORIDE TUBING VIA COPPER(I) CATALYZED AZIDE ALKYNE CYCLOADDITION

3.1 Abstract

Polyvinyl chloride (PVC) tubing is a vital part of many industries, including medicine and food. The ability to chemically modify PVC has previously been reported mainly on powdered or rigid forms of the plastic. Here we describe the chemical modifications of commercial flexible PVC medical tubing with azide and cyanide nucleophiles facilitated by phase transfer catalysts, and characterization of the resulting materials. These modifications provide convenient handles for click chemistry linkages via azide-akyne cycloaddition or tetrazole formation. Azidation was found to occur only in the outermost thin layer of the tubing material and not in the interior, and mechanical flexibility was maintained when reaction times and temperatures were moderated.

This chapter is based upon the work documented in: Beveridge, J.M.; Chenot, H.M.; Jacobs, A.; Crich, A.D.; Finn, M.G. Functionalization of Flexible Polyvinyl Chloride Tubing. Langmuir, 2018, 34 (35) 10407-10412.

3.2 An Introduction to Flexible Plastics and Their Application

Flexible plastics are staple products incorporated into a number of devices, industries, and applications. In many such uses, characteristics such as flexibility and surface hydrophobicity play a significant role in the material's utility. For example, medical tubing must be flexible enough to be employed in or around the human body and with particular equipment, sturdy enough to withstand long-term use, non-toxic, non-

leaching, and resistant to solutions that it could be immersed in or carry. Plasticizers are usually used to separate or lubricate the motions of polymer chains, thereby reducing chain interaction and producing a more deformable material.[57]

At present, as described by Dr. Keko Tarquinio of Children's Healthcare of Atlanta, a major problem in hospital settings encountered by clinicians is bacterial biofilm formation on plastic surfaces. As a means of addressing this problem for intubated patients, endotracheal tubing doped with silver nanoparticles was created; however, it is not FDA approved for pediatrics as its mechanism of action relies on the leaching of silver. Current standard treatment to limit biofilm formation on endotracheal tubing involves rinsing the patient's mouth with an antibacterial wash, followed by regular biofilm removal from the interior of the tubing by pulling the films up with a bristled brush. This treatment is often ineffective, which can give rise of conditions such as ventilator-associated pneumonia and other infections. Thus, a means to covalently modify plastics (which avoids dependence on a leaching mechanism of action), so as to attach antimicrobial functionality is desired.

Polyvinyl chloride (PVC) is one of the most widely used plastics, in part due to its low cost, prevalent availability, and tunable mechanical properties.[58] For flexible products comprised of PVC, common plasticizers include phthalates, citrates, and aliphatic diesters, but plasticizer migration from PVC during chemical processing can be an important problem.[59] The use of surface cross-linking with sodium sulfide and tetrabutylammonium hydrogen sulfide as a phase transfer catalyst (PTC) has been shown to decrease plasticizer migration in certain circumstances when modifying PVC surfaces, however the stress-strain properties of the material were significantly changed.[60]

In order to chemically modify the surface properties of PVC materials, a means of altering surface functionality while retaining key plastic properties including flexibility, color, and material strength are needed. Many reports have appeared describing the making of covalent modifications to PVC, but most have been done on PVC powder, soluble PVC in solution, or on rigid PVC substrates,[61,62,63] which avoid the problem of maintaining deformability in flexible tubing. Even studies which have attempted to covalently add plasticizer to PVC have failed to fully explore the bulk properties of the resulting materials.[64,65] The ability to modify PVC plastic through click chemistry without deformation or loss of other key properties could allow for more diverse and resilient PVC for a number of potential applications, including as antifouling plastics for marine and medical industries.

3.3 Experimental

Here we explore means to address flexible PVC tubing through nucleophilic substitution followed by formation of triazole or tetrazole linkages, as shown in Figure 30. Prior examples of these manipulations on PVC have appeared, but have been similarly restricted to soluble or cast polymer films[64,65,66,67,68] or flat sheets.[69]

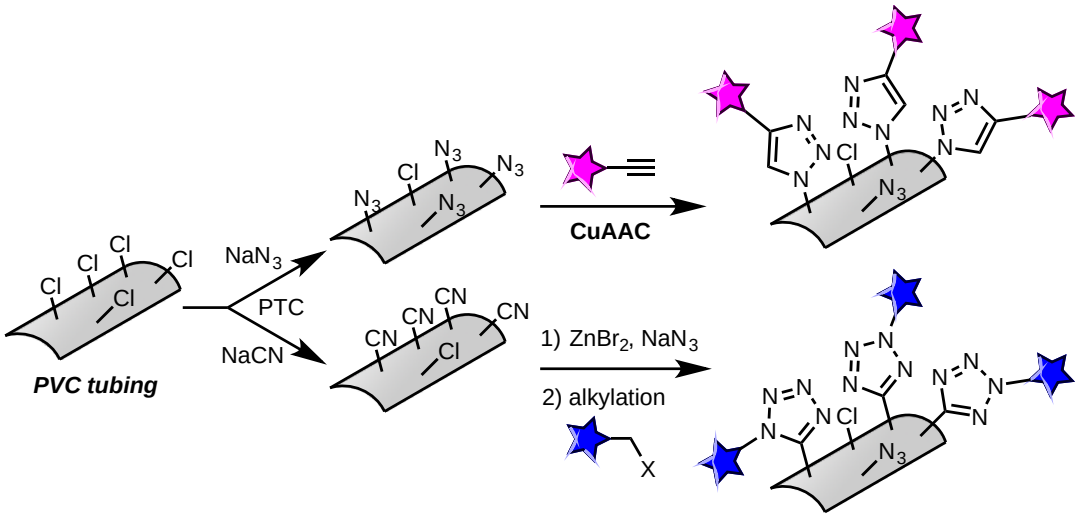

Figure 30. Modification of flexible PVC by nucleophilic substitution and subsequent reactions with modified PVC.

The studies described here used commercial plain endotracheal tubing (ET) (Covidien Mallinckrodt Oral/Nasal Tracheal Tube Cuffless, 4.0 mm inner diameter, 5.6 mm outer diameter) and catheter tubing (CT) (GentleCath Intermittent Urinary Catheter, Size 14 Male Nelaton 16") purchased from the indicated vendors. Both are made from PVC with bis(2-ethylhexyl) phthalate (DEHP) as plasticizer. $mPEG_{2000}$-alkyne was purchased from Advanced Biochemicals. All other reagents used were either available commercially through standard suppliers or synthesized as described in the supplemental information.

3.3.1 XPS measurements

X-ray photoelectron spectroscopy (XPS) was performed using a Thermo Scientific K-Alpha XPS with a monochromated Al Kα source, hemispherical analyzer, and multichannel detector. Spectra were taken by normal emission, with analysis chamber

pressure below 10^{-6} mbar with flood gun on and a spot size of 200 μm. Survey scans were carried out as the average of 4 scans over the 0 to 1350 eV binding energy range with a 1.0 eV step size, a 50 ms dwell time, and an analyzer pass energy of 200 eV. High resolution scans of the N 1s region (392-410 eV) were performed for samples that showed N1s content in the survey scan; these high resolution scans were carried out as the average of 4 scans over the range with a 0.1 eV step size, a dwell time of 50 ms, and an analyzer pass energy set to 50 eV. As azides are known to degrade over time under x-ray exposure,[32] survey measurements of nitrogen content were made in a location adjacent to other measurement areas on the same sample.

3.3.2 TGA/DSC measurements

Thermogravimetric analysis (TGA) and differential scanning calorimetry (DSC) analyses of materials were performed simultaneously on a ThermalAdvantage Q600 SDT instrument, over a range of 50 °C to 600 °C, with a constant temperature ramp of 20 °C / min. Samples were cut with a razor blade into small slices (approximately 2 mg each); each analytical run used several pieces to comprise approximately 10 mg of sample.

3.3.3 Contact angle measurements

Contact angle measurements and images were taken on a ramé-hart standard goniometer.

3.3.4 Young's modulus and hardness measurements

Indenter measurements were made with a Hysitron Triboindenter with a Berkovich 3-sided pyramid tip, radius ~200 nm, calibrated with a polycarbonate standard. Samples

were thinly sliced to create the flattest possible sample and adhered at the ends with kapton tape to the sample holding plate. Values are reported as an average of four 4 measurements separated by 10 microns between points, with increasing force from 250 to 1250 μN.

3.3.5 SEM

Scanning electron microscope (SEM) images were taken on a Hitachi S-3700N Variable Pressure SEM. Samples were thinly sliced and adhered to the sample plate, with a copper tape bridge between the surface of the material and the plate to reduce sample charging. Depending on the conditions used, some samples showed evidence of degradation over time during the SEM process in the area that the electron beam analyzed; variations in conditions used across samples were used to minimize this degradation. The majority of samples were run at 15 kV at 50 Pa or less of vacuum.

3.3.6 Alkyne synthesis

Unless otherwise noted, all reagents were purchased from commercial suppliers.

3.3.6.1 Synthesis of trimethylprop-2-yn-1-aminium iodide (1)

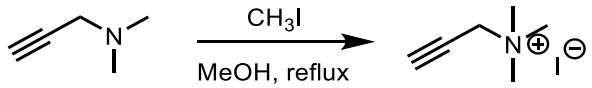

Figure 31. Reaction scheme for the synthesis of trimethylprop-2-yn-1-aminium iodide (1)

Trimethylprop-2-yn-1-aminium iodide was made in a manner similar to the method described by Menger and Venkataram.[70] *N,N*-dimethylpropargylamine (0.97 mL, 9 mmol, 1 equiv) was dissolved in methanol (5 mL) and methyl iodide (840 uL, 13.5 mmol, 1.5

equiv) was added. This was refluxed overnight under argon, then cooled and triterated into diethyl ether. This was filtered, rinsed with ether, and product was obtained as off-white crystals in 91% yield.

1H-NMR (D_2O, 500 MHz): δ (ppm) 3.20 (d, J= 2 Hz, 9H), 3.25 (q, J= 3 Hz, 1H), 4.24 (t, J= 3Hz, 2 H).

FTIR (cm^{-1}): 3167(m), 3002(w), 2941(w), 2121 (w), 1471(m), 897 (m), 762(w), 722(m).

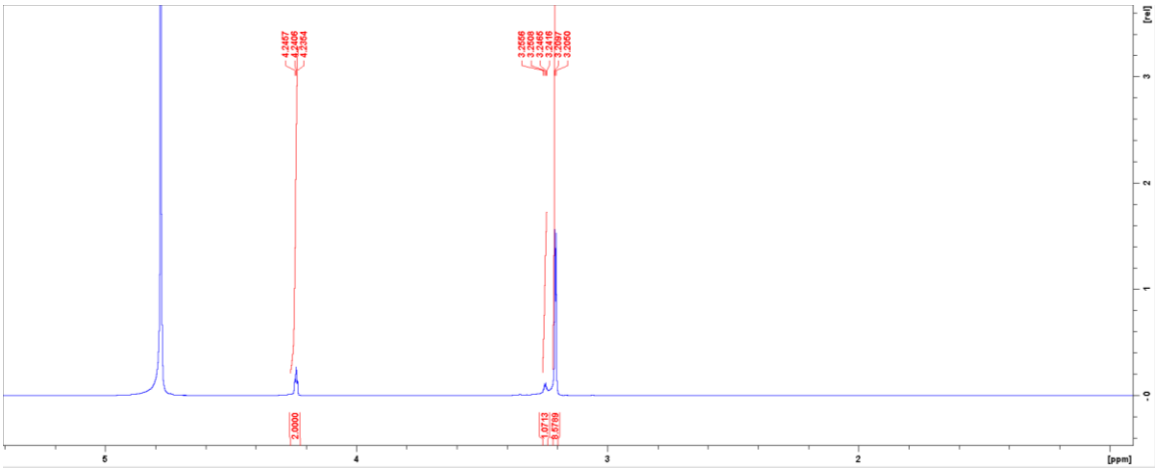

Figure 32. ^{1}H-NMR spectrum for trimethylprop-2-yn-1-aminium iodide (1)

3.3.6.2 Synthesis of perfluoro-N-(prop-2-yn-1-yl)nonanamide (2)

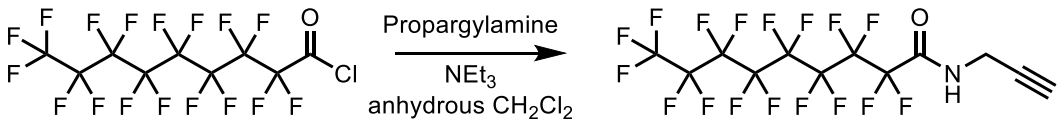

Figure 33. Reaction scheme for the synthesis of perfluoro-N-(prop-2-yn-1-yl)nonanamide (2)

Propargylamine (77 µL, 1.2 mmol, 1.1 equiv.) and triethylamine (225 µL, 1.6 mmol, 1.5 equiv.) were added to dry dichloromethane (5 mL). This was cooled to 0 °C and perfluorononanoyl chloride (100 µL, 1.1 mmol, 1 equiv.) was added dropwise. This was stirred at 0 °C for 30 minutes and at room temperature overnight in a flask sealed with a rubber stopper and vented with a small gauge needle. The solvent was removed via rotary evaporation and columned, eluted with a hexane : ethyl acetate gradient (Rf = 0.77, stains with $KMnO_4$). Product was obtained after rotary evaporation as a white fluffy powder in 49% yield.

1H-NMR ($CDCl_3$, 500 MHz): δ (ppm) 2.35 (t, J= 3Hz, 1H), 4.18 (J= 3Hz, 2H), 6.51 (s, 1H).

FTIR (cm^{-1}): 3334 (m), 3272 (m), 1694(m), 1527 (m), 1195(s), 1138(s).

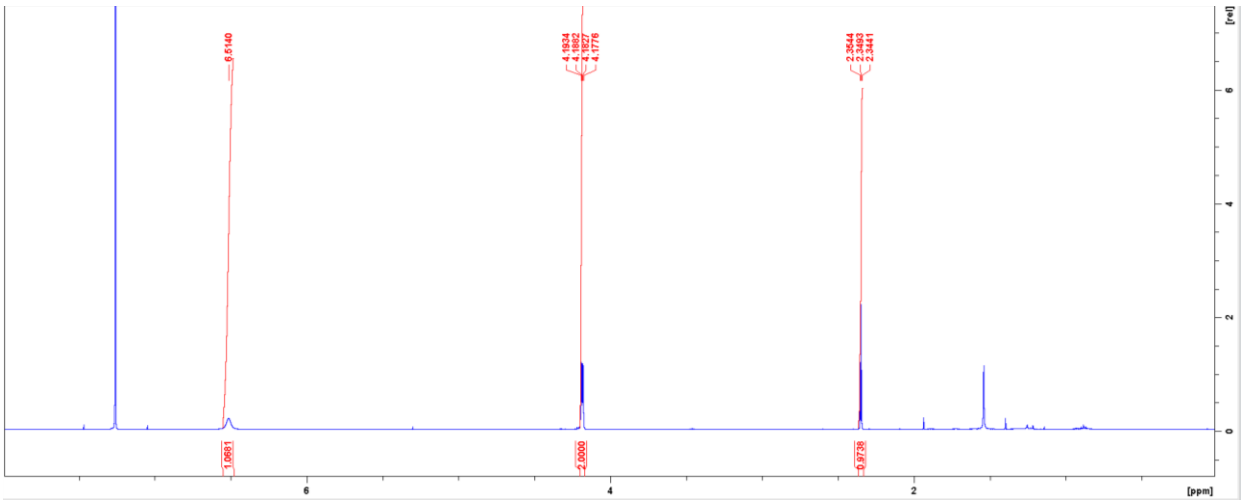

Figure 34. ^{1}H-NMR spectrum for perfluoro-N-(prop-2-yn-1-yl)nonanamide (2)

19F NMR ($CDCl_3$): δ (ppm) -80.7, -119.7 to -119.8, -121.4 to -121.9, -122.4 to -122.7, -126.0 to -126.2 .

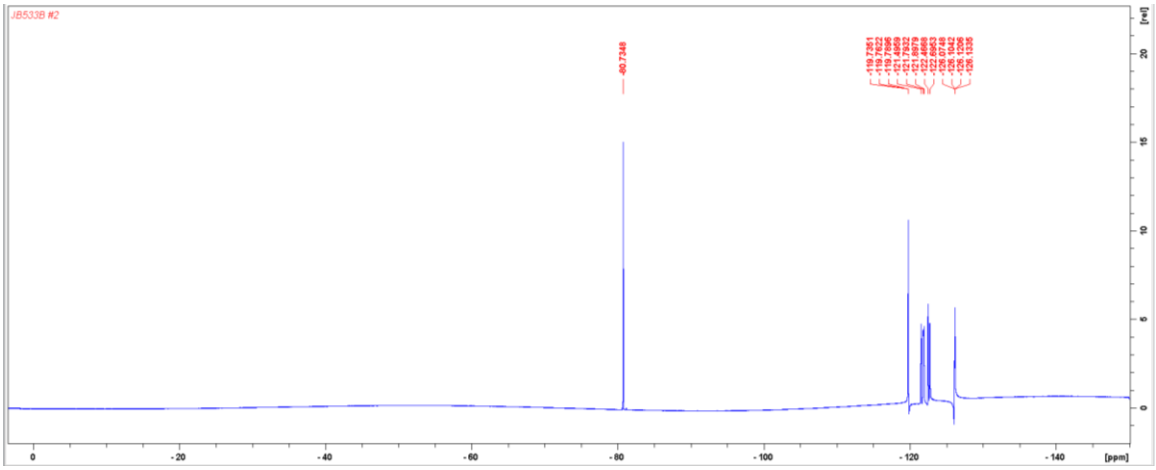

Figure 35. ^{19}F-NMR spectrum for perfluoro-N-(prop-2-yn-1-yl)nonanamide (2).

3.3.6.3 Synthesis of 1-(undec-10-yn-1-yl)pyridin-1-ium (4)

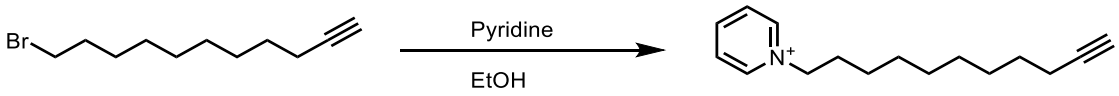

Figure 36. Reaction scheme for the synthesis of 1-(undec-10-yn-1-yl)pyridin-1-ium (4)

1-bromo-10-undecyne (produced by the method of Neef and Schultz,[71] 1 g, 4.3 mmol, 1.4 equiv.) and pyridine (250 µL, 3.1 mmol, 1 equiv.) were combined in ethanol and refluxed overnight under argon. The solvent was removed by rotary evaporation and the residue subjected to a dichloromethane/water extraction. The aqueous layer was retained, subjected to rotary evaporation to remove any lingering organics, and then lyophilized overnight to yield an off-white powder in 51% yield.

^{1}H NMR (D_2O, 500MHz): δ (ppm) 1.2-1.4 (m, 10H), 1.49 (p, J= 7 Hz, 2H), 2.01 (p, J= 7 Hz, 2 H), 2.19 (t of d, J= 2 and 7 Hz, 2H), 2.33 (t, J=2 Hz, 1H), 4.61 (t, J=7 Hz, 2H), 8.06 (t, J=7 Hz, 2H), 8.54 (t, J=7 Hz, 1H), 8.84 (d, J=7 Hz, 2H).

FTIR (cm^{-1}): 3373(m), 3244(w), 3133(w), 3017(w), 2922(m), 2850(m), 1632(m), 1480(m), 1176(m), 777(m), 684(s).

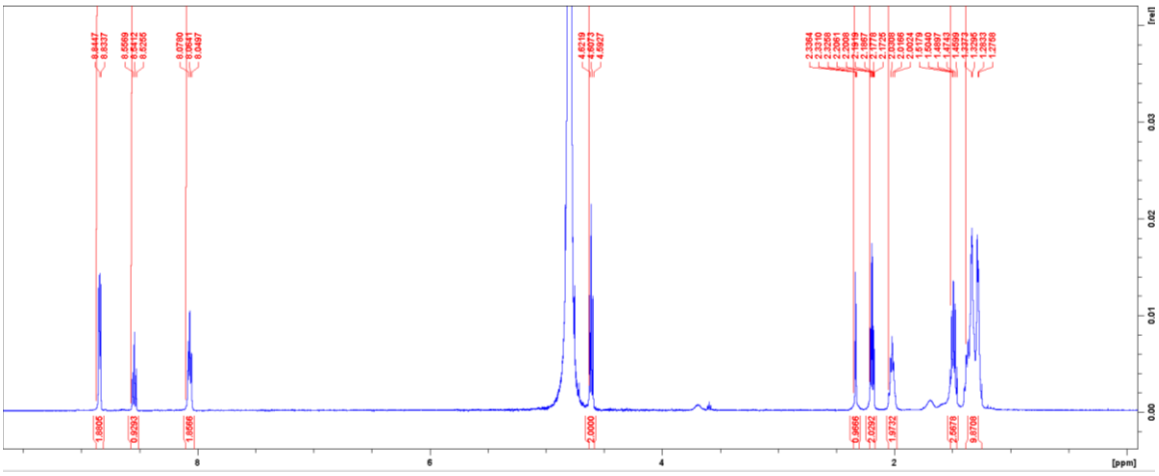

Figure 37. ^{1}H-NMR spectrum for 1-(undec-10-yn-1-yl)pyridin-1-ium (4)

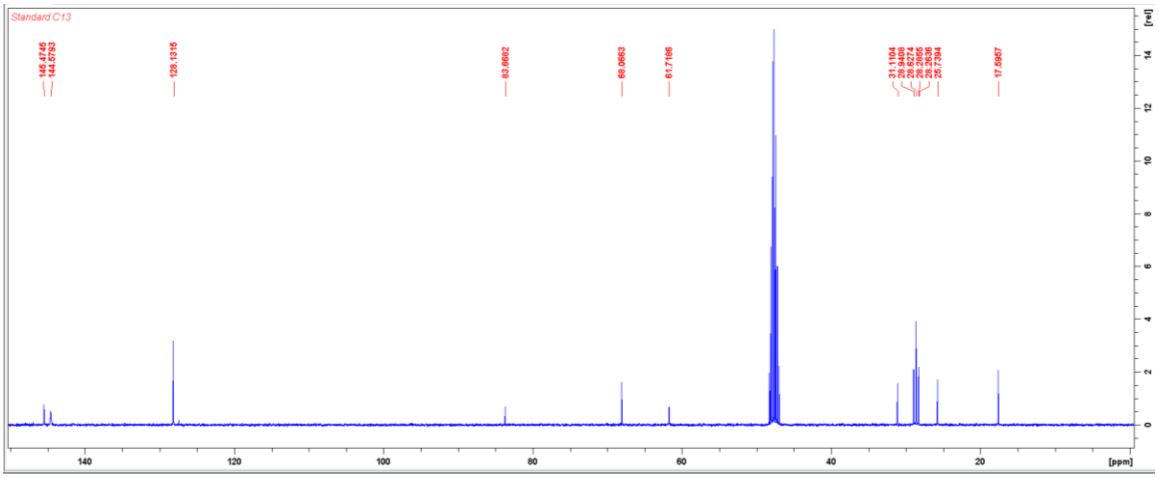

Figure 38. ^{13}C-NMR spectrum for 1-(undec-10-yn-1-yl)pyridin-1-ium (4)

^{13}C-NMR ($CDCl_3$, 500 MHz): δ(ppm) 16.6, 25.7, 28.3, 28.3, 28.6, 28.9, 31.1, 61.7, 68.0, 83.7, 128.1, 144.6, 145.5.

3.4 Results

3.4.1 Azidation of tubing

Several procedures in the literature detail the azidation of PVC, although these methods typically involve organic solvents such as N,N-dimethylformamide with pre-polymerized PVC monomer, PVC powder, or solid inflexible substrates.[61,62,64,67] When applied to flexible tubing, such conditions make the resulting materials inflexible for a variety of aqueous-organic solvent mixtures. Solvent tolerances for endotracheal tubing are displayed in Table 6.

Table 6 – Solvent tolerances for endotracheal tubing. This table reports the approximate largest amount of organic co-solvent (v/v) in water in which tubing can be immersed overnight, at room temperature before becoming inflexible as judged by simple handling.

Solvent	Limiting aqueous mixture	Notes
DMSO	up to 50%	DMSO remains in plastic sample after rinsing with sonication, as determined by XPS.
DMF	up to 12.5%	
methanol	up to 6.25%	
ethanol	up to 6.25%	

We focused instead on azidation in aqueous solutions with the use of a phase transfer catalyst. While tetrabutylammonium bromide has been employed previously for this

purpose,[66,69] we tested several others for their relative activities in facilitating azidation (Figure 39). Small pieces of clear, cut endotracheal tubing (approximately 0.5 x 0.5 cm) were placed in 4 mL of an aqueous solution of 450 mM NaN_3 and 9 mM phase transfer catalyst in sealed vials. Each mixture was heated to 80 °C for 48 hours while shaking vigorously on an orbital shaker. The samples were then rinsed in water in an ultrasonic bath for 1 hour, changing the water at 30 minutes, and then dried overnight at 60 °C.

The results were evaluated by infrared spectroscopy (IR), monitoring the increase in characteristic asymmetric azide stretch at ~2100 cm^{-1} and decrease in C-Cl band at ~610 cm^{-1}).[72] Some samples were also examined by XPS, monitoring the creation of the 2:1 intensity pattern characteristic of azide at 400 and 404 eV, and the overall increase in %N at the expense of a decrease in %Cl. In general, bulkier phase transfer agents with more prominent hydrophobic features were superior to smaller cations, as summarized in Figure 39.

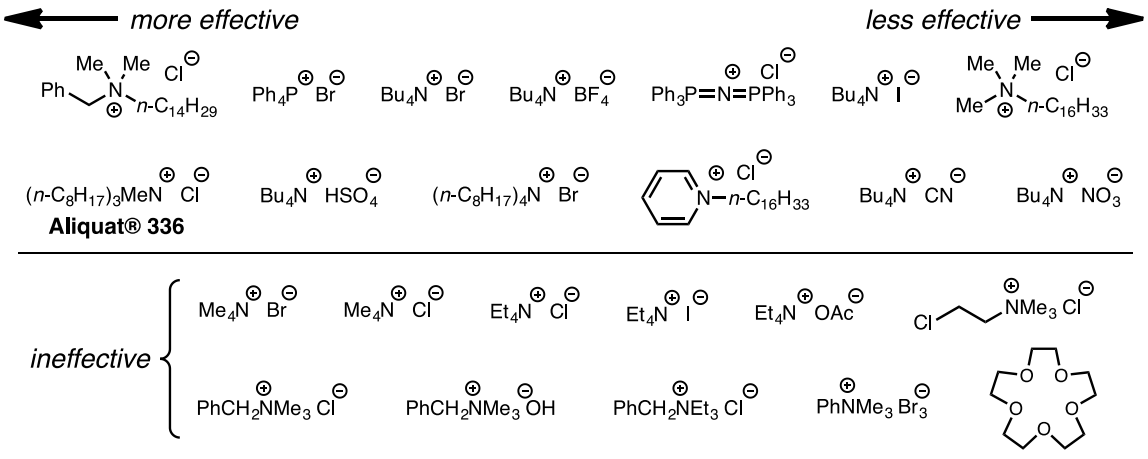

Figure 39. Relative activity of phase transfer catalysts in the azidation of PVC tubing (450 mM NaN_3, 9 mM PTC, 80 °C, 48 h).

Table 7. IR and XPS analysis for ET azidated (48h) with various phase transfer catalysts. Intensity of azide IR signal was normalized to the intensity of the resultant azide peak from azidation with Aliquat 336.

	%C	%O	%Cl	%Si	%Ca	%N	%Na	%P	%F	Intensity of azide IR signal [a]
Unmodified ET tubing	69.77	12.37	13.12	3.46	1.28	ND	ND	ND	ND	0%
Tetrabutylammonium bromide	75.38	13.06	4.40	3.22	1.72	2.24	ND	ND	ND	56%
Aliquat 336	75.51	13.02	1.53	4.16	1.48	4.29	ND	ND	ND	100%
Cetylpyridinium chloride	83.52	7.61	2.92	2.32	1.05	2.57	ND	ND	ND	52%
Tetraphenylphosphonium bromide	72.73	14.24	3.06	3.71	1.53	4.25	0.48	ND	ND	85%
Benzyldimethyltetradecylammonium chloride	74.47	10.99	2.93	4.12	0.82	6.3	0.37	ND	ND	108%
Tetrabutylammonium iodide	73.29	15.48	3.58	4.75	1.13	1.78	ND	ND	ND	38%
Hexadecyltrimethylammonium chloride	85.84	3.97	4.65	1.44	ND	4.1	ND	ND	ND	33%
Tetrabutylammonium nitrate	75.44	13.74	3.36	3.68	1.27	2.05	0.46	ND	ND	36%
Bis(triphenyl)phosphoranylidene-ammonium chloride	80.49	10.82	1.15	3.62	1.50	2.42	ND	ND	ND	49%
Tetrabutylammonium cyanide	75.44	12.45	5.76	3.63	ND	2.09	0.21	0.42	ND	40%
Tetrabutylammonium bisulfate	73.86	13.30	5.65	3.68	1.10	2.42	ND	ND	ND	61%
Tetrabutylammonium tetrafluoroborate	73.95	11.99	4.77	3.68	1.29	3.54	ND	ND	0.78	54%
Tetraoctylammonium bromide	78.89	10.14	3.60	3.30	ND	4.07	ND	ND	ND	56%

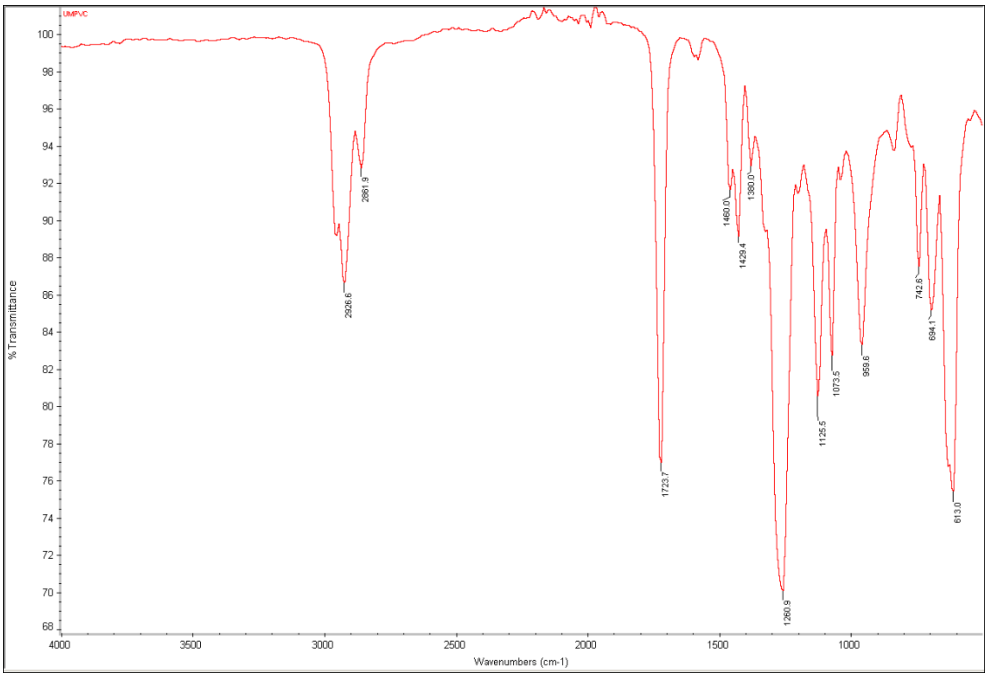

Figure 40. IR spectrum for unmodified ET.

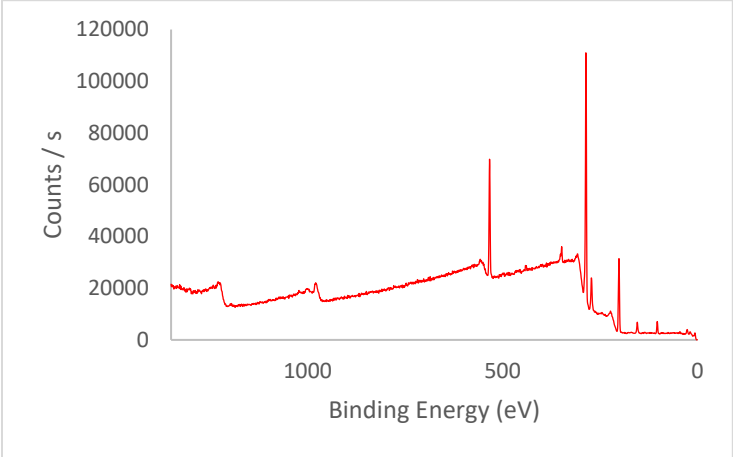

Figure 41. XPS survey spectrum for unmodified ET.

Table 8. XPS survey integration for unmodified ET.

Peak	Atomic %
C1s	69.77
O1s	12.37
Cl2p	13.12
N1s	0
Si2p	3.46
Ca2p	1.28

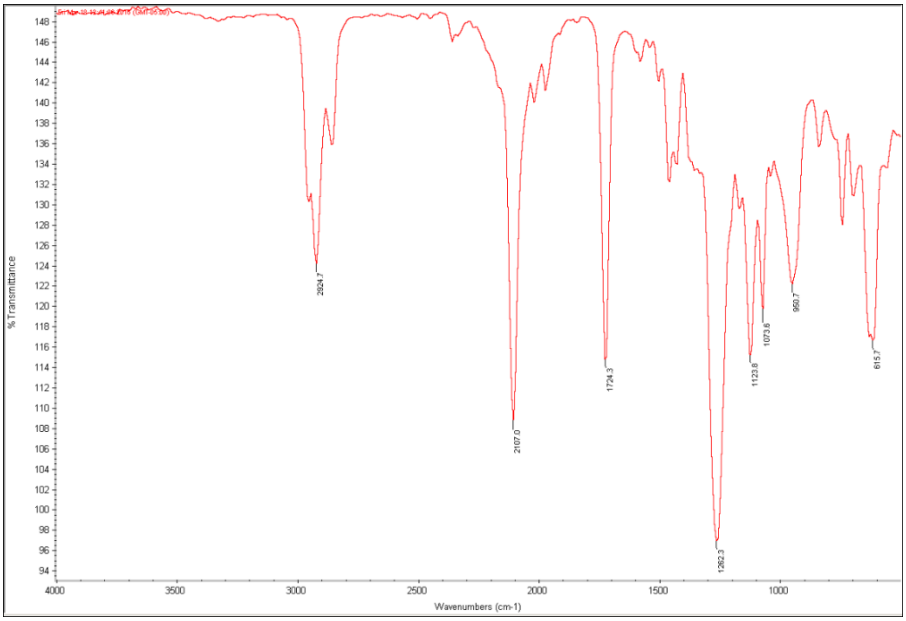

Figure 42. IR spectrum for ET azidated with tetrabutylammonium bromide.

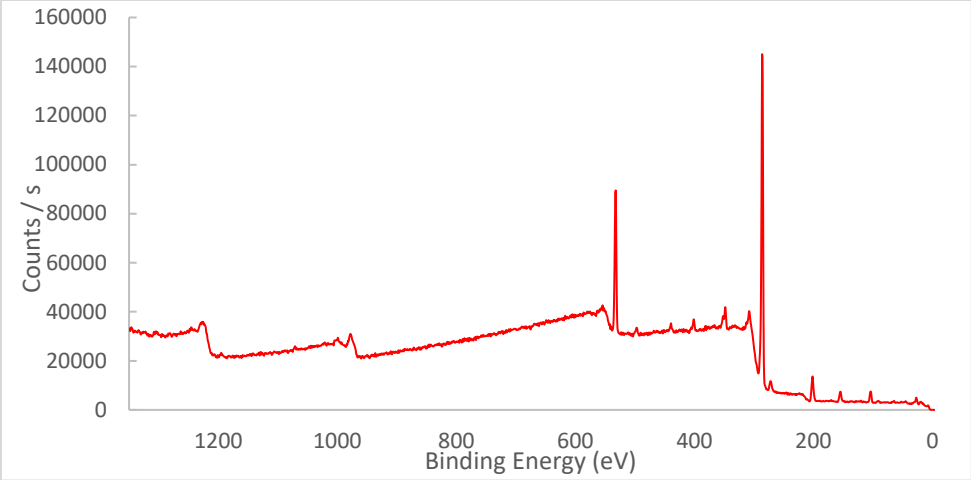

Figure 43. XPS survey spectrum for ET azidated with tetrabutylammonium bromide.

Table 9. XPS survey integration for ET azidated with tetrabutylammonium bromide.

Peak	Atomic %
C1s	75.38
O1s	13.06
Cl2p	4.40
N1s	2.24
Si2p	3.22
Ca2p	1.72

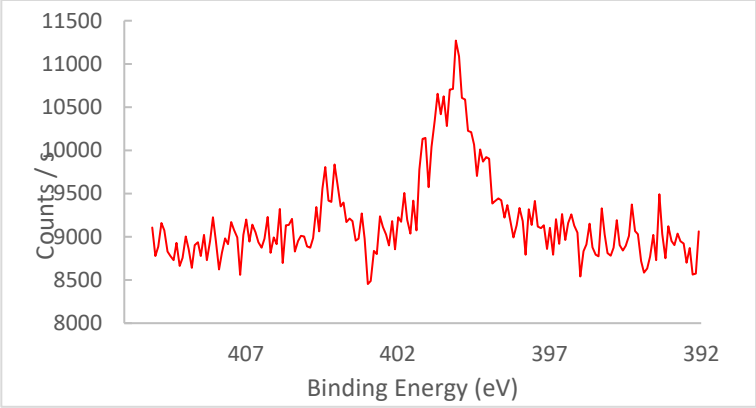

Figure 44. XPS nitrogen spectrum for ET azidated with tetrabutylammonium bromide.

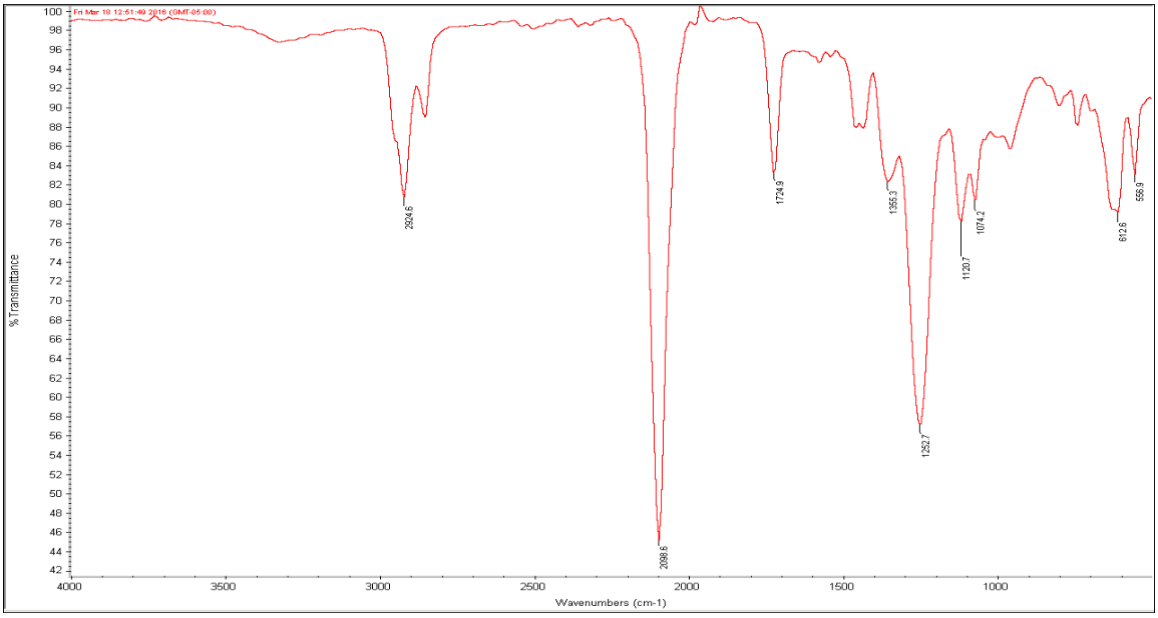

Figure 45. IR spectrum for ET azidated with Aliquat 336.

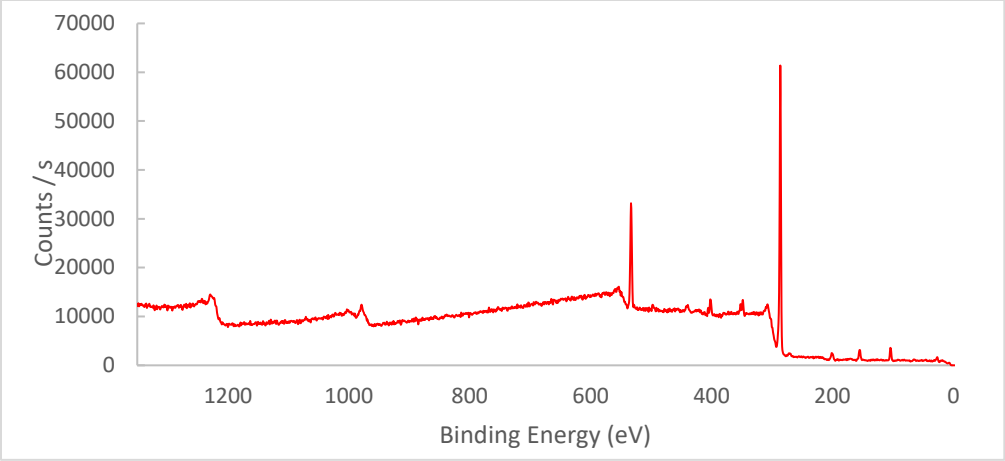

Figure 46. XPS survey spectrum for ET azidated with Aliquat 336.

Table 10. XPS survey integration for ET azidated with Aliquat 336.

Peak	Atomic %
C1s	75.51
O1s	13.02
Cl2p	1.53
N1s	4.29
Si2p	4.16
Ca2p	1.48

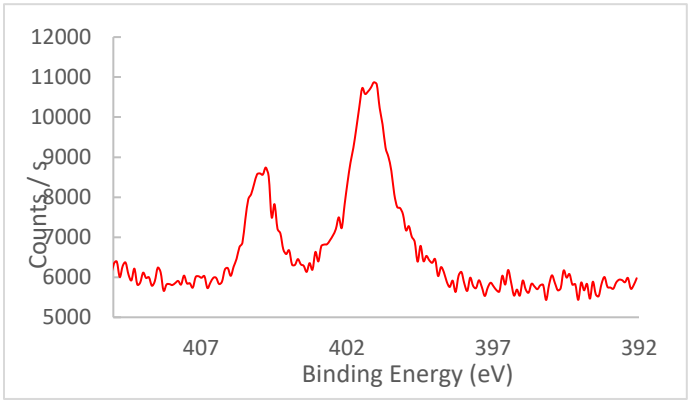

Figure 47. XPS nitrogen spectrum for ET azidated with Aliquat 336.

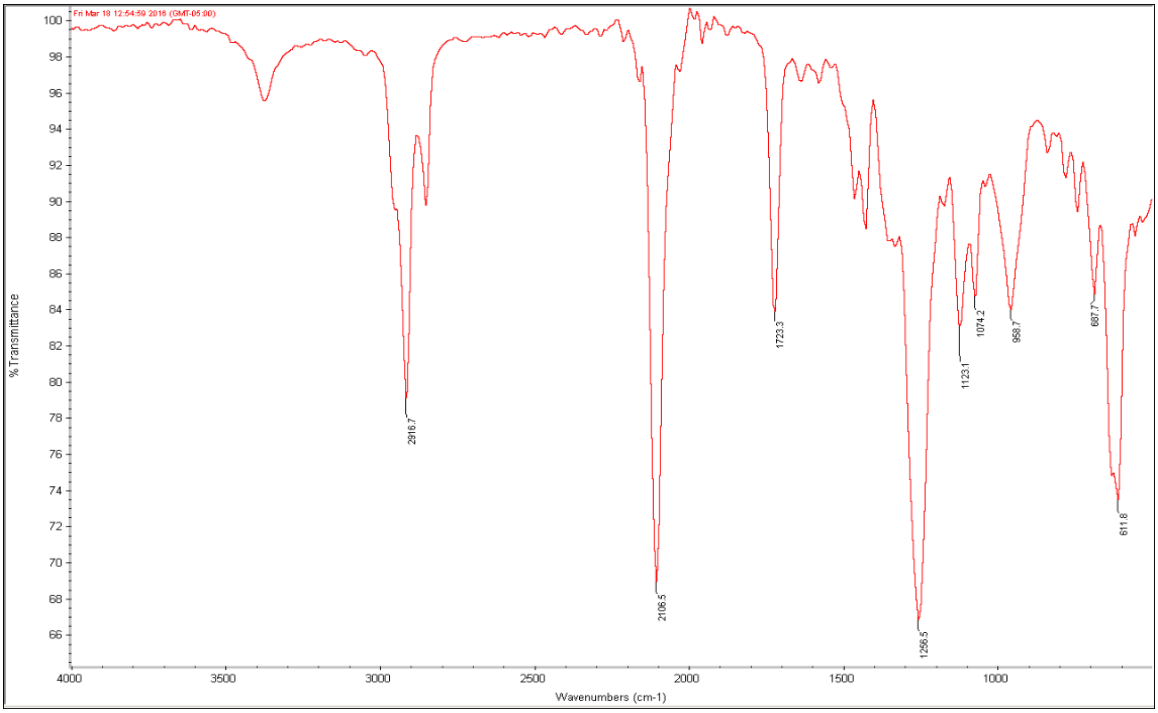

Figure 48. IR spectrum for ET azidated with cetylpyridinium chloride.

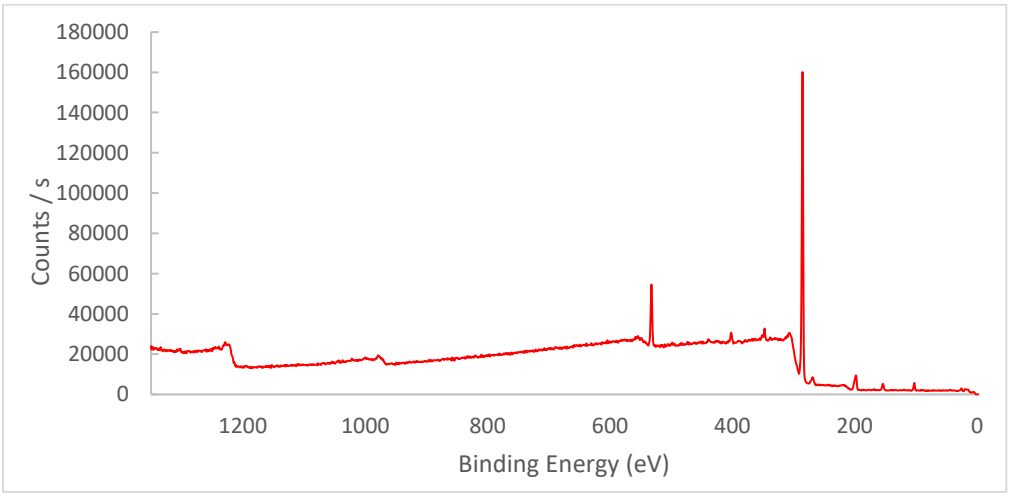

Figure 49. XPS survey spectrum for ET azidated with cetylpyridinium chloride.

Table 11. XPS survey integration for ET azidated with cetylpyridinium chloride.

Peak	Atomic %
C1s	83.52
O1s	7.61
Cl2p	2.92
N1s	2.57
Si2p	2.32
Ca2p	1.05

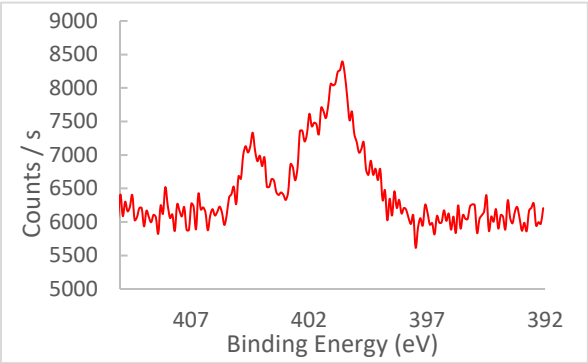

Figure 50. Nitrogen XPS spectrum for ET azidated with cetylpyridinium chloride.

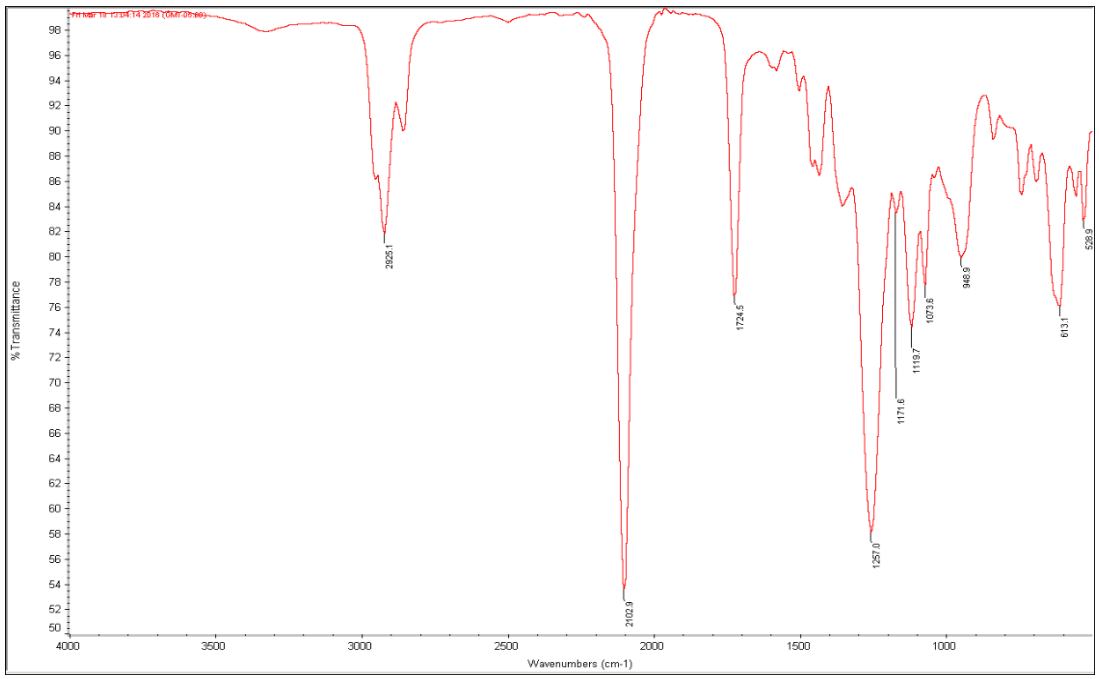

Figure 51. IR spectrum for ET azidated with tetraphenylphosphonium bromide.

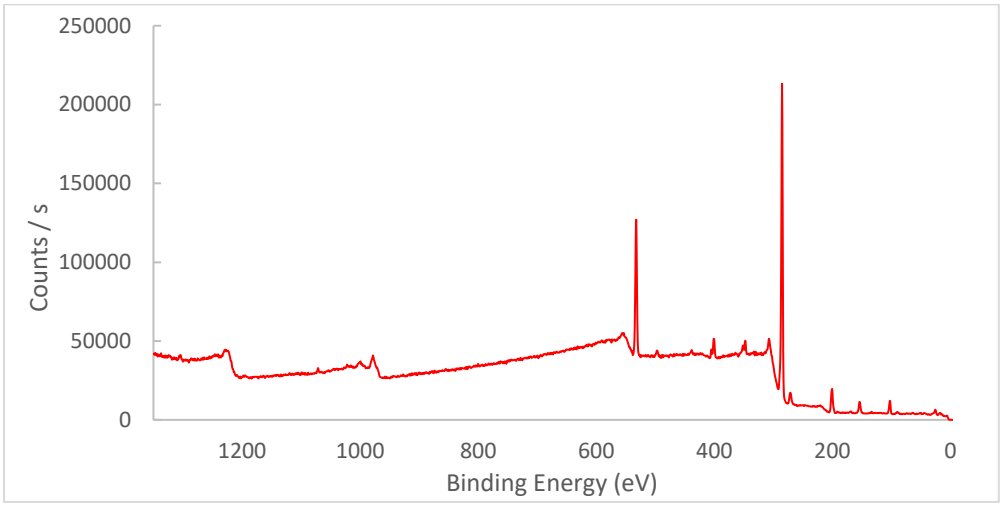

Figure 52. XPS survey spectrum for ET azidated with tetraphenylphosphonium bromide.

Table 12. XPS survey integration for ET azidated with tetraphenylphosphonium bromide.

Peak	Atomic %
C1s	72.73
O1s	14.24
Cl2p	3.06
N1s	4.25
Si2p	3.71
Ca2p	1.53
Na1s	0.48

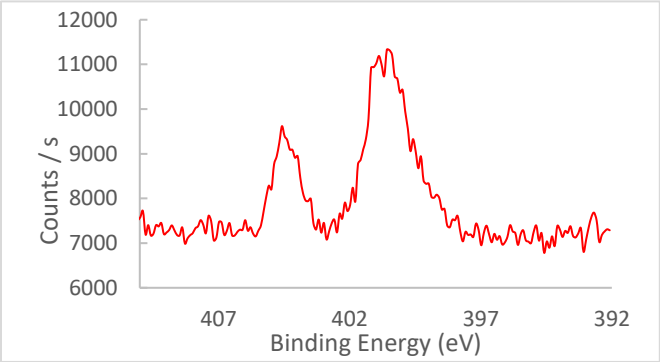

Figure 53. XPS nitrogen spectrum for ET azidated with tetraphenylphosphonium bromide.

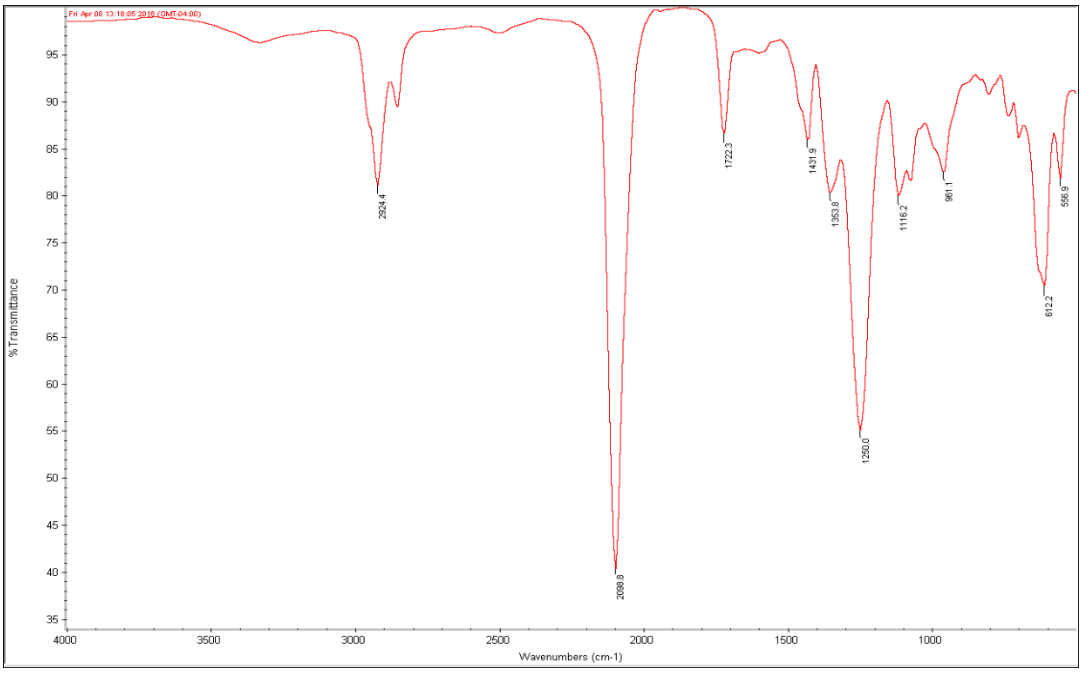

Figure 54. IR spectrum for ET azidated with benzyldimethyltetradecylammonium chloride.

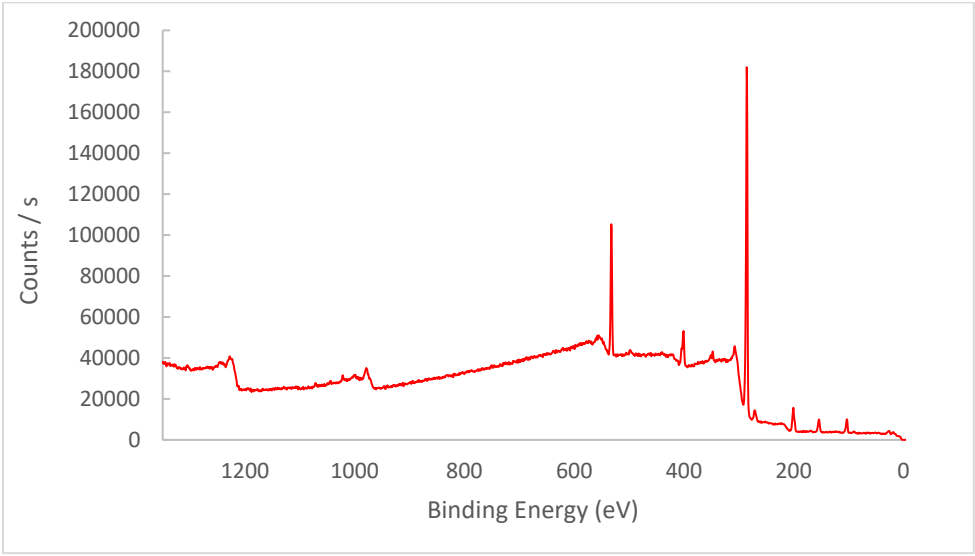

Figure 55. XPS survey spectrum for ET azidated with benzyldimethyltetradecylammonium chloride.

Table 13. XPS survey integration for ET azidated with benzyldimethyltetradecylammonium chloride.

Peak	Atomic %
C1s	74.47
O1s	10.99
Cl2p	2.93
N1s	6.30
Si2p	4.12
Ca2p	0.82
Na1s	0.37

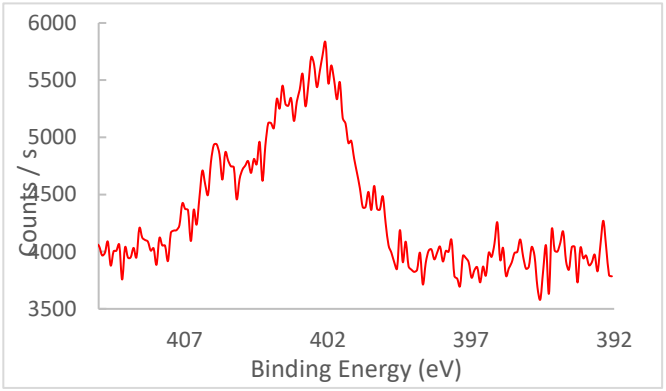

Figure 56. XPS nitrogen survey for ET azidated with benzyldimethyltetradecylammonium chloride.

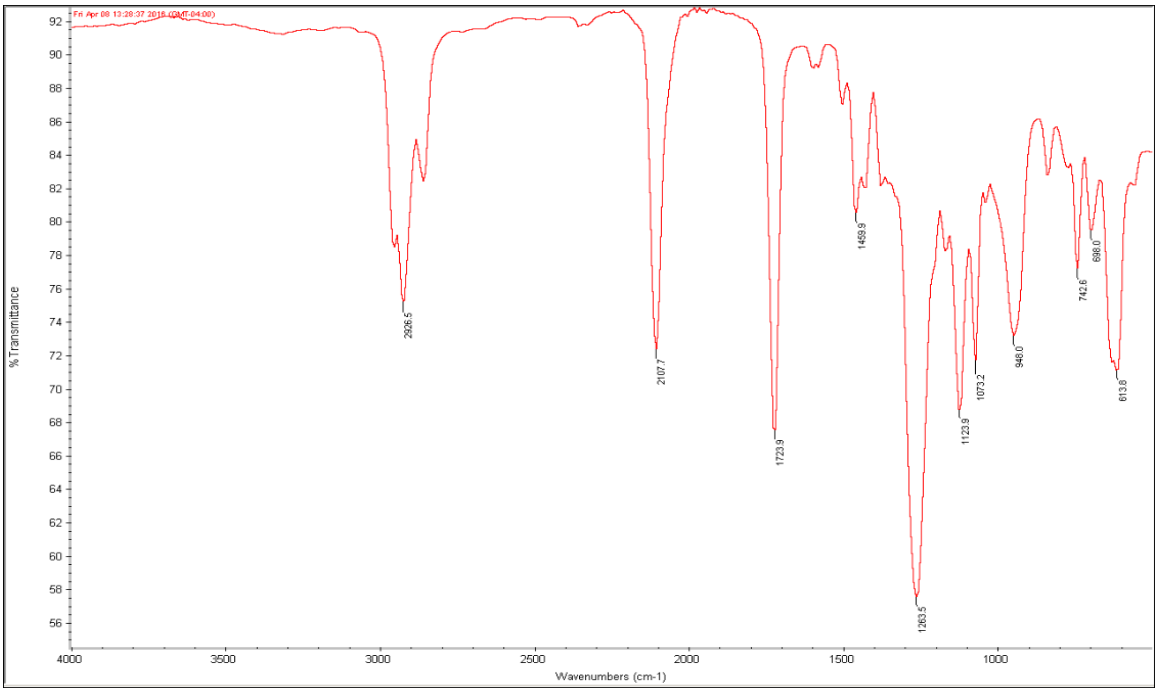

Figure 57. IR spectrum for ET azidated with tetrabutylammonium iodide.

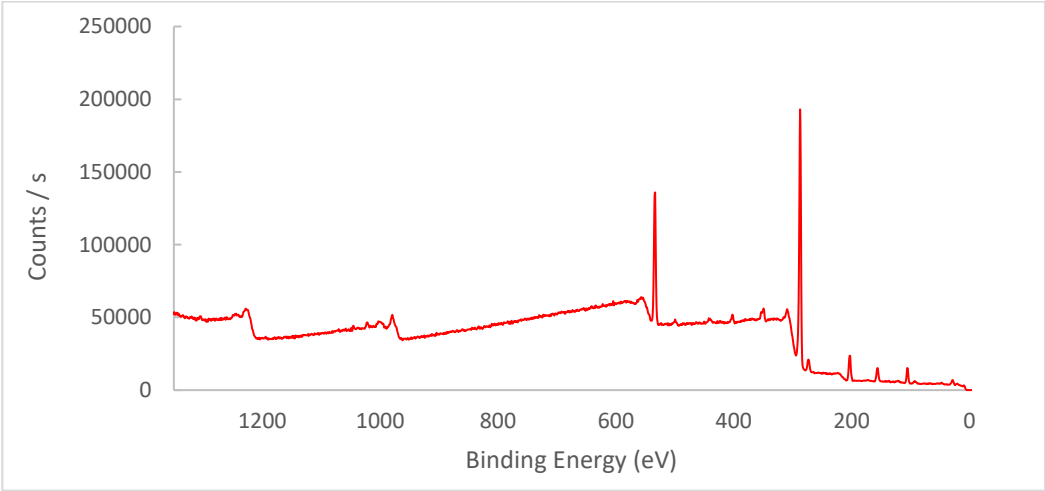

Figure 58. XPS survey spectrum for ET azidated with tetrabutylammonium iodide.

Table 14. XPS survey integration for ET azidated with tetrabutylammonium iodide.

Peak	Atomic %
C1s	73.29
O1s	15.48
Cl2p	3.58
N1s	1.78
Si2p	4.75
Ca2p	1.13

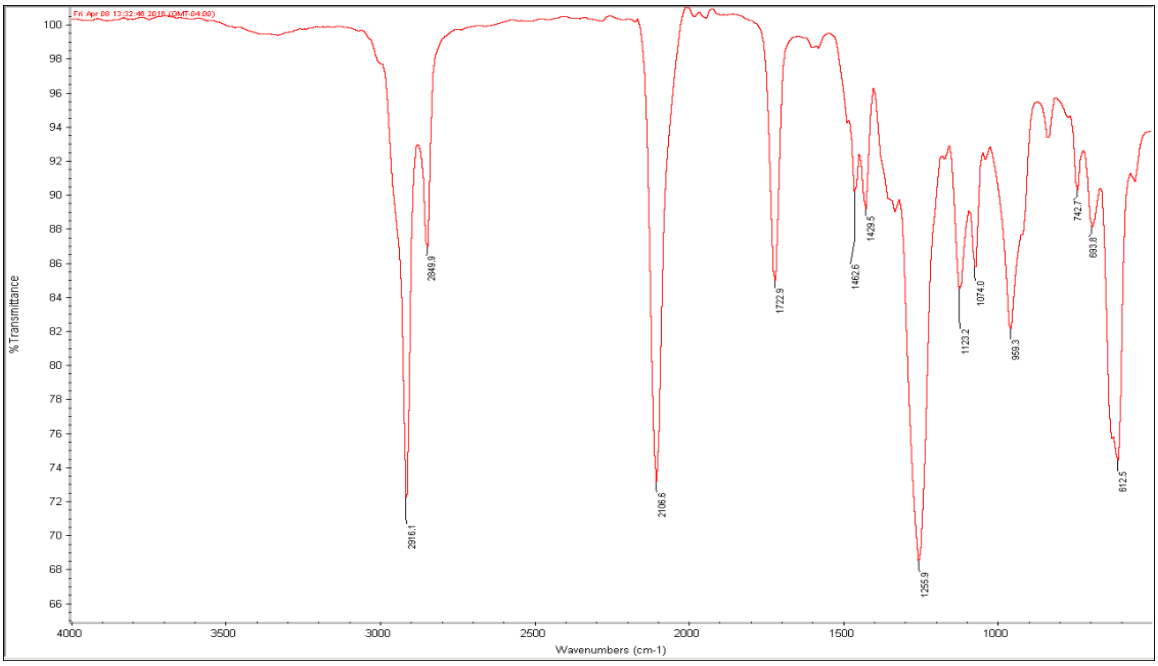

Figure 59. IR spectrum of ET azidated with hexadecyltrimethylammonium chloride.

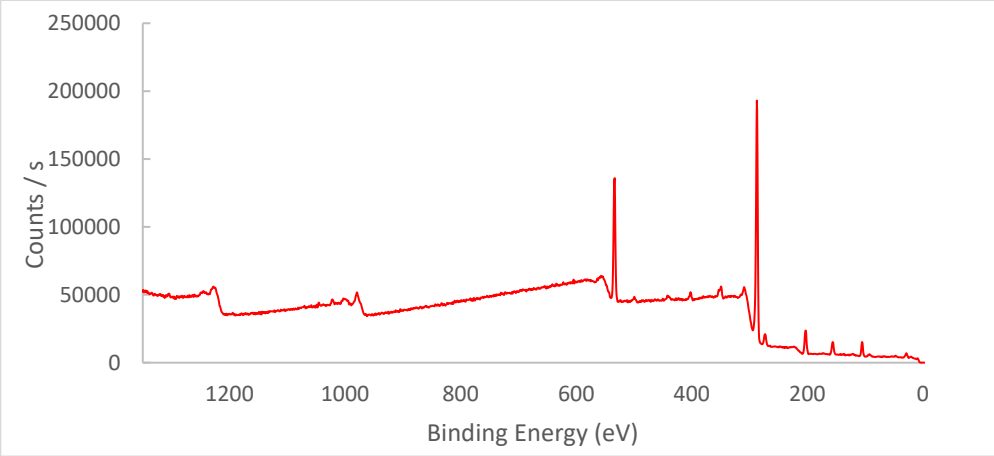

Figure 60. XPS survey spectrum for ET azidated with hexadecyltrimethylammonium chloride.

Table 15. XPS survey integration for ET azidated with hexadecyltrimethylammonium chloride.

Peak	Atomic %
C1s	85.84
O1s	3.97
Cl2p	4.65
N1s	4.10
Si2p	1.44

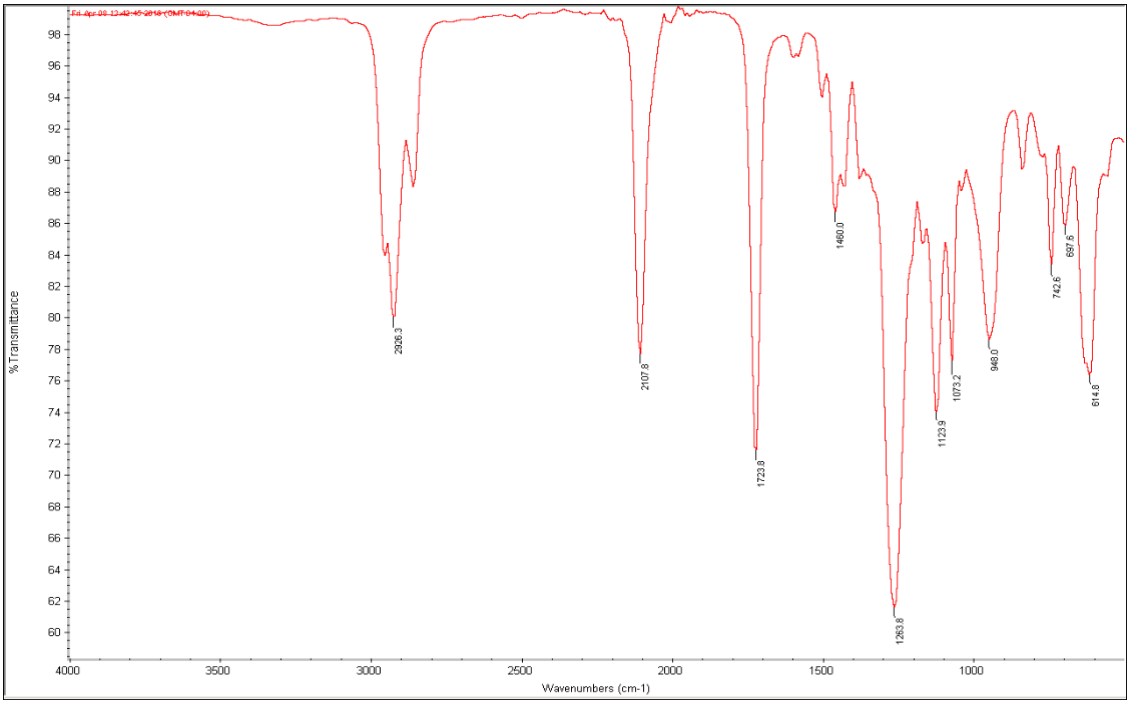

Figure 61. IR spectrum for ET azidated with tetrabutylammonium nitrate.

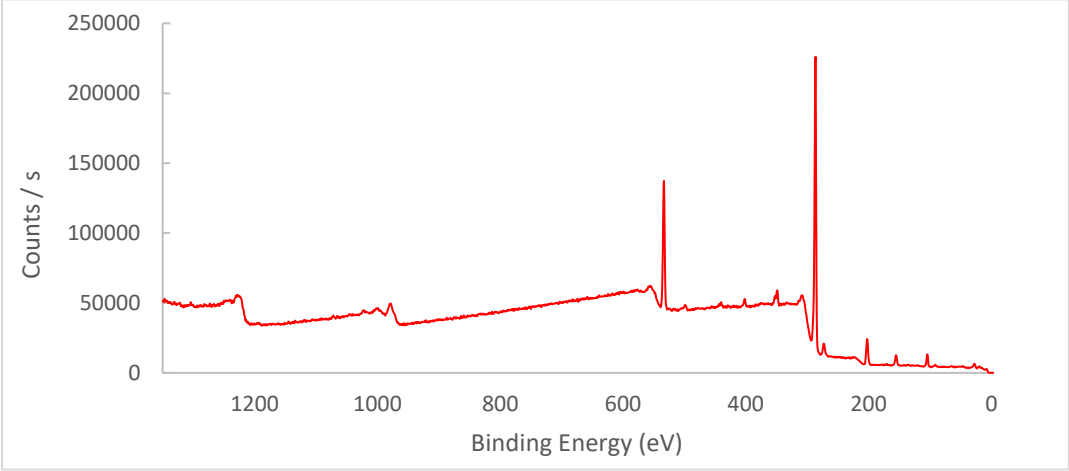

Figure 62. XPS survey spectrum for ET azidated with tetrabutylammonium nitrate.

Table 16. XPS survey integration for ET azidated with tetrabutylammonium nitrate.

Peak	Atomic %
C1s	75.44
O1s	13.74
Cl2p	3.36
N1s	2.05
Si2p	3.68
Ca2p	1.27
Na1s	0.46

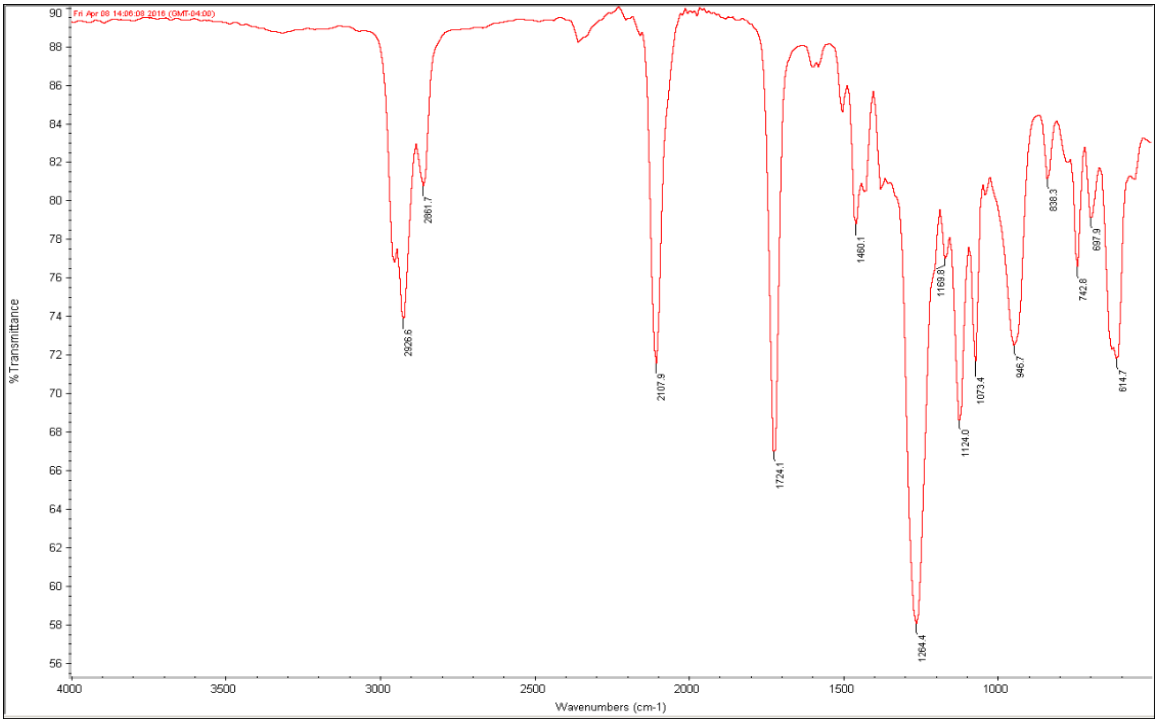

Figure 63. IR spectrum for ET azidated with tetrabutylammonium cyanide.

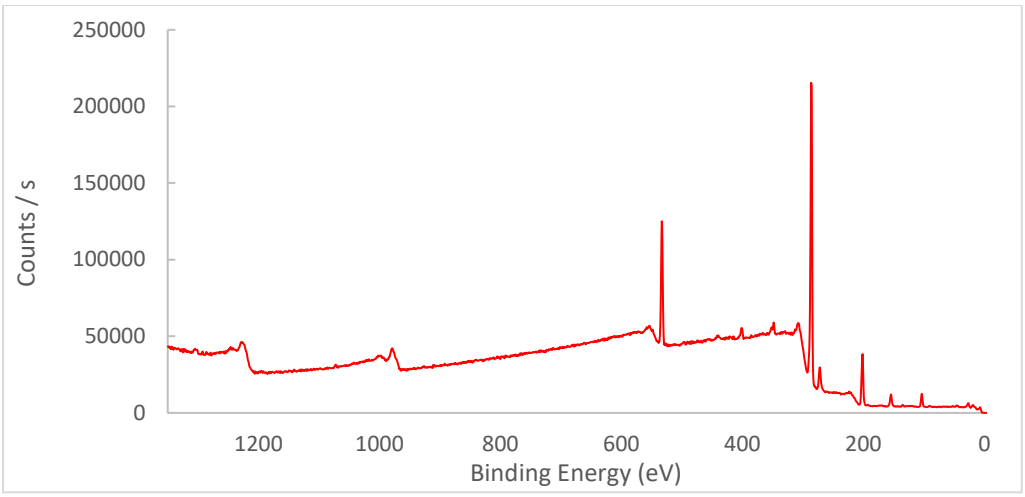

Figure 64. XPS survey spectrum for ET azidated with tetrabutylammonium cyanide.

Table 17. XPS survey integration for ET azidated with tetrabutylammonium cyanide.

Peak	Atomic %
C1s	75.44
O1s	12.45
Cl2p	5.76
N1s	2.09
Si2p	3.63
P2p	0.42
Na1s	0.21

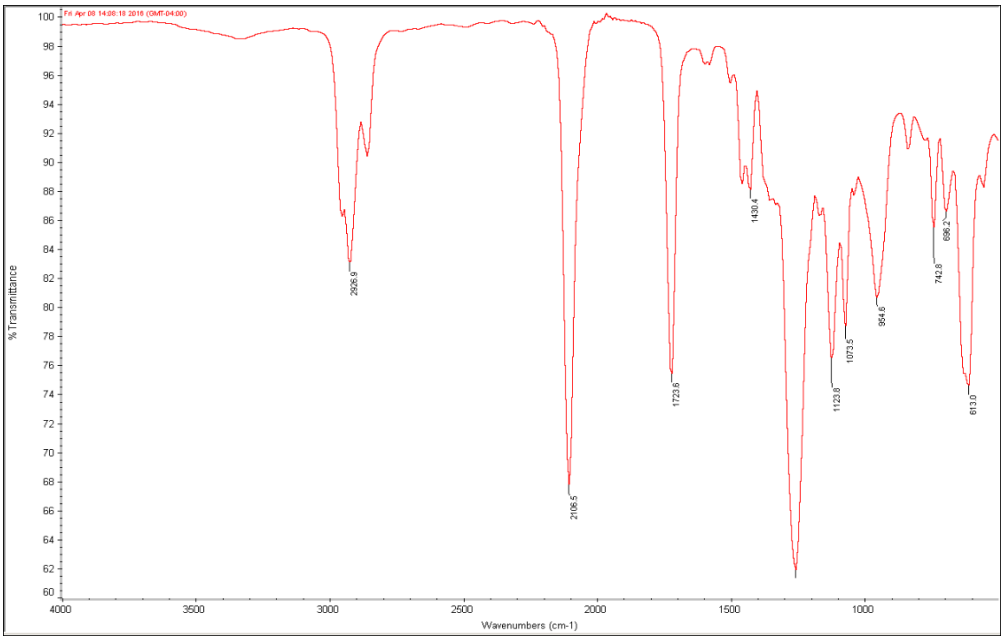

Figure 65. IR spectrum for ET azidated with tetrabutylammonium bisulfate.

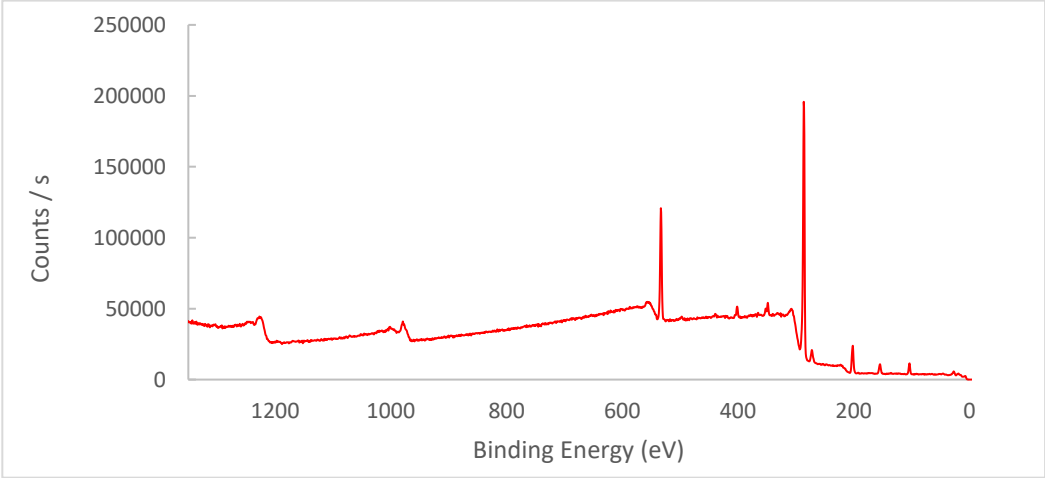

Figure 66. XPS survey spectrum for ET azidated with tetrabutylammonium bisulfate.

Table 18. XPS survey integration for ET azidated with tetrabutylammonium bisulfate.

Peak	Atomic %
C1s	73.86
O1s	13.30
Cl2p	5.65
N1s	2.42
Si2p	3.68
Ca2p	1.10

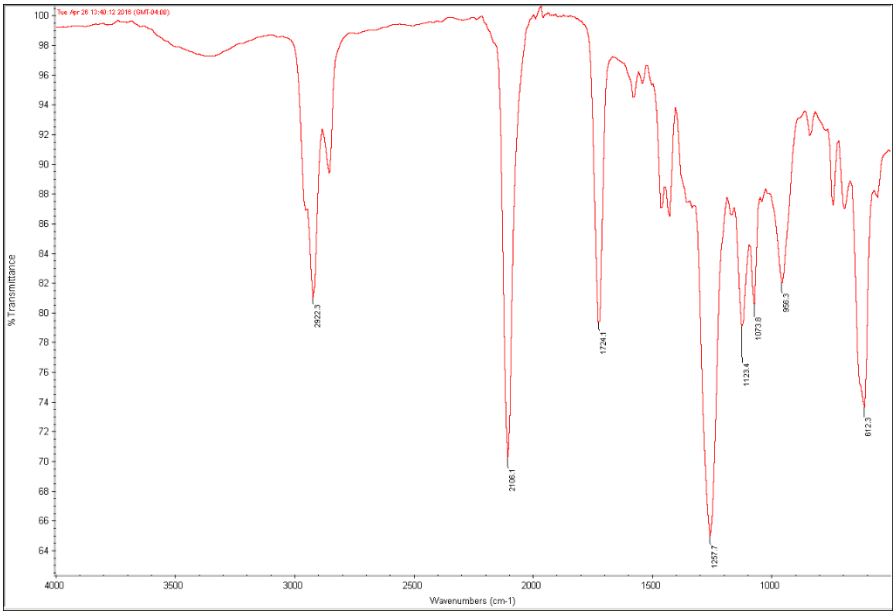

Figure 67. IR spectrum for ET azidated with tetrabutylammonium tetrafluoroborate.

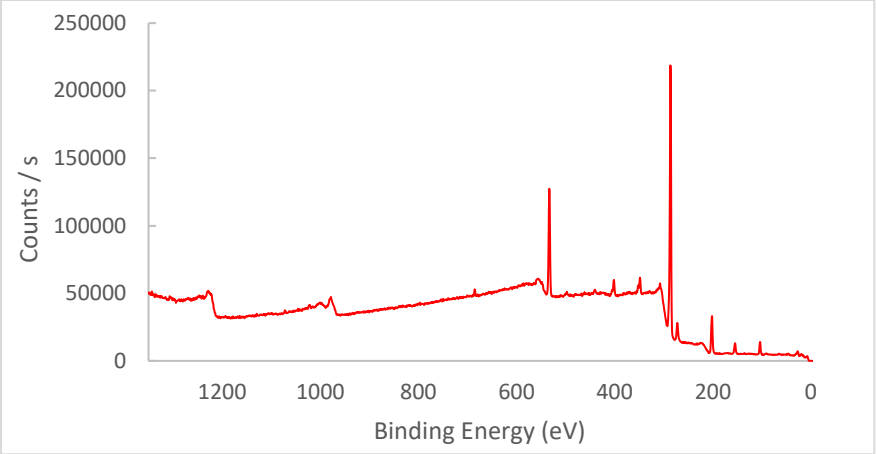

Figure 68. XPS survey spectrum for ET azidated with tetrabutylammonium tetrafluoroborate.

Table 19. XPS survey integration for ET azidated with tetrabutylammonium tetrafluoroborate.

Peak	Atomic %
C1s	73.95
O1s	11.99
Cl2p	4.77
N1s	3.54
Si2p	3.68
Ca2p	1.29
F1s	0.78

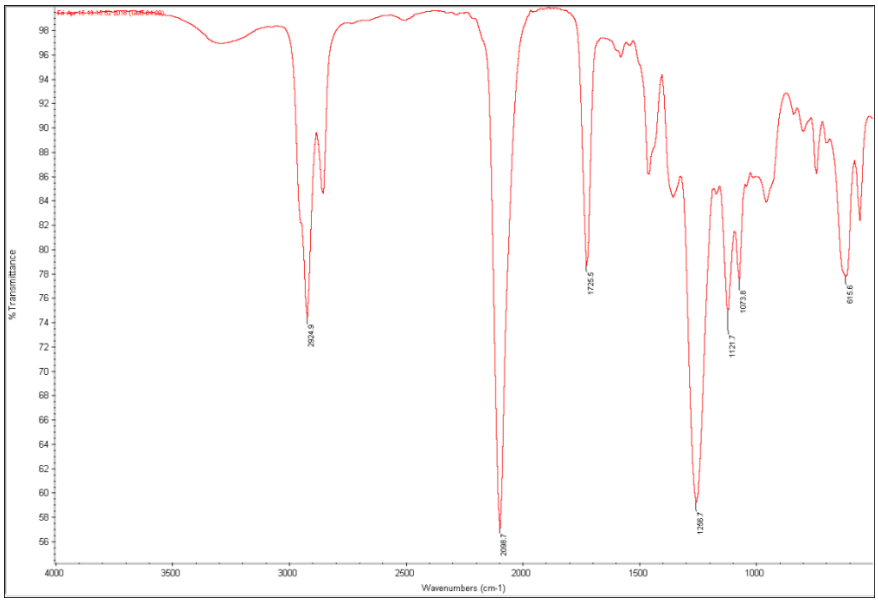

Figure 69. IR spectrum for ET azidated with tetraoctylammonium bromide.

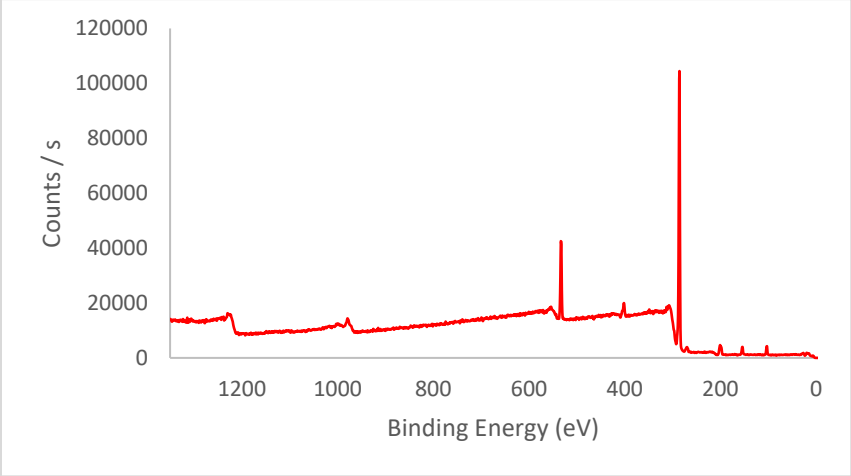

Figure 70. XPS survey spectrum for ET azidated with tetraoctylammonium bromide.

Peak	Atomic %
C1s	78.89
O1s	10.14
Cl2p	3.60
N1s	4.07
Si2p	3.30

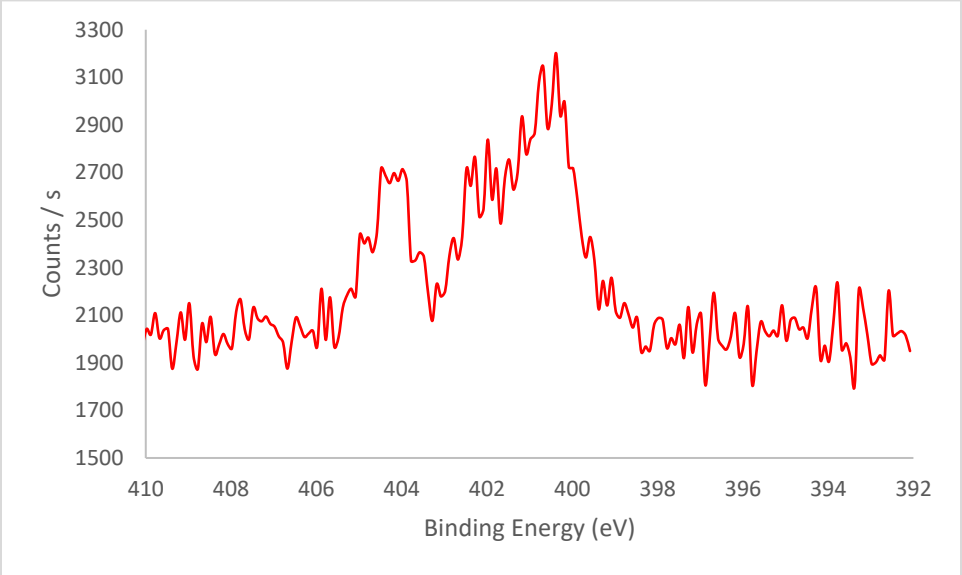

Figure 71. XPS nitrogen scan for ET azidated with tetraoctylammonium bromide.

In this initial evaluation, the degree of functionalization was balanced against the flexibility of the resulting material, with rigidity presumably reflecting the leaching of plasticizer from the material. The extent of reaction for some phase transfer catalysts provided inconsistent reactivity from run to run. Reactions with Aliquat® 336 provided flexible tubing with a reproducible and consistently high degree of azidation as determined by both IR and XPS, so this was selected as the phase transfer agent for subsequent

experiments. XPS analysis of the modified tubing showed only the distinct azide double peak as the predominant nitrogen species.

Greater degrees of azidation were associated with significant discoloration of the tubing, likely the result of competing base-mediated elimination. This pathway was previously noted by Yoshioka and coworkers,[73] but thermal dehydrochlorination, well known for PVC,[74,75] may also play a role. The color of samples of endotracheal and catheter tubing undergoing azidation by these methods are shown in Figure 72 as a function of reaction time and temperature. Less azidation time naturally gave less discoloration, but it could not be completely eliminated. Samples azidated at a lower temperature (60 °C) were slower to discolor, but unfortunately were also slower to undergo the desired reaction. In this case, by the time full azidation was achieved (24 h, judged by IR), the samples were more discolored than for complete azidation at 80 °C, achieved in 12 h. Reactions at 100 °C caused severe discoloration in under 3 hours with less than optimal azidation.

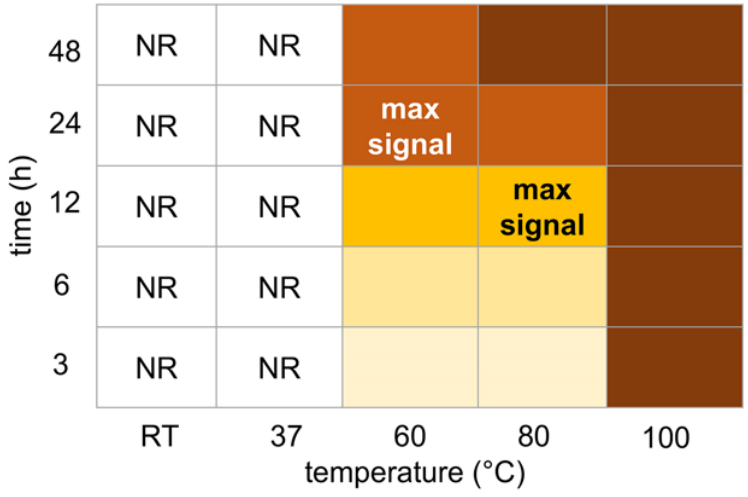

Figure 72. Results of azidation reactions of varying duration and temperature on endotracheal tubing using aqueous solutions of 480 mM sodium azide and 11 mM Aliquat® 336. The color of each box approximates the color of the resulting tubing.

NR = no observed reaction as indicated by IR; max signal = maximum intensity of the organic azide IR stretching band at 2107 nm.

Attempts made at azidation in organic solvent (DMF, THF, methanol, ethanol) resulted in rapid hardening of the plastic. The use of DMSO resulted in absorbtion of that solvent into the tubing which could not be rinsed out by extensive sonication in water as determined by XPS. Variation of pH over a limited range (6-9) for a representative azidation reaction assisted by *n*-Bu_4NBF_4 showed maximum azidation at pH 6.5. Side reactions giving rise to loss of chlorine (elimination or substitution by hydroxide, assessed by XPS) were minimized at acidic pH, as expected. [***Caution!!*** Azidation reactions should never be conducted or worked up under strongly acidic conditions, to avoid the generation of the highly toxic and explosive gas, HN_3.]

3.4.1.1 Correlation of IR and XPS Data

Below, in Table 20, are a table of infrared and x-ray photoelectron spectroscopy signals relating to azide nitrogen for the same samples, and a plot of these data, showing a moderate degree of correlation, as detailed in Figure 73.

Table 20. IR azide peak intensity and percent nitrogen from XPS from phase transfer catalysts for azidation.

Phase transfer catalyst	IR intensity ratio (azide: sp^3 C-H)	% N from XPS
Bu_4NBr (tetrabutylammonium bromide)	1.66 : 1	2.24
Aliquat 336	3.01 : 1	4.29
Pyridine-N-(n-$C_{16}H_{33}$)Cl (cetylpyridinium chloride)	1.61 : 1	2.57
PhP_4Br (tetraphenylphosphonium bromide)	2.69 : 1	4.25
(Bn)$(Me)_2$(n-$C_{14}H_{29}$)NCl (benzyldimethyltetradecylammonium chloride)	3.47 : 1	6.3
(n-Bu)$_4$NI (tetrabutylammonium iodide)	1.25: 1	1.78
(n-octyl)$_4$NBr (tetraoctylammonium bromide)	1.76 : 1	4.07
(n-$C_{16}H_{33}$)Me_3NCl (hexadecultrimethylammonium chloride	1.01 : 1	4.10
(n-Bu)$_4NNO_3$ (tetrabutylammonium nitrate)	1.11 : 1	2.05
(n-Bu)$_4$NCN (tetrabutylammonium cyanide)	1.23 : 1	2.09
(n-Bu)$_4NSO_4H$ (tetrabutylammonium bisulfate)	1.97 : 1	2.42
(n-Bu)$_4NBF_4$ (tetrabutylammonium tetrafluoroborate)	1.67 : 1	3.54

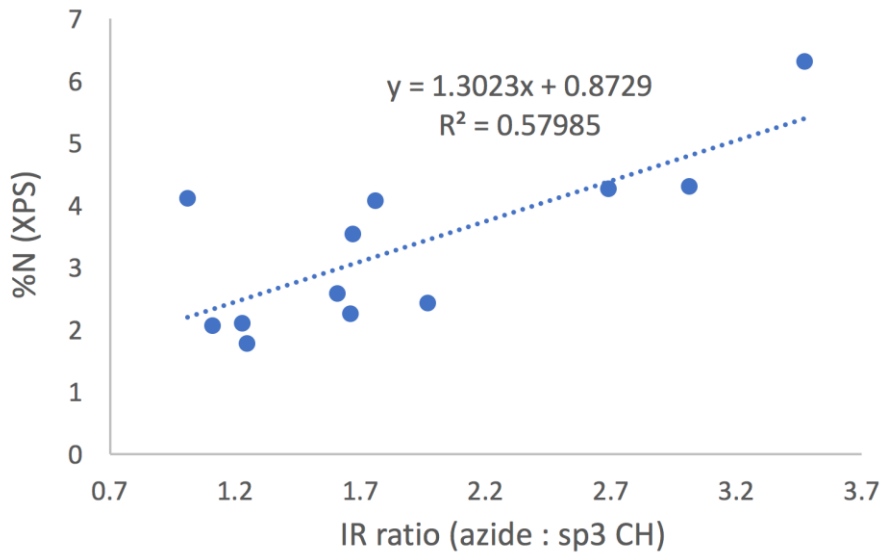

Figure 73. Correlation of percent nitrogen from XPS with IR azide peak intensity.

3.4.1.2 Azidation Occurs Only at PVC surface

Azidation was found to occur only at the surface of the PVC tubing as shown by XPS; examination of the interior of the tubing by XPS as close as 25-50 μm to the surface showed no azide signal, as displayed in Figure 74.

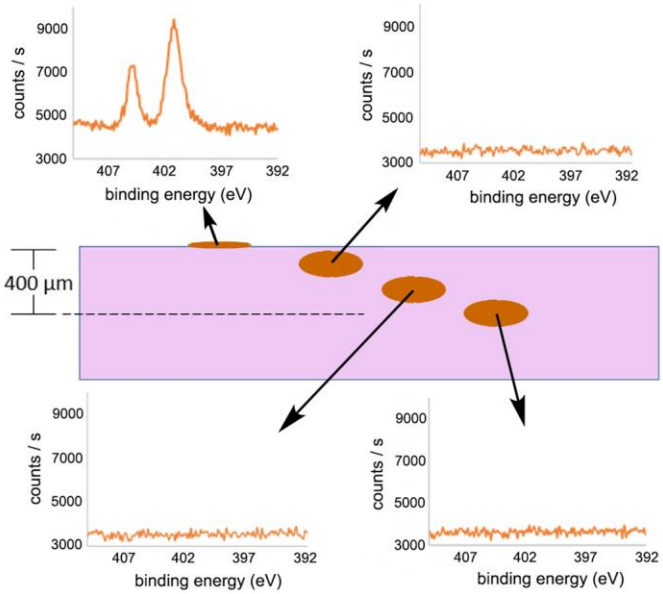

Figure 74. XPS analyses of a representative sample (12 h, 80 °C, with Aliquat® 336) showing azidation at the surface but not in the interior.

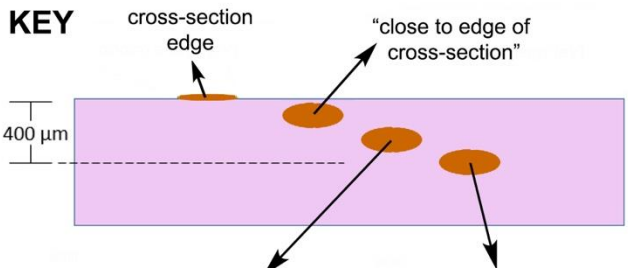

Figure 75. Key for cross-section data.

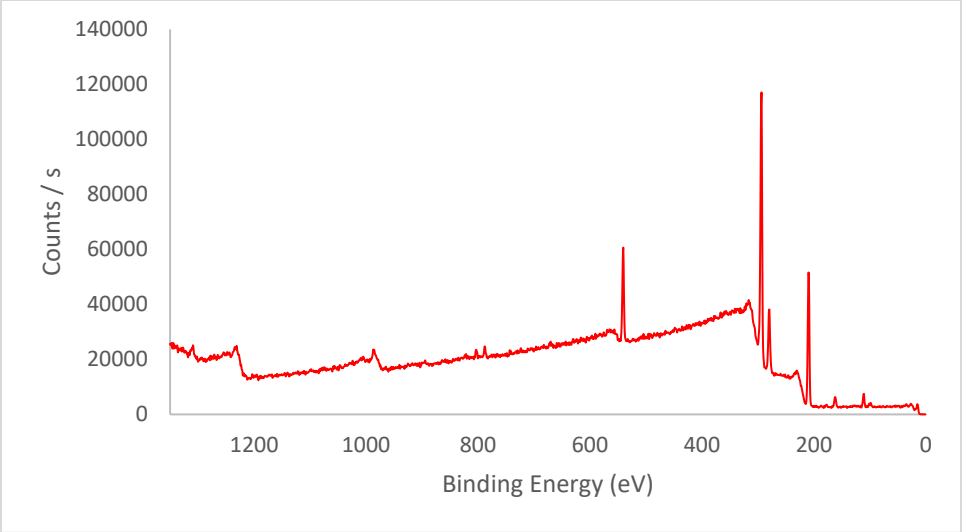

Figure 76. XPS spectra of cross-sectioned azidated ET as a function of PTC. Tetrabutylammonium bromide--close to edge of cross-section.

Table 21. XPS integration for cross-sectioned azidated ET as a function of PTC. Tetrabutylammonium bromide--close to edge of cross-section.

Peak	Atomic %
C1s	83.43
O1s	12.06
Cl2p	4.24
N1s	0
Si2p	3.91

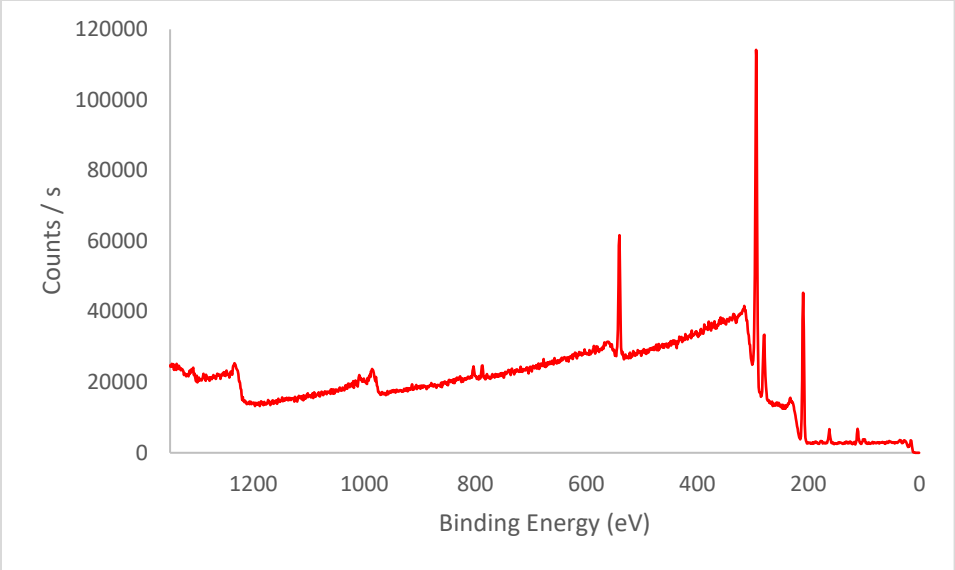

Figure 77. XPS spectra of cross sectioned. Azidated ET as a function of PTC. Tetrabutylammonium bromide--approximately 1/4 of the way through the cross-section.

Table 22. XPS integration for cross-sectioned azidated ET as a function of PTC. Tetrabutylammonium bromide-- approximately 1/4 of the way through the cross-section.

Peak	Atomic %
C1s	83.00
O1s	12.18
Cl2p	2.72
N1s	0
Si2p	2.1

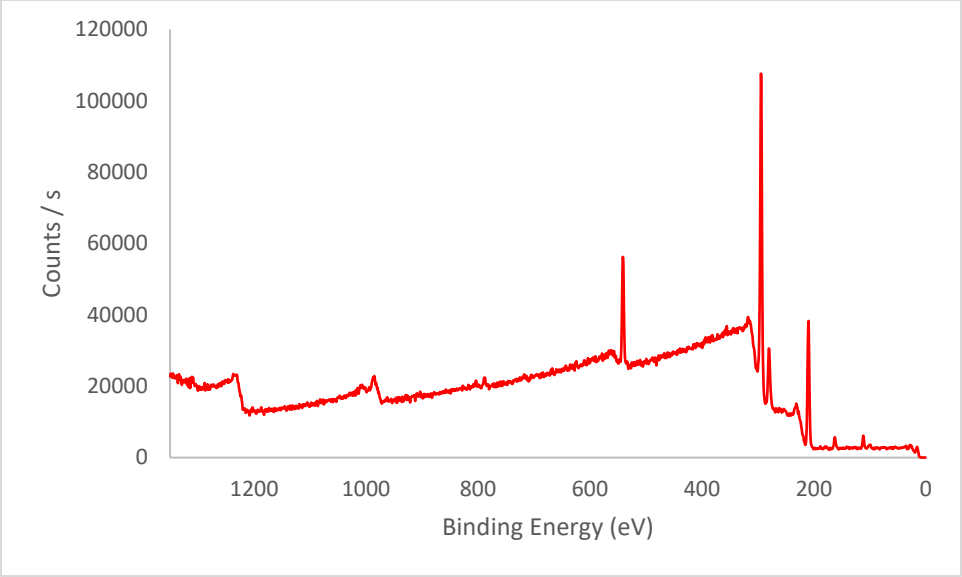

Figure 78. XPS spectra of cross sectioned. Azidated ET as a function of PTC. Tetrabutylammonium bromide--midway way through the cross-section.

Table 23. XPS integration for cross-sectioned azidated ET as a function of PTC. Tetrabutylammonium bromide-- midway way through the cross-section.

Peak	Atomic %
C1s	85.00
O1s	13.22
Cl2p	0
N1s	0
Si2p	1.78

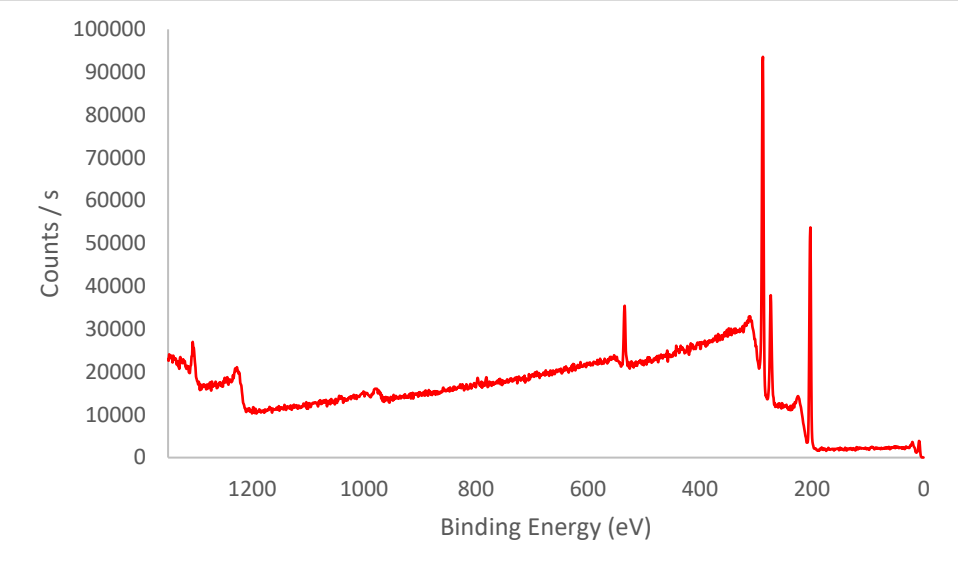

Figure 79. XPS spectra of cross-sectioned azidated ET as a function of PTC. Cetylpyridinium chloride --close to edge of cross-section.

Table 24. XPS integration for cross-sectioned azidated ET as a function of PTC. Cetylpyridinium chloride --close to edge of cross-section.

Peak	Atomic %
C1s	72.98
O1s	6.24
Cl2p	20.54
N1s	0

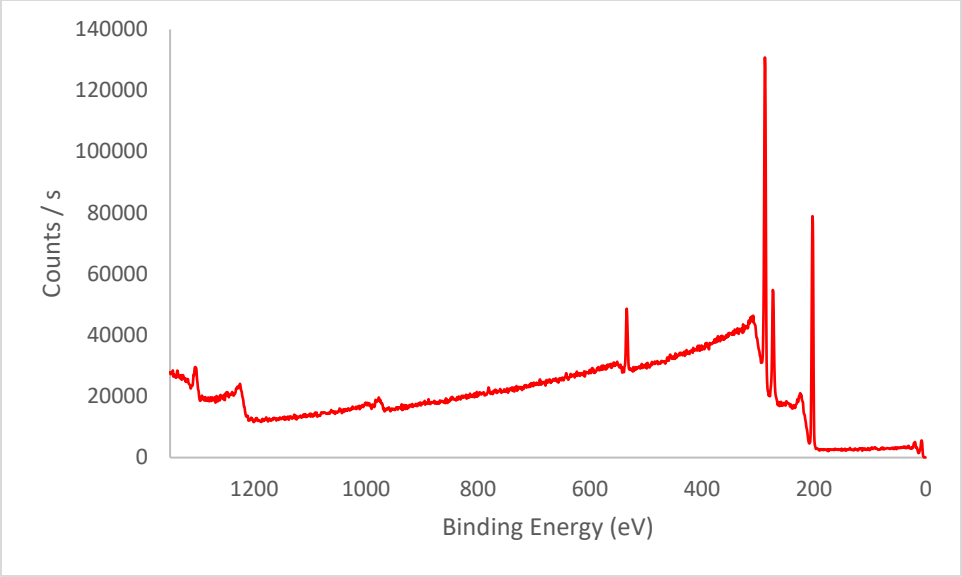

Figure 80. XPS spectra of cross-sectioned azidated ET as a function of PTC. Cetylpyridinium chloride --approximately 1/4 of the way through the cross-section.

Table 25. XPS integration for cross-sectioned azidated ET as a function of PTC. Cetylpyridinium chloride -- approximately 1/4 of the way through the cross-section.

Peak	Atomic %
C1s	64.26
O1s	5.83
Cl2p	29.64
N1s	0

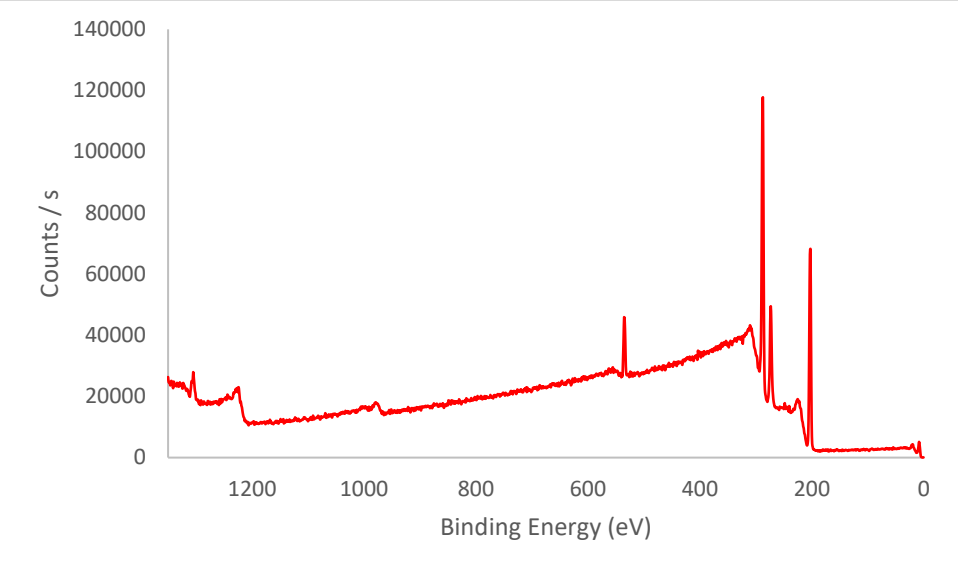

Figure 81. XPS spectra of cross-sectioned azidated ET as a function of PTC. Cetylpyridinium chloride --midway through the cross-section.

Table 26. XPS integration for cross-sectioned azidated ET as a function of PTC. Cetylpyridinium chloride -- midway through the cross-section.

Peak	Atomic %
C1s	72.32
O1s	6.03
Cl2p	20.86
N1s	0
Ca2p	0.01

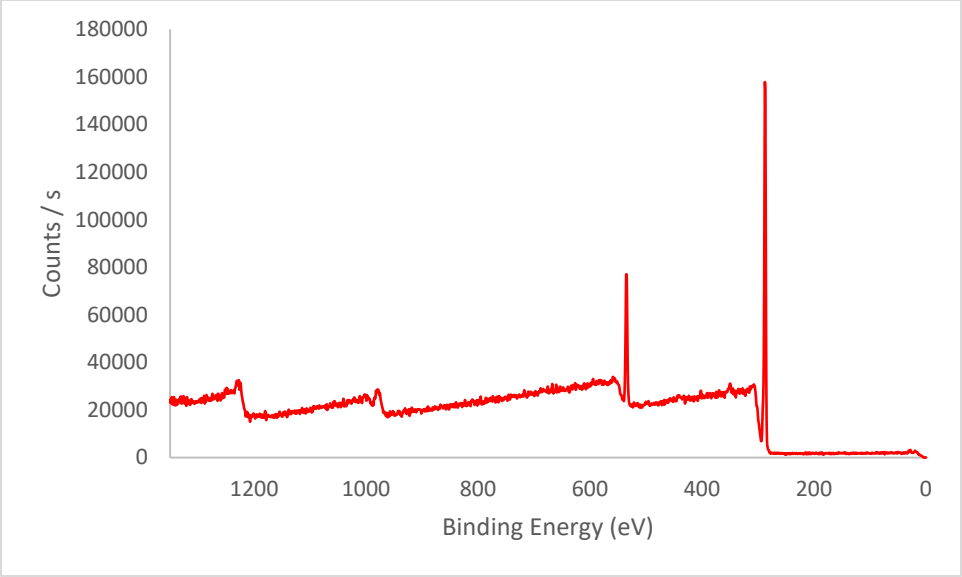

Figure 82. XPS spectra of cross-sectioned azidated ET as a function of PTC. Tetraphenylphosphonium bromide --close to edge of cross-section.

Table 27. XPS integration for cross-sectioned azidated ET as a function of PTC. Tetraphenylphosphonium bromide --close to edge of cross-section.

Peak	Atomic %
C1s	82.61
O1s	13.97
N1s	0
Ca2p	1.64

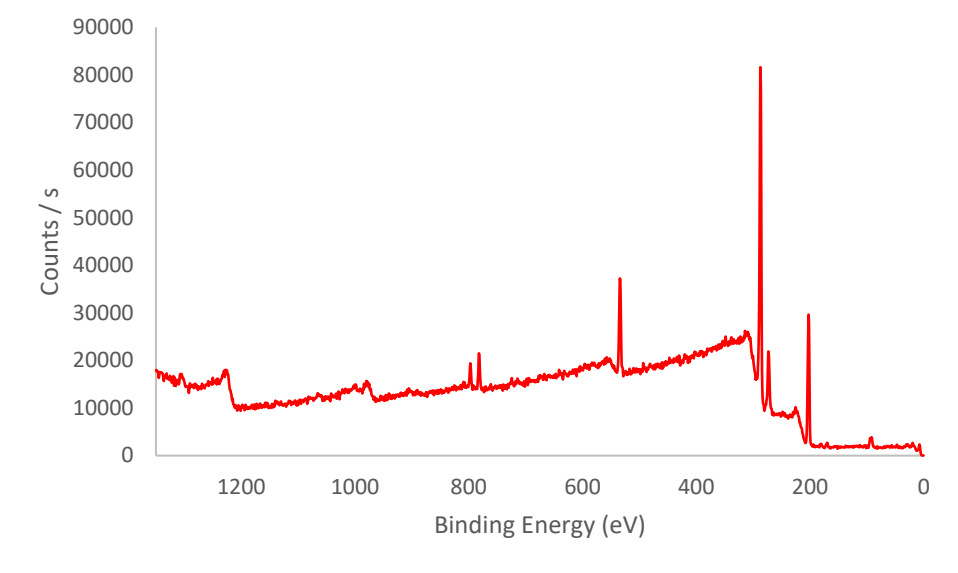

Figure 83. XPS spectra of cross-sectioned azidated ET as a function of PTC. Tetraphenylphosphonium bromide --approximately 1/4 of the way through the cross-section.

Table 28. XPS integration for cross-sectioned azidated ET as a function of PTC. Tetraphenylphosphonium bromide -- approximately 1/4 of the way through the cross-section.

Peak	Atomic %
C1s	76.80
O1s	9.71
Cl2p	12.9
N1s	0

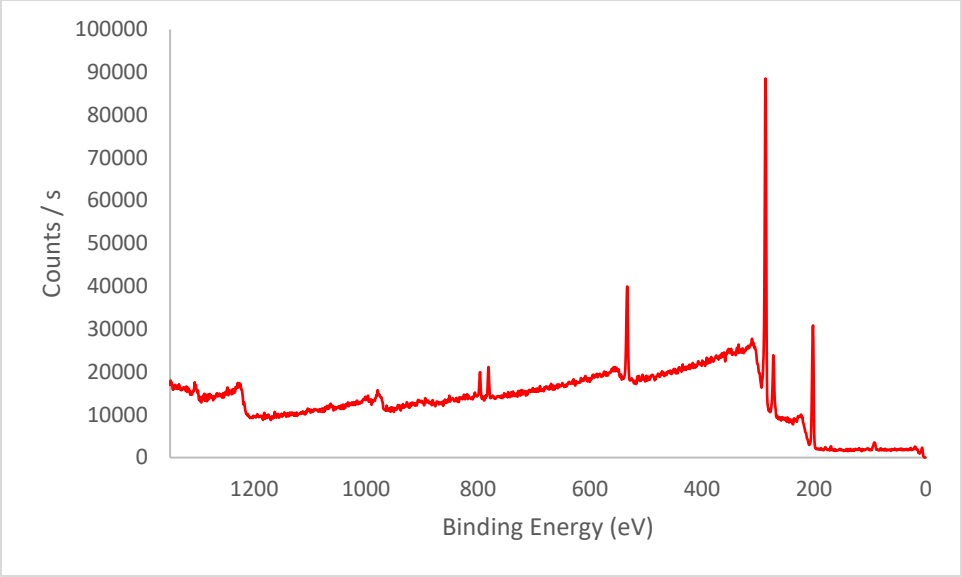

Figure 84. XPS spectra of cross-sectioned azidated ET as a function of PTC. Tetraphenylphosphonium bromide --midway through the cross-section.

Table 29. XPS integration for cross-sectioned azidated ET as a function of PTC. Tetraphenylphosphonium bromide -- midway through the cross-section.

Peak	Atomic %
C1s	76.6
O1s	9.34
Cl2p	12.63
N1s	0

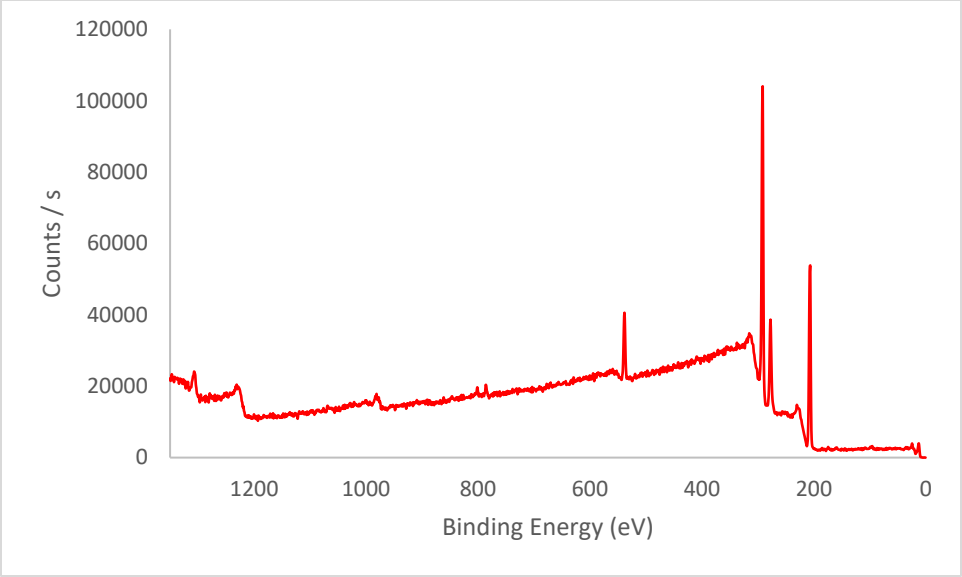

Figure 85. XPS spectra of cross-sectioned azidated ET as a function of PTC. Benzyldimethyltetradecylammonium chloride --close to edge of cross-section.

Table 30. XPS integration for cross-sectioned azidated ET as a function of PTC. Benzyldimethyltetradecylammonium chloride --close to edge of cross-section.

Peak	Atomic %
C1s	74.32
O1s	7.57
Cl2p	18.11
N1s	0

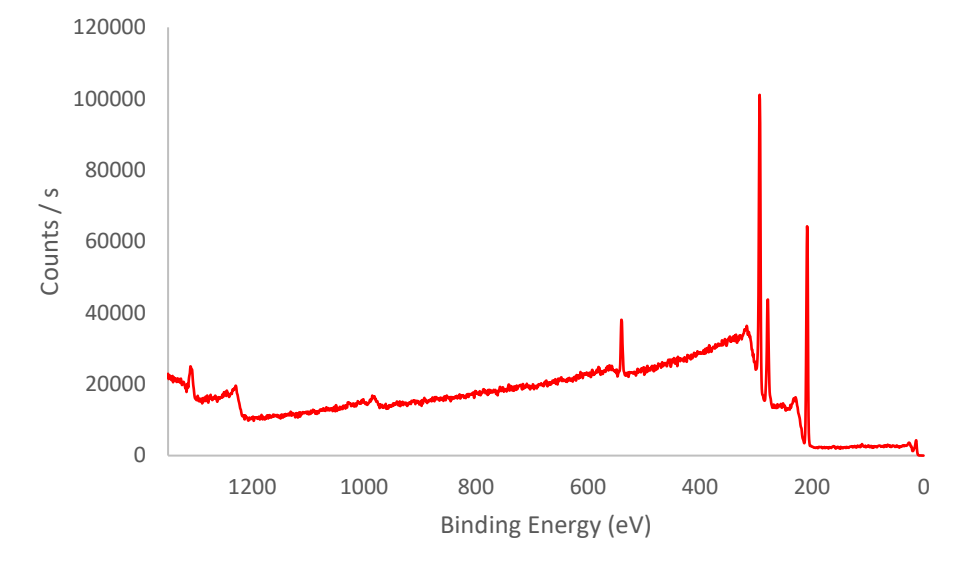

Figure 86. XPS spectra of cross-sectioned azidated ET as a function of PTC. Benzyldimethyltetradecylammonium chloride --approximately 1/4 of the way through the cross-section.

Table 31. XPS integration for cross-sectioned azidated ET as a function of PTC. Benzyldimethyltetradecylammonium chloride --approximately 1/4 of the way through the cross-section.

Peak	Atomic %
C1s	77.45
O1s	6.75
Cl2p	14.90
N1s	0
Ca2p	0.90

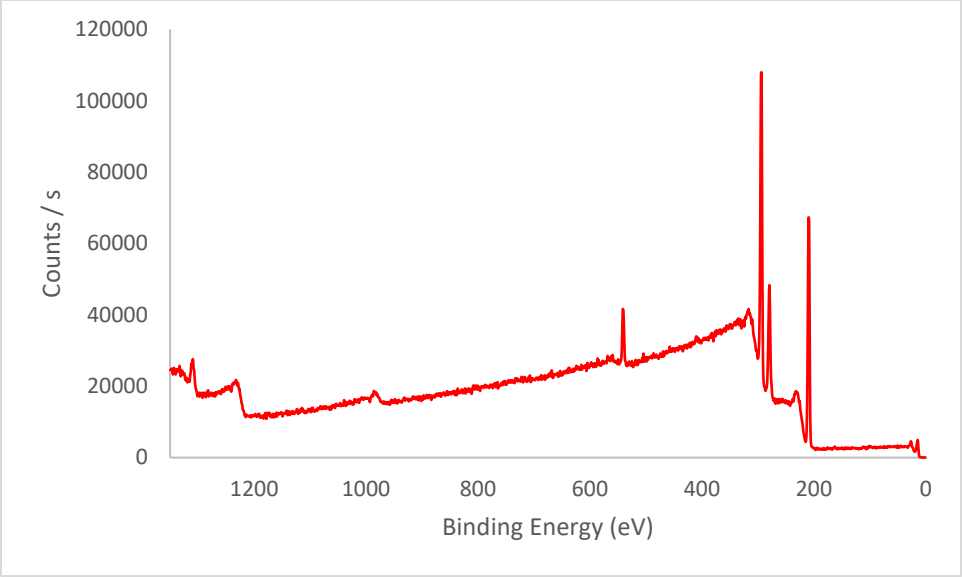

Figure 87. XPS spectra of cross-sectioned azidated ET as a function of PTC. Benzyldimethyltetradecylammonium chloride --midway through the cross-section.

Table 32. XPS integration for cross-sectioned azidated ET as a function of PTC. Benzyldimethyltetradecylammonium chloride --midway through the cross-section.

Peak	Atomic %
C1s	84.16
O1s	7.33
Cl2p	8.51
N1s	0

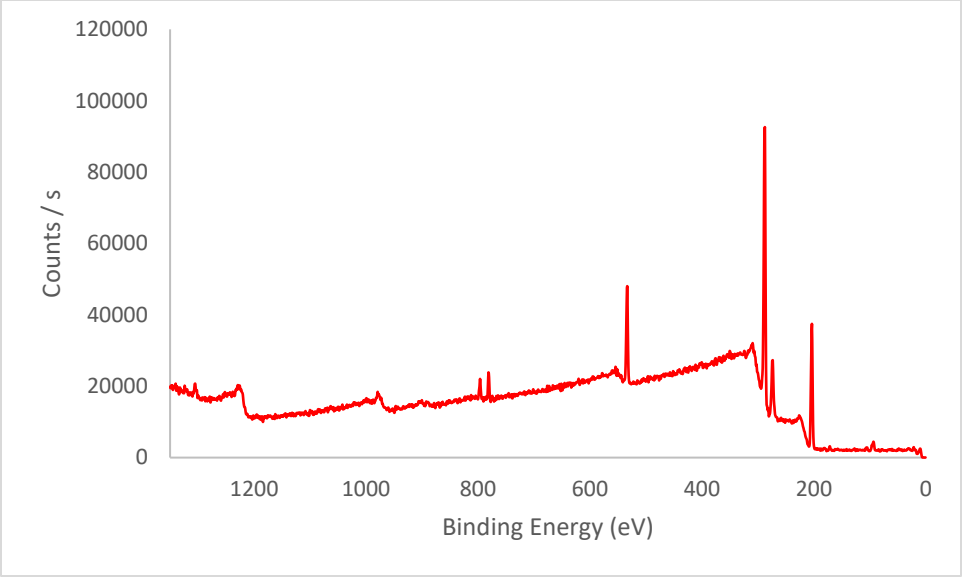

Figure 88. XPS spectra of cross-sectioned azidated ET as a function of PTC. Tetrabutylammonium iodide --close to edge of cross-section.

Table 33. XPS integration for cross-sectioned azidated ET as a function of PTC. Tetrabutylammonium iodide --close to edge of cross-section.

Peak	Atomic %
C1s	73.67
O1s	9.52
Cl2p	13.48
N1s	0

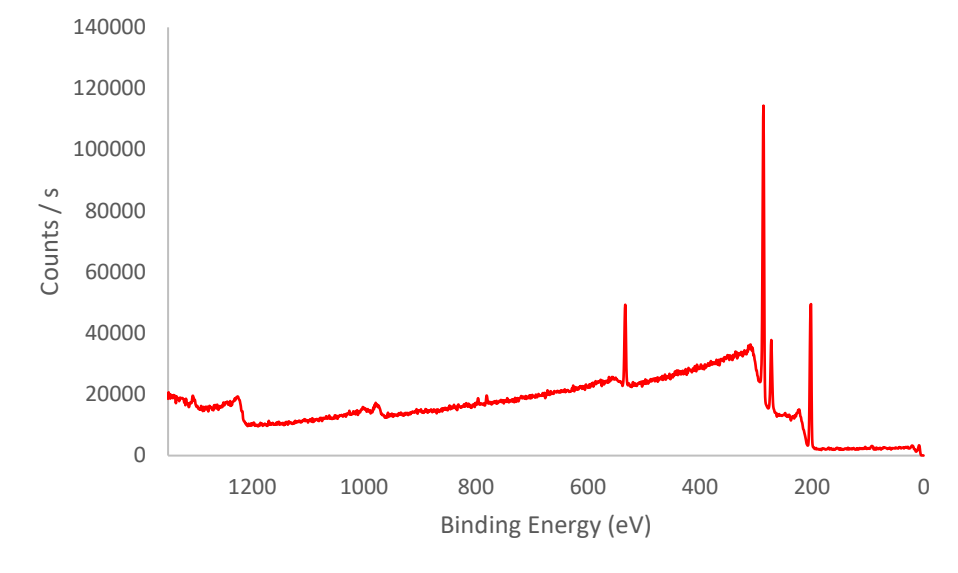

Figure 89. XPS spectra of cross-sectioned azidated ET as a function of PTC. Tetrabutylammonium iodide --approximately 1/4 of the way through the cross-section.

Table 34. XPS integration for cross-sectioned azidated ET as a function of PTC. Tetrabutylammonium iodide --approximately 1/4 of the way through the cross-section.

Peak	Atomic %
C1s	74.09
O1s	8.84
Cl2p	17.08
N1s	0

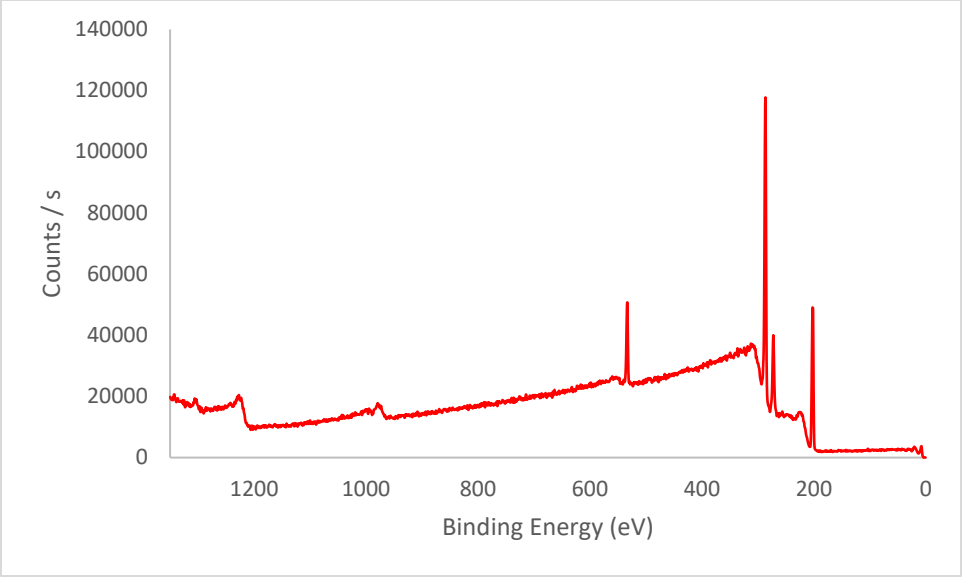

Figure 90. XPS spectra of cross-sectioned azidated ET as a function of PTC. Tetrabutylammonium iodide --midway through the cross-section.

Table 35. XPS integration for cross-sectioned azidated ET as a function of PTC. Tetrabutylammonium iodide --midway through the cross-section.

Peak	Atomic %
C1s	62.92
O1s	7.90
Cl2p	22.11
N1s	0

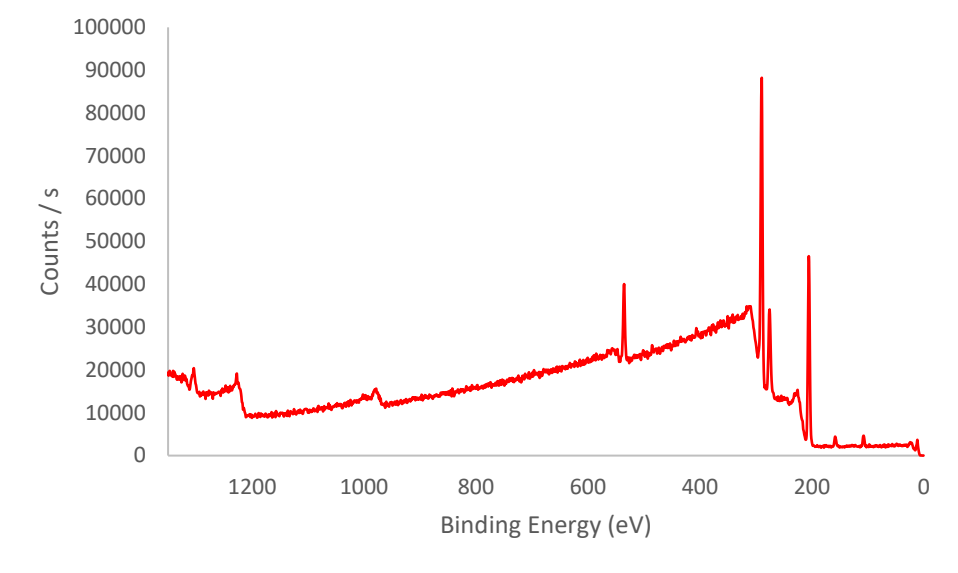

Figure 91. XPS spectra of cross-sectioned azidated ET as a function of PTC. Hexadecyltrimetylammonium chloride --close to edge of cross-section.

Table 36. XPS integration for cross-sectioned azidated ET as a function of PTC. Hexadecyltrimetylammonium chloride --close to edge of cross-section.

Peak	Atomic %
C1s	70.83
O1s	7.64
Cl2p	18.58
N1s	0
Si2p	2.82

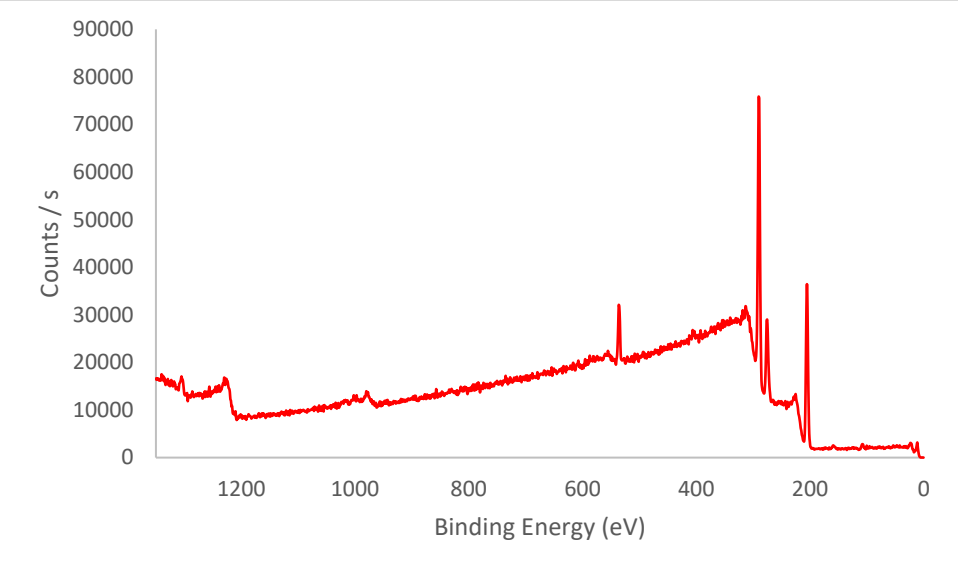

Figure 92. XPS spectra of cross-sectioned azidated ET as a function of PTC. Hexadecyltrimetylammonium chloride --approximately 1/4 of the way through the cross-section.

Table 37. XPS integration for cross-sectioned azidated ET as a function of PTC. Tetrabutylammonium iodide --approximately 1/4 of the way through the cross-section.

Peak	Atomic %
C1s	74.67
O1s	6.73
Cl2p	17.91
N1s	0

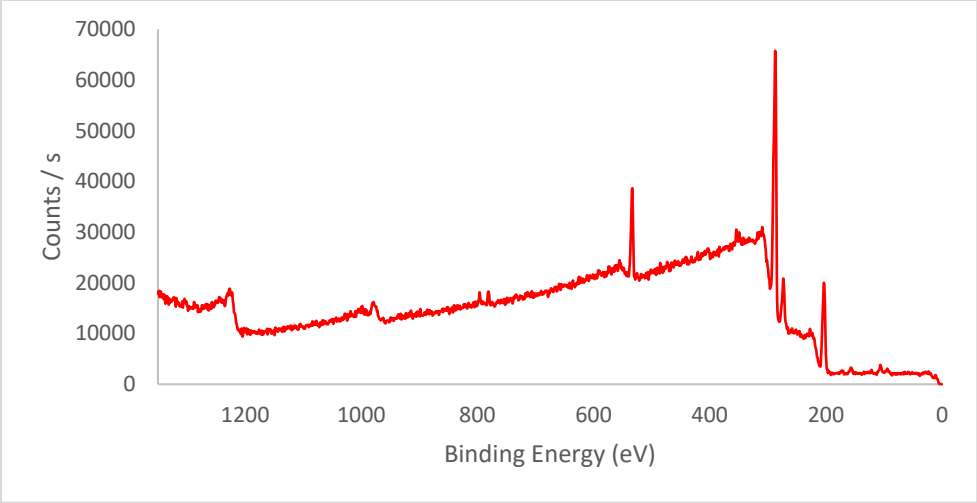

Figure 93. XPS spectra of cross-sectioned azidated ET as a function of PTC. Hexadecyltrimetylammonium chloride--midway through the cross-section.

Table 38. XPS integration for cross-sectioned azidated ET as a function of PTC. Hexadecyltrimetylammonium chloride--approximately 1/4 of the way through the cross-section.

Peak	Atomic %
C1s	75.04
O1s	8.54
Cl2p	11.87
N1s	0
Ca2p	1.05
Si2p	1.71

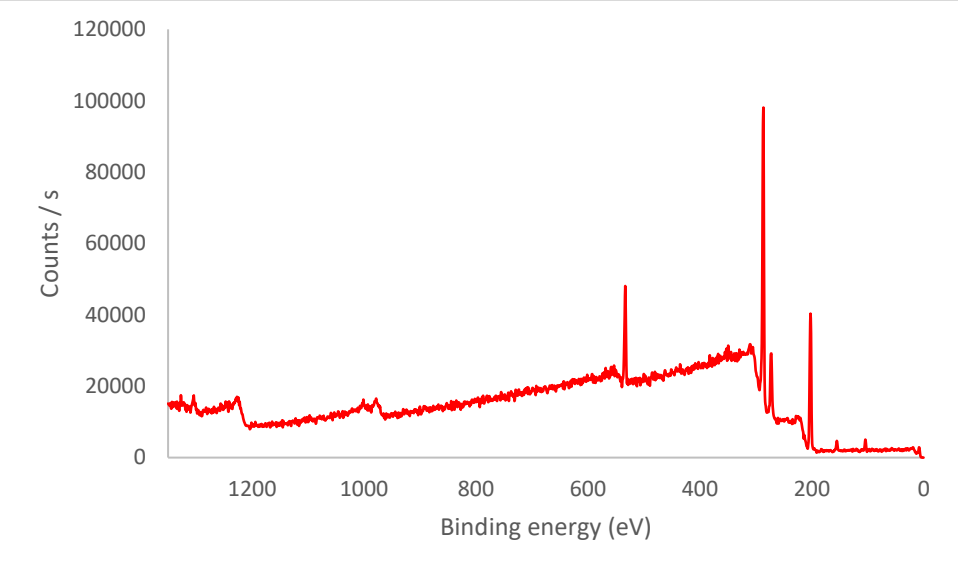

Figure 94. XPS spectra of cross-sectioned azidated ET as a function of PTC. Aliquat 336 (12 h azidation)--close to edge of cross-section.

Table 39. XPS integration for cross-sectioned azidated ET as a function of PTC. Aliquat 336 (12 h azidation)--close to edge of cross-section.

Peak	Atomic %
C1s	68.07
O1s	9.96
Cl2p	18.69
N1s	0
Si2p	2.55

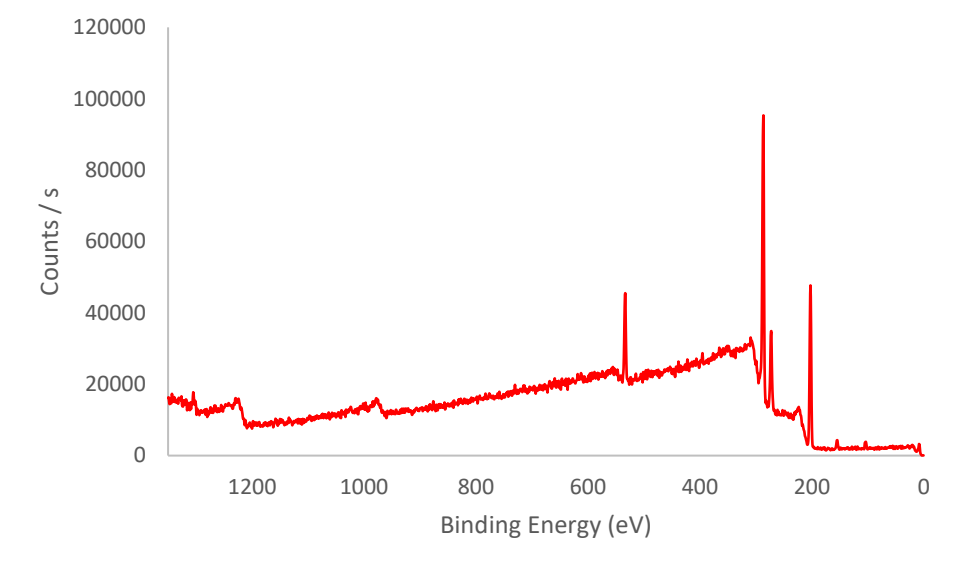

Figure 95. XPS spectra of cross-sectioned azidated ET as a function of PTC. Aliquat 336 (12 h azidation)--approximately 1/4 of the way through the cross-section.

Table 40. XPS integration for cross-sectioned azidated ET as a function of PTC. Aliquat 336 (12 h azidation)--approximately 1/4 of the way through the cross-section.

Peak	Atomic %
C1s	66.67
O1s	9.20
Cl2p	20.22
N1s	0
Si2p	2.03

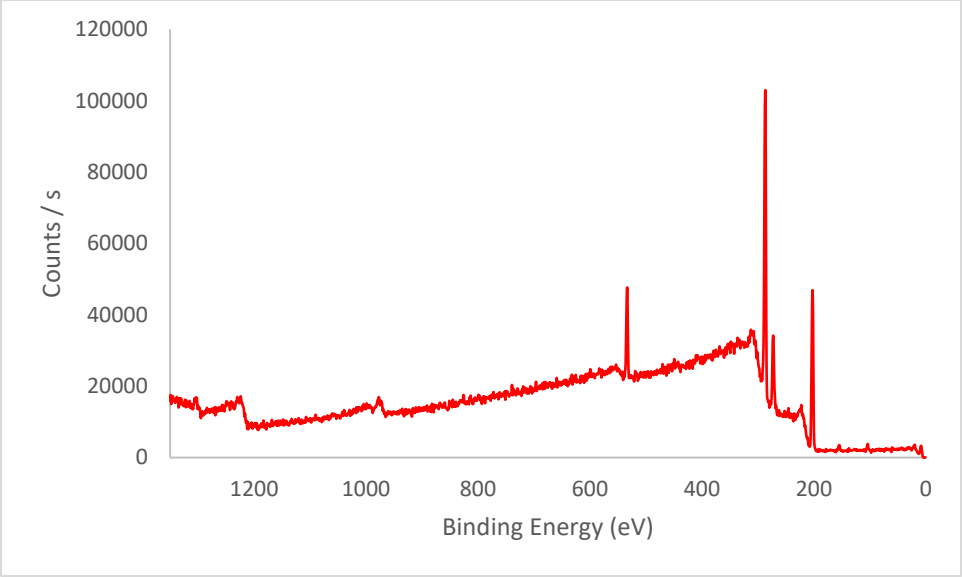

Figure 96. XPS spectra of cross-sectioned azidated ET as a function of PTC. Aliquat 336 (12 h azidation)--midway through the cross-section.

Table 41. XPS integration for cross-sectioned azidated ET as a function of PTC. Aliquat 336 (12 h azidation)-- midway through the cross-section.

Peak	Atomic %
C1s	69.38
O1s	8.74
Cl2p	19.68
N1s	0
Si2p	2.19

The same azidation conditions used for medical tubing were also successfully applied to food-grade flexible PVC tubing (3/8" i.d., ½" o.d., SM Intrade), as demonstrated in Figure 97. This functionalized tubing showed some signs of inhomogeneity, with light and dark patches on the tubing after a 24 hour azidation, but retained its flexibility.

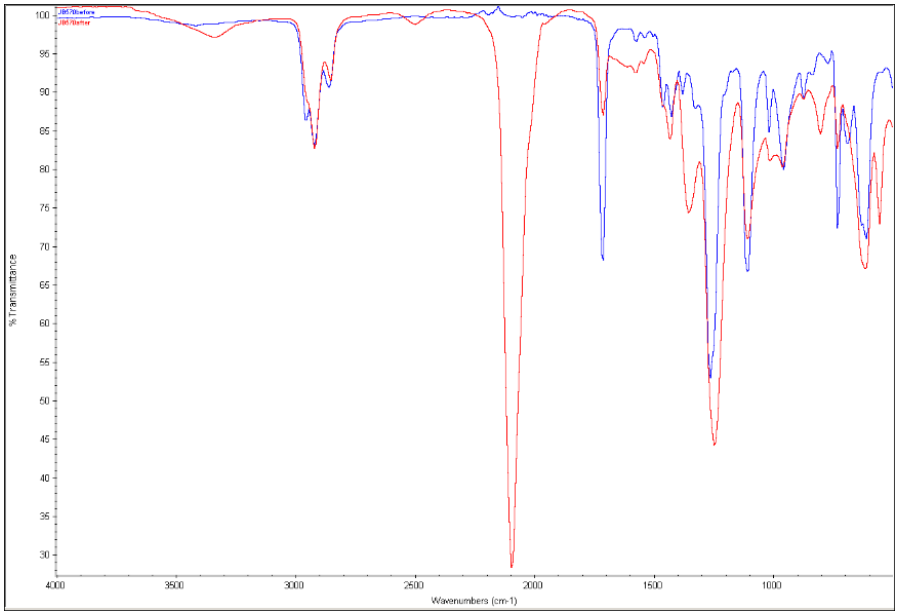

Figure 97. IR of food grade PVC both before (blue) and after azidation (red)

3.4.2 Whole tube modification

To apply the conditions developed above to whole tubing, rather than pieces cut from such tubing, a prototype reactor was constructed as depicted in Figure 98. A whole catheter tube was fed through an Eldon James T06BN nylon T-joint connecter and encased in larger diameter (10 mm ID) silicone tubing, closed at the other end. The other two ends of the T-joint were connected with Masterflex 96410-25 silicone tubing (4.8 mm ID), fed through a peristaltic pump. These materials showed no signs of sensitivity (discoloration, degradation, swelling, or hardening) upon exposure to the solution of sodium azide and Aliquat® 336 for at least one week at 80 °C. This system was filled with an aqueous solution (approximately 40 mL) of 2.9 M sodium azide and 51 mM Aliquat® 336. The outer silicone tubing (containing the catheter tube to be modified) was submerged in an 80

°C water bath for 6 hours while the reaction solution was pumped through at a peristaltic pump setting of 170 mL/min. The catheter tubing was then removed from the system and was rinsed thoroughly with water.

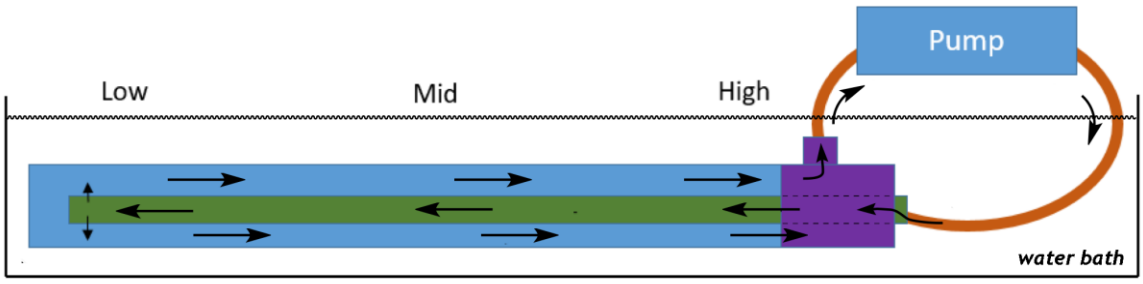

Figure 98. Diagram of whole-tube azidation setup. Green: catheter tubing to be azidated. Blue: silicone tubing used to encase the catheter tubing and solution. Purple: 3-way connector, through which the catheter tubing is fed. Orange: connective silicone tubing. Arrows show fluid flow direction.

With this apparatus, 40-cm lengths of catheter tubing were exposed to a recirculating 40 mL solution of 2.9 M sodium azide containing 51 mM Aliquat® 336, heated at 80 °C for 6 hours. A gradation of functionalization as assessed by IR was observed that matched the pattern of exposure to the circulating fluid. In its most intense areas, azides were installed at lower densities than for the experiments above on cut pieces of tubing, ascribed to a difference in the overall ratio of azide reactant to chloride substrate.

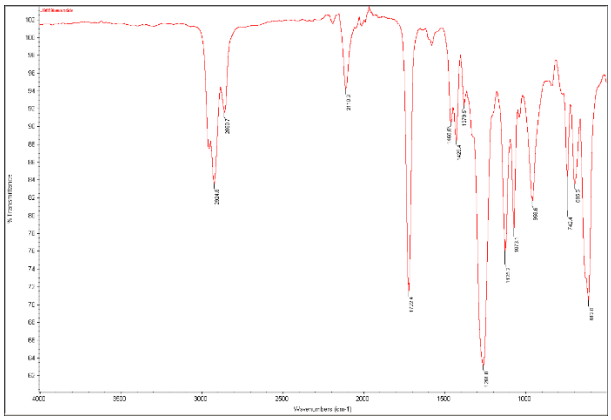

Figure 99. IR spectrum for whole-tube azidation for the lower outside region.

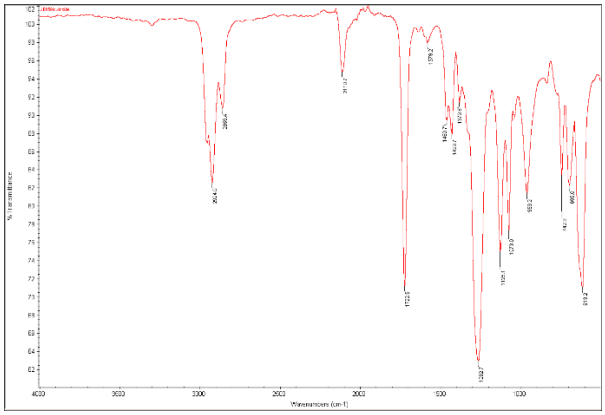

Figure 100. IR spectrum for whole-tube azidation for the lower inside region.

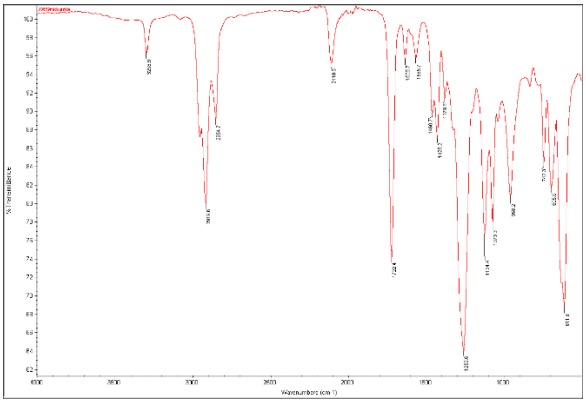

Figure 101. IR spectrum for the whole-tube azidation for the mid-outside region.

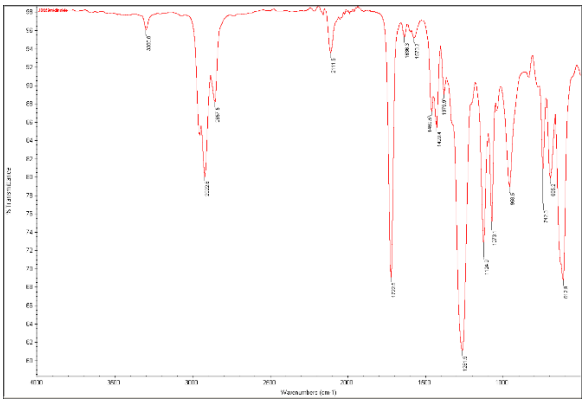

Figure 102. IR spectrum for the whole-tube azidation for the mid-inside region.

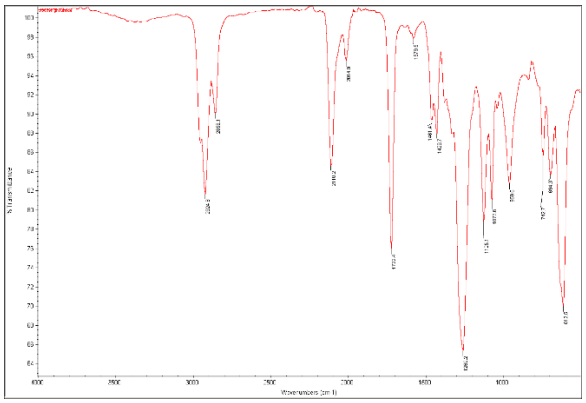

Figure 103. IR spectrum for the whole-tube azidation for the high-outside region.

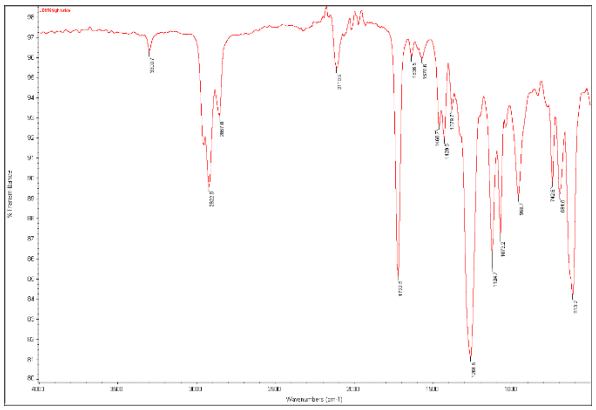

Figure 104. IR spectrum for the whole-tube azidation for the high-inside region.

3.4.3 Copper(I)-catalyzed azide-alkyne cycloaddition to azidated substrates

Copper(I)-catalyzed azide-alkyne cycloaddition (CuAAC) was performed on azidated ET samples (prepared using optimized Aliquat® 336 conditions), followed by washing by sonication in water and analysis of the loss of azide by IR. For the simple CuAAC reaction performed without accelerating ligands, the outcome depended largely on the nature of the alkyne substrate. Quaternary propargylic ammonium cation **1** (Figure 105) was far more reactive than the others tested, achieving complete conjugation at room temperature within a few hours. The other small-molecule alkynes tested, **2**-**4**, required a phase transfer catalyst and heating to facilitate a significant amount of ligation. As with azidation, a lower reaction temperature (60 °C) and shorter reaction time (4.5 h) limited further discoloration to a minimum, at the cost of incomplete azide consumption as assessed by IR (Figure 106).

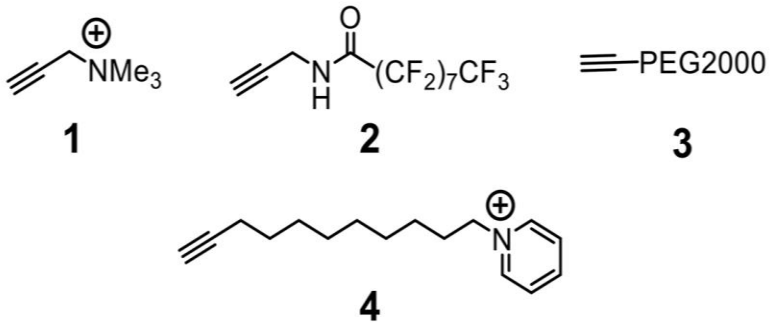

Figure 105. Alkynes used for CuAAC with ET.

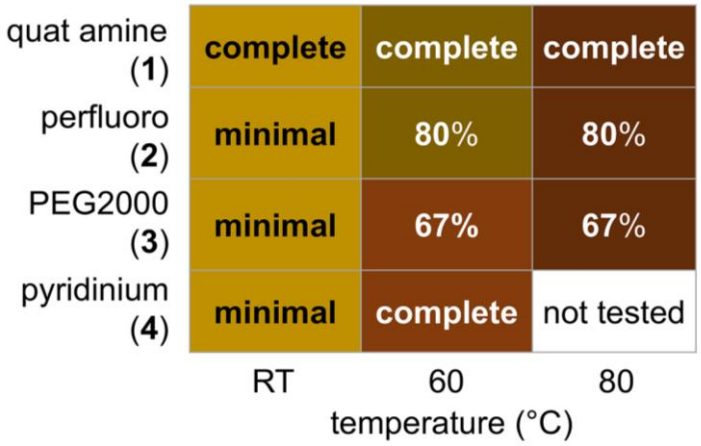

Figure 106. Results of CuAAC reactions at varying temperatures with different alkyne substrates (5 mM) in an aqueous solution of 44 mM $CuSO_4$ and 190 mM sodium ascorbate. The color of each box approximates the color of the resulting tubing. The reaction outcome ("minimal," "complete," etc.) refers to the percent of PVC-azide IR signal that is diminished after the reaction, noting that exposure to the reaction conditions without alkyne gave no loss in this signal; numerical values are approximate (±10%). All reaction times were 4.5 hours with the exception of the quaternary amine 1, which was reacted overnight. Alkynes 2-4 were reacted in the presence of 21 mM Aliquat® 336.

Figure 107. Tubing samples (left to right): unmodified endotracheal tubing, azidated (80 °C, 12 h), CuAAC with 2 (60 °C, overnight), cyanated (80 °C, 3 days), and pentafluorobenzyl tetrazole functionalized via tetrazole.

The fate of the plasticizer imposed strict limits on the CuAAC conditions. For example, triazole linkages were formed somewhat more efficiently in a 1:8 $MeOH/H_2O$ mixture, but the tubing emerged from this reaction with a significant loss in mechanical

flexibility. Small amounts of DMF were tolerated and improved the CuAAC reaction of alkyne **2**, but this effect was not general. Residual copper that sometimes remained on the PVC tubing after CuAAC conjugation (as indicated by XPS) was easily removed by rinsing sequentially with 0.1M EDTA and water. Variation in solution pH was explored for alkyne **4** and was found to have little effect in the range of 6-9.

Table 42. Optimization of conditions for CuAAC on azidated ET

Alkyne and concentration	[$CuSO_4$] (mM)	[Na ascorb.] (mM)	Solvent	Temp (°C)	PTC or ligand and concentration	Extent of reaction (reduction in azide peak intensity by IR)
A1, 5 mM	44	190	H_2O	RT	------	Appears complete
A2, 8 mM	73	337	1:5 DMF/H_2O	60 °C	Aliquat 336, 21 mM	81%
A3, 7.5 mM	235	442	H_2O	80 °C	TBTA-COOH,	68%
A3, 7.5 mM	235	442	H_2O	80 °C	Aliquat 336, 21 mM	74%
A3, 7.5 mM	235	442	H_2O	80 °C	TPPB, 29 mM	71%
A3, 9 mM	80	367	1:10 DMF/H_2O	60 °C	Aliquat 336, 38 mM	76%
A3, 5 mM	44	190	PBS, pH 6	60 °C	Aliquat 336, 21 mM	95%
A3, 5 mM	44	190	PBS, pH 7	60 °C	Aliquat 336, 21 mM	83%
A3, 5 mM	44	190	PBS, pH 8	60 °C	Aliquat 336, 21 mM	93%
A3, 5 mM	44	190	PBS, pH 9	60 °C	Aliquat 336, 21 mM	96%
A4, 5 mM	44	202	H_2O	60 °C	Aliquat 336, 21 mM	98%

RT = Room Temperature, PBS = Phosphate Buffered Saline, DMF = N,N-Dimethylformamide, TPPB = Tetraphenylphosphonium bromide, TBTA-COOH = 4,4',4''-(((nitrilotris(methylene))tris(1H-1,2,3-triazole-4,1-diyl))tris(methylene))tribenzoic acid.

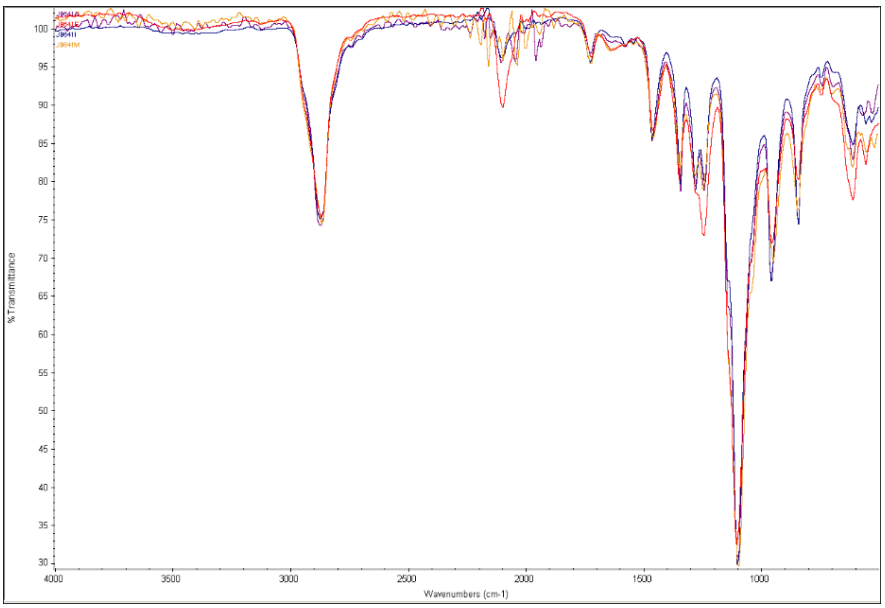

Figure 108. IR spectrum demonstrating the effect of pH on CuAAC reaction through the reduction of the azide peak.

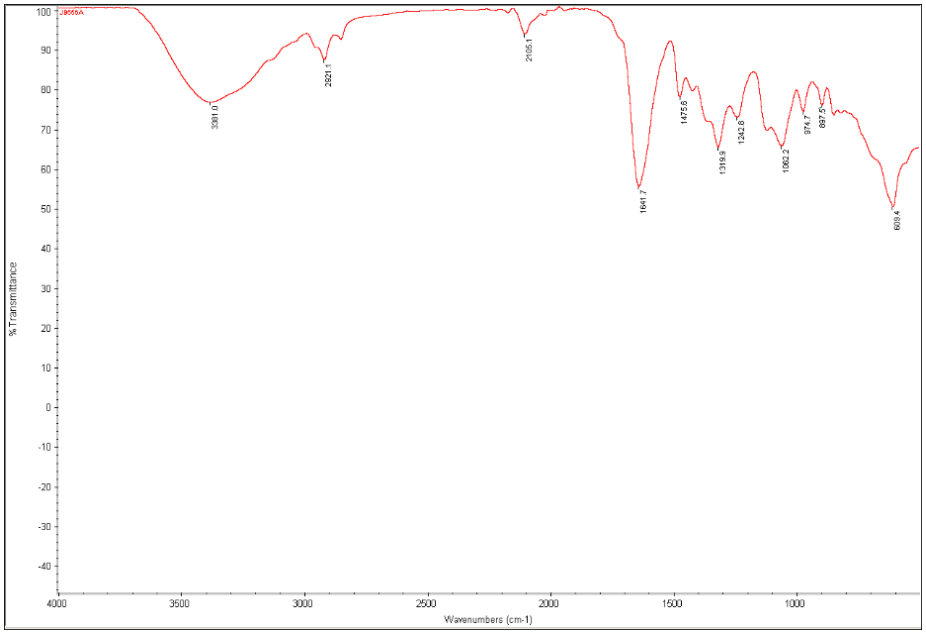

Figure 109. IR spectrum for azidated ET clicked with QA (1)

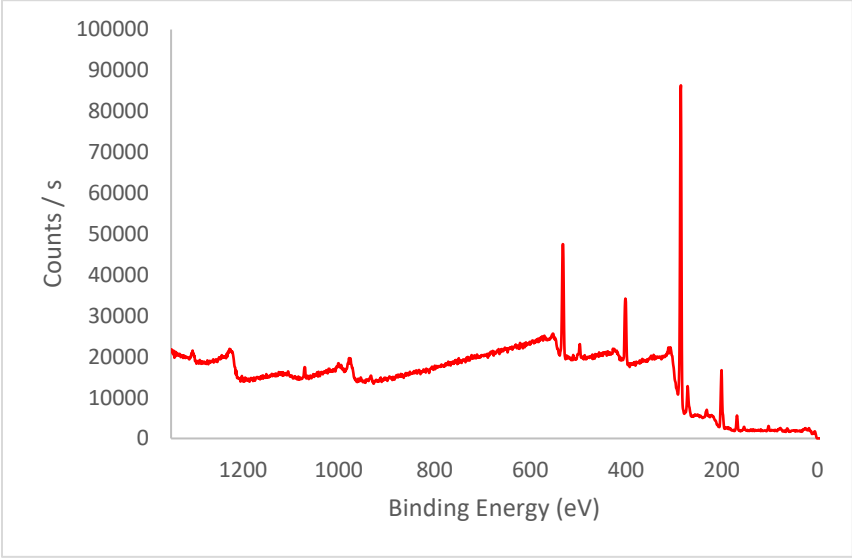

Figure 110. XPS spectrum for azidated ET clicked with QA alkyne (1)

Table 43. XPS integration for azidated ET clicked with QA alkyne (1)

Peak	Atomic %
C1s	68.36
O1s	11.64
Cl2p	5.71
N1s	10.49
Na1s	0.75
Si2p	1.1
S2p	1.94

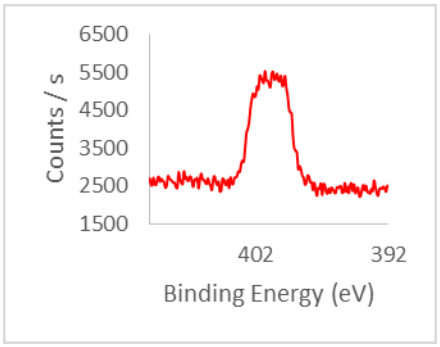

Figure 111. Nitrogen XPS spectrum for azidated ET clicked with QA alkyne (1)

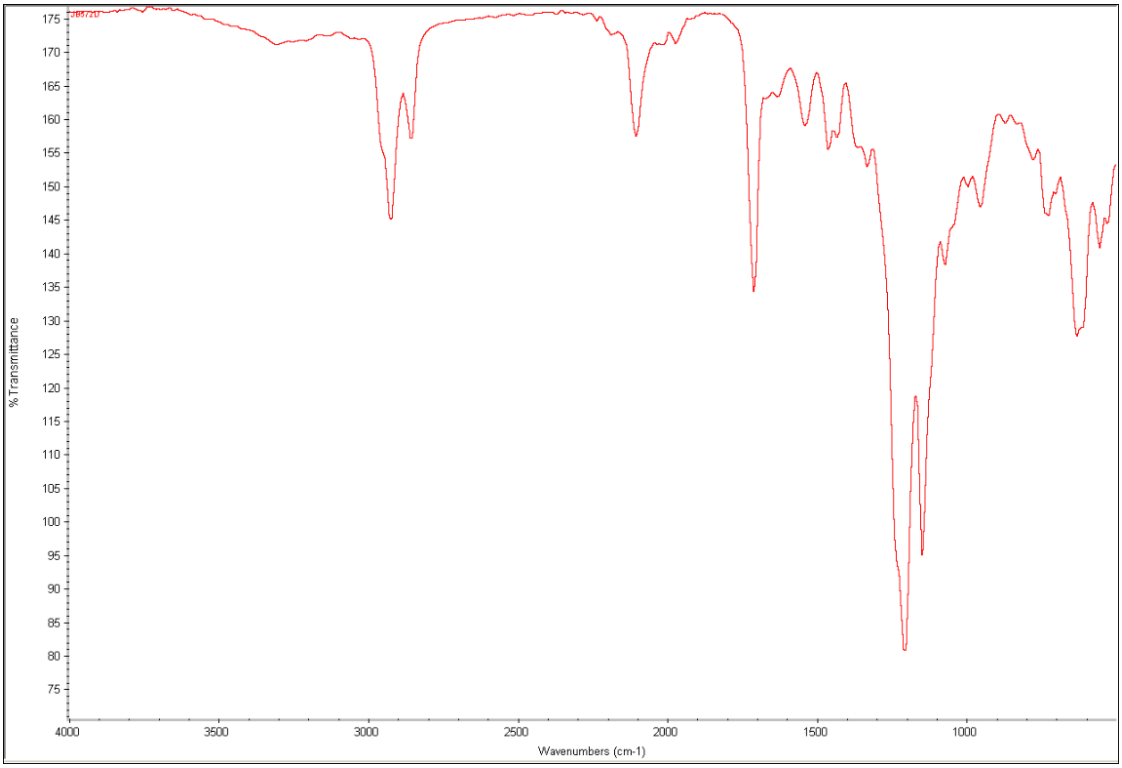

Figure 112. IR spectrum for ET clicked with perfluoro alkyne (2)

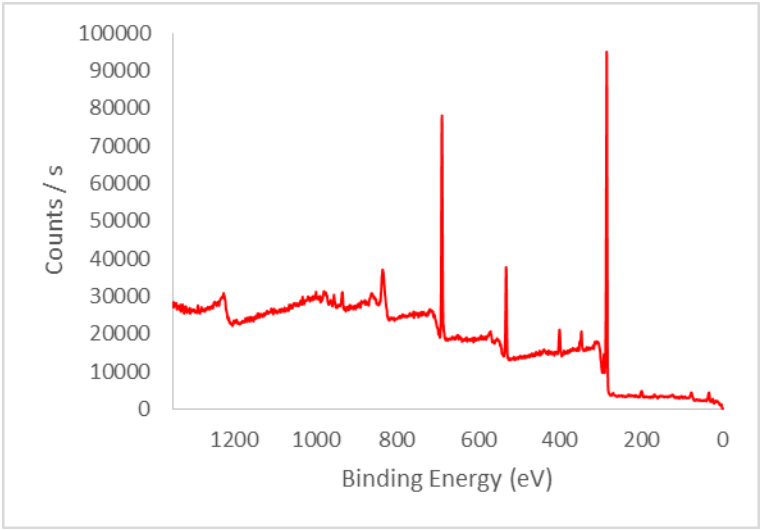

Figure 113. XPS spectrum for ET clicked with perfluoro alkyne (2)

Table 44. XPS integration for azidated ET clicked with perfluoro alkyne (2)

Peak	Atomic %
C1s	69.06
O1s	8.65
Cl2p	1.12
N1s	4.27
F1s	14.84
Ca2p	1.37
Cu2p	0.69

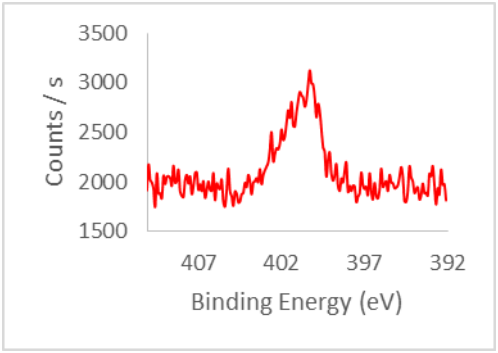

Figure 114. Nitrogen XPS spectrum for azidated ET clicked with perfluoro alkyne (2)

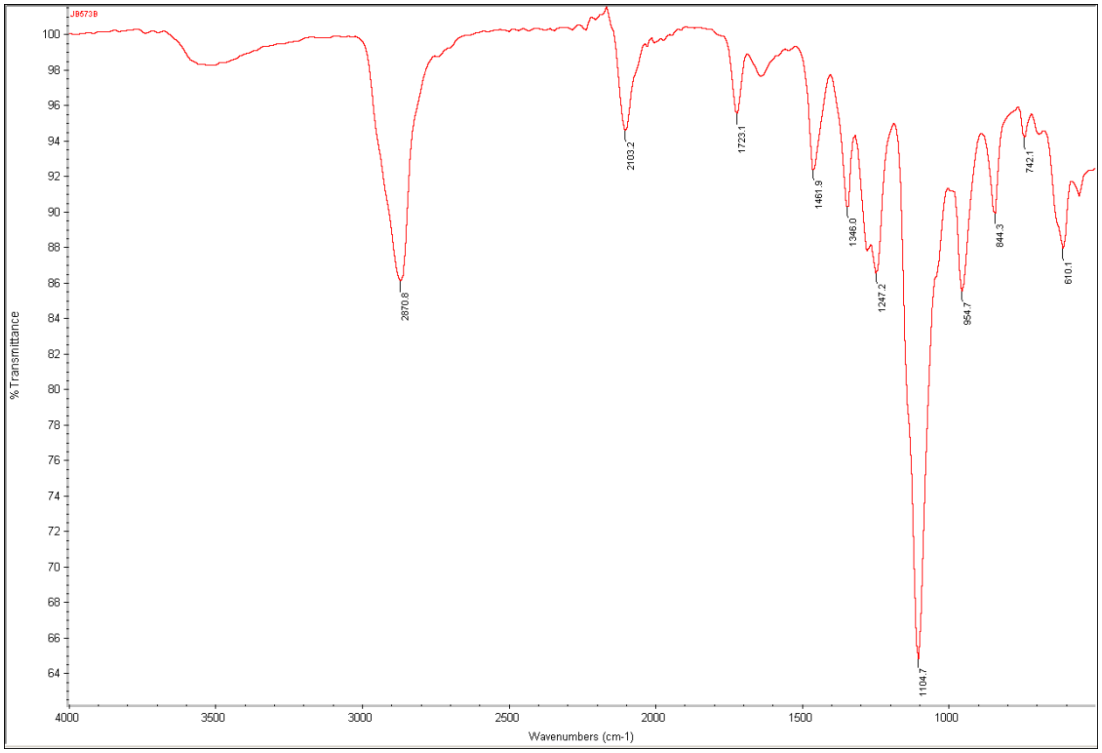

Figure 115. IR spectrum for azidated ET clicked with PEG$_{2000}$ alkyne (3)

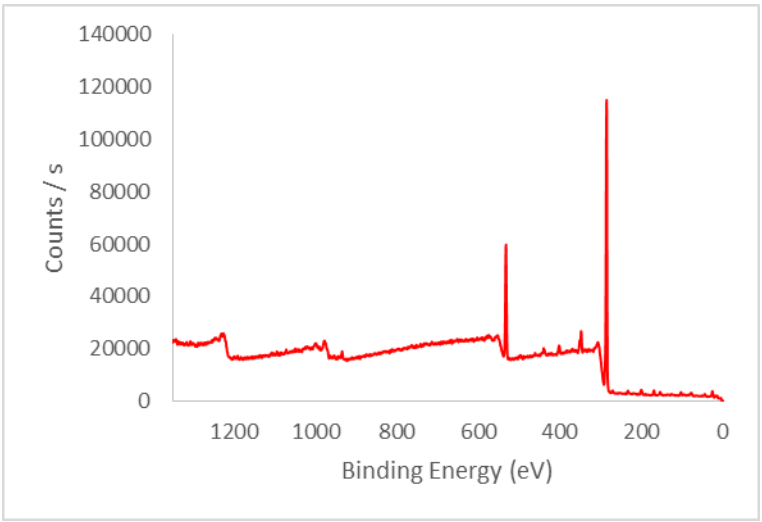

Figure 116. XPS spectrum for azidated ET clicked with PEG$_{2000}$ alkyne (3)

Table 45. XPS integration for azidated ET clicked with PEG_{2000} alkyne (3)

Peak	Atomic %
C1s	79.20
O1s	13.13
Cl2p	1.02
N1s	2.45
Ca2p	1.83
Cu2p	0.31
S2p	0.8
Si2p	1.26

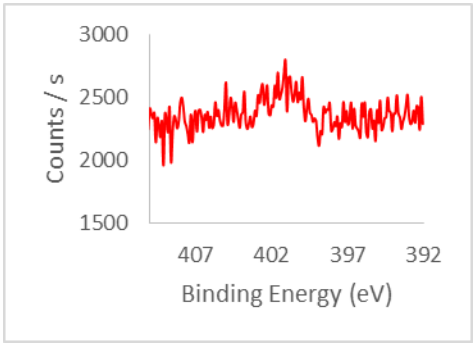

Figure 117. Nitrogen XPS spectrum for azidated ET clicked with PEG_{2000} alkyne (3)

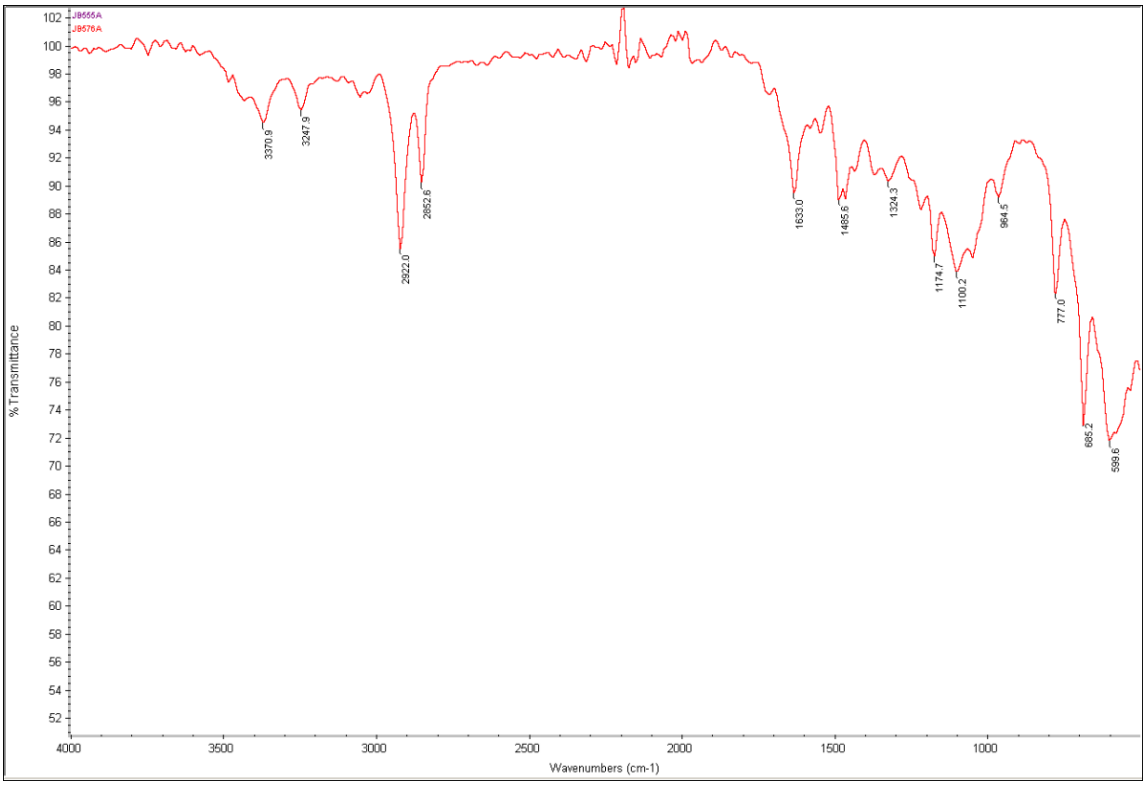

Figure 118. IR spectrum for azidated ET clicked with pyridinium alkyne (4)

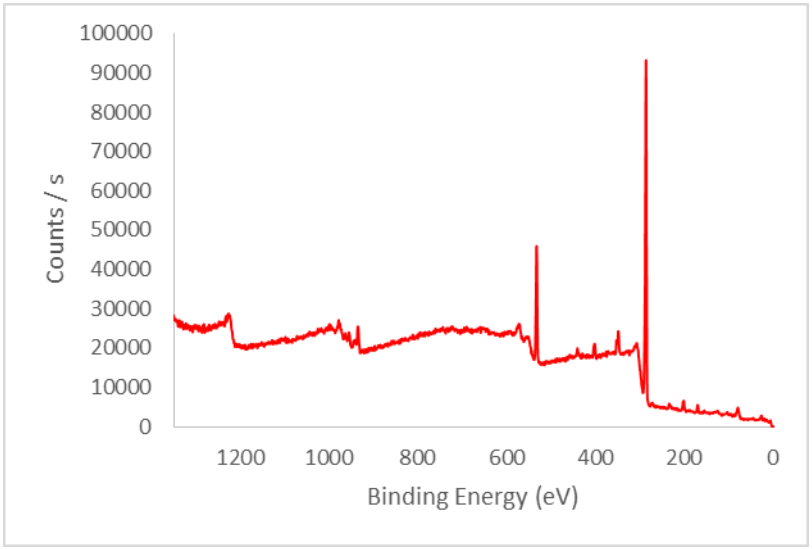

Figure 119. XPS Spectrum for azidated ET clicked with pyridinium alkyne (4)

Table 46. XPS integration for azidated ET clicked with pyridinium alkyne (4)

Peak	Atomic %
C1s	81.21
O1s	11.47
Cl2p	1.61
N1s	2.93
Ca2p	1.66
Cu2p	1.12

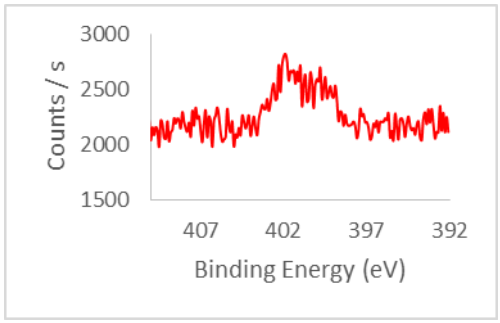

Figure 120. Nitrogen XPS spectrum for azidated ET clicked with pyridinium alkyne (4)

3.4.4 Tetrazole formation from cyanated substrates

To demonstrate the applicability of phase transfer catalysis to the displacement of chloride with other nucleophiles, cyanide was used in place of azide under otherwise identical conditions. The characteristic IR signal for cyanide (~2200 cm^{-1}) is much weaker than for azide, so only a few PTC candidates generated enough reactivity to be easily visible by IR. As with azide, Aliquat® 336 was found to give good and even substitution with retention of tubing flexibility.

Table 47. XPS summary for ET cyanated with various PTCs

	%C	%O	%Cl	%Si	%Ca	%N	%Na
Aliquat 336	82.29	10.84	0.51	3.17	ND	3.19	ND
Tetrabutylammonium cyanide	78.95	11.82	3.43	2.16	1.73	1.91	ND
Cetylpyridinium chloride	84.8	7.71	0.85	1.13	0.64	4.27	0.61

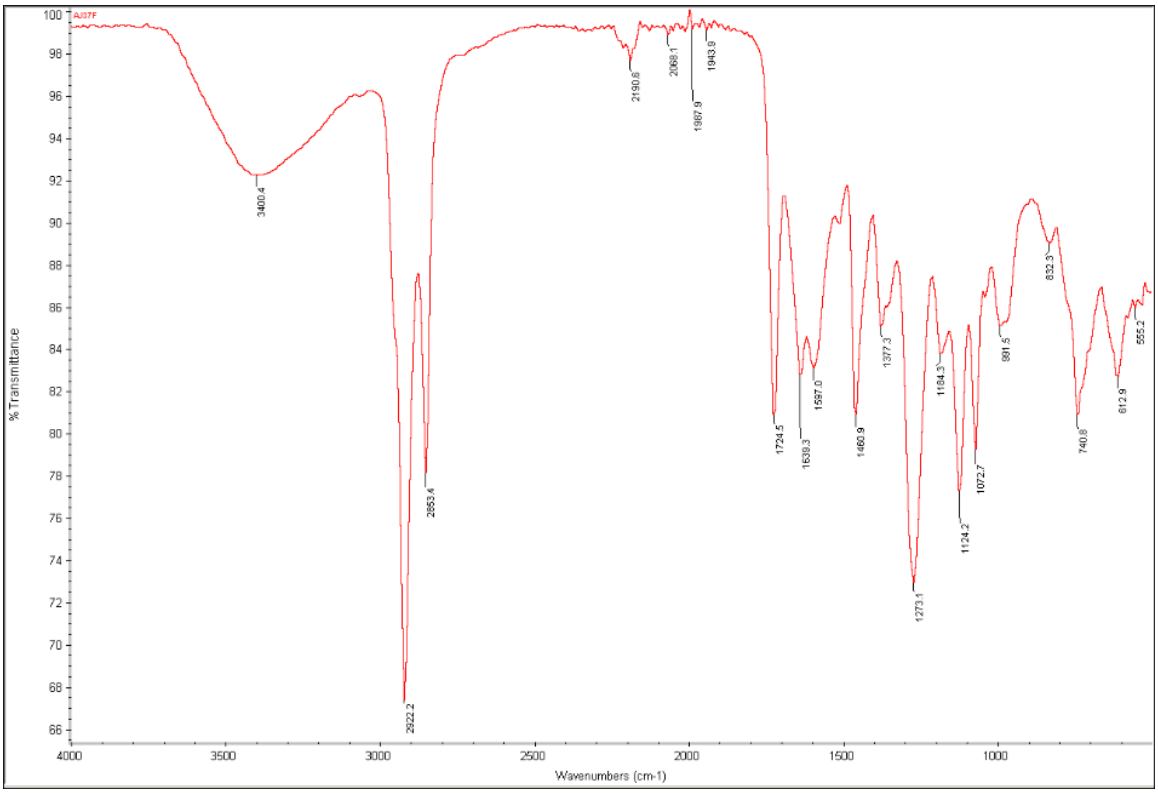

Figure 121. IR spectrum for ET cyanated with cetylpyridinium chloride

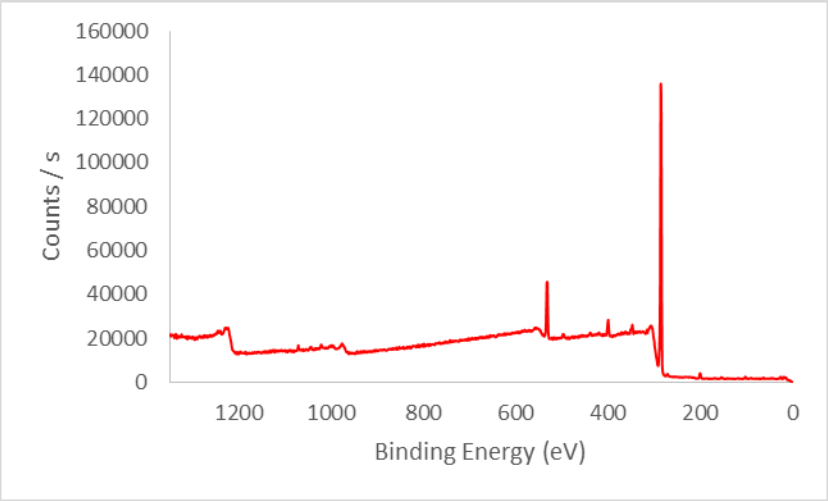

Figure 122. XPS spectrum for ET cyanated with cetylpyridinium chloride

Table 48. XPS integration for ET cyanated with cetylpyridinium chloride

Peak	Atomic %
C1s	84.80
Cl2p	0.85
O1s	7.71
N1s	4.27
Si2p	1.13
Ca2p	0.64
Na1s	0.61

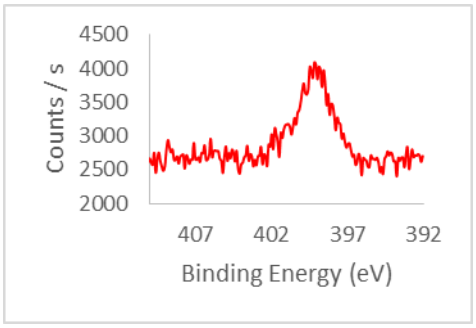

Figure 123. Nitrogen XPS spectrum for ET cyanated with cetylpyridinium chloride

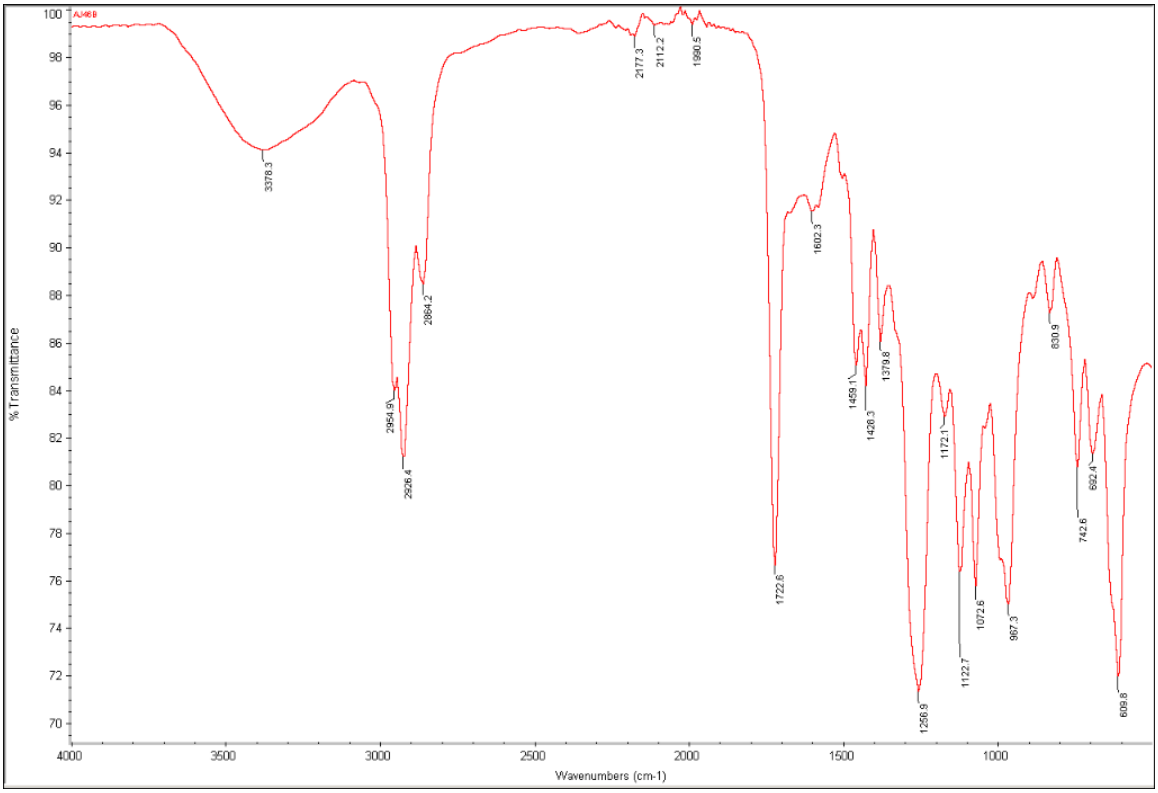

Figure 124. IR spectrum for ET cyanated with tetrabutylammonium cyanide

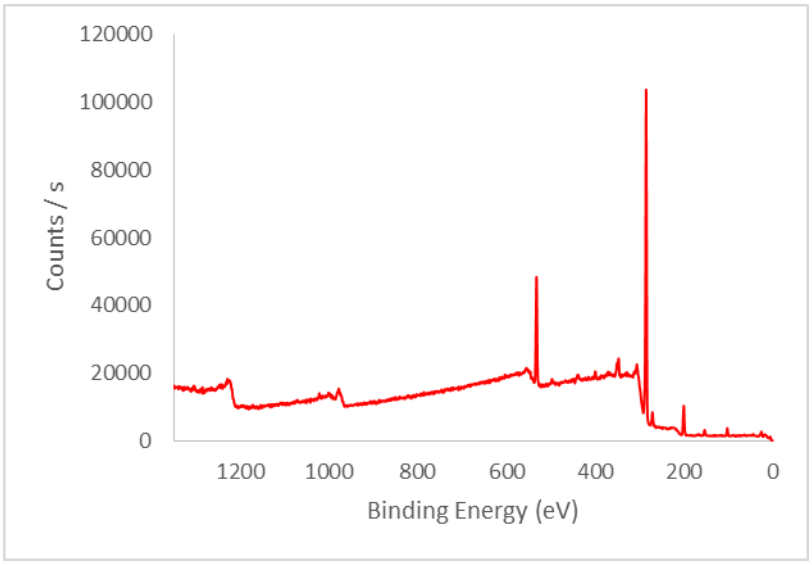

Figure 125. XPS spectrum for ET cyanated with tetrabutylammonium cyanide

Table 49. XPS integration for ET cyanated with tetrabutylammonium cyanide

Peak	Atomic %
C1s	78.95
Cl2p	3.43
O1s	11.82
N1s	1.91
Si2p	2.16
Ca2p	1.73

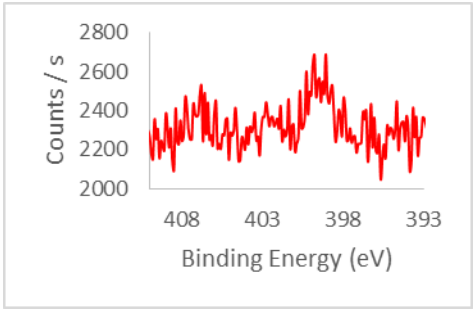

Figure 126. Nitrogen XPS for ET cyanated with tetrabutylammonium cyanide

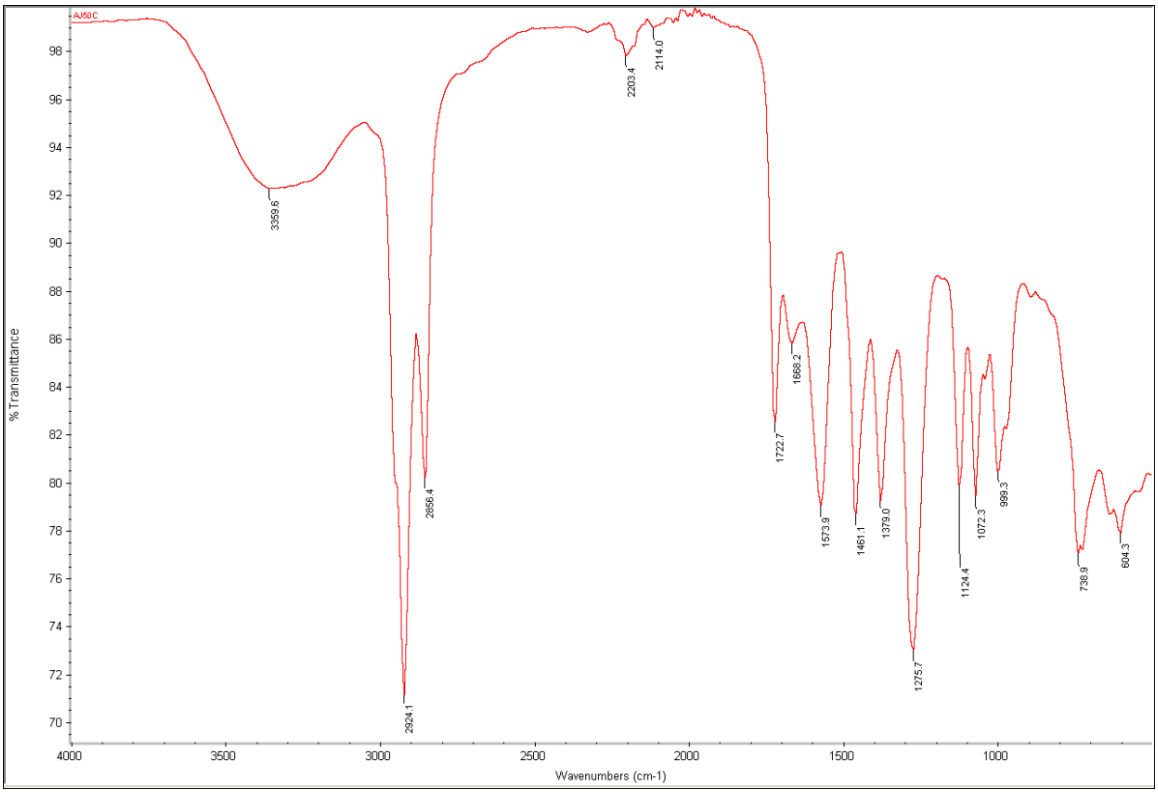

Figure 127. IR spectrum for ET cyanated with Aliquat 336

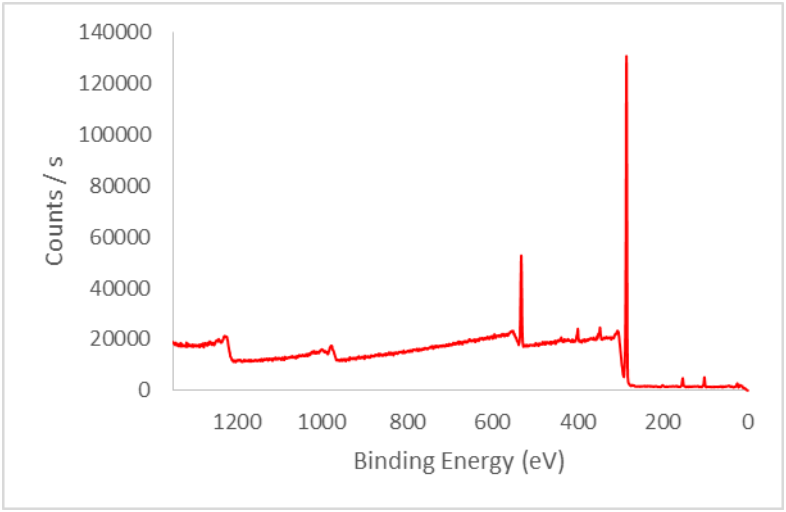

Figure 128. XPS spectrum for ET cyanated with Aliquat 336

Table 50. XPS integration for ET cyanated with Aliquat 336

Peak	Atomic %
C1s	82.29
Cl2p	0.51
O1s	10.84
N1s	3.19
Si2p	3.17

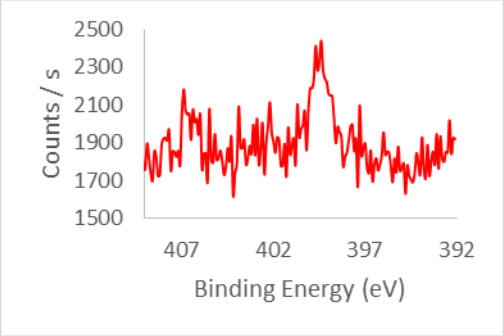

Figure 129. Nitrogen XPS spectrum for ET cyanated with Aliquat 336

Representative cyanated endotracheal tubing (prepared by reaction of pieces of tubing with 450 mM NaCN and 9 mM Aliquat® 336 at 80°C for 48h) were subjected to 485 mM sodium azide and 440 mM zinc bromide in water at 100 °C for 72 h to form 5-substituted 1*H*-tetrazoles[76] on the material surface. These samples outgassed rapidly when subjected to XPS analysis, which suggests tetrazole formation, as both azide and cyano modification to the PVC are at least somewhat tolerant of x-ray analysis for a limited number of scans.. These samples were then immersed in a solution of 360 mM potassium carbonate and 48 mM 2,3,4,5,6-pentafluorobenzyl bromide, and shaken at 80 °C overnight. After washing, IR and XPS analysis showed some evidence of covalent fluoride attachment (fluoride percentage of 19.26% via XPS integration) but the samples were very dark and

unpliable. To account for non-covalent adhesion of the perfluoro compound, a control sample was subjected to the exact same conditions except without potassium carbonate, and demonstrated a much lower fluoride percentage via XPS integration (3.62%).

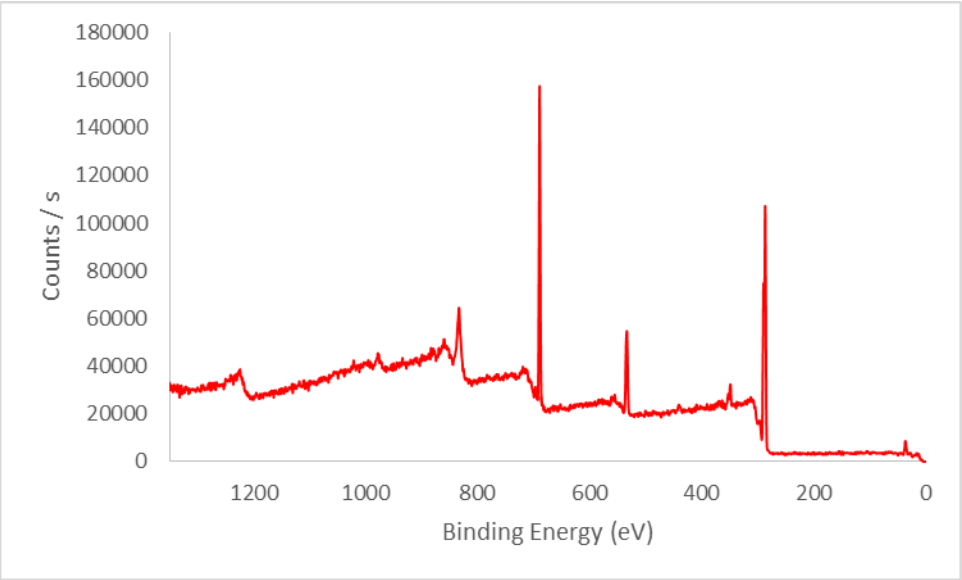

Figure 130. XPS survey spectrum for cyanated ET reacted with sodium azide and zinc bromide to form a 1*H*-tetrazole, then reacted with potassium carbonate and 2,3,4,5,6-pentafluorobenzyl bromide to make the alkylated tetrazole

Table 51. XPS integration for cyanated ET reacted with sodium azide and zinc bromide to form a 1*H*-tetrazole, then reacted with potassium carbonate and 2,3,4,5,6-pentafluorobenzyl bromide to make the alkylated tetrazole

Peak	Atomic %
C1s	69.25
F1s	19.26
O1s	9.69
Ca2p	1.80

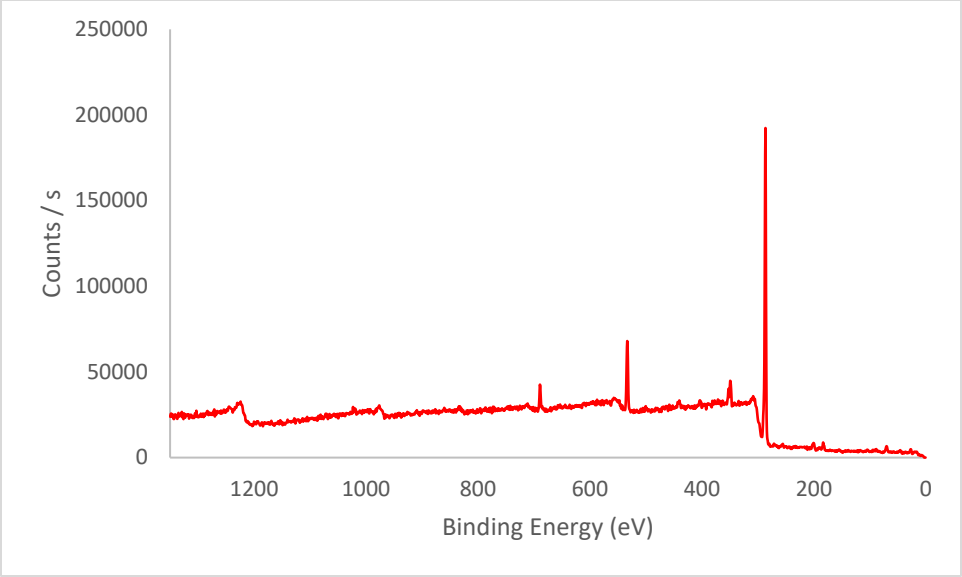

Figure 131. XPS survey spectrum for control sample, subject to the same conditions for substituted tetrazole formation but without base.

Table 52. XPS survey integration for control sample, subject to the same conditions for substituted tetrazole formation but without base.

Peak	Atomic %
C1s	83.69
F1s	3.62
O1s	9.21
Cl2p	1.20
N1s	1.44
Br3d	0.85

3.4.5 Characterization of material properties after modification

Successful attachment of new functional groups by azidation and CuAAC ligation was indicated by contact angle measurements showing increased surface hydrophilicity

after reaction with ammonium (**1**, **4**) and pegylated (**3**) alkynes, but not with perfluoroalkylamide **2**.

Table 53. Contact angle measurements for unmodified and modified ET and CT

Type of Tubing	Contact angle (degrees)	Type of Tubing	Contact angle (degrees)
ET unmodified	85.95 ± 11.3	CT unmodified	94.2 ± 10.4
ET azidated	64.2 ± 7.4	CT azidated	88.4 ± 6.0
ET cyanated	89.5 ± 1.2	CT cyanated	94.5 ± 18.9
ET post-CuAAC (PEG2000 alkyne **3**)	43.8 ± 5.8	CT post-CuAAC (PEG2000 alkyne **3**)	50.3 ± 5.8
ET post-CuAAC (perfluorinated alkyne **2**)	85.1 ± 1.0	CT post-CuAAC (perfluorinated alkyne **2**)	91.8 ± 8.1
ET post CuAAC (quaternary amine alkyne **1**)	68.6 ± 8.2	CT post CuAAC (quaternary amine alkyne **1**)	48.1 ± 7.8
ET post CuAAC (pyridinium alkyne **4**)	57.4 ± 5.8	CT post CuAAC (pyridinium alkyne **4**)	59.8 ± 16.7

Detailed thermal gravimetric, differential scanning calorimetry, and nanoindentation analysis were performed on a variety of sample. An invariant TGA trace for representative samples of each modification was observed, with the unmodified tubing showing an initial thermal transition at approximately 50°C higher temperature (310°C *vs.* 260°C).

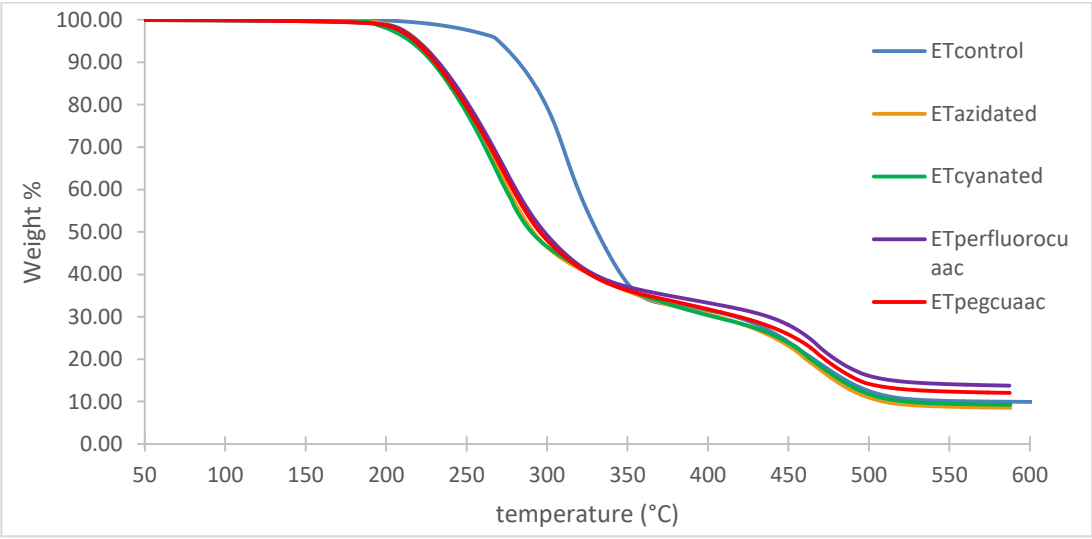

Figure 132. TGA of unmodified and modified ET

The same behavior was observed after incubation of fresh tubing with Aliquat 336 at elevated temperature, and thus probably reflects a minor change in plasticizer or water content.

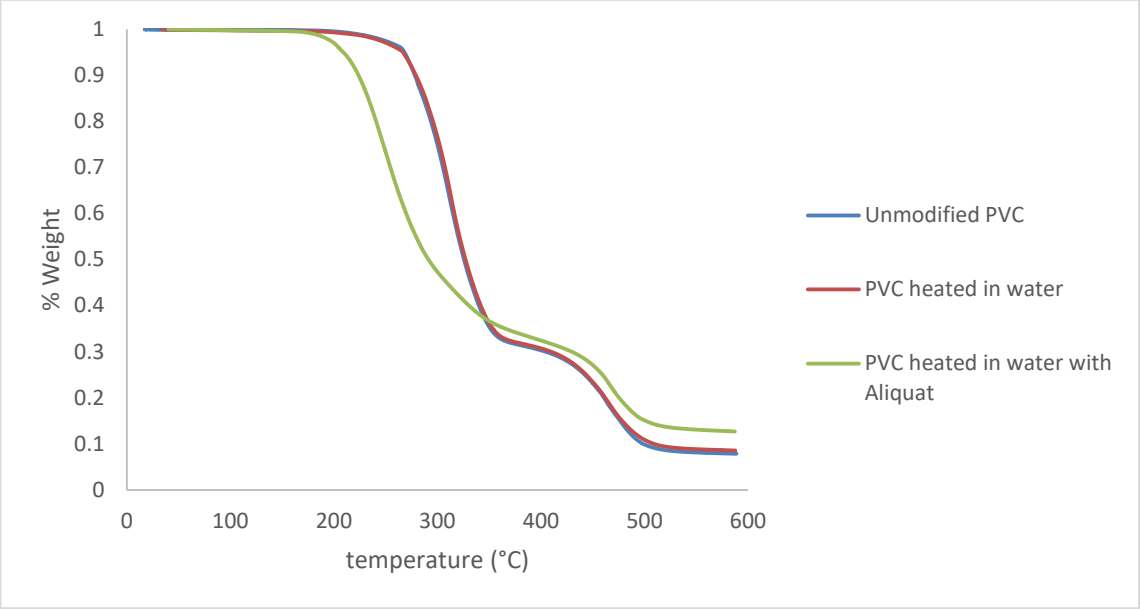

Figure 133. TGA of ET incubated in water and in water with PTC, but without presence of nucleophile

Azidation was found to be minimally disturbing to the mechanical properties of the material, giving similar values of hardness and Young's modulus as the original tubing. However, both parameters were significantly different (harder and less deformable) after CuAAC ligation, with significant differences in the magnitude of the change.

Table 54. Indentation analysis of unmodified and modified ET.

Type of Tubing	Hardness (MPa)	Young's modulus (MPa)
ET unmodified	3.8 ± 0.6	67.6 ± 9.1
ET azidated (12 h, Aliquat 336)	3.1 ± 0.8	50.4 ± 12.8
ET cyanated (72 h, Aliquat 336)	6.8 ±3.8	31.9 ±12.6
ET post CuAAC (quaternary amine alkyne **1**)	18.1 ± 5.4	164.4 ±43.6
ET post-CuAAC (perfluorinated alkyne **2**)	6.5 ± 2.0	40.0 ± 9.7
ET post-CuAAC (PEG2000 alkyne **3**)	8.9 ± 2.7	38.7 ± 8.5
ET post CuAAC (pyridinium alkyne **4**)	21.6 ± 0.8	168.3 ± 23.4

Scanning electron microscopy of endotracheal and catheter tubing showed minimal changes after azidation, and different cracked (**1**, **2**, **4**) or patterned (**3**) surface morphologies following CuAAC attachment of the different alkynes.

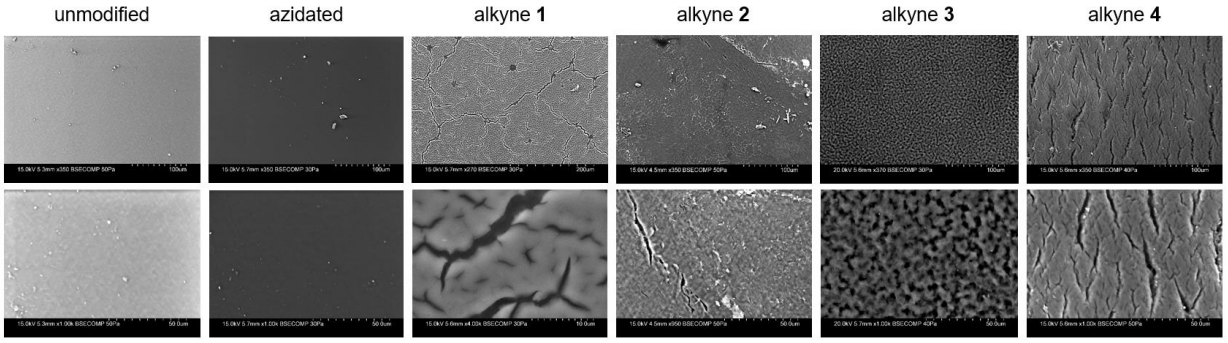

Figure 134. SEM images of endotracheal tubing after the indicated treatment. Magnification of top and bottom images: unmodified = 350x, 1000x; azidated = 350x, 1000x; CuAAC of alkyne 1 = 270x, 4000x; CuAAC of alkyne 2 = 350x, 950x; CuAAC of alkyne 3 = 370x, 1000x; CuAAC of alkyne 4 = 350x, 1000x.

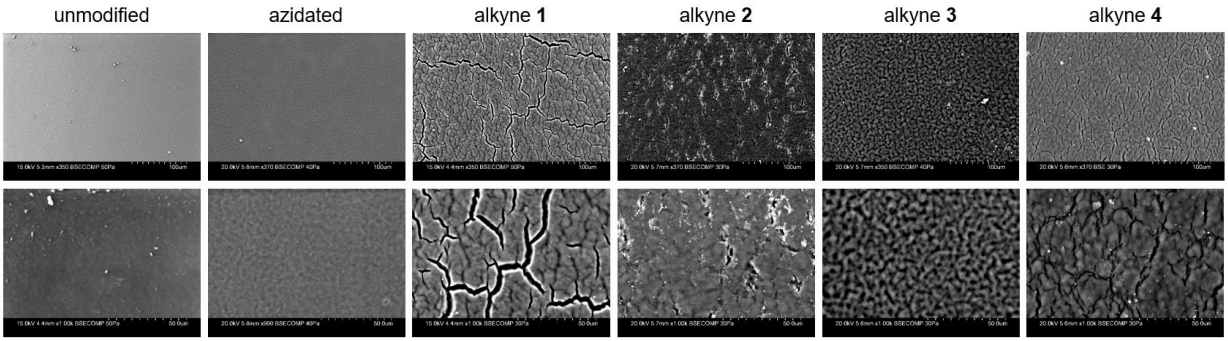

Figure 135. SEM images of catheter tubing after the indicated treatment. Magnification of top and bottom images: unmodified = 350x, 1000x; azidated = 370x, 900x; CuAAC of alkyne 1 = 350x, 1000x; CuAAC of alkyne 2 = 370x, 1000x; CuAAC of alkyne 3 = 350x, 1000x; CuAAC of alkyne 4 = 370x, 1000x.

These changes were induced only under active CuAAC conditions; for example, omission of the alkyne in the reaction mixture gave no change in surface morphology showing that the copper ion, ascorbate, and reactive oxygen species generated in air[55] do not visibly damage the azidated PVC surface.

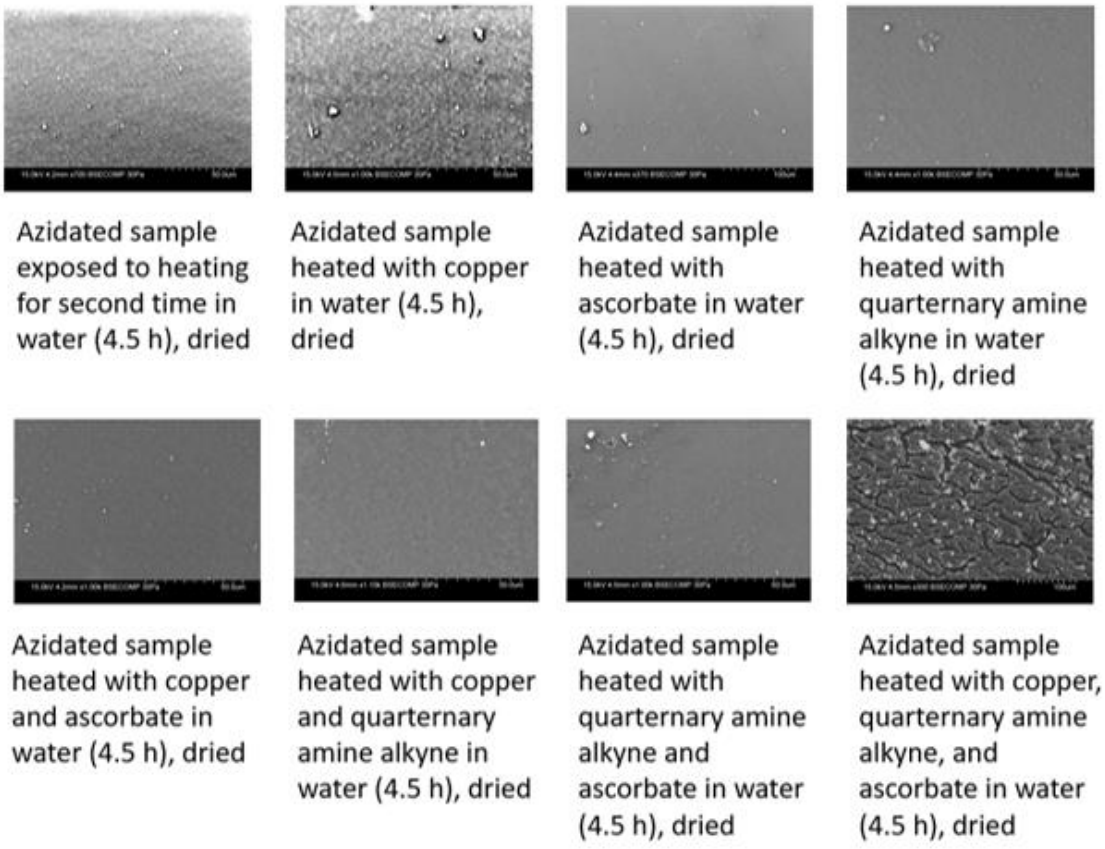

Figure 136. SEM images of ET treated with CuAAC solvents and reagents, demonstrating surface deformations are only occurring when CuAAC is transpiring.

Atomic force microscopy shows that modified surfaces appear more uniform than the original PVC, however, there is little apparent difference between the azidated and clicked surfaces, as displayed in Figure 137.

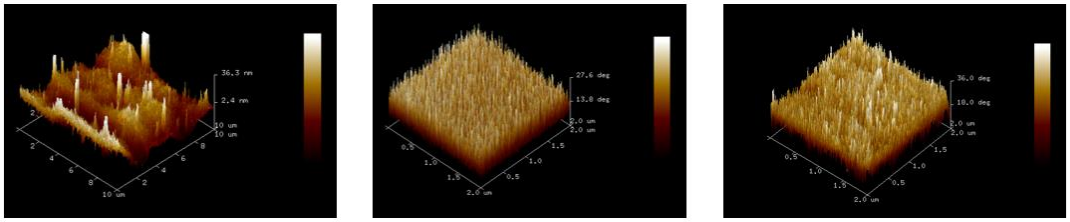

Figure 137. AFM images of the PVC surfaces for ET before and after modifications and average roughness for each surface.

3.5 Discussion

Azidation and CuAAC facilitated via a phase-transfer catalyst allows for the direct modification of flexible PVC while still maintaining key properties, including flexibility and some transparency, although with discoloration. The nature of the phase transfer catalyst itself appears to be important in its efficacy, as well as the tendency of the phase transfer catalyst to adhere to the polymer surface, only to be removed through extensive rinsing. In general, large, bulkier phase transfer catalysts conferred the most azidation, although it should be noted that for some applications, a maximal amount of azidation may not be needed (if a lower surface density of the triazole product is sufficient for the application) and use of a weaker phase transfer catalyst may be desirable if it reduces discoloration. These phase transfer catalysts also worked to facilitate the substitution of another small nucleophile, cyanide, which suggests a general applicability of this methodology to the substitution of other small nucleophiles.

CuAAC on the material surface allowed for the functionalization of the azidated PVC, however, CuAAC also conferred additional discoloration and measurably different

hardness, although the plastic remained pliably flexible. Via SEM, cracking was observed for clicked PVC, although it is suspected that this cracking may be able to be mitigated through a lower surface density of azidation and triazole formation.

3.6 Conclusion

The substitution of azide for chloride, and the subsequent addressing of the resulting organic azide groups with alkynes, have been described before by several investigators.[64,65,66,67,68,69] However, no studies have so far appeared on the modification of commercial PVC tubing, for which medical applications are particularly important and dependent on the mechanical properties of the material. Azidation and CuAAC reactions are shown here to be practical for the surface derivatization of commercial PVC tubing, with some challenges remaining in retaining flexibility and translucency. Various phase-transfer catalysts were found to give different results, suggesting that future exploration of this and other parameters may provide further improvements. X-ray photoelectron spectroscopy analysis revealed for the first time that phase-transfer-assisted azidation occurred only in the outermost thin layer of the tubing, making potential covalent immobilization of plasticizing molecules in the bulk of the material[64,65] impractical, but also suggesting that fast surface chemistry may beat the speed of plasticizer leaching. Characterization by contact angle measurement, TGA, nanoindentation, and SEM provided a good picture of the properties and surface architecture, although the density of functionalization remains to be established. Plasticizer loss was found to be a greater problem for cyano group modification, as conversion to surface alkylated tetrazoles resulted in greater loss of mechanical flexibility than triazole formation from azides. Future work to attach antimicrobial groups that could either kill bacteria or reduce their

adhesion to the plastic would make this methodology particularly relevant to a clinical setting.

3.7 Acknowledgement

This work was performed in coordination with Haley Chenot, who assisted in screening phase transfer catalysts for azidation and constructed the whole-tube azidation equipment setup, Alexander Crich who assisted in optimizing the CuAAC reaction on PVC samples, and Alexis Jacob who assisted in screening phase transfer catalysts for cyanation. This work was supported by a research partnership between Children's Healthcare of Atlanta and the Georgia Institute of Technology, by the President Undergraduate Research Award to H.C., as well as an R25 summer program in Pediatric Engineering (PERSE) award to A.C. It was performed in part at the Georgia Tech Institute for Electronics and Nanotechnology, a member of the National Nanotechnology Coordinated Infrastructure, which is supported by the National Science Foundation (Grant ECCS-1542174). We thank Dr. Zhishuai Geng and Dr. Allison G. Aioub for helpful conversations, as well as Dr. Michael Baksh, Dr. Carlos Sanhueza-Chavez, Mr. George Ward, and Mr. Brian Schmatz for experimental assistance.

CHAPTER 4. COVALENT FUNCTIONALIZATION OF SU-8 NEGATIVE PHOTORESIST VIA COPPER(I) CATALYZED AZIDE ALKYNE CYCLOADDITION

4.1 Abstract

SU-8 negative photoresist is a polymer used primarily for electronics and microelectromechanical systems. In recent years, there has been great interest in making use of remaining epoxide functionality to chemically modify SU-8; click chemistry could provide a facile means to create diverse functionality on SU-8. SU-8 photoresist was photocrosslinked and patterned with an easily constructed lab setup of a hot plate, a vacuum oven, and a handheld UV lamp. Subsequently, the SU-8 surface was azidated and underwent CuAAC with a variety of alkynes. By clicking an ATRP initiator to the SU-8 surface and subjecting the sample to ATRP conditions, polymerization was attempted from the polymer surface and some evidence of this polymerization was observed. The SU-8 surface was rendered cytotoxic toward *E. coli* DH5α cells by clicking on a basic quaternary ammonium alkyne. Gram-positive *S. aureus* bacteria, cultured CHO cells and erythrocytes showed no ill effects upon exposure to this material. This work opens up the SU-8 polymer to many potential applications enabled by the CuAAC reaction.

4.2 Introduction to SU-8 negative photoresist

SU-8 is a highly-crosslinked high-aspect-ratio negative photoresist reported in 1989 by IBM, which results from the polymerization of bisphenol A glycidyl ether

novolac.[77] SU-8 solutions are comprised of the SU-8 monomer, a photoinitiator (triarylsulfonium hexafluoroantimonate salts), and a solvent (usually either gamma-butyrolactone or cyclopentanone). The SU-8 polymer is biocompatible,[78,79] thermally stable,[80] chemically resistant, and has high transparency above 360 nm.[81] Its applications thus far have largely been for microelectromechanical and microfluidic systems.

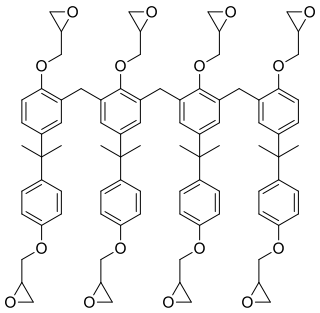

Figure 138. SU-8 monomer.

A number of approaches have been taken to chemically modify SU-8 through unreacted epoxides following polymerization and these approaches are summarized in Figure 139. These modifications include polymerization directly from the SU-8 surface,[82] amination,[83,84,85,86,87] acid-catalyzed epoxide ring opening and subsequent reaction.[88,89,90,91,92,93]

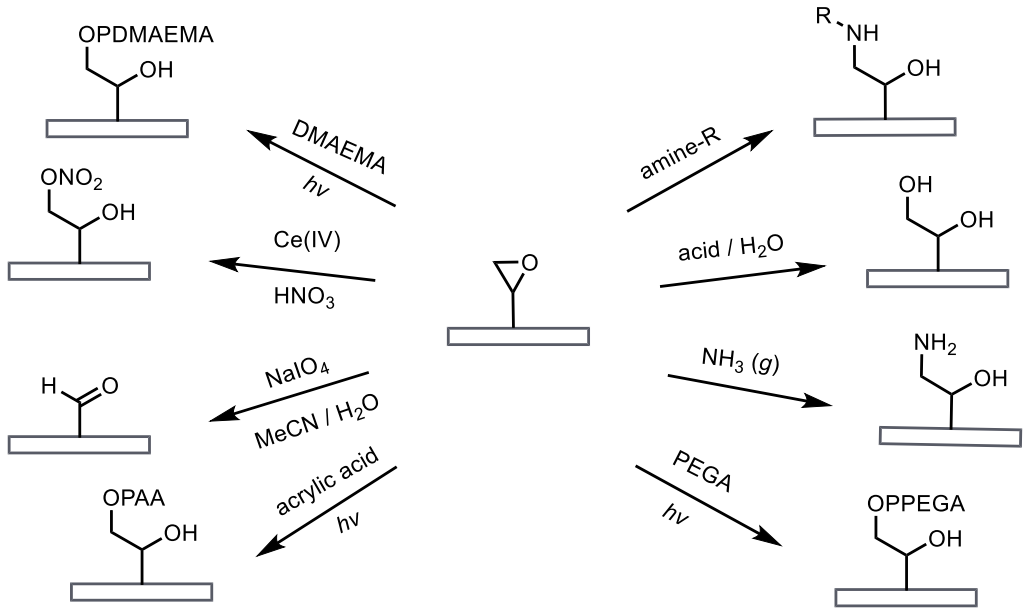

Figure 139. Summary of previous SU-8 chemical modifications.

Azides have been incorporated into SU-8 previously only through the incorporation of an azide-functionalized epoxide monomer,[29] however this incorporation reduces the number of potential crosslinks within the material and could impact SU-8 polymer mechanical and structural properties. Instead, a means to introduce azide functionality after polymerization is desirable. Azide nucleophilic attack at epoxides is an old and highly reliable procedure, which is summarized in Figure 140.[94,95,96,97] Here I describe the use of this reaction on photocrosslinked SU-8 and subsequent derivatization of the resulting surface-tethered organic azides.

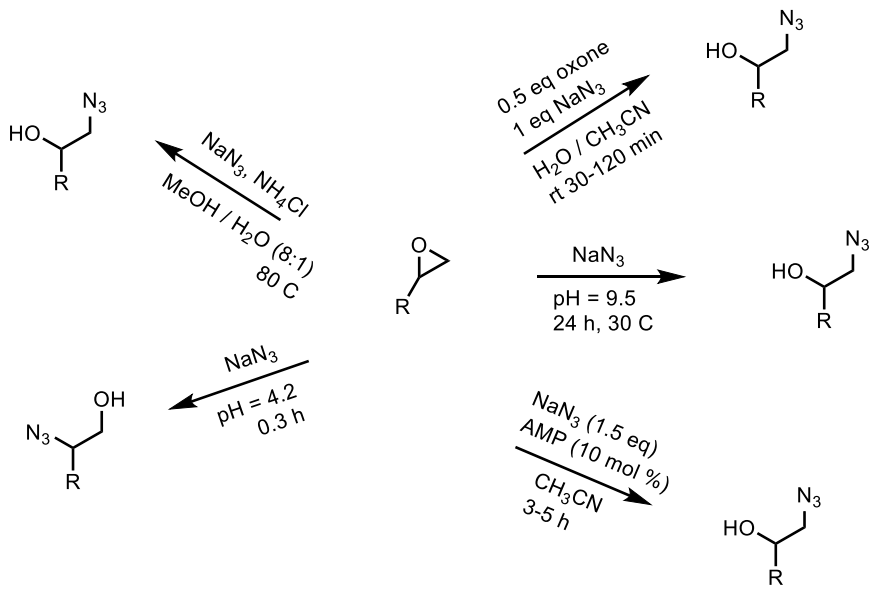

Figure 140. Summary of azide nucleophilic attack at epoxides from the literature.

4.3 Experimental

4.3.1 Printed photomasking

Photomasks were designed on a computer and printed onto transparency paper, such that areas to be crosslinked had no ink, whereas areas to be without SU-8 material were entirely covered by layers of ink. These printed photomasks facilitated photolithography without the need to spincoat the SU-8 sample onto a surface for photomasking. Designs produced included Georgia Tech logos as well as grid patterns. Examples of resultant SU-8 polymers made from the negative photomask are shown in Figure 141.

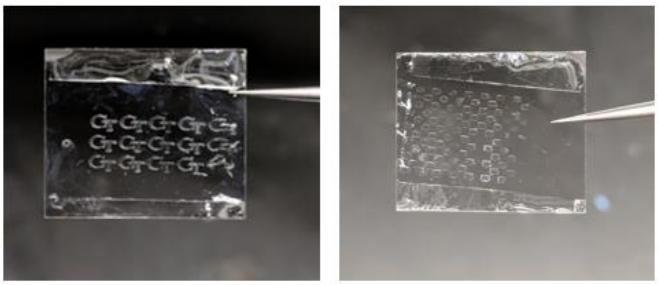

Figure 141. Examples of photomasked SU-8 patterns.

4.3.2 Alkyne synthesis

Unless otherwise noted, all reagents were purchased from commercial suppliers. Trimethylprop-2-yn-1-aminium iodide (referred to as quaternary ammonium or QA hereafter) was synthesized as described in Section 3.3.6.1. Propargyl 2-bromo-2-methylpropionamide was synthesized as described by Xu, Yuddin, and Yei.[98]

4.3.3 XPS measurements

X-ray photoelectron spectroscopy (XPS) was performed using a Thermo Scientific K-Alpha XPS with a monochromated Al Kα source, hemispherical analyzer, and multichannel detector. Spectra were taken by normal emission, with analysis chamber pressure below 10^{-6} mbar with flood gun on and a spot size of 200 μm. Survey scans were carried out as the average of 4 scans over the 0 to 1350 eV binding energy range with a 1.0 eV step size, a 50 ms dwell time, and an analyzer pass energy of 200 eV. High resolution scans of the N1s region (392-410 eV) were performed for samples that showed N1s content in the survey scan; these high resolution scans were carried out as the average of 4 scans over the range with a 0.1 eV step size, a dwell time of 50 ms, and an analyzer pass energy

set to 50 eV. As azides are known to degrade over time under x-ray exposure,[15] survey measurements of nitrogen content were made in a location adjacent to other measurement areas on the same sample. Similarly, high resolution scans of the Br3d region (62-74 eV) were performed for samples that showed Br3d content in the survey scan; these high resolution scans were carried out as the average of 8 scans over the range with a 0.1 eV step size.

4.3.4 SEM

Scanning electron microscope (SEM) images were taken on a Hitachi S-3700N Variable Pressure SEM. Samples were thinly sliced and adhered to the sample plate, with a copper tape bridge between the surface of the material and the plate to reduce sample charging. Depending on the conditions used, some samples showed evidence of degradation over time during the SEM process in the area that the electron beam analyzed; variations in conditions used across samples were used to minimize this degradation. The majority of samples were run at 15 kV at 70 Pa or less of vacuum.

4.3.5 Atomic Force Microscopy (AFM)

Atomic Force Microscopy was performed on a Veeco Dimension 3100 AFM with a 40N/m, 300kHz, symmetric tip.

4.3.6 Contact angle measurements

Contact angle measurements and images were taken on a ramé-hart standard goniometer.

4.3.7 Bacterial Culture and Growth

E. coli DH5α were grown from a frozen glycerol stock in sterile LB. Bacteria were grown to confluence overnight, spun down and resuspended in an equal volume Dulbecco's phosphate buffered saline (PBS) without calcium and magnesium. This was diluted by a factor of 10 and mixed with Sytox Red at a concentration of 1 μL / mL. Then, 600 μL of this was applied directly to the substrate surface.

S. aureus Xen 29 were grown from a frozen glycerol stock in sterile LB with 100 μL / mL kanamycin. Bacteria were grown to confluence overnight, spun down and resuspended in an equal volume of Dulbecco's PBS without calcium and magnesium. This was diluted by a factor of 10 and mixed with Sytox Red at a concentration of 1 μL / mL. Then, 600 μL of this was applied directly to the substrate surface.

4.3.8 Red blood cell isolation

Freshly drawn whole human blood (with EDTA) (3 mL) was spun down at 150xg for 15 minutes without breaking. The plasma and buffy coat layers were removed and the red blood cells were washed thrice with sterile PBS (with 1.5 mg / mL EDTA), inverting gently each time to mix and spinning down at 150xg for 15 minutes. From the red blood cell concentrate, 8 μL was added gently to 40 mL of PBS with EDTA and was gently mixed. This dilute solution was used for incubation studies within five hours of the blood being drawn from the donor. For incubation, 5 mL of the dilute solution was used to cover SU-8 substrates in 6-well flat bottomed dishes, and was left undisturbed for 1 hour at room temperature.

4.3.9 Chinese Hamster Ovary (CHO) cell growth

CHO cells, obtained from ATCC, were cultured in Dulbecco's Modified Eagle Medium (DMEM), supplemented with pen/strep, sodium pyruvate and glutamax-1 (all three at 1X final concentration), and 10% FBS. For microscopy, cells in the supplemented DMEM were deposited onto SU-8 substrates in 6-well flat bottom dishes and grown for 24 hours at 37° C and 5% CO_2.

4.3.10 Microscopy

Microscope images were taken on a Nikon Ti-U inverted microscope. Images were processed with ImageJ software.

4.3.11 Fluorescence quantitation

The fluorescence intensity per unit area was calculated in ImageJ software by tracing the polymer edge and comparing this intensity on the polymer to the intensity per unit area off the polymer.

4.3.12 Methyl Methacrylate (MMA) Polymerization from the SU-8 surface

To polymerize methyl methacrylate (MMA) from the surface, similar to the literature procedure of Xu et. al.,[98] MMA monomer (1.69 mL, 15.9 mmol) and copper(I) bromide (22 mg, 0.15 mmol) were combined in isopropyl alcohol (15 mL). Argon was bubbled through the solution for 10 minutes. Tris[2-(dimethylamino)ethyl]amine (Me_6-TREN) (48 μL, 0.3 mmol) was added to the solution and stirred for 20 minutes. The substrate with attached clickable intiator was then added and shaken gently on an orbital

shaker for 10 minutes at 80 °C. Finally, sodium ascorbate (30 mg, 0.15 mmol) was added and the solution was shaken gently on an orbital shaker at 80 °C for 4 hours. After 4 hours, the sample had detached from the surface. Sample was rinsed with water and methanol, and immersed in 0.1 M EDTA for approximately 2 minutes. This was then rinsed again with water and methanol.

4.3.13 4-Vinylpyridine Polymerization from the SU-8 surface

To polymerize 4-vinylpyridine (4VP) from the surface, similar to the method described by Tsarevsky et. al.,[99] 4-vinylpyridine (1.5 mL, 13.9 mmol) was dissolved in 15 mL of a 1:1 methanol / water mixture. Argon was bubbled through the solution for 10 minutes. Copper(I) bromide (22 mg, 0.153 mmol), tris(2-pyridylmethyl)amine (80 mg, 0.276 mmol), and sodium ascorbate (20 mg, 0.101 mmol) were added gently shaken. The substrate with attached clickable initiator was then added and the container blanketed with argon and sealed. The solution was gently shaken on an orbital shaker for 12 hours at 30 °C. Upon removal of sample from solution, a color change was noted (clear / white to brown). The sample was rinsed with methanol and water, then submerged in a 0.1 M EDTA solution for approximately 15 minutes.

4.4 Results

4.4.1 Azidation of SU-8

Several procedures exist in the literature for epoxide ring opening with azides, as detailed in Section 4.2, although these have not yet been applied to the unreacted epoxides present on the surface of the SU-8 polymer. Azidation was attempted with several of these.

For each sample, SU-8 polymer was deposited as small drops onto a glass coverslip. A stream of argon gas was used to spread the SU-8 solution across the coverslip surface into a thin layer. This was exposed to long-wavelength UV light for 30 minutes, then dried in a vacuum oven overnight. Azidation conditions attempted are detailed in Table 55. Following exposure to the conditions listed in the table, all samples were rinsed, then dried in a vacuum oven.

Table 55. Azidation conditions screened for azidating SU-8 substrates.

Conditions	Outcome
480 mM NaN_3 (1 eq) 240 mM oxone (0.5 eq) 8 mL H_2O / MeCN (1:9) Shaken on shaker plate Stopped at 3 hours	No clear and distinct azidation as determined by both survey and nitrogen region XPS scans
480 mM NaN_3 (1 eq) 240 mM oxone (0.5 eq) 20 mM TBAB (0.04 eq) 8 mL H_2O / MeCN (1:9) Shaken on shaker plate Stopped at 3 hours	Azidation evident via XPS survey (2.5% N) and nitrogen scans
480 mM NaN_3 8 mL pH 9 phosphate buffer Shaken on shaker plate Stopped at 3 hours	Not clear if azidation had occurred from XPS survey (1.7% N) and nitrogen scans
480 mM NaN_3 (1 eq) 240 mM NH_4Cl (0.5 eq) 8 mL of MeOH / H_2O (8:1) Heated to 80°C for 3 hours while shaking on shaker plate	Sample detached from glass surface. Clear azidation had occurred from XPS survey (> 5% N) and nitrogen scans

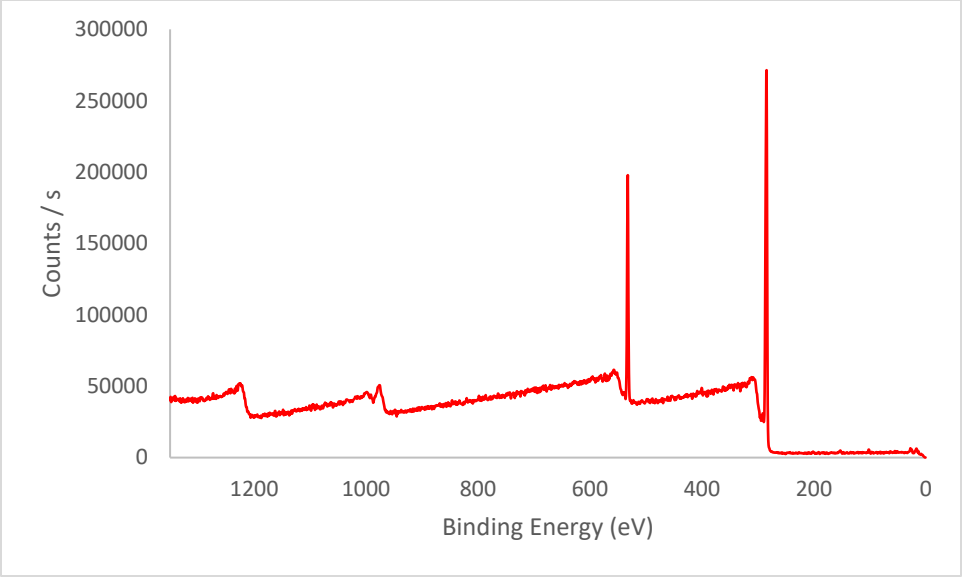

Figure 142. XPS spectrum for SU-8 sample treated to azidation conditions of 480 mM NaN_3 and 240 mM oxone in 8 mL of water / acetonitrile (1:9) for 3 hours.

Table 56. XPS integration table for SU-8 samples treated to azidation conditions of 480 mM NaN_3 and 240 mM oxone in 8 mL of water / acetonitrile (1:9) for 3 hours.

Peak	Atomic %
C1s	82.06
O1s	16.88
N1s	0
Si2p	1.06

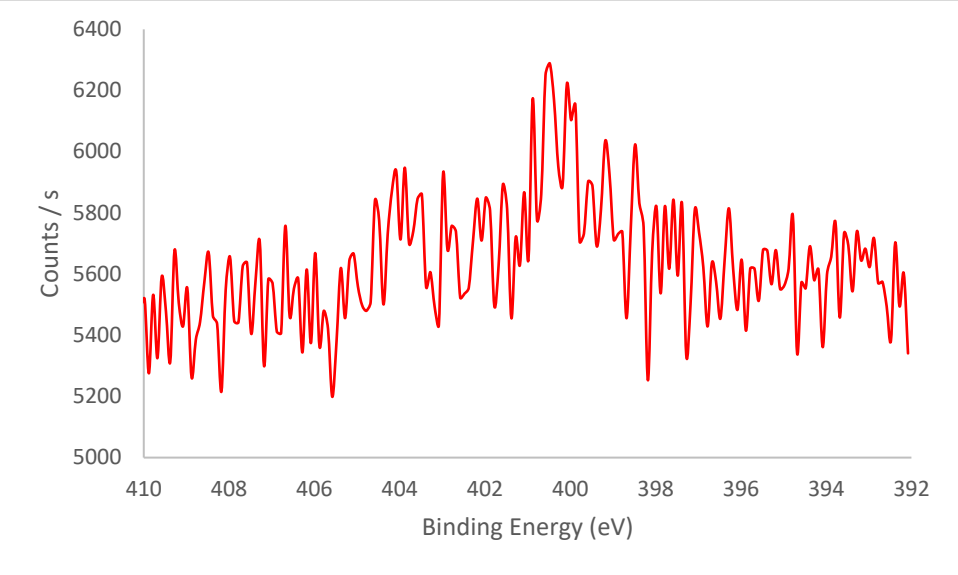

Figure 143. XPS nitrogen spectrum for SU-8 samples treated to azidation conditions of 480 mM NaN_3 and 240 mM oxone in 8 mL of water / acetonitrile (1:9) for 3 hours.

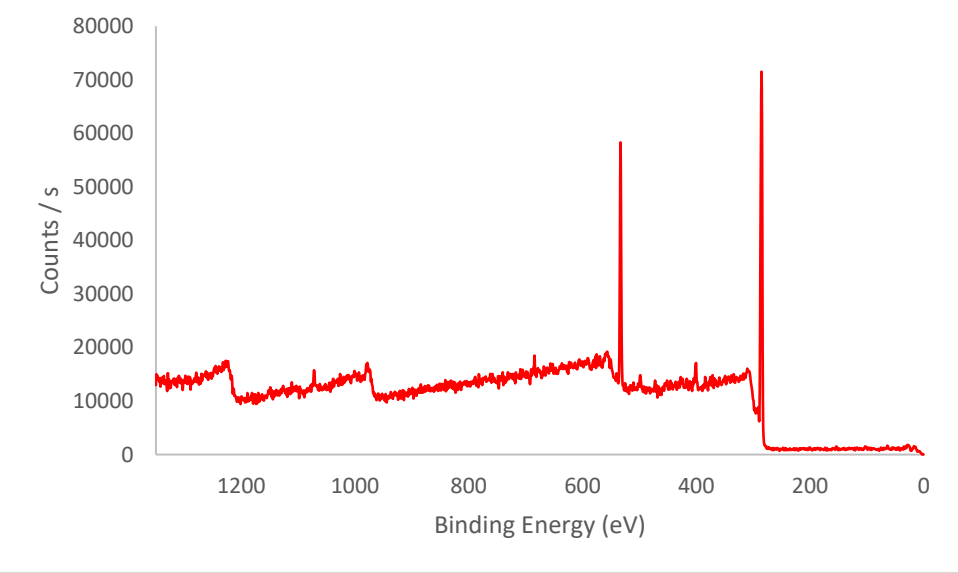

Figure 144. XPS spectrum for SU-8 samples treated to azidation conditions of 480 mM NaN_3, 240 mM oxone, and 20 mM TBAB in 8 mL of water / acetonitrile (1:9) for 3 hours.

Table 57. XPS integration table for SU-8 samples treated to azidation conditions of 480 mM NaN_3, 240 mM oxone, and 20 mM TBAB in 8 mL of water / acetonitrile (1:9) for 3 hours.

Peak	Atomic %
C1s	79.81
O1s	17.69
N1s	2.50

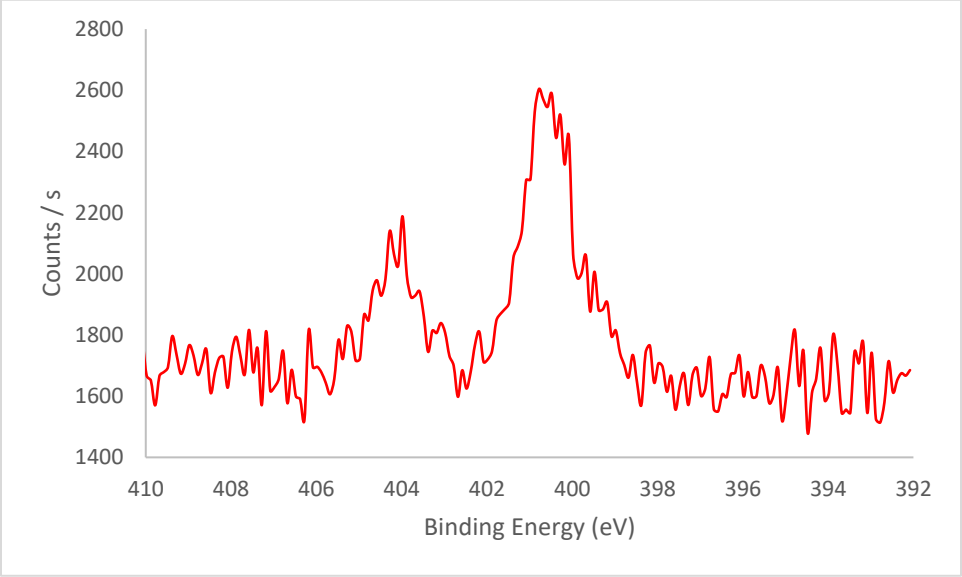

Figure 145. XPS nitrogen spectrum for for SU-8 samples treated to azidation conditions of 480 mM NaN_3, 240 mM oxone, and 20 mM TBAB in 8 mL of water / acetonitrile (1:9) for 3 hours.

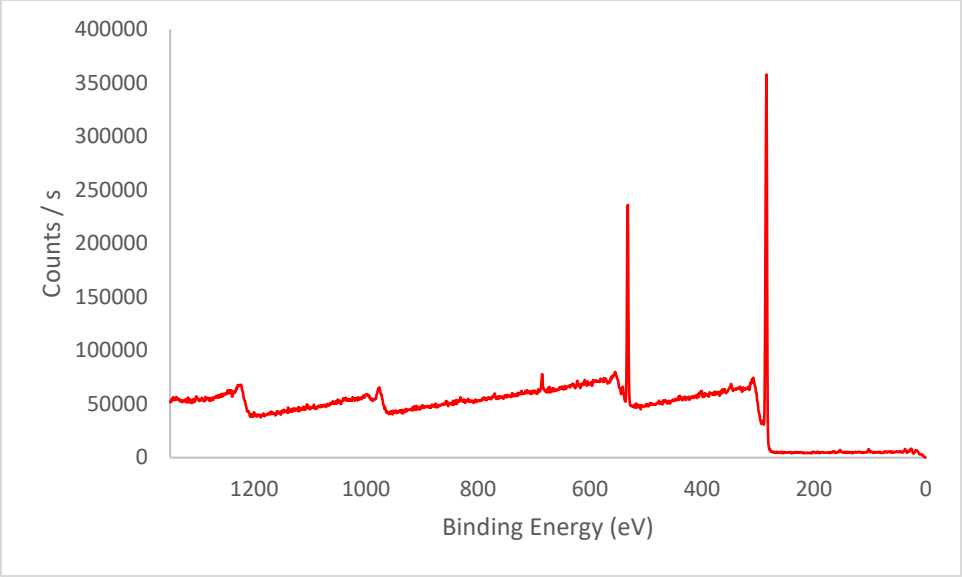

Figure 146. XPS spectrum for SU-8 samples treated to azidation conditions of 480 mM NaN_3 in pH = 9 sodium phosphate buffer.

Table 58. XPS integration table for SU-8 samples treated to azidation conditions of 480 mM NaN_3 in pH = 9 sodium phosphate buffer. (Note: Starred peaks were integrated by the XPS software, although at the particular peak, the instrument was unable to discern between noise in the signal and an actual peak.)

Peak	Atomic %
C1s	78.78
O1s	16.24
N1s*	1.7
Si2p*	1.01
F1s*	1.74
Ca2p*	0.53

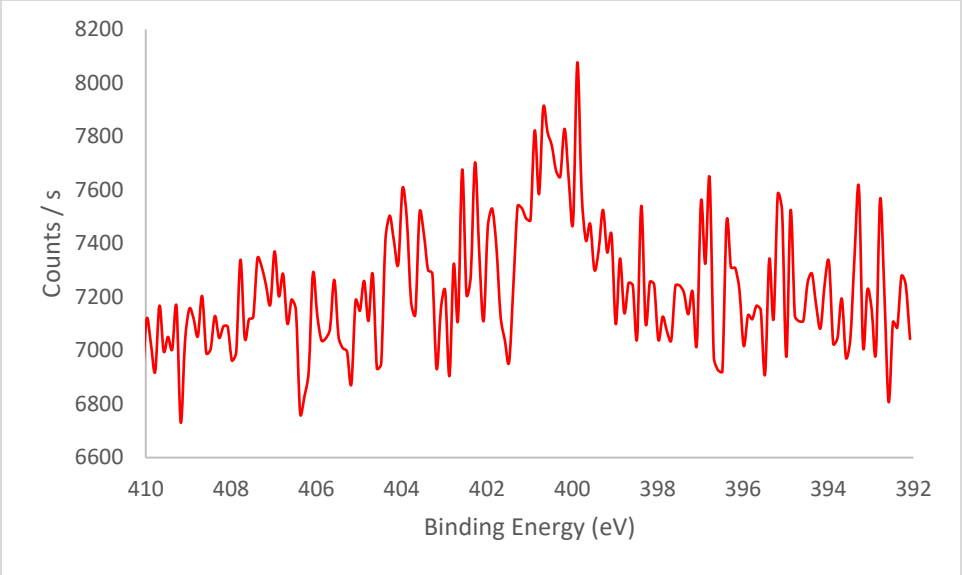

Figure 147. XPS nitrogen spectrum for SU-8 samples treated to azidation conditions of 480 mM NaN_3 in pH = 9 sodium phosphate buffer.

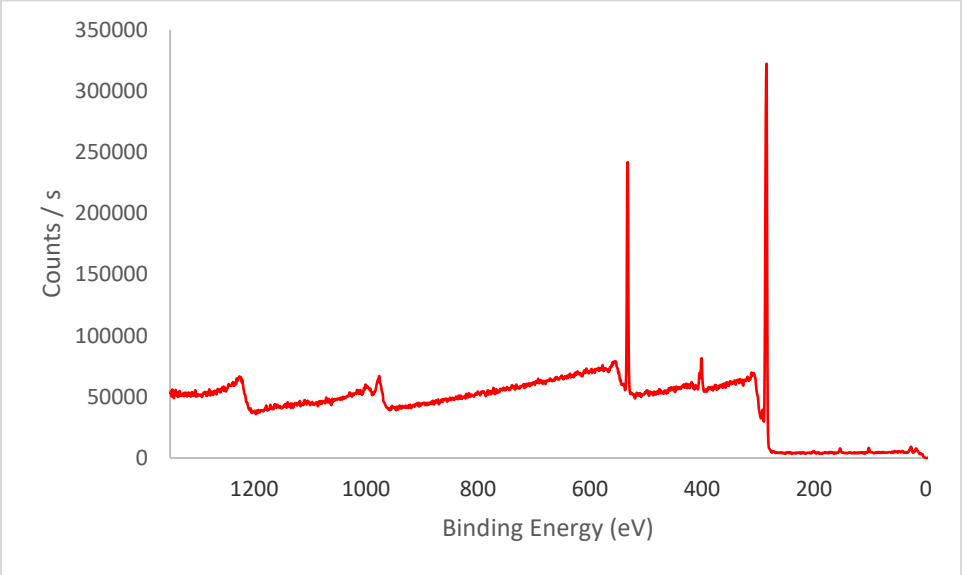

Figure 148. XPS spectrum for SU-8 samples treated to 480 mM NaN_3 and 240 mM NH_4Cl in 8 mL of methanol / water (8:1).

Table 59. XPS survey integration for SU-8 samples treated to 480 mM NaN_3 and 240 mM NH_4Cl in 8 mL of methanol / water (8:1).

Peak	Atomic %
C1s	77.35
O1s	16.01
N1s	5.16
Si2p	1.48

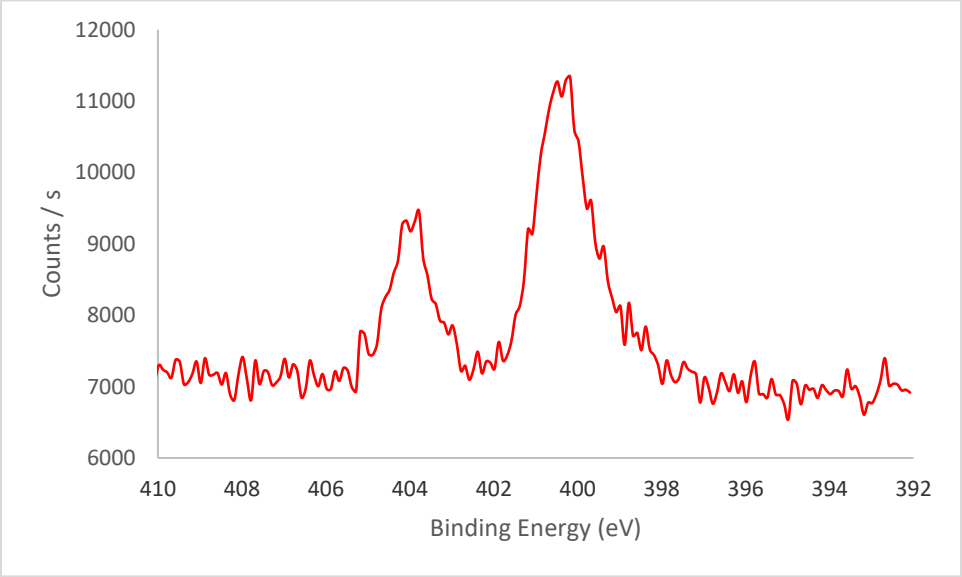

Figure 149. XPS nitrogen spectrum for SU-8 samples 480 mM NaN_3 and 240 mM NH_4Cl in 8 mL of methanol / water (8:1).

This screening demonstrates the successful azidation of SU-8 by more than one means, however, the route which azidated with sodium azide and ammonium chloride was selected for further optimization and consideration.

4.4.1.1 Optimized Deposition and Azidation

Based on initial screening, azidation was most readily achieved with the SU-8 substrate using sodium azide and ammonium chloride, and was later optimized to a

standard protocol to address detachment issues, which is detailed as follows: Indium-tin-oxide (ITO) coated glass (1.5 mm thickness) was etched with argon plasma, then baked for 5 minutes at 95 °C on a hot plate. SU-8 was deposited onto the ITO coated glass. A glass cover slip was used to spread the SU-8 into a thin layer on the ITO glass. This was baked in a vacuum oven at 65°C for 5 minutes, then exposed to long-wave UV light for 10 minutes (under a standard lab TLC analysis lamp secured to the roof of a cardboard box, so as to provide a dark environment otherwise) through the printed photomask detailed in Section 4.3.1. The coated glass was placed on a 95 °C hot place for 3 minutes, then swirled in the SU-8 developer, 1-methoxy-2-propylacetate, which removed uncrosslinked monomer from the glass surface, while leaving cross-linked polymer intact. Samples were rinsed with isopropyl alcohol, placed on the 95 °C hot plate for 2 minutes, then dried in the 65°C vacuum oven for 30 minutes. (Note: In general SU-8 polymers produced by this method exhibited clear features for patterns, particular at the center of the slide, however, at times the edges of the polymerized surface appeared slightly distorted following development, which suggests poor crosslinking at this area. This was remedied through a slightly longer crosslinking time and shortening the distance between the sample and the long-wave UV source; the distance used for most samples was approximately 5 inches.)

The samples were then immersed in a solution comprised of 460 mg of sodium azide (final concentration 0.26 M) and 375 mg of ammonium chloride (final concentration 0.26 M) dissolved in a methanol / water mixture (8:1, 24 mL and 3 mL) and, then heated to 60 °C for 30 minutes while gently shaking on an orbital shaker. These samples were rinsed thoroughly with water and methanol, then immediately dried. (Note: Leaving samples to

air-dry rather than drying immediately with a KimWipe resulted in greater detachment of the polymer from the ITO surface).

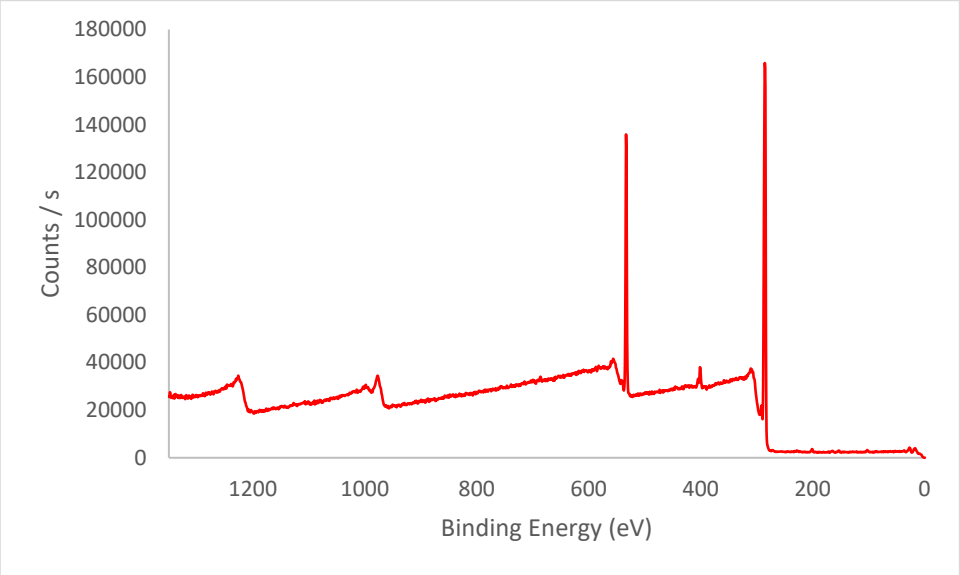

Figure 150. XPS spectrum for azidated SU-8 prepared through the optimized deposition and azidation.

Table 60. XPS integration for azidated SU-8 prepared through the optimized deposition and azidation

Peak	Atomic %
C1s	80.26
O1s	16.61
N1s	3.14

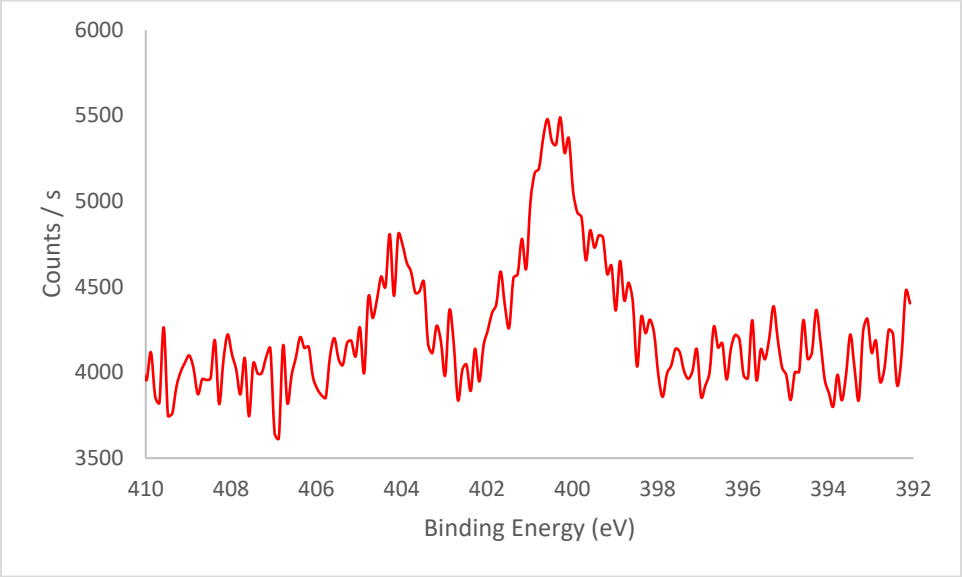

Figure 151. XPS nitrogen spectrum for azidated SU-8 prepared through the optimized deposition and azidation.

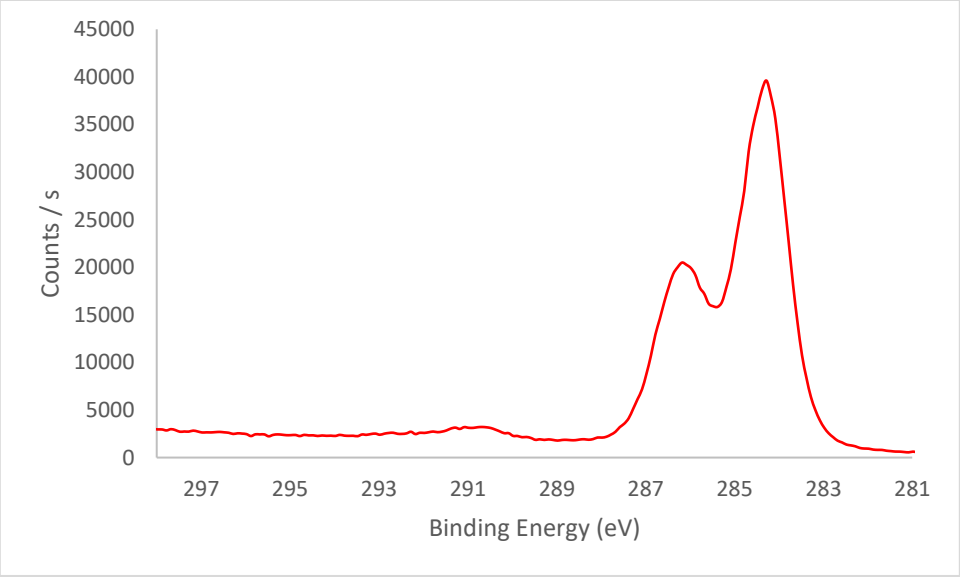

Figure 152. XPS carbon spectrum for azidated SU-8 prepared through the optimized deposition and azidation.

4.4.2 CuAAC on azidated SU-8 substrates

A number of different alkyne substrates were attached to the SU-8, including a quaternary ammonium cation, propargyl alcohol, TAMRA-alkyne dye, and an ATRP initiator that was then subject to subsequent graft-from ATRP conditions with methyl methacrylate and 4-vinyl pyridine. These alkynes, and the subsequent reactions (if any) were chosen to demonstrate the wide array of functionality that could be conferred to the SU-8 by functionalizing with CuAAC.

4.4.2.1 CuAAC of Quaternary Ammonium Cation onto SU-8 surface

To attach trimethylprop-2-yn-1-aminium iodide to the SU-8 surface via CuAAC, 20 mg of the quaternary ammonium salt, 44 mg of copper sulfate, and 160 mg sodium ascorbate were dissolved in 20 mL water. The azidated SU-8 substrate was then submerged in the solution and shaken gently for 2 hours at room temperature on an orbital shaker plate. The sample was then removed and rinsed with water and methanol, then submerged for 15 minutes in a 0.1 M EDTA solution. The sample was then rinsed with water and methanol and was immediately dried.

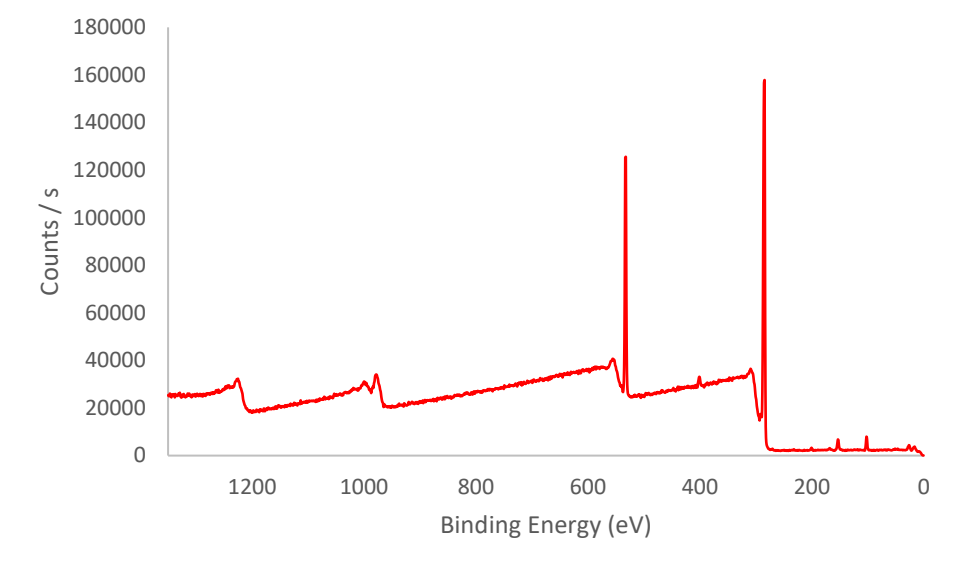

Figure 153. XPS spectrum for azidated SU-8 subject to CuAAC with trimethylprop-2-yn-1-aminium iodide.

Table 61. XPS integration for azidated SU-8 subject to CuAAC with trimethylprop-2-yn-1-aminium iodide.

Peak	Atomic %
C1s	77.19
O1s	18.1
N1s	2.27
Si2p	2.45

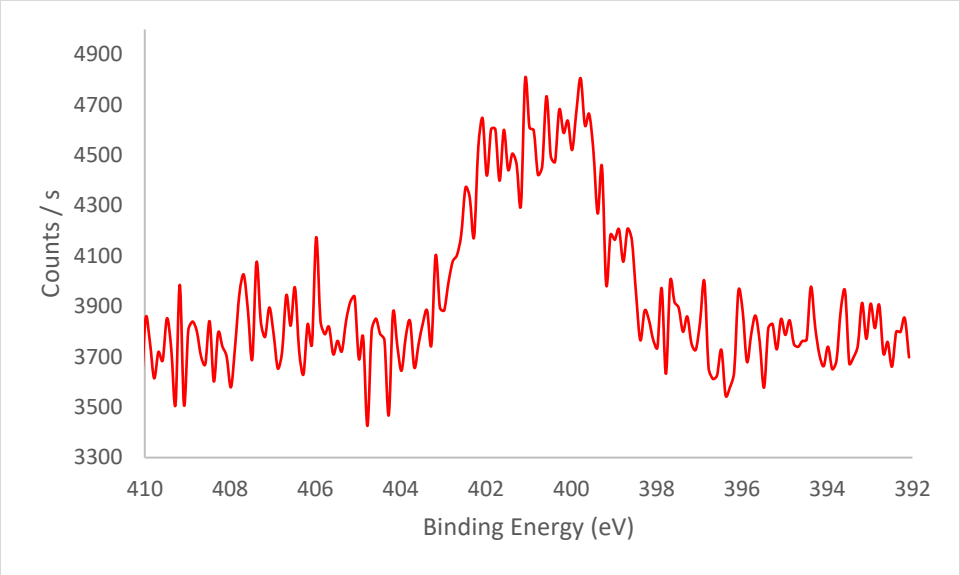

Figure 154. XPS nitrogen spectrum for azidated SU-8 subject to CuAAC with trimethylprop-2-yn-1-aminium iodide.

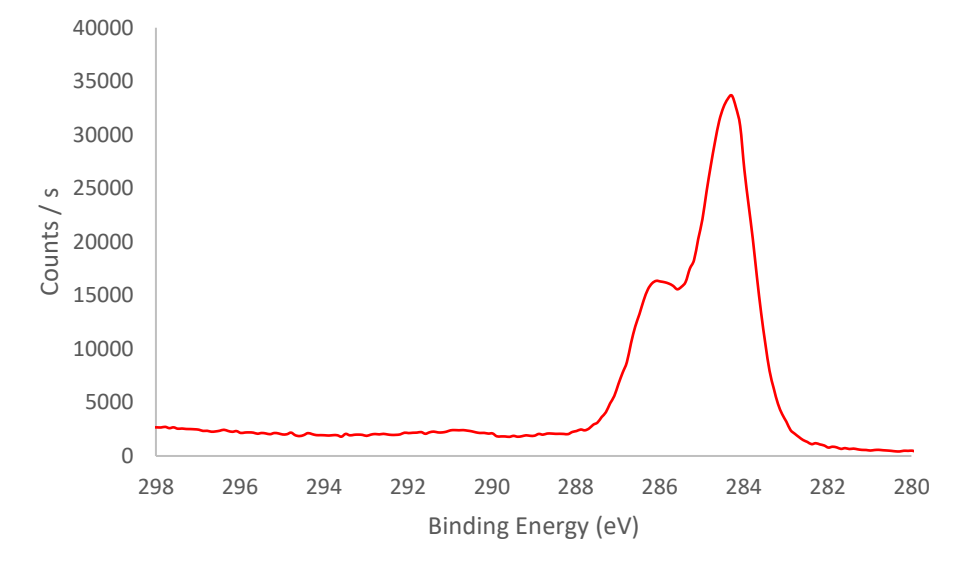

Figure 155. XPS carbon spectrum for azidated SU-8 subject to CuAAC with trimethylprop-2-yn-1-aminium iodide.

4.4.2.2 CuAAC of Propargyl Alcohol ono the SU-8 surface

Propargyl alcohol (PA) (200 µL, 3.47 mmol) was clicked onto azidated SU-8 with copper sulfate (22 mg, 0.14 mmol), sodium ascorbate (160 mg, 0.81 mmol), and tetrabutylammonium bromide (10 mg, 0.03 mmol) in 20 mL water. This was reacted for 2 hours at room temperature while shaking gently on an orbital shaker, rinsed thoroughly with water and methanol, rinsed in 0.1 M EDTA, and rinsed again with water and methanol. This was dried immediately and was analyzed via XPS.

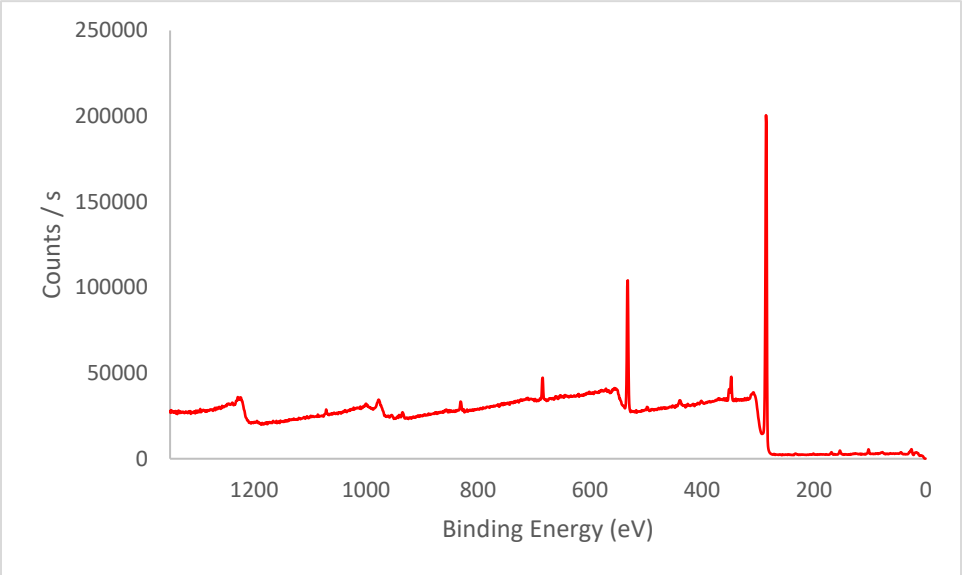

Figure 156. XPS survey spectrum for azidated SU-8 clicked with propargyl alcohol.

Table 62. XPS survey integration for azidated SU-8 clicked with propargyl alcohol.

Peak	Atomic %
C1s	83.37
O1s	13.92
N1s	0.72
Na1s	0.28

Ca2p	0.55
Si2p	1.17

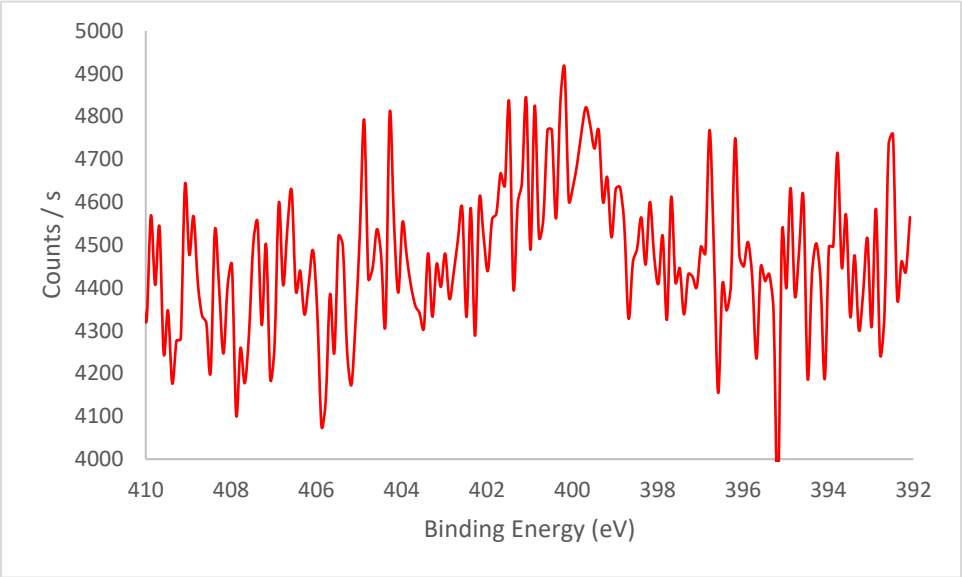

Figure 157. Nitrogen XPS scan for azidated SU-8 clicked with propargyl alcohol.

4.4.2.3 CuAAC of TAMRA-alkyne onto SU-8 surface

To attach a TAMRA-alkyne to the SU-8 surface via CuAAC, 10 µL of the alkyne dye at 1.67 mg / mL in ethanol, 2 mg copper sulfate, and 8 mg of sodium ascorbate were dissolved in 15 mL water. To this, an azidated substrate was added. This was protected from light by wrapping the containers in aluminum foil and shaken gently at room temperature for 2 hours. The substrate was removed from the solution, and rinsed with methanol, water, and was rinsed by immersing and swirling in a solution of approximately 100 mg cetylpyridinium chloride in 10 mL water. It was again rinsed with water and methanol. A control substrate was treated via the same methods, with the exception that

no copper was added to the CuAAC solution. Fluorescent microscopy images were taken of both the control and clicked sample, which can be found in Figure 158.

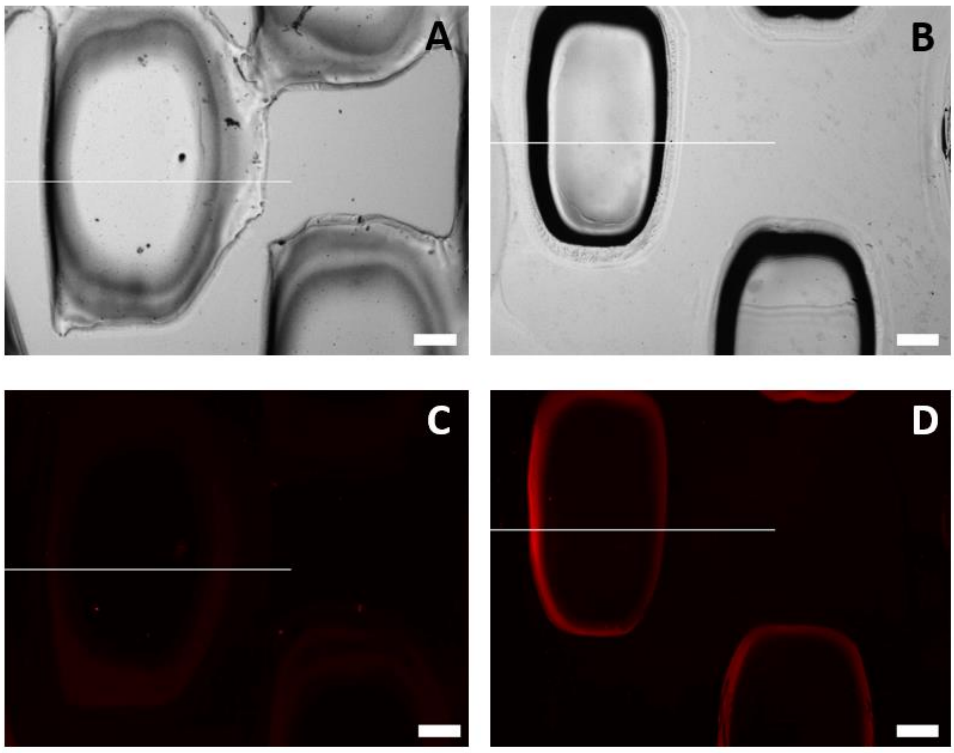

Figure 158. All scale bars are 200 microns. A) Control: Brightfield image of azidated SU-8, subjected to click conditions without the addition of copper, for a TAMRA-alkyne. B) Brightfield image of azidated SU-8, subjected to click conditions for a TAMRA-alkyne. C) Control: Fluorescent image of azidated SU-8, subjected to click conditions without the addition of copper, for a TAMRA-alkyne. D) Fluorescent image of azidated SU-8, subjected to click conditions for a TAMRA-alkyne.

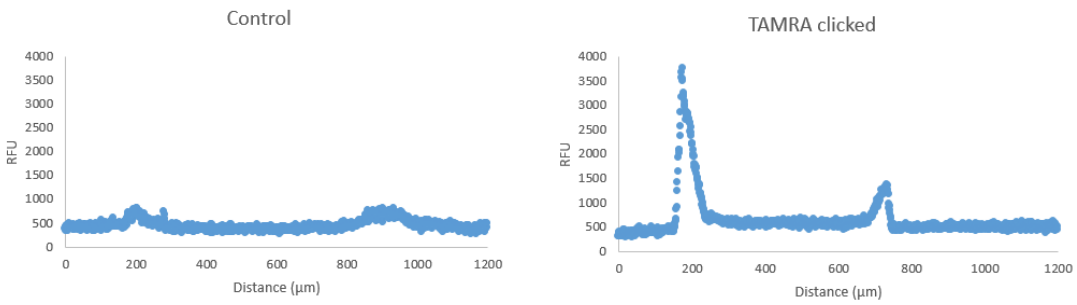

Figure 159. Fluorescent intensity across Figure 158 images C and D.

Figure 158 and Figure 159 demonstrates a significant difference in the fluorescent activity of D over C, which indicates that the fluorescent activity displayed in D is predominantly due to clicked attachment of the TAMRA dye, rather than the minute levels of nonconvalent adhesion displayed in C. The greater fluorescent intensities at the edges is attributed to CuAAC of the TAMRA alkyne along the sloped sides of the material.

4.4.2.4 CuAAC of ATRP initiator onto SU-8 surface and polymerization from surface

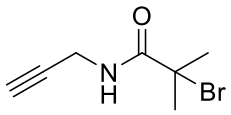

Figure 160. Structure of the clickable ATRP initiator, propargyl 2-bromo-2-methylpropionamide

To attach propargyl 2-bromo-2-methylpropionamide to the SU-8 surface via CuAAC, 8 mg of the clickable initiator, 2 mg copper sulfate, 8 mg sodium ascorbate, and 10 mg tetrabutylammonium bromide were dissolved in 15 mL water and an azidated SU-8 substrate was added. This was shaken at room temperature for 2 hours gently on an

orbital shaker plate. The sample was then removed and rinsed with water and methanol, then dried immediately. Examples of XPS spectra for these samples can be found in Figure 163 and Figure 164, which demonstrate the appearance of a bromide peak, as well as a peak on the carbon spectrum indicating presence of a carbonyl (~288-298 eV).

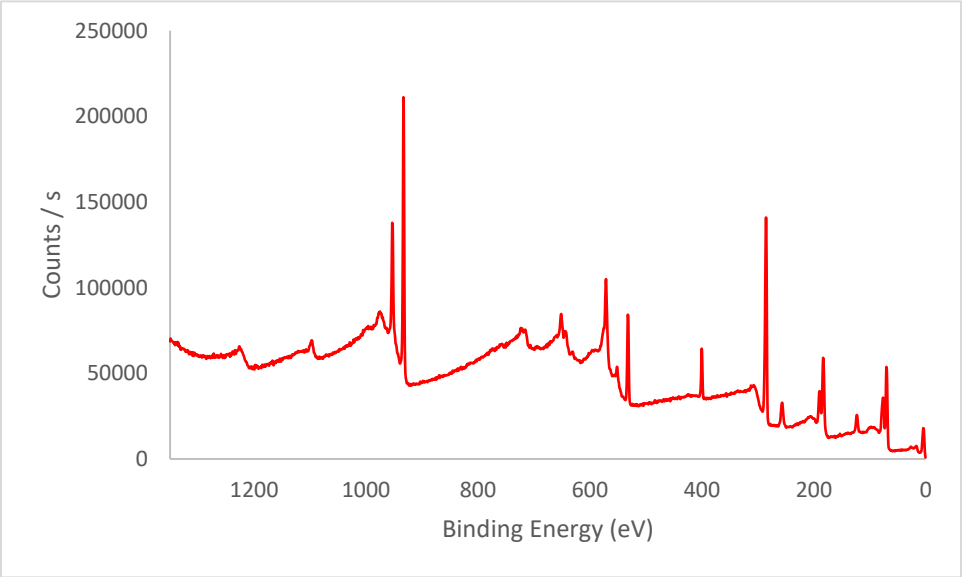

Figure 161. XPS spectrum for azidated SU-8 reacted via CuAAC with a clickable initiator, propargyl 2-bromo-2-methylpropionamide.

Table 63. XPS integration for azidated SU-8 reacted via CuAAC with a clickable initiator, propargyl 2-bromo-2-methylpropionamide.

Peak	Atomic %
C1s	67.33
O1s	10.82
N1s	8.10
Br3d	6.42
Cu2p3	7.33

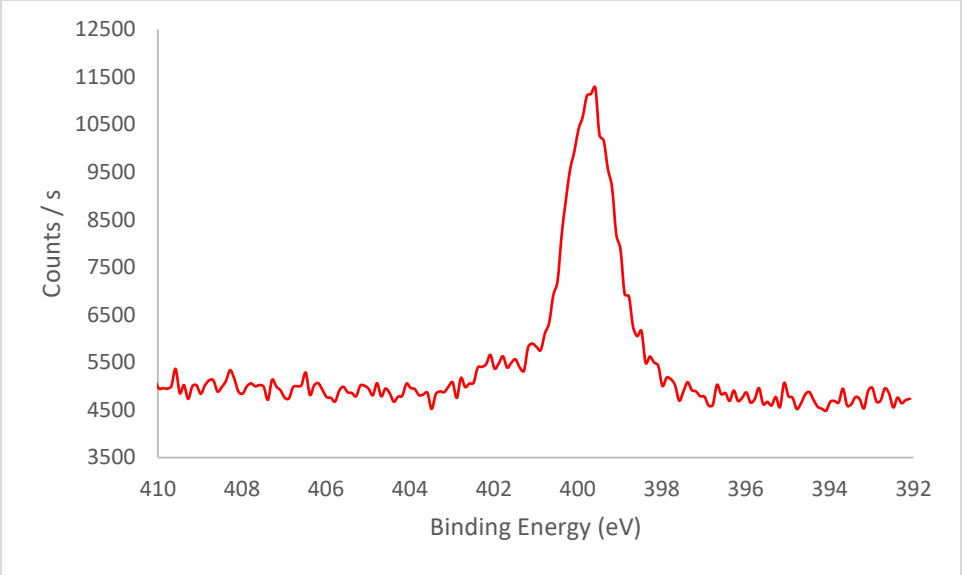

Figure 162. Nitrogen XPS spectrum for azidated SU-8 reacted via CuAAC with a clickable initiator, propargyl 2-bromo-2-methylpropionamide.

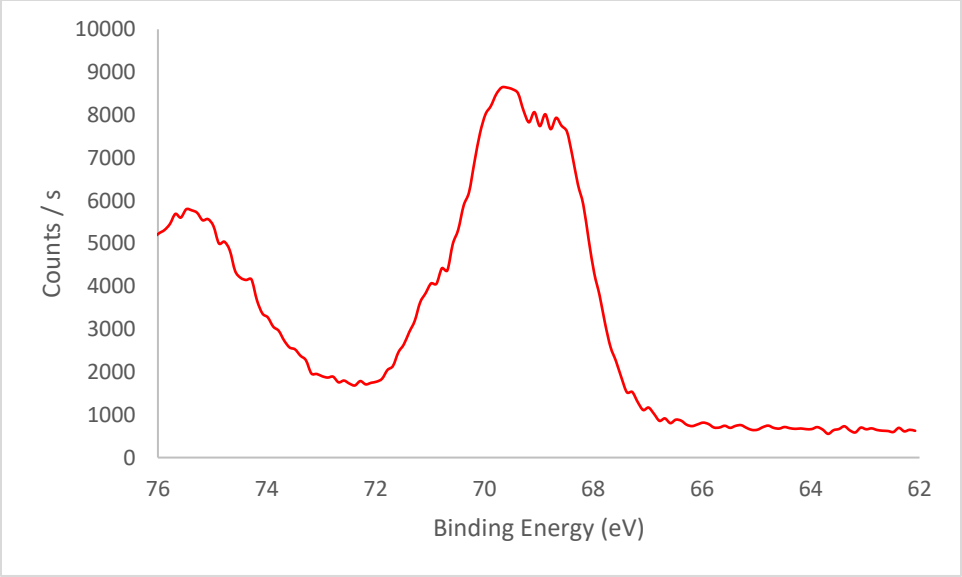

Figure 163. Bromine XPS spectrum for azidated SU-8 reacted via CuAAC with a clickable initiator, propargyl 2-bromo-2-methylpropionamide.

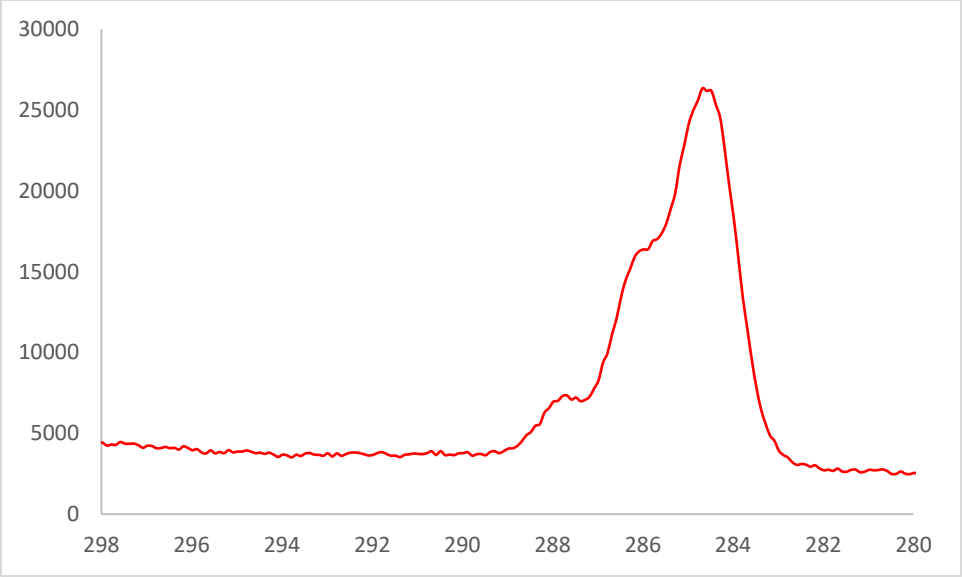

Figure 164. XPS carbon spectrum for azidated SU-8 reacted via CuAAC with a clickable initiator, propargyl 2-bromo-2-methylpropionamide.

These samples were then subject to ATRP conditions.

For the polymerization of MMA from the SU-8 surface, XPS analysis shows depletion of bromide from the surface, better definition of carbonyl peak (~288-289 eV), as well as a difference in nitrogen signal, which may indicate that the polymerization transpired but that Me_6-TREN may remain adhered.

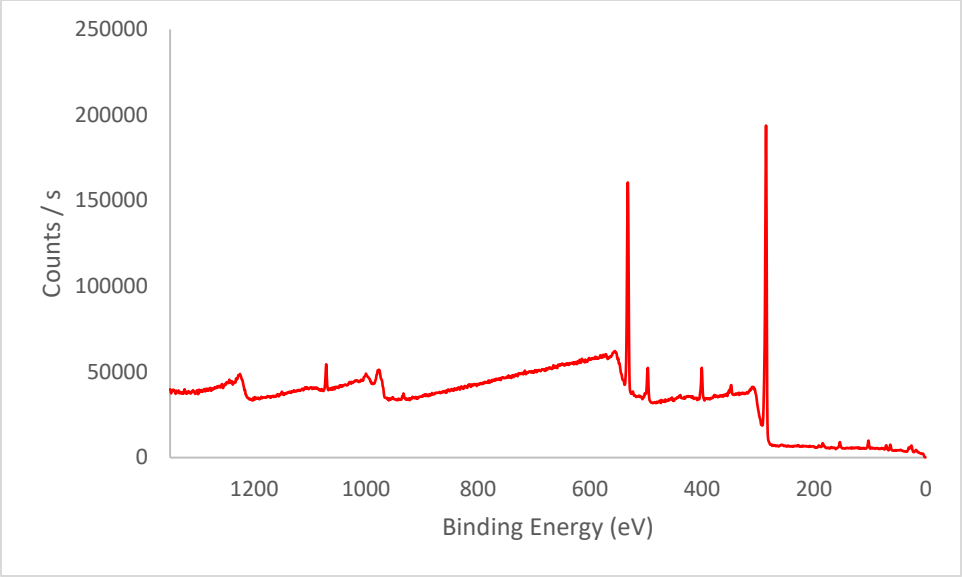

Figure 165. XPS spectrum for azidated SU-8 clicked with clickable initiator, then subject to ATRP conditions with MMA.

Table 64. XPS integration for azidated SU-8 clicked with clickable initiator, then subject to ATRP conditions with MMA.

Peak	Atomic %
C1s	71.65
O1s	20.58
N1s	5.02
Na1s	1.12
Si2p	1.62

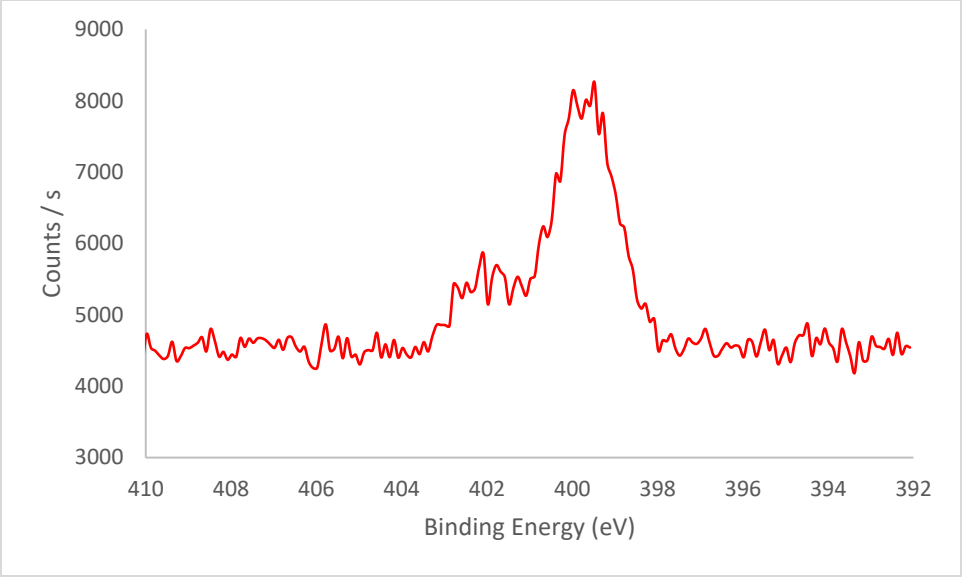

Figure 166. XPS nitrogen spectrum for azidated SU-8 clicked with clickable initiator, then subject to ATRP conditions with MMA.

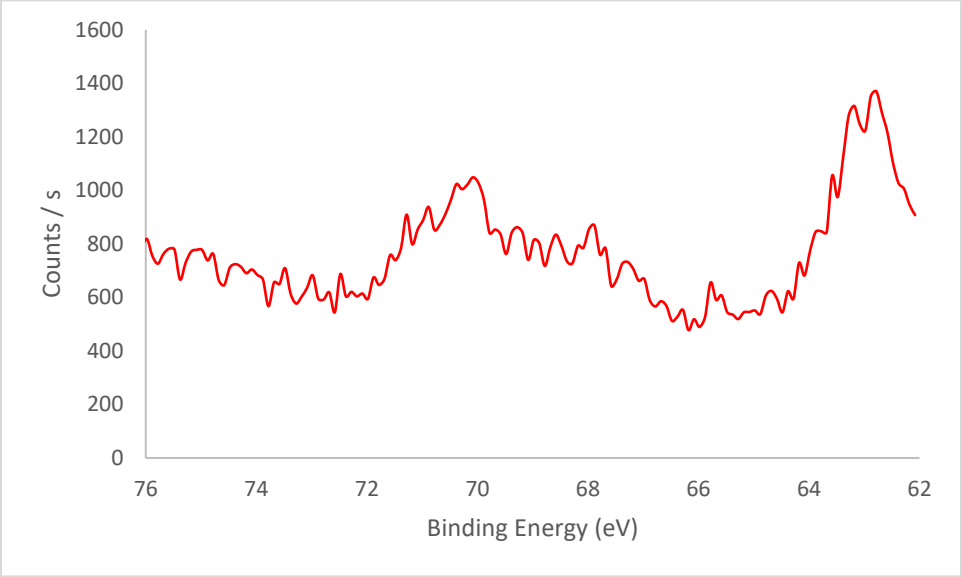

Figure 167. XPS bromine spectrum for azidated SU-8 clicked with clickable initiator, then subject to ATRP conditions with MMA.

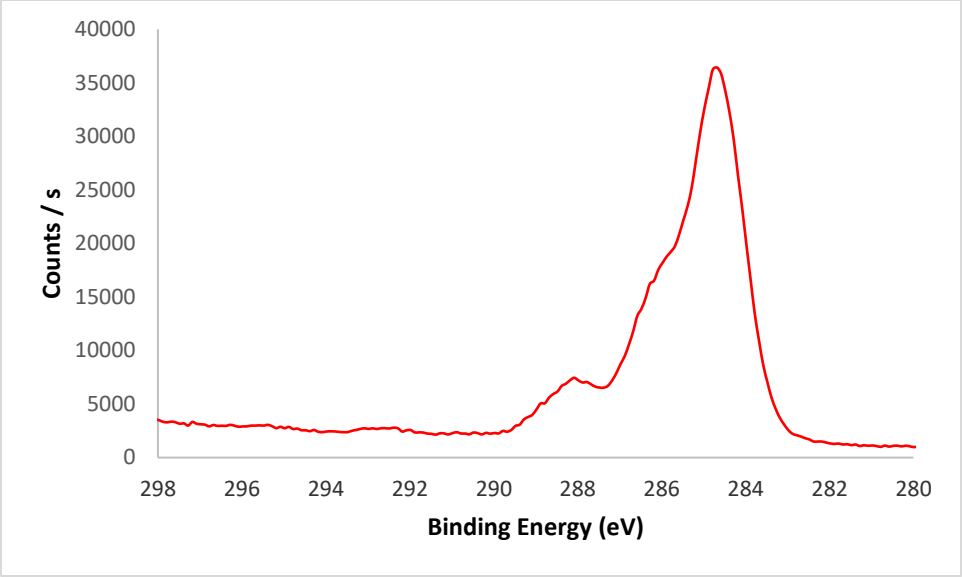

Figure 168. XPS carbon spectrum for azidated SU-8 clicked with clickable initiator, then subject to ATRP conditions with MMA.

For the sample where 4-vinylpyridine was polymerized from the SU-8 surface, a color change from clear / white to brown was noted, and XPS analysis showed removal of the bromide peak.

Figure 169. Image of azidated SU-8, subjected to CuAAC with a clickable ATRP initiator, then subject to ATRP conditions with 4-vinyl pyridine. The color of the sample changed from clear to brown during the reaction and could not be removed by extensive rinsing with water and methanol.

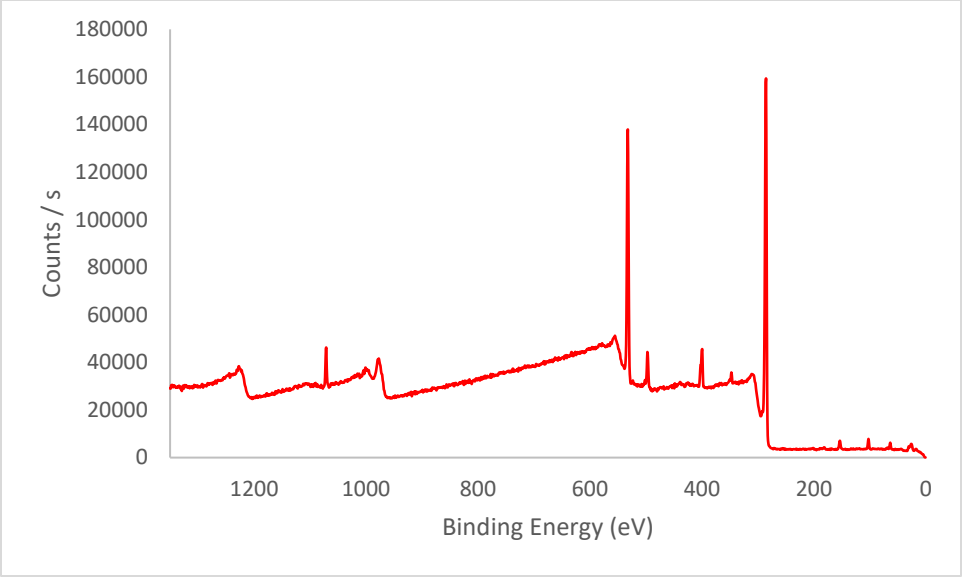

Figure 170. XPS survey spectrum for azidated SU-8 clicked with clickable initiator, then subject to ATRP conditions with 4VP.

Table 65. XPS survey spectrum integration for azidated SU-8 clicked with clickable initiator, then subject to ATRP conditions with 4VP.

Peak	Atomic %
C1s	71.15
O1s	20.05
N1s	5.85
Na1s	1.42
Si2p	1.62

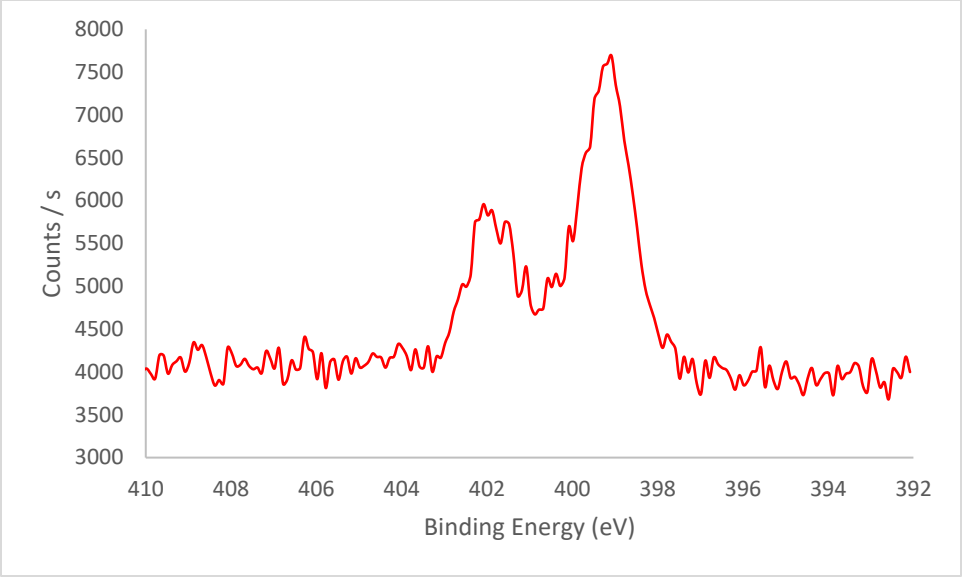

Figure 171. XPS nitrogen spectrum for azidated SU-8 clicked with clickable initiator, then subject to ATRP conditions with 4VP.

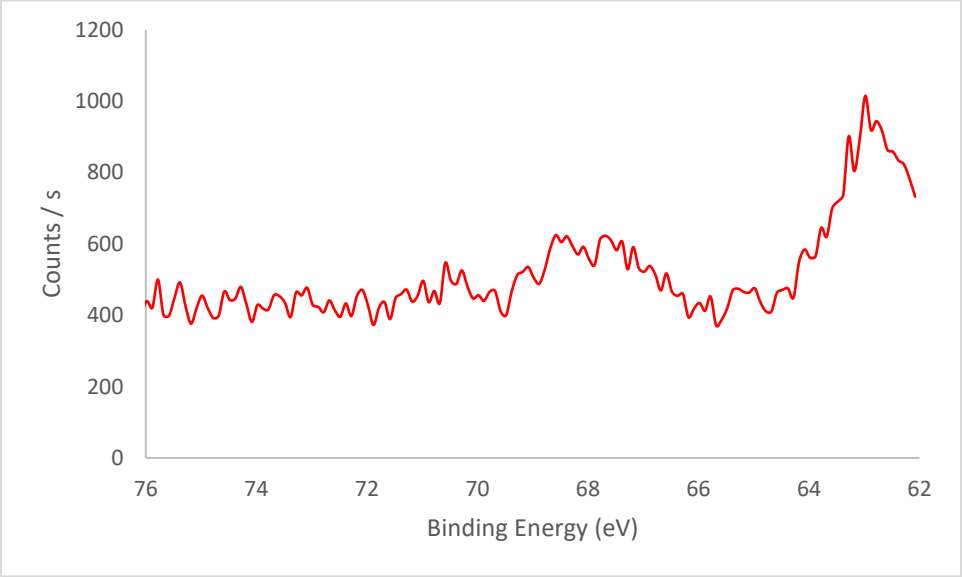

Figure 172. XPS bromine spectrum for azidated SU-8 clicked with clickable initiator, then subject to ATRP conditions with 4VP.

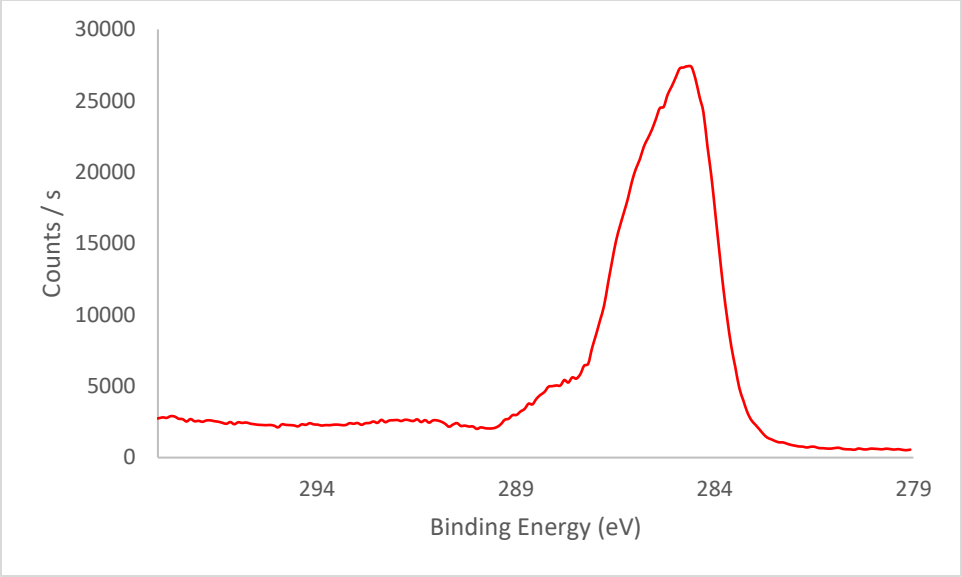

Figure 173. XPS carbon spectrum for azidated SU-8 clicked with clickable initiator, then subject to ATRP conditions with 4VP.

4.4.3 Characterization of Materials

4.4.3.1 Contact Angle

Modifications made to the surface of SU-8 exhibited large changes in contact angle, from initially hydrophobic surfaces, to hydrophilic surfaces when charged groups were attached. Contact angle measurements can be viewed in

Table 66.

Table 66. Measured contact angle for SU-8 substrates.

Substrate	Contact Angle
Unmodified SU-8	79.0 ± 2.1
Azidated SU-8	63.0 ± 4.3
Azidated SU-8 clicked with quaternary amine	37.0 ± 12.2
Azidated SU-8 clicked with ATRP initiator	49.2 ± 7.7
Azidated SU-8 clicked with ATRP initiator and subjected to polymerization conditions with MMA	71.5 ± 8.1
Azidated SU-8 clicked with ATRP initiator and subjected to polymerization conditions with 4-vinylpyridine. Value in parenthesis represents Contact angle at pH = 3.	50.0 ± 2.8 (54.9 ± 5.6)
Azided SU-8 clicked with propargyl alcohol	79.4 ± 2.9

4.4.3.2 Scanning Electron Microscopy

Unmodified SU-8 as viewed by SEM is relatively smooth, with only a few small raised bumps extending from the surface.

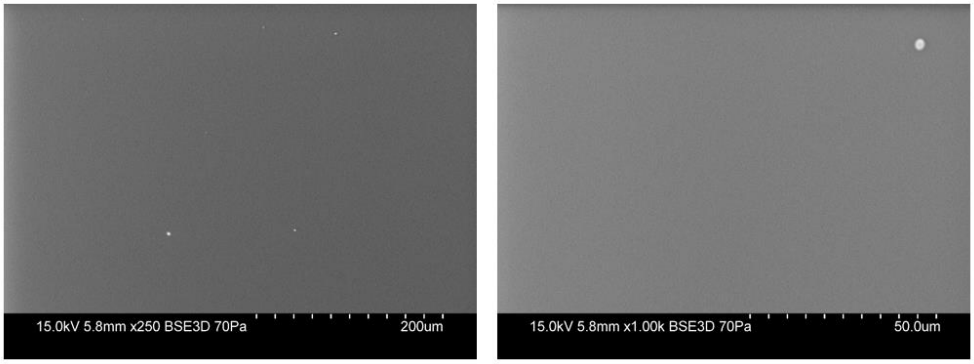

Figure 174. SEM images for unmodified SU-8.

For samples that were azidated, the surface appeared relatively smooth, with only a few more raised blemishes on the surface as visual by observation under SEM.

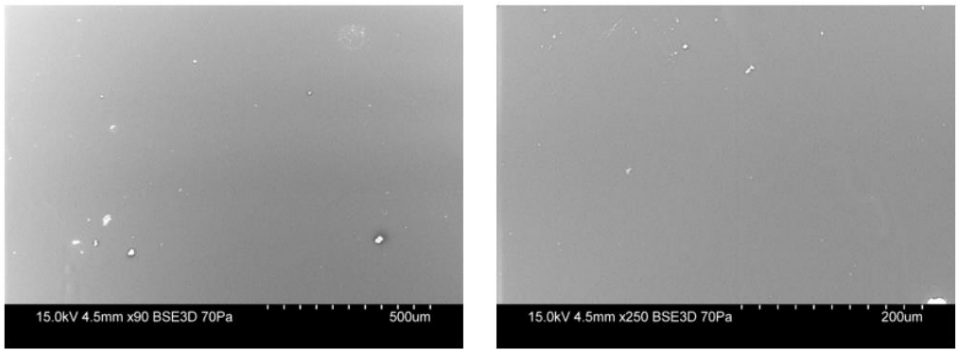

Figure 175. SEM images of azidated SU-8.

For samples azidated and clicked with quaternary amine, more small raised areas were present, and some cracking was visible near polymer edges.

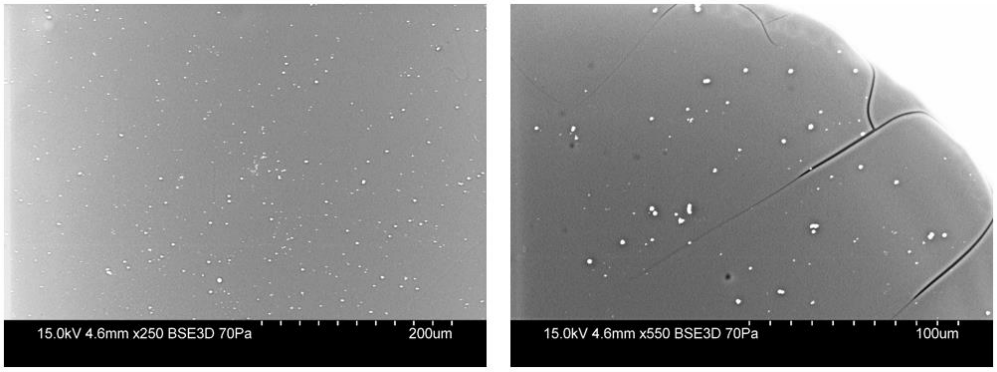

Figure 176. SEM images of azidated SU-8 clicked with quaternary amine.

For samples azidated and clicked with the clickable initiator, SEM images of the surface show small raised areas and some cracking, as displayed in Figure 177.

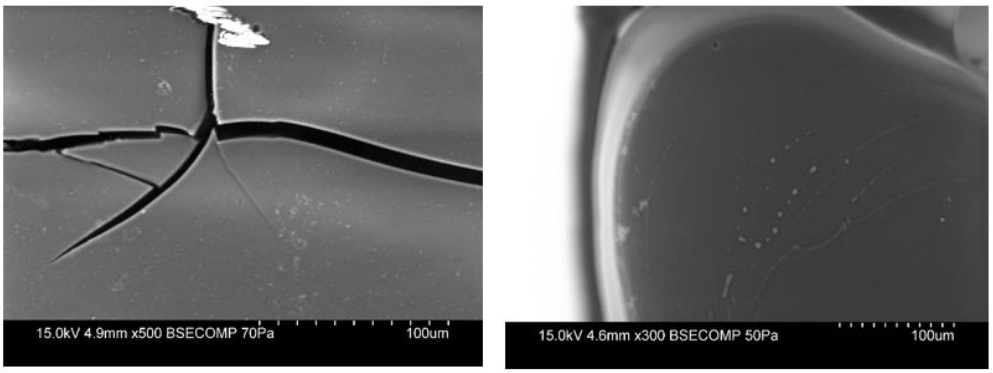

Figure 177. SEM images of azidated SU-8 reacted via CuAAC with a clickable initiator, propargyl 2-bromo-2-methylpropionamide.

For samples that were subjected to polymerization conditions with 4VP, SEM images showed less apparent cracking than samples that had not been subjected to polymerization conditions, which may suggest a successful polymerization from the surface.

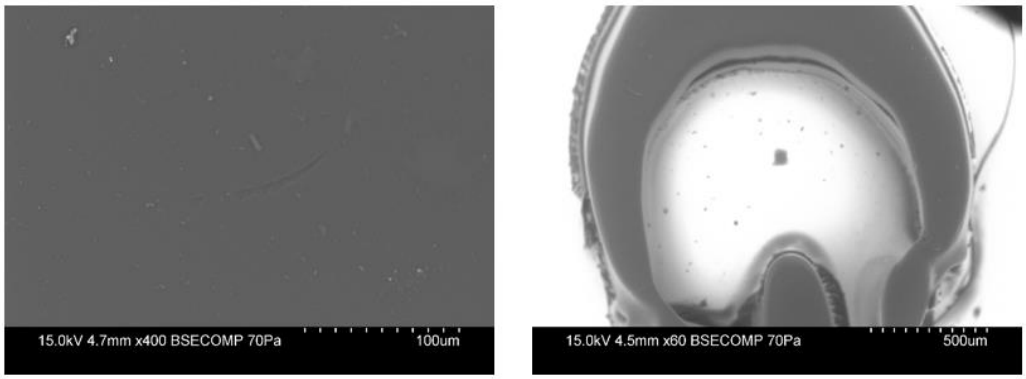

Figure 178. SEM images from azidated SU-8 clicked with clickable initiator, then subject to ATRP conditions with 4VP.

4.4.4 Biological Interactions with CuAAC-modified SU-8

4.4.4.1 Mammalian Cell Toxicity

Substrates (azidated and azidated clicked with quaternary ammonium cation) were immersed in a solution of freshly split CHO cells in supplemented DMEM media. These were incubated for 24 hours. The cells were then evaluated under a microscope to access morphology. The cells all demonstrated typical morphology and normal adherence to the surface, with no indications of cell death when subjected to Sytox Red to label dead cells, which suggests no evident toxicity of the surface to the cells.

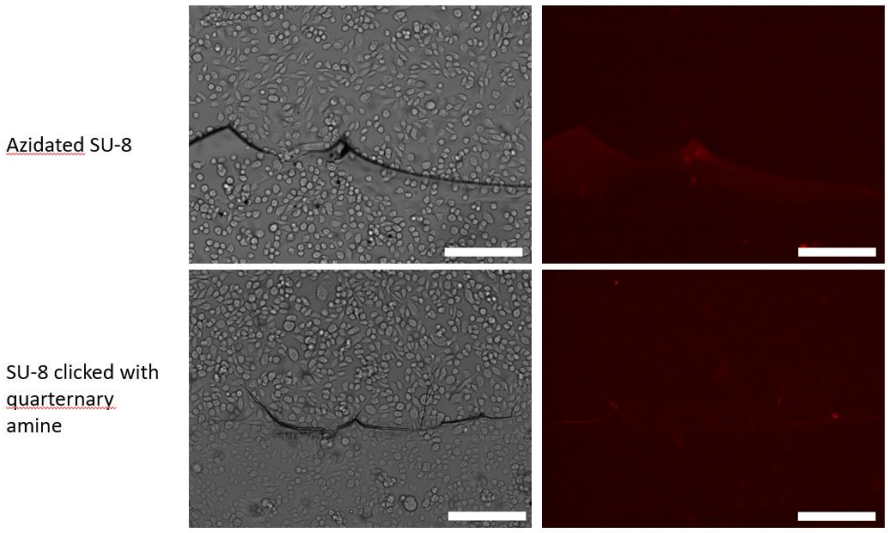

Figure 179. Top left: Brightfield image of CHO cells on SU-8 substrate (bottom half of image). Top right: Fluorescent image of CHO cells on SU-8 substrate with Sytox red. Bottom left: Brightfield image of CHO cells on SU-8 substrate (top half of image). Bottom right: Fluorescent image of CHO cells on SU-8 substrate with Sytox red. All scale bars are 200 µm.

Red blood cells were also incubated with the substrates. Cells were allowed to settle for 40 minutes, then incubated for 1 hour. Erythrocytes which deposited onto the quaternary ammonium surface (and to some extent the azidated surface) exhibited Burr cell-like morphology, although not lysed (as evaluated by absorbance measurements at 414 nm), while erythrocytes that deposited onto control slides with either plain ITO or azidated SU-8 clicked with propargyl alcohol exhibited typical morphology. Figure 180 depicts the erythrocyte morphology.

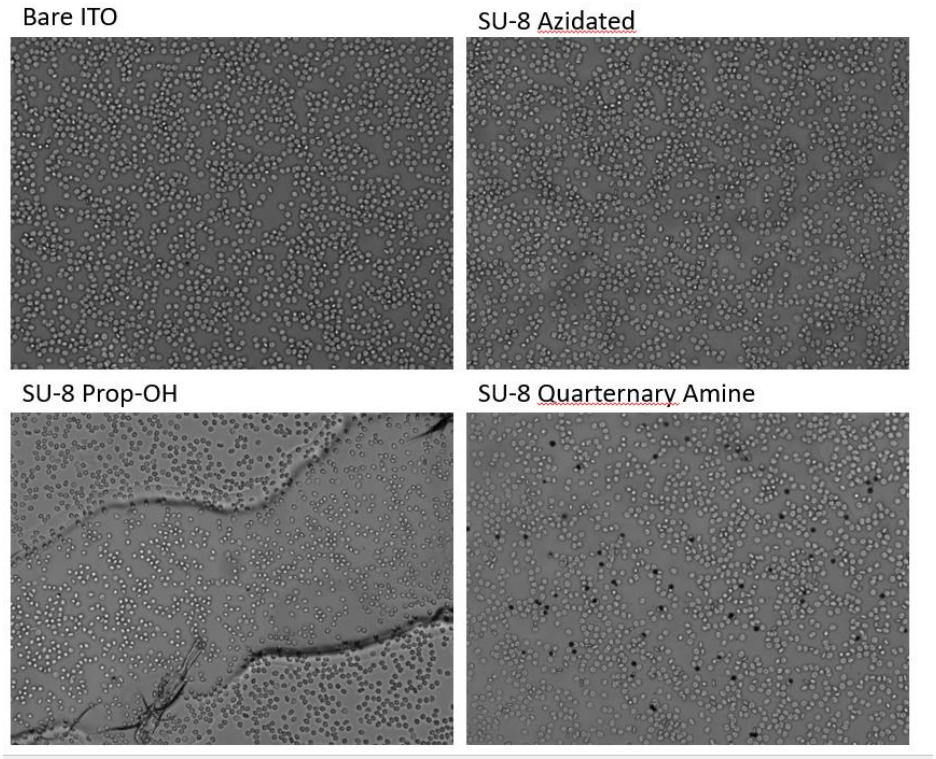

Figure 180. Brightfield images of red blood cells on SU-8 substrates at 100x whole field views.

4.4.4.2 Bacteria Killing with Quaternary Ammonium Cation Substrates.

Positively charged polymer surfaces have been noted to kill bacteria.[100,101] Following in this vein, as a demonstration for potential application, versatility, and

function, we clicked quaternary ammonium surfaces to the SU-8 surface and assessed the ability of this surface to kill bacteria.

With E. coli DH5α, killing was observed on the quaternary ammonium surface after 20 minutes to allow bacteria to settle and following a 60 minute incubation period, as depicted in Figure 181. The bacterial killing ability of the quaternary ammonium SU-8 (as visualized with Sytox Red) was directly compared to azidated SU-8 clicked with propargyl alcohol, which exhibited only minor amounts of fluorescence.

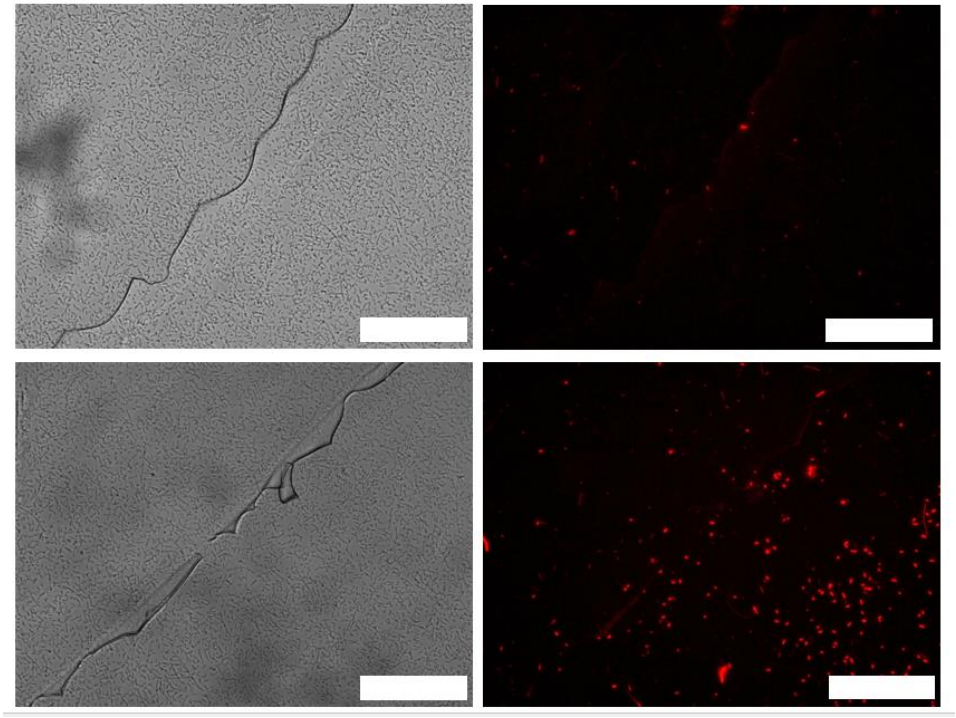

Figure 181. All images at 60 minutes, following a 20 minute settling time. All scale bars are 50 µm. Top left: Brightfield image of E. coli DH5α on ITO glass (left) and azidated SU-8 clicked with propargyl alcohol (right) with Sytox red. Top right: Fluorescent image of E. coli DH5α on ITO glass (left) and azidated SU-8 clicked with propargyl alcohol (right) with Sytox red. Bottom left: Brightfield image of E. coli DH5α on ITO glass (left) and azidated SU-8 clicked with QA (right). Bottom right: Fluorescent image of E. coli DH5α on ITO glass (left) and azidated SU-8 clicked with QA (right) with Sytox red.

After 20 minutes of settling and 270 or 330 minutes incubation time, fluorescence was observed for areas even without polymer, which was attributed to cells dying and rolling off the polymer surface to other areas of the slide, while the control sample exhibited little fluorescence, as displayed in Figure 182 and Figure 183.

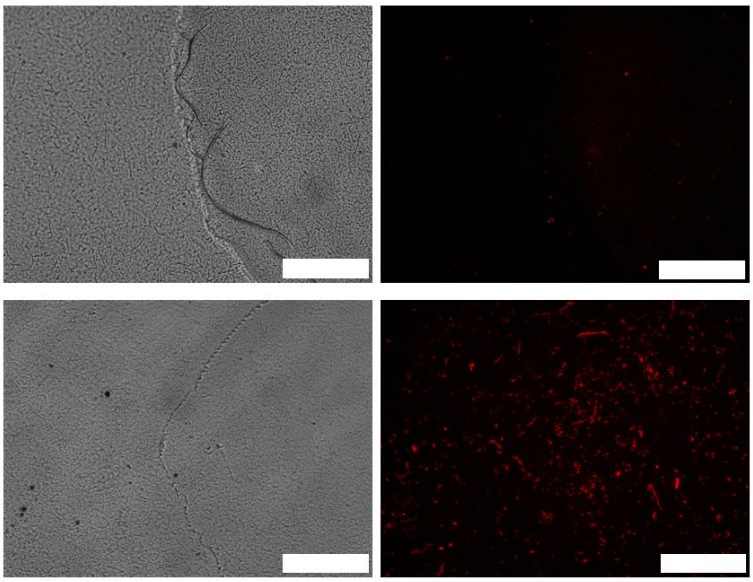

Figure 182. All images at 270 minutes, following a 20 minute settling time. All scale bars are 50 µm. Top left: Brightfield image of E. coli DH5α on ITO glass (left) and azidated SU-8 clicked with propargyl alcohol (right) with Sytox red. Top right: Fluorescent image of E. coli DH5α on ITO glass (left) and azidated SU-8 clicked with propargyl alcohol (right) with Sytox red. Bottom left: Brightfield image of E. coli DH5α on ITO glass (left) and azidated SU-8 clicked with QA (right). Bottom right: Fluorescent image of E. coli DH5α on ITO glass (left) and azidated SU-8 clicked with QA (right) with Sytox red.

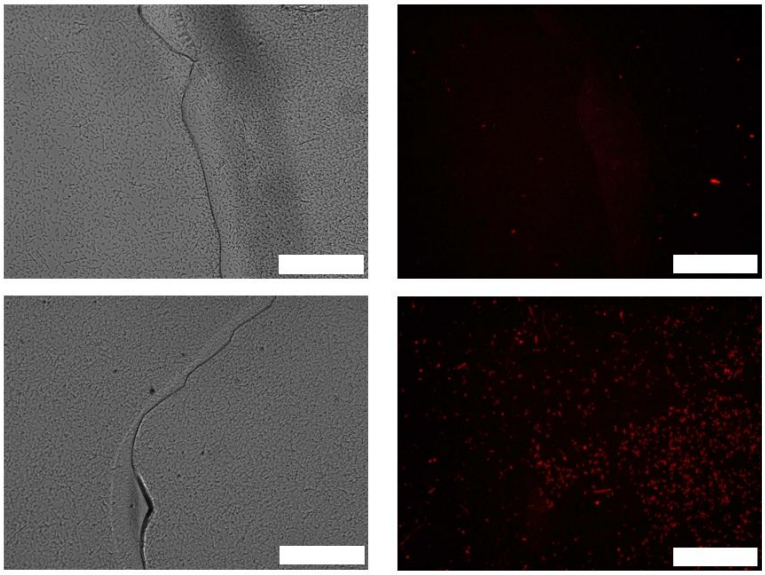

Figure 183. All images at 330 minutes, following a 20 minute settling time. All scale bars are 50 µm Top left: Brightfield image of E. coli DH5α on ITO glass (left) and azidated SU-8 clicked with propargyl alcohol (right) with Sytox red. Top right: Fluorescent image of E. coli DH5α on ITO glass (left) and azidated SU-8 clicked with propargyl alcohol (right) with Sytox red. Bottom left: Brightfield image of E. coli DH5α on ITO glass (left) and azidated SU-8 clicked with QA (right). Bottom right: Fluorescent image of E. coli DH5α on ITO glass (left) and azidated SU-8 clicked with QA (right) with Sytox red.

The intensity per unit area on and off the polymer was calculated for all DH5α images and demonstrates a significant difference between the polymer and ITO surface, however, it does not fully represent the total killing effect, as it is suspected that dead cells are detaching from the QA surface and are rolling onto bare ITO areas, thereby decreasing the overall difference in fluorescence intensity per unit area for QA surfaces as depicted in Figure 184.

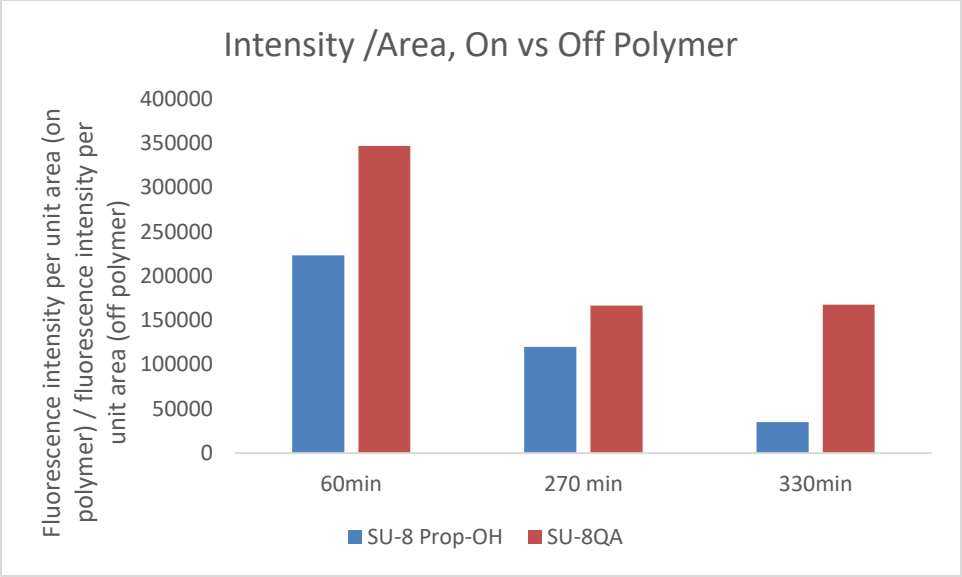

Figure 184. Fluorescence quantitation for DH5α killing activity of quaternary amine SU-8.

No significant killing was observed for *S. aureus* on the quaternary ammonium surface in comparison to the control azidated SU-8 surface that had been clicked with propargyl alcohol.

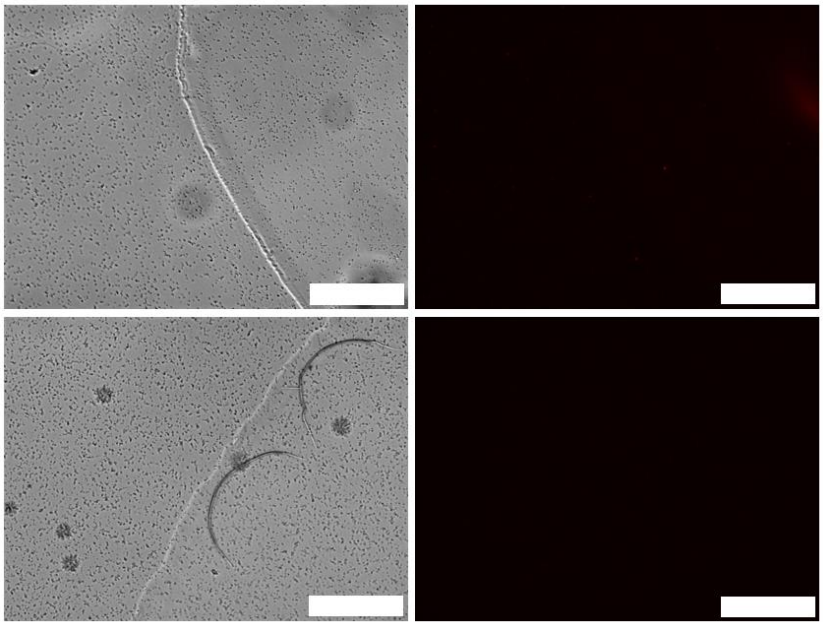

Figure 185. All images at 330 minutes, following a 20 minute settling time. All scale bars are 50 µm. Top left: Brightfield image of S. aureus on ITO glass (left) and azidated SU-8 clicked with propargyl alcohol (right) with Sytox red. Top right: Fluorescent image of S. aureus on ITO glass (left) and azidated SU-8 clicked with propargyl alcohol (right) with Sytox red. Bottom left: Brightfield image of S. aureus on ITO glass (left) and azidated SU-8 clicked with QA (right). Bottom right: Fluorescent image of S. aureus on ITO glass (left) and azidated SU-8 clicked with QA (right) with Sytox red.

4.5 Discussion

The process of forming patterned SU-8 polymer with the printed photomask, UV-light, and hot plate then subjecting it to azidation and CuAAC in a laboratory setting (without a cleanroom) was relatively simple. Some challenges arose, however, in obtaining good attachment to the ITO glass substrates, particularly after subjecting it to chemical processes, and the polymer itself was brittle and fragile. By reducing reaction time and temperature, these challenges were reduced, although still present. Modified SU-8

remained biocompatible, although a difference in erythrocyte morphology was observed on the surface decorated with a positive charge group.

The attachment of a very simple positively charged quaternary ammonium group to the SU-8 surface had a significant killing effect for *E.coli*. It could then be anticipated that the attachment of compounds or polymers reported to have stronger antibacterial activity would have an even greater effect and may be able to affect a broader set of bacterial strains, if such functionality was desired. Other applications could include sensors and implantable electronics, which require new and chemically addressable materials to bring their technology to a wider array of uses and environments.

4.6 Conclusions

SU-8 is a negative photoresist useful for a number of applications including electronics and microelectromechanical systems. By creating a route to derivitize SU-8 for click chemistry, devising CuAAC conditions for a variety of alkynes, and addressing some of the challenges associated with these modifications, this work makes SU-8 chemically addressable for a broader variety of uses, as desired by the user. Assays with CHO cells and erythrocytes verifies that the modifications made (and in general, triazole formation) do not affect SU-8's biocompatibility, which allows for use of this chemistry on SU-8 toward biological applications.

4.7 Acknowledgement

This work was performed in coordination with Dr. Michael Baksh, who assisted with the photo-polymerization of SU-8, performed the optical and fluorescent microscopy, and cultured CHO cells. This work was performed in part at the Georgia Tech Institute for Electronics and Nanotechnology, a member of the National Nanotechnology Coordinated Infrastructure, which is supported by the National Science Foundation (Grant ECCS-1542174). We thank Dr. Caroline Hansen, Dr. Elaissa Hardy, Dr. Yongzhi Qiu, and Dr. Yumiko Sakurai of the Lam lab at Georgia Tech for providing whole blood, as well as Ruyi Yang for experimental assistance with contact angle measurements. We also thank the Roy Lab at Georgia Tech for use of instrumentation.

CHAPTER 5. OUTLOOK FOR FURTHER DEVELOPMENT

5.1 Further Developments with Lipids

One potential criticism of the works performed herein with lipids could be that the lipids used to understand CuAAC kinetics and behavior in and between membrane systems are quite dissimilar from biological lipids—namely that the synthesized lipids are lyso-like lipids (which do occur in nature, however, are less predominant in membranes than lipids with alkyl two-chains and have different rates of dissociation from membranes[102,103,104,105]) and positioned within the membrane by either quaternary ammonium cations or glycosylation. Although the azidocoumarin indicator provided a useful tool to probe reactivity in and between membranes, future kinetic studies would benefit from the synthesis of more relevant click lipids, which could provide more information about the orientation of the lipids within the membrane. Additionally, natural membranes contain cholesterol, a bidirectional regulator of membrane fluidity. A more fluid membrane system as would be expected with cholesterol also would be expected to show an even faster rate for the intravesicular reaction between azide and alkyne lipids, which may provide further differentiation between the intravesicular and intervesicular reactions in- and between-lipid vesicles.

5.2 Further Developments with PVC

5.2.1 Surfaces to prevent biofouling

With the ability to easily modify a flexible PVC surface while maintaining the material properties, it follows that this would have great applications for biofouling in

medical and marine industries. By clicking on polymer functional groups known to have antifouling properties, a broad class of modified PVC derivatives can be created to allow for surfaces that can respond to biological encroachment in a variety of ways, either repelling or killing on contact. Examples of moieties to be clicked on include polymeric quaternary ammonium compounds,[106] proteins known to effect antimicrobial activity,[107] and other polymers demonstrating antifouling activity.[108]

5.3 Further Development with SU-8

5.3.1 Better surface adhesion for SU-8 substrates

The composition of SU-8 has been somewhat optimized over time, to allow for better adhesion to some materials. In the course of this work, however, it became clear that when subject to some reaction conditions, namely prolonged exposure to moisture, SU-8 tended to detach from glass and (at times) ITO surfaces. While this was limited through short exposure times to moisture and proper pre-treatment of ITO glass, detachment still sometimes occurred. Improvements to the SU-8 monomer solution to allow better glass adhesion or other pre-treatment methods that allow for a stronger adhesion to glass or ITO glass would be a welcome improvement to facilitate implementation and use of SU-8 materials.

5.3.2 SU-8 developments to reduce fragility

SU-8, as a polymer has a number of desirable characteristics, namely, its facile polymerization and high aspect ratio; however, the polymer itself is extremely fragile and inflexible, particularly after handling and modification. It has a tendency to crack, fracture,

and break off in chunks when pressure is applied. Efforts to improve the resilience of the polymer, by methods such as co-polymerization or the addition of plasticizers could limit the cracking and fracturing of SU-8 and improve its ease of use for other applications, although care would need to be taken to minimize changes to other desired properties of the polymer.

5.3.3 Rad-Hard Electronics

SU-8, as a polymer, is considered rad-hard, meaning, when exposed to significant amounts of radiation it maintains its structure and properties.[109] Additional surface modification through techniques detailed here could be used to provide new classes of materials for space or nuclear electronics applications, although work would be needed to understand the stability of modifications made to SU-8 and triazole formation under extended exposure to ionizing radiation.

5.3.4 Implantable electronics

Based on the apparent biocompatibility of each of the SU-8 samples evaluated, it is likely that other SU-8 derivatives would also be non-toxic to cells. This would allow for the use of derivatized SU-8 for implantable electronics, which may alleviate some of the challenges with silicon rubber coated electronics such as an unpredictable life-time and water permeation, where an inflexible circuit would not be prohibitively challenging.[110]

5.3.5 Sensors

SU-8 has a number of desirable properties for sensors, including a high aspect ratio and easy patterning. By modifying specific areas, it is possible to create areas of chemical

functionality adjacent to an electrode in order to sense a desired change and provide local feedback through an electronic means.

REFERENCES

[1] Kolb, H. C.; Finn, M. G.; Sharpless, K. B., Click Chemistry: Diverse Chemical Function from a Few Good Reactions. *Angewandte Chemie International Edition* **2001,** *40* (11), 2004-2021.

[2] Rostovtsev, V. V.; Green, L. G.; Fokin, V. V.; Sharpless, K. B., A Stepwise Huisgen Cycloaddition Process: Copper(I)-Catalyzed Regioselective "Ligation" of Azides and Terminal Alkynes. *Angewandte Chemie International Edition* **2002**, *41* (14), 2596-2599.

[3] Tornøe, C. W.; Christensen, C.; Meldal, M., Peptidotriazoles on Solid Phase: [1,2,3]-Triazoles by Regiospecific Copper(I)-Catalyzed 1,3-Dipolar Cycloadditions of Terminal Alkynes to Azides. *The Journal of Organic Chemistry* **2002,** *67* (9), 3057-3064.

[4] Worrell, B. T.; Malik, J. A.; Fokin, V. V., Direct Evidence of a Dinuclear Copper Intermediate in Cu(I)-Catalyzed Azide-Alkyne Cycloadditions. *Science* **2013,** *340* (6131), 457-460.

[5] Huisgen, R., 1,3-Dipolar Cycloadditions. Past and Future. *Angewandte Chemie International Edition in English* **1963,** *2* (10), 565-598.

[6] Presolski, S. I.; Hong, V.; Cho, S. H.; Finn, M. G., Tailored ligand acceleration of the Cu-catalyzed azide-alkyne cycloaddition reaction: practical and mechanistic implications. *J Am Chem Soc* **2010,** *132* (41), 14570-6.

[7] Lewis, W. G.; Green, L. G.; Grynszpan, F.; Radic, Z.; Carlier, P. R.; Taylor, P.; Finn, M. G.; Sharpless, K. B., Click chemistry in situ: acetylcholinesterase as a reaction vessel for the selective assembly of a femtomolar inhibitor from an array of building blocks. *Angewandte Chemie* **2002,** *41* (6), 1053-7.

[8] Chan, T. R.; Hilgraf, R.; Sharpless, K. B.; Fokin, V. V., Polytriazoles as copper(I)-stabilizing ligands in catalysis. *Organic Letters* **2004**, *6* (17), 2853-5.

[9] Lewis, W. G.; Magallon, F. G.; Fokin, V. V.; Finn, M. G., Discovery and characterization of catalysts for azide-alkyne cycloaddition by fluorescence quenching. *J Am Chem Soc* **2004,** *126* (30), 9152-3.

[10] McKay, C. S.; Finn, M. G., Click chemistry in complex mixtures: bioorthogonal bioconjugation. *Chem Biol* **2014,** *21* (9), 1075-101.

[11] Malkoch, M.; Schleicher, K.; Drockenmuller, E.; Hawker, C. J.; Russell, T. P.; Wu, P.; Fokin, V. V., Structurally Diverse Dendritic Libraries: A Highly Efficient Functionalization Approach Using Click Chemistry. *Macromolecules* **2005,** *38* (9), 3663-3678.

[12] Wu, P.; Malkoch, M.; Hunt, J. N.; Vestberg, R.; Kaltgrad, E.; Finn, M. G.; Fokin, V. V.; Sharpless, K. B.; Hawker, C. J., Multivalent, bifunctional dendrimers prepared by click chemistry. *Chem Commun (Camb)* **2005,** (46), 5775-7.

[13] McKay, C. S.; Finn, M. G., Polyvalent Catalysts Operating on Polyvalent Substrates: A Model for Surface-Controlled Reactivity. *Angewandte Chemie* **2016,** *55* (41), 12643-9.

[14] Goess, B. C.; Hannoush, R. N.; Chan, L. K.; Kirchhausen, T.; Shair, M. D., Synthesis of a 10,000-Membered Library of Molecules Resembling Carpanone and Discovery of Vesicular Traffic Inhibitors. *Journal of the American Chemical Society* **2006,** *128* (16), 5391-5403.

[15] Fazio, F.; Bryan, M. C.; Blixt, O.; Paulson, J. C.; Wong, C.-H., Synthesis of Sugar Arrays in Microtiter Plate. *Journal of the American Chemical Society* **2002,** *124* (48), 14397-14402.

[16] Tron, G. C.; Pirali, T.; Billington, R. A.; Canonico, P. L.; Sorba, G.; Genazzani, A. A., Click chemistry reactions in medicinal chemistry: applications of the 1,3-dipolar cycloaddition between azides and alkynes. *Med Res Rev* **2008,** *28* (2), 278-308.

[17] Sen Gupta, S.; Raja, K. S.; Kaltgrad, E.; Strable, E.; Finn, M. G., Virus-glycopolymer conjugates by copper(I) catalysis of atom transfer radical polymerization and azide-alkyne cycloaddition. *Chem Commun (Camb)* **2005,** (34), 4315-7.

[18] Parrish, B.; Breitenkamp, R. B.; Emrick, T., PEG- and Peptide-Grafted Aliphatic Polyesters by Click Chemistry. *Journal of the American Chemical Society* **2005,** *127* (20), 7404-7410.

[19] Binder, W. H.; Kluger, C., Combining Ring-Opening Metathesis Polymerization (ROMP) with Sharpless-Type "Click" Reactions: An Easy Method for the Preparation of Side Chain Functionalized Poly(oxynorbornenes). *Macromolecules* **2004,** *37* (25), 9321-9330.

[20] Sumerlin, B. S.; Tsarevsky, N. V.; Louche, G.; Lee, R. Y.; Matyjaszewski, K., Highly Efficient "Click" Functionalization of Poly(3-azidopropyl methacrylate) Prepared by ATRP. *Macromolecules* **2005,** *38* (18), 7540-7545.

[21] Díaz, D. D.; Punna, S.; Holzer, P.; McPherson, A. K.; Sharpless, K. B.; Fokin, V. V.; Finn, M. G., Click chemistry in materials synthesis. 1. Adhesive polymers from

copper-catalyzed azide-alkyne cycloaddition. *Journal of Polymer Science Part A: Polymer Chemistry* **2004,** *42* (17), 4392-4403.

[22] Meng, J. C.; Averbuj, C.; Lewis, W. G.; Siuzdak, G.; Finn, M. G., Cleavable linkers for porous silicon-based mass spectrometry. *Angewandte Chemie* **2004,** *43* (10), 1255-60.

[23] Collman, J. P.; Devaraj, N. K.; Chidsey, C. E. D., "Clicking" Functionality onto Electrode Surfaces. *Langmuir* **2004,** *20* (4), 1051-1053.

[24] Lummerstorfer, T.; Hoffmann, H., Click Chemistry on Surfaces: 1,3-Dipolar Cycloaddition Reactions of Azide-Terminated Monolayers on Silica. *The Journal of Physical Chemistry B* **2004,** *108* (13), 3963-3966.

[25] Rodionov, V. O.; Presolski, S. I.; Gardinier, S.; Lim, Y. H.; Finn, M. G., Benzimidazole and related ligands for Cu-catalyzed azide-alkyne cycloaddition. *J Am Chem Soc* **2007,** *129* (42), 12696-704.

[26] Rodionov, V. O.; Presolski, S. I.; Diaz, D. D.; Fokin, V. V.; Finn, M. G., Ligand-accelerated Cu-catalyzed azide-alkyne cycloaddition: a mechanistic report. *J Am Chem Soc* **2007,** *129* (42), 12705-12.

[27] Meng, F.; Qiao, Z.; Yao, Y.; Luo, J., Synthesis of polyurethanes with pendant azide groups attached on the soft segments and the surface modification with mPEG by click chemistry for antifouling applications. *RSC Advances* **2018,** *8* (35), 19642-19650.

[28] Daugaard, A. E.; Hvilsted, S.; Hansen, T. S.; Larsen, N. B., Conductive Polymer Functionalization by Click Chemistry. *Macromolecules* **2008,** *41* (12), 4321-4327.

[29] Kumar, A. A process for preparing polymer composition of functionalized epoxy resist, polymer composition and applications thereof. **2013**. WO2013008072A2.

[30] Evans, C. E.; Lovell, P. A., Click chemistry as a route to surface functionalization of polymer particles dispersed in aqueous media. *Chem Commun (Camb)* **2009,** (17), 2305-7.

[31] Jayakrishnan, A.; Sunny, M. C., Phase transfer catalysed surface modification of plasticized poly(vinyl chloride) in aqueous media to retard plasticizer migration. *Polymer* **1996,** *37* (23), 5213-5218.

[32] Nunney, T., XPS Characterization of 'Click' Surface Chemistry. ThermoFisher, Ed. **2011**.

[33] Moulder, J. F. S., W.F; Sobol, P.E.; Bomben, K.D., *Handbook of X-Ray Photoelectron Spectroscopy*. Physical Electronics Eden Prairie, MN, 1993.

[34] Joubert, L. M., Variable Pressure-SEM: a versatile tool for visualization of hydrated and non-conductive specimens. In *Microscopy and imaging science: practical approaches to applied research and education*, Mendez-Vilas, A., Ed. 2017; pp 655-662.

[35] Simons, K.; Vaz, W. L. C., Model Systems, Lipid Rafts, and Cell Membranes. *Annual Review of Biophysics and Biomolecular Structure* **2004,** *33* (1), 269-295.

[36] Edidin, M., The state of lipid rafts: From model membranes to cells. *Annual Review of Biophysics and Biomolecular Structure* **2003,** *32*, 257-283.

[37] van Meer, G.; Voelker, D. R.; Feigenson, G. W., Membrane lipids: where they are and how they behave. *Nature reviews. Molecular cell biology* **2008,** *9* (2), 112-124.

[38] M'Baye, G.; Mély, Y.; Duportail, G.; Klymchenko, A. S., Liquid Ordered and Gel Phases of Lipid Bilayers: Fluorescent Probes Reveal Close Fluidity but Different Hydration. *Biophysical Journal* **2008,** *95* (3), 1217-1225.

[39] Menger, F. M.; Azov, V. A., Cytomimetic Modeling in Which One Phospholipid Liposome Chemically Attacks Another. *Journal of the American Chemical Society* **2000,** *122* (27), 6492-6493.

[40] Menger, F. M.; Caran, K. L.; Seredyuk, V. A., Chemical Reaction between Colliding Vesicles. *Angewandte Chemie International Edition* **2001,** *40* (20), 3905-3907.

[41] Jones, J. D.; Thompson, T. E., Spontaneous Phosphatidylcholine Transfer by Collision Between Vesicles at High Lipid-Concentration. *Biochemistry* **1989,** *28* (1), 129-134.

[42] Brown, R. E.; Hyland, K. J., Spontaneous Transfer of Ganglioside GM1 from Its Micelles to Lipid Vesicles of Differing Size. *Biochemistry* **1992,** *31* (43), 10602-10609.

[43] Kunze, A.; Svedhem, S.; Kasemo, B., Lipid Transfer between Charged Supported Lipid Bilayers and Oppositely Charged Vesicles. *Langmuir* **2009,** *25* (9), 5146-5158.

[44] Weisiger, R. A.; Zucker, S. D., Transfer of fatty acids between intracellular membranes: roles of soluble binding proteins, distance, and time. *American Journal of Physiology-Gastrointestinal and Liver Physiology* **2002,** *282* (1), G105-G115.

[45] Jao, C. Y.; Roth, M.; Welti, R.; Salic, A., Metabolic labeling and direct imaging of choline phospholipids in vivo. *Proceedings of the National Academy of Sciences* **2009,** *106* (36), 15332-15337.

[46] Rodionov, V. O.; Fokin, V. V.; Finn, M. G., Mechanism of the ligand-free CuI-catalyzed azide-alkyne cycloaddition reaction. *Angewandte Chemie* **2005,** *44* (15), 2210-5.

[47] Gaebler, A.; Milan, R.; Straub, L.; Hoelper, D.; Kuerschner, L.; Thiele, C., Alkyne lipids as substrates for click chemistry-based in vitro enzymatic assays. *Journal of lipid research* **2013,** *54* (8), 2282-90.

[48] Gubbens, J.; Ruijter, E.; de Fays, L. E.; Damen, J. M.; de Kruijff, B.; Slijper, M.; Rijkers, D. T.; Liskamp, R. M.; de Kroon, A. I., Photocrosslinking and click chemistry enable the specific detection of proteins interacting with phospholipids at the membrane interface. *Chem Biol* **2009,** *16* (1), 3-14.

[49] Baskin, J. M.; Prescher, J. A.; Laughlin, S. T.; Agard, N. J.; Chang, P. V.; Miller, I. A.; Lo, A.; Codelli, J. A.; Bertozzi, C. R., Copper-free click chemistry for dynamic in vivo imaging. *Proceedings of the National Academy of Sciences* **2007,** *104* (43), 16793-16797.

[50] Maier, O.; Oberle, V.; Hoekstra, D., Fluorescent lipid probes: some properties and applications (a review). *Chemistry and Physics of Lipids* **2002,** *116* (1–2), 3-18.

[51] Hardy, M. D.; Yang, J.; Selimkhanov, J.; Cole, C. M.; Tsimring, L. S.; Devaraj, N. K., Self-reproducing catalyst drives repeated phospholipid synthesis and membrane growth. *Proceedings of the National Academy of Sciences* **2015,** *112* (27), 8187-8192.

[52] Sivakumar, K.; Xie, F.; Cash, B. M.; Long, S.; Barnhill, H. N.; Wang, Q., A fluorogenic 1,3-dipolar cycloaddition reaction of 3-azidocoumarins and acetylenes. *Organic letters* **2004,** *6* (24), 4603-6.

[53] Soriano del Amo, D.; Wang, W.; Jiang, H.; Besanceney, C.; Yan, A. C.; Levy, M.; Liu, Y.; Marlow, F. L.; Wu, P., Biocompatible Copper(I) Catalysts for in Vivo Imaging of Glycans. *Journal of the American Chemical Society* **2010,** *132* (47), 16893-16899.

[54] Abramson, M. B.; Katzman, R.; Gregor, H. P., Aqueous Dispersions of Phosphatidylserine: Ionic Properties. *Journal of Biological Chemistry* **1964,** *239* (1), 70-76.

[55] Hong, V.; Presolski, S. I.; Ma, C.; Finn, M. G., Analysis and optimization of copper-catalyzed azide-alkyne cycloaddition for bioconjugation. *Angewandte Chemie* **2009,** *48* (52), 9879-83.

[56] Chapman, D.; Quinn, P. J., Method for Modulation of Membrane Fluidity - Homogeneous Catalytic Hydrogenation of Phospholipids and Phospholipid-Water Model Biomembranes. *Proceedings of the National Academy of Sciences* **1976,** *73* (11), 3971-3975.

[57] Rahman, M.; Brazel, C. S., The plasticizer market: an assessment of traditional plasticizers and research trends to meet new challenges. *Progress in Polymer Science* **2004,** *29* (12), 1223-1248.

[58] Asadinezhad, A.; Lehocký, M.; Sáha, P.; Mozetič, M., Recent Progress in Surface Modification of Polyvinyl Chloride. *Materials* **2012,** *5* (12), 2937-2959.

[59] Marcilla, A.; García, S.; García-Quesada, J. C., Study of the migration of PVC plasticizers. *Journal of Analytical and Applied Pyrolysis* **2004,** *71* (2), 457-463.

[60] Jayakrishnan, A.; Lakshmi, S., Immobile plasticizer in flexible PVC. *Nature* **1998,** *396* (6712), 638-638.

[61] Martínez, G., Synthesis of PVC-g-PS through stereoselective nucleophilic substitution on PVC. *Journal of Polymer Science Part A: Polymer Chemistry* **2006,** *44* (8), 2476-2486.

[62] Hidalgo, M.; Gonzalez, L.; Mijangos, C., Crosslinking of plasticized poly(vinyl chloride) by substitution and free-radical reaction. *Journal of Applied Polymer Science* **1996,** *61* (8), 1251-1257.

[63] Lamanna, M.; D'Accorso, N., New copolymers with heterocyclic pendant groups obtained from PVC using microwave-assisted process. *Journal of Applied Polymer Science* **2011,** *121* (2), 951-956.

[64] Pawlak, M.; Mistlberger, G.; Bakker, E., In situ surface functionalization of plasticized poly(vinyl chloride) membranes by 'click chemistry'. *Journal of Materials Chemistry* **2012,** *22* (25), 12796.

[65] Earla, A.; Braslau, R., Covalently Linked Plasticizers: Triazole Analogues of Phthalate Plasticizers Prepared by Mild Copper-Free "Click" Reactions with Azide-Functionalized PVC. *Macromolecular Rapid Communications* **2014,** *35* (6), 666-671.

[66] Earla, A.; Li, L.; Costanzo, P.; Braslau, R., Phthalate plasticizers covalently linked to PVC via copper-free or copper catalyzed azide-alkyne cycloadditions. *Polymer* **2017,** *109*, 1-12.

[67] Pawlak, M.; Grygolowicz-Pawlak, E.; Crespo, G. A.; Mistlberger, G.; Bakker, E., PVC-Based Ion-Selective Electrodes with Enhanced Biocompatibility by Surface Modification with "Click" Chemistry. *Electroanalysis* **2013,** *25* (8), 1840-1846.

[68] Liu, Y.; Xue, Y.; Tang, H.; Wang, M.; Qin, Y., Click-immobilized K+-selective ionophore for potentiometric and optical sensors. *Sensors and Actuators B: Chemical* **2012,** *171–172*, 556-562.

[69] Lakshmi, S.; Kumar, S. S. P.; Jayakrishnan, A., Bacterial adhesion onto azidated poly(vinyl chloride) surfaces. *Journal of Biomedical Materials Research* **2002,** *61* (1), 26-32.

[70] Menger, F. M.; Venkataram, U. V., A microscopic hydrophobicity parameter. *Journal of the American Chemical Society* **1986,** *108* (11), 2980-2984.

[71] Neef, A. B.; Schultz, C., Selective fluorescence labeling of lipids in living cells. *Angewandte Chemie* **2009,** *48* (8), 1498-500.

[72] Lieber, E.; Rao, C. N. R.; Chao, T. S.; Hoffman, C. W. W., Infrared Spectra of Organic Azides. *Analytical Chemistry* **1957,** *29* (6), 916-918.

[73] Kameda, T.; Fukuda, Y.; Grause, G.; Yoshioka, T., Chemical modification of rigid poly(vinyl chloride) by the substitution with nucleophiles. *J. Appl. Polym. Sci.* **2010,** *116*, 36-44.

[74] Starnes, W. H.; Ge, X. L., Mechanism of autocatalysis in the thermal dehydrochlorination of poly(vinyl chloride). *Macromolecules* **2004,** *37*, 352-359.

[75] Starnes, W. H., Structural and mechanistic aspects of the thermal degradation of poly(vinyl chloride). *Prog. Polym. Sci.* **2002,** *27*, 2133-2170.

[76] Demko, Z. P.; Sharpless, K. B., Preparation of 5-Substituted 1H-Tetrazoles from Nitriles in Water. *The Journal of Organic Chemistry* **2001,** *66* (24), 7945-7950.

[77] Shaw, J. M.; Gelorme, J. D.; LaBianca, N. C.; Conley, W. E.; Holmes, S. J., Negative photoresists for optical lithography. *IBM Journal of Research and Development* **1997,** *41* (1.2), 81-94.

[78] Voskerician, G.; Shive, M. S.; Shawgo, R. S.; Recum, H. v.; Anderson, J. M.; Cima, M. J.; Langer, R., Biocompatibility and biofouling of MEMS drug delivery devices. *Biomaterials* **2003,** *24* (11), 1959-1967.

[79] Matarèse, B. F. E.; Feyen, P. L. C.; Falco, A.; Benfenati, F.; Lugli, P.; deMello, J. C., Use of SU8 as a stable and biocompatible adhesion layer for gold bioelectrodes. *Scientific Reports* **2018,** *8* (1), 5560.

[80] Lorenz, H.; Laudon, M.; Renaud, P., Mechanical characterization of a new high-aspect-ratio near UV-photoresist. *Microelectronic Engineering* **1998,** *41-42*, 371-374.

[81] http://www.microchem.com.

[82] Wang, Y.; Bachman, M.; Sims, C. E.; Li, G. P.; Allbritton, N. L., Simple Photografting Method to Chemically Modify and Micropattern the Surface of SU-8 Photoresist. *Langmuir* **2006,** *22* (6), 2719-2725.

[83] Bhimji, A.; Zaragoza, A. A.; Live, L. S.; Kelley, S. O., Electrochemical Enzyme-Linked Immunosorbent Assay Featuring Proximal Reagent Generation: Detection of Human Immunodeficiency Virus Antibodies in Clinical Samples. *Analytical Chemistry* **2013,** *85* (14), 6813-6819.

[84] Marie, R.; Schmid, S.; Johansson, A.; Ejsing, L.; Nordstrom, M.; Hafliger, D.; Christensen, C. B.; Boisen, A.; Dufva, M., Immobilisation of DNA to polymerised SU-8 photoresist. *Biosens Bioelectron* **2006,** *21* (7), 1327-32.

[85] Cavalli, G.; Banu, S.; Ranasinghe, R. T.; Broder, G. R.; Martins, H. F. P.; Neylon, C.; Morgan, H.; Bradley, M.; Roach, P. L., Multistep Synthesis on SU-8: Combining Microfabrication and Solid-Phase Chemistry on a Single Material. *Journal of Combinatorial Chemistry* **2007,** *9* (3), 462-472.

[86] Nordström, M.; Marie, R.; Calleja, M.; Boisen, A., Rendering SU-8 hydrophilic to facilitate use in micro channel fabrication. *Journal of Micromechanics and Microengineering* **2004,** *14* (12), 1614-1617.

[87] Joshi, M.; Kale, N.; Lal, R.; Ramgopal Rao, V.; Mukherji, S., A novel dry method for surface modification of SU-8 for immobilization of biomolecules in Bio-MEMS. *Biosens Bioelectron* **2007,** *22* (11), 2429-35.

[88] Tao, S. L.; Popat, K.; Desai, T. A., Off-wafer fabrication and surface modification of asymmetric 3D SU-8 microparticles. *Nature protocols* **2007,** *1*, 3153.

[89] Tao, S. L.; Popat, K. C.; Norman, J. J.; Desai, T. A., Surface Modification of SU-8 for Enhanced Biofunctionality and Nonfouling Properties. *Langmuir* **2008,** *24* (6), 2631-2636.

[90] Joshi, M.; Pinto, R.; Rao, V. R.; Mukherji, S., Silanization and antibody immobilization on SU-8. *Applied Surface Science* **2007,** *253* (6), 3127-3132.

[91] Stangegaard, M.; Wang, Z.; Kutter, J. P.; Dufva, M.; Wolff, A., Whole genome expression profiling using DNA microarray for determining biocompatibility of polymeric surfaces. *Molecular BioSystems* **2006,** *2* (9), 421-428.

[92] Wang, Y.; Pai, J.-H.; Lai, H.-H.; Sims, C. E.; Bachman, M.; Li, G. P.; Allbritton, N. L., Surface graft polymerization of SU-8 for bio-MEMS applications. *Journal of Micromechanics and Microengineering* **2007,** *17* (7), 1371-1380.

[93] Blagoi, G.; Keller, S.; Johansson, A.; Boisen, A.; Dufva, M., Functionalization of SU-8 photoresist surfaces with IgG proteins. *Applied Surface Science* **2008,** *255* (5), 2896-2902.

[94] Amantini, D.; Fringuelli, F.; Piermatti, O.; Tortoioli, S.; Vaccaro, L., Nucleophilic ring opening of 1,2-epoxides in aqueous medium. *Arkivoc* **2002,** *xi*, 293-311.

[95] Sabitha, G.; Babu, R. S.; Reddy, M. S.; Yadav, J. S., Ring Opening of Epoxides and Aziridines with Sodium Azide using Oxone®in Aqueous Acetonitrile: A Highly Regioselective Azidolysis Reaction. *Synthesis* **2002,** (15), 2254-2258.

[96] Fringuelli, F.; Piermatti, O.; Pizzo, F.; Vaccaro, L., Ring Opening of Epoxides with Sodium Azide in Water. A Regioselective pH-Controlled Reaction. *The Journal of Organic Chemistry* **1999,** *64* (16), 6094-6096.

[97] Das, B.; Reddy, V. S.; Krishnaiah, M.; Rao, Y. K., Highly regio- and stereoselective ring-opening of epoxides and aziridines with sodium azide using ammonium-12-molybdophosphate. *Journal of Molecular Catalysis A: Chemical* **2007,** *270* (1-2), 89-92.

[98] Xu, Z.; Uddin, K. M. A.; Ye, L., Boronic Acid Terminated Thermo-Responsive and Fluorogenic Polymer: Controlling Polymer Architecture for Chemical Sensing and Affinity Separation. *Macromolecules* **2012,** *45* (16), 6464-6470.

[99] Tsarevsky, N. V.; Braunecker, W. A.; Brooks, S. J.; Matyjaszewski, K., Rational Selection of Initiating/Catalytic Systems for the Copper-Mediated Atom Transfer Radical Polymerization of Basic Monomers in Protic Media: ATRP of 4-Vinylpyridine. *Macromolecules* **2006,** *39* (20), 6817-6824.

[100] Tiller, J. C.; Liao, C. J.; Lewis, K.; Klibanov, A. M., Designing surfaces that kill bacteria on contact. *Proc Natl Acad Sci U S A* **2001,** *98* (11), 5981-5.

[101] Terada, A.; Yuasa, A.; Kushimoto, T.; Tsuneda, S.; Katakai, A.; Tamada, M., Bacterial adhesion to and viability on positively charged polymer surfaces. *Microbiology* **2006,** *152* (Pt 12), 3575-83.

[102] Hamilton, J. A., Fatty acid transport: difficult or easy? *Journal of lipid research* **1998,** *39* (3), 467-481.

[103] Pokorny, A.; Almeida, P. F. F.; Melo, E. C. C.; Vaz, W. L. C., Kinetics of Amphiphile Association with Two-Phase Lipid Bilayer Vesicles. *Biophysical Journal* **2000,** *78* (1), 267-280.

[104] Zhang, F.; Kamp, F.; Hamilton, J. A., Dissociation of Long and Very Long Chain Fatty Acids from Phospholipid Bilayers. *Biochemistry* **1996,** *35* (50), 16055-16060.

[105] Needham, D.; Zhelev, D. V., Lysolipid exchange with lipid vesicle membranes. *Annals of Biomedical Engineering* **1995,** *23* (3), 287-298.

[106] Zubris, D.; Minbiole, K.; Wuest, W., Polymeric Quaternary Ammonium Compounds: Versatile Antimicrobial Materials. *Current Topics in Medicinal Chemistry* **2016,** *17* (3), 305-318.

[107] Ganz, T., The role of antimicrobial peptides in innate immunity. *Integr Comp Biol* **2003,** *43* (2), 300-4.

[108] Liu, P.; Xu, G.; Pranantyo, D.; Xu, L. Q.; Neoh, K.-G.; Kang, E.-T., pH-Sensitive Zwitterionic Polymer as an Antimicrobial Agent with Effective Bacterial Targeting. *ACS Biomaterials Science & Engineering* **2018,** *4* (1), 40-46.

[109] Key, M. J.; Cindro, V.; Lozano, M., On the radiation tolerance of SU-8, a new material for gaseous microstructure radiation detector fabrication. *Radiation Physics and Chemistry* **2004,** *71* (5), 1003-1007.

[110] Debelle, A.; Hermans, L.; Bosquet, M.; Dehaeck, S.; Lonys, L.; Scheid, B.; Nonclercq, A.; Vanhoestenberghe, A., Soft Encapsulation of Flexible Electrical Stimulation Implant: Challenges and Innovations. *Eur J Transl Myol* **2016,** *26* (4), 6298.